

Doctorate Thesis

**Computing Global Postseismic Deformation in a Spherically
Symmetric, Non-Rotating, Viscoelastic and Isotropic (SNRVEI)
Earth Without Artificial Assumptions**

Submitted to

Department of Earth and Planetary Science,

The University of Tokyo

Yoshiyuki Tanaka

Geographical Survey Institute,

Ministry of Land, Infrastructure and Transport

January, 2006

Abstract

We introduce a new method by which to compute global postseismic deformation in a self-gravitating, spherically symmetric, non-rotating, viscoelastic and isotropic (SNRVEI) Earth model. Previous methods are based on too simplified Earth models that neglect compressibility and/or the continuous variation of the radial structure of Earth. This is because the previous mode summation techniques cannot avoid intrinsic numerical difficulties caused by the *innumerable* modes that appear in a realistic Earth model that considers such effects. In contrast, the proposed method enables both of these effects to be taken into account simultaneously. We carry out numerical inverse Laplace integration, which allows evaluation of the contribution from all of the innumerable modes of the realistic Earth model. Using this method, a complete set of Green's functions is obtained, including functions of the time variation of the displacement, gravity change, and the geoid height change at the surface for strike-slip, dip-slip, horizontal and vertical tensile point dislocations. As an Earth model, we employ the Preliminary Reference Earth Model (PREM) and a continuously varying viscosity profile. We further elucidate the effects of fine layering and compressibility on the postseismic deformation rate for large earthquakes ($M_w \sim 8$). The result shows that the difference between the Earth model employed in this study and those used in the previous studies is detectable with modern observational techniques such as GPS. This means that there is a possibility that we should re-examine a role of viscoelastic relaxation as a mechanism of postseismic deformation. As an example, we apply the method to the postseismic deformation due to the 2003 Tokachi-Oki Earthquake ($M_w = 8.0$) and show that the observed postseismic deformation can be explained by viscoelastic relaxation. This serves as a counterevidence against the results which explain the deformation purely by afterslip. In conclusion, the effects which have been neglected so far should be considered for theory to meet observational accuracy.

CONTENTS

- 1 Introduction: toward the establishment of a new method for computing global postseismic deformation based on a realistic Earth model
 - 1.1 Observation and theory of global deformation caused by earthquakes
 - 1.2 Postseismic deformation as observational facts
 - 1.3 Why spherical theory?
 - 1.4 Possible mechanisms of postseismic deformation and their determination
 - 1.5 Existing theories of global postseismic deformation and their intrinsic limitations
 - 1.6 Aims of the present study
- 2 Existing theories of global deformation mechanisms
 - 2.1 Overview of theoretical framework of global deformation
 - 2.2 Normal mode method
 - 2.3 Numerical difficulties in the normal mode method
 - 2.4 Avoid the numerical difficulties using the unwarranted assumptions
- 3 A new method for computing global postseismic deformation
 - 3.1 Principles of the method
 - 3.2 Determination of the appropriate path
 - 3.3 Visible effects of compressibility on the integrand
 - 3.4 Growth mode
 - 3.5 Formulation of the new method
 - 3.6 Summary
- 4 Computational results
 - 4.1 Confirmation of the algorithm
 - 4.2 Green's function
 - 4.3 Behavior of Green's function
 - 4.4 Mechanisms that govern various patterns of postseismic deformation
 - 4.5 Effect of fine layering
 - 4.6 Effect of compressibility

4

4.7 Summary

5 Application of the new method

5.1 The 2003 Tokachi-Oki Earthquake

5.2 The Sumatra-Andaman Islands Earthquake of 26 December 2004

6 Conclusions

A Numerical solution of the differential equation

A1 Spheroidal mode

A2 Toroidal mode

B Proof that s is a real number

C Postseismic deformations at an arbitrary point

1 INTRODUCTION: TOWARD THE ESTABLISHMENT OF A NEW METHOD FOR COMPUTING GLOBAL POSTSEISMIC DEFORMATION BASED ON A REALISTIC EARTH MODEL

1.1 Observation and theory of global deformation caused by earthquakes

It is known from various geodetic observations and theoretical studies that earthquakes generate local and regional crustal movement (e.g., Steketee 1958; Matsu'ura 1977; Bock et al. 1993; Massonnet et al. 1993; Tsuji et al. 1995; Nishimura et al. 2003). Crustal deformations induced by large earthquakes ($M \sim 8$) with spatial scales exceeding 100 km have also been detected along the circum-Pacific seismic zone (Melbourne et al. 2002; Zweck et al. 2002; Hetland & Hager 2003; Ueda et al. 2003; Vergnolle et al. 2003) from early geodetic survey data (Fujii & Nakane 1983; Matsu'ura 1983) and recently developed global observational networks that use space geodetic techniques such as the Global Positioning System (GPS) (e.g., Seeber 2003). A remarkable example of such large-scale crustal deformation is that caused by the Sumatra-Andaman Islands Earthquake ($M=9.3$) on December 26, 2004. Figure 1 shows time series data of daily horizontal coordinates before and after the event at continuous GPS observation stations operated by the International GNSS (Global Navigation Satellite Systems) Service (Beutler et al. 1999). Analysis results of the coordinate data are provided by the Scripps Orbit and Permanent Array Center (SOPAC) via the internet (<http://sopac.ucsd.edu/>). The coseismic jump and subsequent rate change are observed even at sites with an epicentral distance in excess of 1,000 km.

To calculate such large crustal motions using a geophysical model, spherical Earth models should be used to ensure higher accuracy (Sun & Okubo 1993; Piersanti et al. 1995; Pollitz 1997; Wang 1999), rather than the flat-Earth approximations that are commonly used in computations of local and regional deformation (Sato & Matsu'ura 1973; Matsu'ura et al. 1981; Rundle 1982; Okada 1985). We can define such theories that consider the Earth's curvature as 'theories on global deformation'. We can also term crustal deformation at spatial scales in excess of approximately 100 km as 'global deformation'.

In the present thesis, we deal with theories on global deformation caused by large earthquakes,

including coseismic and postseismic deformations. We develop a new computational method that enables us to consider effects that have been neglected in previous theories on global postseismic deformation. The conclusion of the present study is that differences between the new method and conventional methods can amount to 50-60% at the maximum displacement rate, which is detectable with current observational techniques. In the rest of this chapter, we explain the background and purpose of this research in more detail.

1.2 Postseismic deformation as observational facts

We begin by defining the term postseismic deformation as used in the present thesis. Postseismic deformation is the transient motion observed following coseismic deformation, showing a gradually decaying displacement rate over a wide range of characteristic time-scales from a few weeks to more than 10 yrs. Tide gauge records and leveling data reveal that large earthquakes tend to cause postseismic deformations at longer time-scales (≥ 10 yrs.) (Thatcher & Rundle 1979, 1984; Barrientos et al. 1992; Larsen et al. 2003). In addition, the recent advent of space-borne geodetic techniques has successfully led to the detection of deformations caused by large events that occur at shorter time-scales (e.g., Bock et al. 1993; Deng et al. 1998; Heki & Tamura 1997; Jonsson et al. 2003).

As an example of postseismic deformation observed using GPS, we examine postseismic deformation caused by the 2003 Tokachi-Oki Earthquake (M8.0). Figure 2 displays a sequence of daily displacement data for the period from 8 yrs before the event until 2 yrs after the event, as measured at a station of the GPS Earth Observation Network in Japan, GEONET (Tsuji et al. 1995). The location of the source and the two GPS stations, including a fixed point, are shown in Fig. 3. Site 960532 is located approximately 100 km from the source. The baseline change, involving horizontal and vertical displacements of station 960532 relative to the fixed point 950154, clearly shows the instantaneous coseismic step and subsequent postseismic deformation that decays exponentially with time (Fig. 2). The secular trend 1.5 yrs after the event has yet to recover to that prior to the event, indicating that postseismic deformation is ongoing. The GEONET network also detected postseismic deformation in the same manner at inland stations with epicentral

distances in excess of 100 km (see Chapter 5). Changes in horizontal displacement velocity of a few millimeters per year is sufficient to be detected by the GPS network for an observation period of several years.

Several mechanisms have been proposed to explain different spatial and temporal patterns of postseismic deformation. Therefore, we define postseismic deformation only in terms of observational facts here, and will discuss mechanisms of postseismic deformation later in the text (Section 1.4).

1.3 Why spherical theory?

We have observed examples of global coseismic and postseismic deformation. To model such deformation, we need to consider the curvature of the Earth. By comparing theories based on spherical geometry with those based on a half-space medium, we show that the effect of neglecting Earth sphericity is not negligible for modern observational techniques.

A very small change in coseismic gravity related to the 2003 Tokachi-Oki Earthquake was detected by superconducting gravimeters to a precision of ‘sub-micro gal’ ($1 \text{ micro gal} = 10^{-8} \text{ m/s}^2$) at an observation site located approximately 1,000 km from the epicenter (Imanishi et al. 2004). Figure 3 illustrates the observational array of the superconducting gravimeters (indicated as SG). The triangle and circle symbols in Fig. 4 denote the observed and computed gravity change for the spherical Earth model, respectively (Sun & Okubo 1993; Imanishi et al. 2004). We added a gravity variation computed for the same fault model as that used by Imanishi et al. (2004), using Okubo’s theory for a flat-Earth model (Okubo 1992) (indicated by squares in Fig. 4). The error bars of the observed gravity change are too small to show in the figure ($0.005 \sim 0.009 \text{ microgal}$). Clearly, the effect of Earth sphericity should be considered because the difference between the two approaches is far in excess of the observational error involved in detecting coseismic change.

The effect of the curvature increases even more for postseismic deformation. Nostro et al. (1999) undertook a comprehensive study of the effect of sphericity on coseismic and postseismic deformation. The authors showed that the effect is significantly amplified in postseismic defor-

mation (Fig. 5). Antonioli et al. (1998) also recommended consider the effect of curvature for computations of postseismic stress diffusion associated with major earthquakes.

In addition to evaluating postseismic deformation in the far-field, spherical models are indispensable for investigating global deformation such as variations in Earth flattening and rotation, as large earthquakes necessarily perturb lower-degree spherical harmonics of the Earth's gravity field (Chao & Gross 1987). The lower-degree gravity field is precisely monitored by satellite gravity measurements such as the Gravity Recovery and Climate Experiment, GRACE (Dickey et al. 1997; Tapley et al. 2004), with accuracy of a few millimeters in determining the geoid height at a spatial resolution as small as 400 km. Changes in the lower-degree coefficients due to large earthquakes are routinely computed by the National Aeronautics and Space Administration (NASA), USA. For example, the detectability of the effects of the 2004 Sumatra-Andaman Islands Earthquake is discussed by Chao & Gross (2005).

1.4 Possible mechanisms of postseismic deformation and their determination

Coseismic crustal movements caused by earthquakes are well explained within the framework of elasticity dislocation theory, as introduced by Steketee (1958). In contrast, the possible mechanisms that cause postseismic deformation remains a controversial topic.

One mechanism is viscoelastic relaxation in the asthenosphere (e.g., Piersanti et al. 1997; Deng et al. 1998; Pollitz et al. 2001). This mechanism is based on the concept that the asthenosphere beneath the elastic lithosphere behaves as a viscous liquid over geological time-scales of more than several thousands of years, which is evident in postglacial rebound (Haskell 1935) and the concept of mantle convection (Richter & Parsons 1975). Physically, viscoelasticity can be modeled by combining a spring and a dash pot, with Maxwell time (ratio of viscosity to rigidity) representing the relaxation time. This means that the time-scale of a viscoelastic deformation is proportional to viscosity in the asthenosphere. Therefore, to model postseismic deformation having time-scales that range from several years to several tens of years, we have to assume that viscosity in the asthenosphere is a few orders of magnitude less than the value derived from observations of postglacial rebound. It follows that the existence of a lower-viscosity layer is indicated by employing

this mechanism, which is reasonable when we consider viscoelastic structure in plate boundary zones (see Chapter 5). Theories on global postseismic deformation, which adopt viscoelastic relaxation, are typically used to model long-lasting postseismic deformation over decades caused by large earthquakes in such plate boundary zones (e.g., Piersanti et al. 1997).

A second mechanism of postseismic deformation is afterslip (Heki & Tamura 1997; Miyazaki et al. 2004; Ozawa et al. 2004), which is commonly used to explain rapid postseismic deformations that take place from several days to several years following an event. In this mechanism, postseismic deformation is considered to be caused by slow fault slip that occurs around asperities (areas with large coseismic slip), without seismic radiation. We term such fault slip afterslip. This mechanism is supported by combining the following two facts. First, it is known from numerical simulations based on the results of rock fracture experiments that differences in frictional properties in the asperity compared to the non-asperity cause instantaneous slip in the former and peripheral afterslip in the latter (Tse & Rice 1986). Second, postseismic fault slip inferred from an inversion method using actual geodetic data distributes around the asperity (Ozawa et al. 2004); however, we note that the dynamic equation incorporating the frictional law employed in Tse & Rice (1986) is not solved in the inversion.

Inversion methods used to infer slip distribution, as in afterslip, are commonly used to account for other transient events that release stress without an abrupt coseismic slip event (Kawasaki et al. 1995; Dragert et al. 2001; Ozawa et al. 2002; Sagiya 2004).

Poroelastic deformation is also a possible mechanism of postseismic deformation, accompanied by liquid transfer induced by a coseismic stress change (Jonsson et al. 2003). This model is basically applied to explain transient motions at time-scales of several months (Jonsson et al. 2003).

In principle, we can determine the dominant mechanism of postseismic deformation by comparing the above three models with an observed postseismic deformation, as the theoretically predicted deformation patterns and characteristic time-scales are different for each of the three models. In practice, however, we cannot identify the dominant mechanism if we continue to use previously proposed methods of global viscoelastic relaxation, as the postseismic relaxation pre-

dicted by existing theories is based on unjustified assumptions and is therefore unreliable. This is considered in detail in the next section.

1.5 Existing theories of global postseismic deformation and their intrinsic limitations

In this section, we first review previous theories of global postseismic deformation, and then highlight the unjustified assumptions on which these theories are based.

In theories of global postseismic deformation, spherically symmetric Earth models are commonly used that employ radial variations in density, elastic constants, and viscosity. In addition, all such theories are based on ‘the normal mode method’, which is considered in detail in Chapter 2 (Table 1). Pollitz (1992) solved global postseismic deformation in a spherically symmetric, non-rotating, viscoelastic and isotropic (SNRVEI) Earth for the first time in the absence of self-gravitation, and approximately incorporated the effect in his subsequent theory (Pollitz 1997). The error of this approximation, however, exceeds 10% for deformations with wavelengths longer than 400 km (Pollitz 1997). Furthermore, his model consists of a limited number of layers, in which the allowable radial structure of density and gravity in the unperturbed state is restricted by the artificial constraint of $\rho(r)g(r) \equiv \frac{const.}{r}$. In addition, time variations in gravity changes are assumed to be zero from the beginning. Piersanti et al. (1995) developed a computational method assuming only incompressibility. This method has been widely used to explain observed postseismic deformation and its effect on polar motion (Piersanti et al. 1997; Boschi et al. 1997; Soldati et al. 2001). Wang (1999) considered compressibility by combining the normal mode method and reciprocity theorem (Okubo 1993). The Earth model in this method, however, is again oversimplified, with just 11 layers. Therefore, previous studies have used approximations of negligible compressibility and/or an oversimplified viscoelastic structure of the Earth (Table 1).

If we could practically neglect the effects of compressibility and the continuous radial structure of the Earth, there would then be no scope for improving the theory; however, these assumptions are not necessarily valid. By comparing their incompressible model with Okada’s (1985) flat-Earth model, which includes compressibility, Nostro et al. (1999) demonstrated that the effect of compressibility in the near-field can exceed 10% of coseismic displacement. Sabadini & Vermeersen

(1997) used incompressible theory (Piersanti et al. 1995) to demonstrate that the effect of stratification has a major influence on postseismic deformation. For example, postseismic displacements for a ten-layer model and a four-layer model differ by a factor. These results indicate that the assumptions outlined above are not valid, even in the above limited cases. In other words, the effects of compressibility and a continuously varying Earth structure on postseismic deformation have yet to be assessed.

The reason that such assumptions have been employed despite evidence that the assumptions are invalid is that intrinsic numerical difficulties arise in the absence of the assumptions. These difficulties stem from two kinds of singularities in the computation; assumptions of negligible compressibility and simplified viscoelastic structure are therefore employed to prevent the singularities from occurring. In Sections 2.2 and 2.3, we illustrate how the numerical difficulties occur and how existing theories have coped with these difficulties.

In fact, similar numerical difficulties to those discussed above occur in the computation of postglacial rebound, which has a common theoretical origin to that of postseismic deformation (Han & Wahr 1995). In the field of postglacial rebound, several authors have developed computational methods to deal with these difficulties, including analytical approximations and direct numerical approaches (see Section 2.4). In the realm of global postseismic deformation, however, such computational methods have not been employed, as far as the author knows.

1.6 Aims of the present study

We have documented that unjustified assumptions have been employed in previously proposed theories to avoid intrinsic numerical difficulties; however, these assumptions prevent us from distinguishing the dominant mechanism of postseismic deformation. These two facts give rise to the following two aims for this study.

1.6.1 Aim I - Remove unjustified assumptions concerning global postseismic deformation-

First, we develop a new method to calculate viscoelastic deformation without the assumptions described above. We also comprehensively document the effects of these assumptions on previous

calculations. It follows that we will obtain a global postseismic deformation for a spherically symmetric, self-gravitating, compressible, and realistically stratified Earth model, such as PREM (Dziewonski & Anderson 1981), for the first time.

In addition to enabling us to estimate a more reliable global postseismic deformation, the new method enables us to infer a more plausible viscosity profile. In viscoelastic relaxation theory, predicted deformation rates are in inverse proportion to viscosity. Therefore, we can use an inversion method to infer the optimum viscosity profile that best explains the observed deformation rate. Using an unreliable theory leads us to overestimate or underestimate viscosity. This means that viscosity profiles estimated using existing theories of global postseismic deformation are likely to be inaccurate. As discussed later, the differences in postseismic deformation rate predicted by our method and existing methods can amount to 50-60%, which is not negligible in terms of current observation techniques (see Chapter 4). It follows that our method provides an improvement in the theoretical accuracy of estimating viscosity to the same extent.

Determining the viscosity profile is important in a geophysical sense because the profile governs the speed of the time-evolution of viscoelastic deformation and viscous flow. Despite this, there are few other methods that provide constraints on the viscosity profile; exceptions include estimating postglacial rebound and reproducing the current geoid undulation with a mantle convection model (e.g., Ricard & Wuming 1991). To determine the viscosity profile in an island arc setting at low latitudes, the detection and modeling of postseismic deformation is indispensable, as the effect of postglacial rebound is less dominant in such regions.

1.6.2 Aim II - Identify the mechanism of postseismic deformation-

The theoretical improvements involved in our new method provide grounds for re-examining the dominant mechanism of postseismic deformation. If our improved theory of viscoelastic relaxation explains all or part of the observed postseismic deformation that has previously been explained purely in terms of afterslip, we might find that the distribution and duration of the afterslip has been overestimated or underestimated. Overestimate or underestimate of the afterslip affects how stress accumulation from plate motion is balanced by coseismic and postseismic stress release

during an earthquake cycle (Miyazaki et al. 2004). The continuation of afterslip indicates that fault strength around the asperity has not yet recovered. Therefore, if viscoelastic relaxation explains observed postseismic deformation better than afterslip, the recovery of fault strength is more rapid than previously thought.

In addition to the possibility that the calculated contribution of afterslip may change with the application of the new method, there is an intrinsic difference between employing afterslip and employing viscoelastic relaxation. Viscoelastic mechanisms predicts the time evolution of a postseismic deformation using only the initial condition (coseismic moment). On this basis, once we determine the viscosity profile at the target region, we can predict the relaxation rate of interseismic stress accumulation, as well as postseismic deformation that will occur in the same area. In contrast, the time-evolution of postseismic deformation cannot be predicted by inferring the optimum space-temporal distribution in each period via inversion unless we solve the dynamic equation involving the frictional law. Valuable information concerning viscosity is not obtained, either.

In the following chapters, we explore the theoretical background of existing methods of global postseismic deformation and the mechanism of numerical instabilities (Chapter 2). We then introduce our new approach that is designed to avoid such instabilities (Chapter 3). In Chapter 4, we show a computational result obtained using the proposed method and discuss whether the effects of compressibility and continuously varying viscoelastic structures are distinguishable using current observational techniques. Finally, in Chapter 5, we show that far-field postseismic deformation associated with the 2003 Tokachi-Oki Earthquake is largely explained by viscoelastic relaxation. We also estimate global gravity variation resulting from the Sumatra-Andaman Islands Earthquake.

2 EXISTING THEORIES OF GLOBAL DEFORMATION MECHANISMS

2.1 Overview of theoretical framework of global deformation

In this section, we review the mathematical relationship of theories on global postseismic deformation with those on other global deformations such as postglacial rebound.

In theories of global deformation, spherically symmetric, non-rotating, elastic and isotropic (SNREI) or viscoelastic (SNRVEI) Earth models are commonly used. Such models can be categorized in terms of two key components: the constitutive law of the medium, and boundary conditions. Table 2 shows the different categories of models and corresponding geophysical phenomena.

2.1.1 *Global elastic deformation*

First, we consider global deformation where elastic constitutive law is employed (Fooke's law, the upper law in Table 2). The theoretical framework of global elastic deformation is given by Love (1911) and Pekeris & Jarosch (1958), who solved the free vibration of an elastic uniform sphere and a radially heterogeneous sphere, respectively. According to this framework, most global deformations are obtained by solving the sixth-order ordinary differential equation under certain boundary conditions (see also Section 2.2.4). For example, tidal deformation occurs when the free surface condition and gravity attraction from the motion of other celestial bodies are applied to the Earth's surface and body, respectively (Love 1911). In addition, boundary conditions of surface load and traction are used to express deformation caused by changes in ocean mass and atmospheric pressure etc. (Longman 1962; Farrell 1972; Van Dam & Wahr 1987; MacMillan & Gipson 1994).

When a point dislocation is given in the internal Earth together with a free surface condition, free oscillation occurs and is observed as seismic wave propagation (normal modes) (Alterman et al. 1959; Saito 1967; Takeuchi & Saito 1972). 'Coseismic' crustal deformation is here defined as the permanent deformation obtained by neglecting the inertia term in the differential equation used to calculate free oscillation. Recently, Okubo (1993), Sun & Okubo (1993), and Sun et al. (1996) developed a theory in which coseismic deformations are derived from deformations for the former

boundary conditions (upper left-hand box in Table 2, i.e., surface traction, etc.) (see also Section 3.5).

2.1.2 Global viscoelastic deformation

Next, we consider global deformation where viscoelastic constitutive law is adopted, such as the Maxwell and Kelvin models (Pollitz 2003a) (lower law in Table 2). The theoretical framework of global viscoelastic deformation is given by Peltier (1974), who calculated deglaciation-induced relaxation processes using a spherical Earth model.

As for elastic deformation, two types of boundary conditions are considered (Table 2). The boundary conditions of the surface load have been used to describe postglacial rebound and its effects on polar wander (e.g., Peltier 1974; Wu & Peltier 1982; Yoder et al. 1983; Sabadini & Yuen 1989). Internal point dislocation with Heaviside source-time function, together with free surface, is used to model postseismic deformation (Pollitz 1992; Piersanti et al. 1995; Wang 1999).

We can derive the above viscoelastic deformations from theories on global elastic deformations for the corresponding boundary conditions (Table 2). It follows that we can obtain global postseismic deformation using the theory on free oscillation or global coseismic deformation. This mathematical technique, attributing viscoelastic problems to elastic ones, is known as the correspondence principle, and was first introduced into the field of global viscoelastic relaxation by Peltier (1974). As the theories associated with elastic deformation caused by earthquakes are based on the normal mode method (e.g., Takeuchi & Saito 1972), we also term Peltier (1974)'s method 'the normal mode method'. In the next section, we describe the theory on global postseismic deformation based on the normal mode method.

2.2 Normal mode method

2.2.1 Correspondence principle

In Peltier (1974)'s theory, Maxwell's constitutive equation is employed:

$$\dot{\tau}_{ij} + \frac{\mu}{\eta}(\tau_{ij} - \frac{1}{3}\tau_{kk}\delta_{ij}) = \lambda\dot{e}_{kk}\delta_{ij} + 2\mu\dot{e}_{ij}, \quad (1)$$

where τ_{ij} and e_{ij} denote the components of the stress and strain tensors, respectively, λ and μ are Lamé's constants, and η is viscosity. A dot above a variable denotes its derivative with respect to time. The Laplace transform of Eq. (1) yields

$$\tilde{\tau}_{ij} = \lambda(s)\tilde{e}_{kk}\delta_{ij} + 2\mu(s)\tilde{e}_{ij} \quad (2)$$

where

$$(\tilde{\tau}_{ij}(r, s), \tilde{e}_{ij}(r, s)) = \int_0^\infty (\tau_{ij}(r, t), e_{ij}(r, t))e^{-st}dt \quad (3)$$

$$\lambda(s) = \frac{\lambda s + \mu K/\eta}{s + \mu/\eta}, \quad K = \lambda + \frac{2}{3}\mu, \quad (4)$$

$$\mu(s) = \frac{\mu s}{s + \mu/\eta}. \quad (5)$$

Equation (2) is of the same form as that of the elastic global deformation. Therefore, we can easily obtain the solution in the Laplace domain with theories on global elastic deformation. It follows that the viscoelastic solution is given by taking its inverse Laplace transform.

2.2.2 Spherical expansion of the solution

Next, we expand the deformation in the time domain with spherical harmonics. In the subsequent derivation, we use the notation of Takeuchi & Saito (1972), Sun & Okubo (1993), and Okubo (1993). The displacement \mathbf{u} , stress tensor $\boldsymbol{\tau}$, and potential ψ are expanded as follows:

$$\mathbf{u}(r, \theta, \phi, t) = \sum_{n,m} [y_1(r, t; n, m)\mathbf{R}_n^m(\theta, \phi) + y_3(r, t; n, m)\mathbf{S}_n^m(\theta, \phi) + y_1^T(r, t; n, m)\mathbf{T}_n^m(\theta, \phi)] \quad (6)$$

$$\begin{aligned} \boldsymbol{\tau}(r, \theta, \phi, t) \cdot \mathbf{e}_r = \sum_{n,m} [y_2(r, t; n, m)\mathbf{R}_n^m(\theta, \phi) + y_4(r, t; n, m)\mathbf{S}_n^m(\theta, \phi) \\ + y_2^T(r, t; n, m)\mathbf{T}_n^m(\theta, \phi)] \end{aligned} \quad (7)$$

$$\psi(r, \theta, \phi, t) = \sum_{n,m} y_5(r, t; n, m)Y_n^m(\theta, \phi) \quad (8)$$

where

$$\mathbf{R}_n^m(\theta, \phi) = \mathbf{e}_r Y_n^m(\theta, \phi) \quad (9)$$

$$\mathbf{S}_n^m(\theta, \phi) = [\mathbf{e}_\theta \frac{\partial}{\partial \theta} + \mathbf{e}_\phi \frac{1}{\sin \theta} \frac{\partial}{\partial \phi}] Y_n^m(\theta, \phi) \quad (10)$$

$$\mathbf{T}_n^m(\theta, \phi) = [\mathbf{e}_\theta \frac{1}{\sin \theta} \frac{\partial}{\partial \phi} - \mathbf{e}_\phi \frac{\partial}{\partial \theta}] Y_n^m(\theta, \phi) \quad (11)$$

$$Y_n^m(\theta, \phi) = P_n^m(\cos \theta) e^{im\phi}, \quad m = 0, \pm 1, \pm 2, \dots, \pm n. \quad (12)$$

Here, (r, θ, ϕ) and \mathbf{e}_i are the conventional polar coordinates and unit vectors, $P_n^m(\cos \theta)$ is the unnormalized Legendre's function, and

$$P_n^{-|m|}(\cos \theta) \equiv (-1)^m P_n^{|m|}(\cos \theta). \quad (13)$$

$y_1(r, t; n, m)$, $y_3(r, t; n, m)$, and $y_5(r, t; n, m)$ are the radial functions representing the vertical and horizontal displacements and the potential change, respectively, for the spheroidal mode that includes volumetric change and gravity variation. An additional function $y_6(r)$ is introduced to aid mathematical handling of the free boundary condition at the surface (Eq. (17)):

$$y_6(r) \equiv \frac{dy_5}{dr} - 4\pi G \rho y_1 + \frac{n+1}{r} y_5 \quad (14)$$

where ρ is density and G is Newton's constant ($= 6.672 \times 10^{-11} \text{ Nm}^2 \text{ kg}^{-2}$). $y_1^T(r, t; n, m)$ and $y_3^T(r, t; n, m)$ express displacement and the stress field, respectively, for the toroidal mode comprised of only horizontal motions. In the following section, we derive the equivalent elastic solution in the Laplace domain for each mode.

2.2.3 Spheroidal mode

By replacing $\{y_i(r, t; n, m), i=1, \dots, 6\}$ with their Laplace transform, we define the apparent elastic deformation as $\{\tilde{y}_i(r, s; n, m), i=1, \dots, 6\}$. The apparent elastic deformation at a Laplace variable s satisfies the following differential equation, which is governed by the linearized equations of equilibrium, the stress-strain relation, and Poisson's equation:

$$\frac{d\tilde{y}_i(r, s; n, m)}{dr} = \sum_j A_{ij}(r, s; n) \tilde{y}_j(r, s; n, m) + \tilde{S}_i(s; n, m) \quad (j = 1, \dots, 6) \quad (15)$$

where the coefficients A_{ij} are given in Appendix A1. The inhomogeneous term $\tilde{S}_i \equiv \tilde{y}_i(r_s + 0, s; n, m) - \tilde{y}_i(r_s - 0, s; n, m)$ represents the excitation by a point dislocation at $r = r_s$ (Saito 1967). The source time function is Dirac's delta. The solution of Eq. (15) can be written as

$$\tilde{y}_i(r, s; n, m) = Q_1 y_{i1}(r, s; n, m) + Q_2 y_{i2}(r, s; n, m) + Q_3 y_{i3}(r, s; n, m) + \hat{y}_i^s(r, s; n, m) \quad (16)$$

where $\{Q_i, i=1,2,3\}$ are coefficients that will be determined later by a boundary condition and $\{y_{ij}, j=1,2,3\}$ are three independent solutions of the homogeneous equation of Eq. (15) that are regular at the center of the Earth (Appendix A1). The term \hat{y}_i^s denotes a particular solution that is obtained by numerically integrating Eq. (15) from r_s to the surface a with the initial value

$$\begin{cases} \hat{y}_i^s(r_s) = \tilde{S}_i(s; n, m), & m = 0, \pm 1, \pm 2 \\ \hat{y}_i^s(r < r_s) = 0. \end{cases}$$

Note that no deformation occurs for $|m| > 2$.

The boundary condition of the free surface is imposed as

$$\tilde{y}_2(a) = \tilde{y}_4(a) = \tilde{y}_6(a) = 0 \quad (17)$$

(Takeuchi & Saito 1972). Substituting Eq. (16) into (17) gives

$$\tilde{y}_i(r, s; n, m) = -\frac{\bar{y}_i(r, s; n, m)}{\Delta(s; n, m)} + \hat{y}_i^s(r, s; n, m), \quad (18)$$

where

$$\Delta(s) \equiv \det M, \quad (19)$$

$$M \equiv \begin{pmatrix} y_{21}(a) & y_{22}(a) & y_{23}(a) \\ y_{41}(a) & y_{42}(a) & y_{43}(a) \\ y_{61}(a) & y_{62}(a) & y_{63}(a) \end{pmatrix}, \quad (20)$$

$$\begin{aligned} \bar{y}_i(r, s; n, m) = & \sum_j [\hat{y}_2^s(a, s; n, m) \Delta_{1j}(s) \tilde{y}_{ij}(r, s; n, m) \\ & + \hat{y}_4^s(s) \Delta_{2j}(s) \tilde{y}_{ij}(r, s; n, m) \\ & + \hat{y}_6^s(a, s; n, m) \Delta_{3j}(s) \tilde{y}_{ij}(r, s; n, m)], \end{aligned} \quad (21)$$

and $\Delta_{ij}(s)$ is the co-factor of M (Eq. (20)). Thus, we obtain the equivalent spheroidal solution for a given Laplace variable s .

2.2.4 Toroidal mode

The same manipulation is performed for the toroidal mode. The apparent elastic deformation $\{\tilde{y}_i^T(r, s; n, m), i=1, 2\}$ at a Laplace variable s satisfies the following differential equation:

$$\frac{d\tilde{y}_i^T(r, s; n, m)}{dr} = \Sigma_j B_{ij}(r, s; n) \tilde{y}_j^T(r, s; n, m) + \tilde{S}_i^T(s; n, m) \quad (22)$$

where the coefficients B_{ij} are given in Appendix A2. The inhomogeneous term $\tilde{S}_i^T \equiv \tilde{y}_i^T(r_s + 0, s; n, m) - \tilde{y}_i^T(r_s - 0, s; n, m)$ is given in Takeuchi & Saito (1972). The solution of Eq. (22) can be written as

$$\tilde{y}_i^T(r, s; n, m) = Q^T y_{i1}^T(r, s; n, m) + \hat{y}_i^{sT}(r, s; n, m) \quad (23)$$

where Q^T is determined from the free surface condition below (Eq. (24)) and y_{i1}^T is the solution obtained by integrating an initial value at the core-mantle boundary upward (Appendix A2). The term \hat{y}_i^{sT} denotes a particular solution that is obtained by numerically integrating Eq. (22) from r_s to the surface a with the initial value

$$\begin{cases} \hat{y}_i^{sT}(r_s) = \tilde{S}_i^T(s; n, m), & m = \pm 1, \pm 2 \\ \hat{y}_i^{sT}(r < r_s) = 0 \end{cases}$$

(Takeuchi & Saito 1972). Note that toroidal mode is not excited for $m = 0$.

The boundary condition of the free surface is imposed as

$$\tilde{y}_2^T(a) = 0 \quad (24)$$

(Takeuchi & Saito 1972). Substituting Eq. (23) into (24) gives

$$\tilde{y}_i^T(r, s; n, m) = -\frac{\tilde{y}_i^T(r, s; n, m)}{\Delta^T(s; n, m)} + \hat{y}_i^{sT}(r, s; n, m), \quad (25)$$

where

$$\Delta(s)^T \equiv y_{21}^T(a, s; n, m), \quad (26)$$

and

$$\tilde{y}_i^T(r, s; n, m) = \hat{y}_2^{sT}(a, s; n, m) y_{i1}^T(r, s; n, m). \quad (27)$$

Thus, the equivalent toroidal solution for a given Laplace variable s is obtained.

2.2.5 Normal mode expansion and the eigenvalue problem

Having obtained the solution for the equivalent elastic problem (Eqs. (18)-(21) for the spheroidal mode and (25)-(27) for the toroidal mode), we can obtain the viscoelastic solution in the time domain by taking its inverse Laplace transform:

$$y_i(r, t; n, m) = \frac{1}{2\pi i} \int_{c-i\infty}^{c+i\infty} \tilde{y}_i(r, s; n, m) \frac{e^{st}}{s} ds, \quad i = 1, \dots, 6, \quad (28)$$

$$y_i^T(r, t; n, m) = \frac{1}{2\pi i} \int_{c-i\infty}^{c+i\infty} \tilde{y}_i^T(r, s; n, m) \frac{e^{st}}{s} ds, \quad i = 1, 2. \quad (29)$$

Here, s appears in the denominator assuming Heaviside's step function for the source time function.

For the spheroidal mode, substituting the right-hand side of Eqs. (18) and (21) into (22), and after some calculation, we obtain the viscoelastic solution in terms of normal modes (Takeuchi & Saito 1972):

$$y_i(r, t; n, m) = -\frac{1}{2\pi i} \int_{c-i\infty}^{c+i\infty} \frac{\bar{y}_i(r, s; n, m)}{\Delta(s)} \frac{e^{st}}{s} ds \quad (30)$$

$$= -\sum_{k=1}^N \frac{y_i^e(r, s_k; n, m)}{[\partial\Delta(s)/\partial s]_{s=s_k}} \frac{e^{s_k t}}{s_k}. \quad (31)$$

The derivation of Eq. (31) is carried out by considering that s_k , a root of the characteristic equation $\Delta(s) = 0$, acts as a first order pole in Eq. (30) (N represents the total number of the roots), and that \bar{y}_i coincides with the eigenfunction y_i^e , satisfying the free surface condition (Eq. (17)) at the limit of $s \rightarrow s_k$. Thus, the viscoelastic deformation is represented by the superposition of the normal modes. The same derivation holds for the toroidal mode.

To evaluate Eq. (31), all the roots should be searched numerically by computing $\Delta(s)$. Figure 6 shows an example of the numerical search, in which the zero-points correspond to eigenvalues. The residue, which represents the strength of each mode, is computed using the energy integration and the variational principle (Takeuchi & Saito 1972). Information concerning the geometry of the point dislocation \tilde{S}_i (Eq. (15)) is included in the representation of the residue. The meaning of each eigen mode is described in the following section.

2.2.6 Viscoelastic modes

One benefit of normal mode theory is that we can identify the origin of viscoelastic deformation by dividing the total response into eigen modes. Wu & Peltier (1982) undertook a detailed mode analysis to address the postglacial rebound problem. According to their study, each mode originates from contrasts in the density and/or viscoelastic structure in the employed Earth model. It follows that excited modes differ for different Earth models. The origins of eigen modes are listed in Table 3. The amplitude and radial profile of internal deformation for each mode varies for each degree

of spherical harmonics (e.g., Wu & Peltier 1982; Tromp & Mitrovica 1999b). As an example, we show Wu & Peltier (1982)'s result for a compressible Earth model with the density and elastic constants of 1066B (Gilbert & Dziewonski 1975), including the Mohorovicic, 420 km, and 670 km discontinuities, core-mantle and inner-outer core boundaries, viscosity contrast of the elastic lithosphere of 120 km thickness, and inviscid core (L1 model of Wu & Peltier (1982)). The C0 mode associated with the core-mantle boundary (Table 3) has a relative amplitude of 40% in the total surface deformation for $n=2$, but just 5% for $n=6$, indicating that the lower-degree deformation reflects the deep structure. On the whole, however, the largest contribution to the surface deformation is from the M0 mode (90% for $n \geq 15$ (Wu & Peltier 1982)). Figure 6 shows the characteristic times and relative strengths of the modes for $n=6$ (indicated by values in parentheses).

In Fig. 6, the value of the characteristic equation is not provided in the area between the dashed vertical lines. In fact, innumerable zero-crossing points exist in this region due to compressibility (D mode in Table 3). In the next section, we discuss the intrinsic difficulties involved in the normal mode method that are related to these innumerable poles.

2.3 Numerical difficulties in the normal mode method

Considering the continuously varying viscoelastic structure of the Earth and/or compressibility produces densely distributed poles. This precludes using the algorithm to determine the numerical root (Parsons 1972; Han & Wahr 1995; Fang et al. 1995; Sabadini & Vermeersen 1997; Vermeersen & Sabadini 1997). These roots appear in two regions along the s axis, corresponding to the effects of innumerable layers and compressibility, respectively (Han & Wahr 1995). Furthermore, the numerical search algorithm can detect an apparent eigen value due to an irregular change of sign of the characteristic function. In the following text, we summarize the mathematical mechanisms that cause these numerical difficulties.

2.3.1 Multilayer-induced problem

In the first region, in which $-s \sim \mu/\eta$, the number of poles increases as the number of layers increases, unless μ/η remains constant between two adjacent layers (T modes in Table 3). There-

fore, the smoothly varying viscoelastic structure of the Earth model generally generates innumerable poles. A serious numerical instability then occurs. It is necessary to integrate the ordinary differential equation using the Runge-Kutta propagation technique (Eq. (15) or (22)) to compute an eigen mode from the bottom to the surface; however, $\mu(s)$ becomes singular for a certain depth (Eq. (5)) (Fang et al. 1995; Han & Wahr 1995). If the number of layers is small, the singularities can be removed before the integration (Piersanti et al. 1995; Boschi et al. 1999). For a continuously changing structure, however, it is impossible to continue the computation because the integrand becomes continuously undefined. This difficulty is common to both the spheroidal and toroidal modes.

2.3.2 *Instability due to compressibility*

In the second region, in which $-s \sim \frac{\kappa\mu}{\beta\eta}$ where $\beta = \lambda + 2\mu$, the characteristic function for the spheroidal mode (Eq. (19)) oscillates very rapidly due to compressibility (Han & Wahr 1995), crossing the real axis of s . This oscillation is generated as follows. The first two of three independent solutions used as initial values for the basic differential equation include the spherical Bessel function of the first kind, $j_n(kr)$ (Appendix A1), where $k^2 \propto (\beta s + \kappa\mu/\eta)^{-1}$. When s approaches $-\frac{\kappa\mu}{\beta\eta}$, $k(s)$ becomes very large and $j_n(s)$ behaves as $\sin(kr)/kr$. Therefore, the initial values, including $j_n(s)$, change very rapidly for a small change in s . Consequently, the determinant (Eq. (19)) obtained by integrating these initial values oscillates very rapidly in the region of s .

Additional problems stem from the combined effects of compressibility and a finely-layered structure. Innumerable poles degenerate into inverse Maxwell time μ/η at the incompressible limit (Vermeersen & Sabadini 1996). It follows that a single value of μ/η corresponds to one compressible mode. This indicates that the number of compressible modes increases markedly if we employ a multi-layer model with different values of μ/η .

The numerical search algorithm cannot determine the positions of such continuously distributed poles. To do so requires that the interval of s used to compute the sign of the determinant along the real axis must be infinitely small, which is numerically impossible.

2.3.3 Apparent eigenvalues

For the spheroidal mode, the sign of the characteristic function can suddenly change even if it is not related to an eigenvalue (apparent zero-crossings) (Han & Wahr 1995). This phenomenon stems from the necessity to modify the expression of the wave number in the two independent solutions to ensure that the sign of the content in the square-root is positive (Eq. (A14) in Appendix A1). The expression is divided into five cases according to the value of s (Wu & Peltier 1982). When the wave number switches from one to another at a certain s , the apparent zero-crossing occurs. The automatic numerical search cannot distinguish such apparent eigenvalues. This sign change does not occur when incompressibility is assumed because the two independent solutions are substituted by linear combinations with the power of r .

2.4 Avoid the numerical difficulties using the unwarranted assumptions

We have demonstrated that the normal mode method suffers from intrinsic numerical difficulties. In this section, we first review steps to avoid those difficulties in the computation of postglacial rebound.

The difficulties associated with multi-layered models can be avoided by either of the following two procedures. The first is to reduce the number of layers via the volume-averaged method (Vermeersen & Sabadini 1997). To assess the validity of this approach, the authors developed an analytical expression for multi-layer models and studied the effect of increasing the number of layers for the loading problem. The results indicate that the effect was saturated for an Earth model with several tens of layers. Secondly, we can use Fang et al. (1995)'s method of evaluating contributions from innumerable poles for incompressible Earth models.

The difficulty related to compressibility is circumvented by simply neglecting the compressible modes when taking the summation (Eq. (31)) or assuming incompressibility so that the innumerable poles degenerate. The latter solution is the standard method employed in computations of postglacial rebound because it simultaneously ensures that miscounts of apparent eigenvalues are avoided (Section 2.3.3). Once we assume incompressibility, we can theoretically predict the total number of modes by taking into consideration their origin and a given viscoelastic structure of

the Earth model (Section 2.2.6). By comparing the predicted number of modes with the number of numerically detected modes, we can assess whether all the modes have been found. Another method is to approximately evaluate the contribution from compressible modes via an analytical formula (Vermeersen & Sabadini 1996); however, this method remains invalid for fine-graded Earth models because of the difficulties described in Section 2.3.1.

To avoid the difficulties described above, recent studies in the field of postglacial rebound have taken to using time-domain approaches (e.g., Paulson et al. 2005).

In the field of global postseismic deformation, assumptions concerning compressibility and the fine structure of the Earth continue to be used (Table 1). The effects of these assumptions on the accuracy of calculations have yet to be sufficiently examined, as stated above (Section 1.5). In the next chapter, we therefore propose a new computational scheme that avoids computational difficulties without the need for making unwarranted assumptions.

3 A NEW METHOD FOR COMPUTING GLOBAL POSTSEISMIC DEFORMATION

3.1 Principles of the method

The normal mode method provides a clear physical model (Section 2.2.6) but suffers from the intrinsic numerical difficulty that we cannot add up all the modes of realistically stratified and/or compressible Earth models (Section 2.3). In this chapter, we propose a new method that is intrinsically immune to this difficulty.

A fully numerical approach, such as a finite element method in the time domain, is a possible solution to the above problem, however, we propose a different method that in part uses the analytical expression in the normal mode method. As discussed in the previous sections, the weakness of the normal mode method is that we cannot isolate innumerable modes (Eq. (31)). To address this problem, we perform a numerical inverse Laplace integration that enables us to estimate the contribution from all modes at a set time (Eqs. (28) and (29)). In other words, we avoid all the difficulties described in Sections 2.3.1-2.3.3 by using a path on which no singularity of innumerable poles occurs. This means that the singularity caused by multi-layered models does not occur because s is now a complex number and the denominators of Eqs. (4) and (5) do not become zero. In addition, compressible modes do not cause rapid oscillation of the integrand on the path (see Section 3.3), and contributions from all the poles are automatically counted without the risk of miscounting apparent eigenvalues.

An important question here is the path that should be employed. In principle, we can select any path that encloses all of the poles. Modifying the integration path in Eqs. (28) and (29), we have

$$y_i(r, t; n, m) = \frac{1}{2\pi i} \oint \tilde{y}_i(r, s; n, m) \frac{e^{st}}{s} ds, i = 1, \dots, 6, \quad (32)$$

$$y_i^T(r, t; n, m) = \frac{1}{2\pi i} \oint \tilde{y}_i^T(r, s; n, m) \frac{e^{st}}{s} ds, i = 1, 2. \quad (33)$$

Here, the integrand is evaluated at s on the complex plane. In practice, however, the accuracy of the integration decreases rapidly unless an appropriate path is chosen. In fact, Fang & Hager (1994) employ a similar approach using a half-round path for the loading problem with incompressible models. Their method, however, encounters a numerical instability at large t ($> 5,000$ yrs). In

contrast, the path that we propose does not cause such an instability. We will describe the process of choosing such a path in the next section.

3.2 Determination of the appropriate path

Based on the fact that all of the poles appear on the real axis of s (see Appendix B), we can set a ‘rectangular’ path once we determine the positions of the largest and smallest poles (Fig. 7). Note that the positions change for different Earth models and for each degree n . We set $s_1=2.2\text{E-}14$, $s_2=1\text{E-}11$, and $s_3=-3.5\text{E-}10$ (sec.^{-1}) for all calculations in this thesis to avoid the need to modify the path according to changes in degree n .

The reason that we employ such a rectangular shape is explained as follows (the reason for employing a symmetric path about the real axis is discussed in Section 3.2.1.). To maintain as high an accuracy of the integration as possible, we consider the following trade-off so that neither $\tilde{y}_i(r, s; n, m)$ nor $\frac{e^{st}}{s}$ in Eqs. (32) and (33) varies rapidly:

Condition 1: $\tilde{y}_i(r, s; n, m)$ is smoother on the path, requesting a greater separation from the real axis (larger $|s_2|$) (Fig. 7).

Condition 2: The cancellation of significant digits in the integration along intervals B and C (Fig. 7) should be avoided, requesting a smaller separation from the real axis (smaller $|s_2|$).

Condition 1 is visualized in Fig. 8. It shows $\tilde{y}_1(a, s; n = 2, m = 2)$ along an interval on the path parallel to the real axis (solid line in the lower figure) for a continuously layered compressible Earth model with a convex viscosity profile (Model 1 in Fig. 10). The small dots on the real axis represent the densely distributed poles. It is evident that when s_2 is small, $\tilde{y}_1(a, s; n = 2, m = 2)$ varies rapidly due to singularities (white circles). Choosing a larger $s_2 (= 10^{-11} [\text{sec}^{-1}])$ means that no singularities occur along the path (black circles). Condition 2 is necessary because frequent oscillation of $\frac{\exp(st)}{s}$ has to be avoided. The sign of the integrand along interval B alternates fifty times for the value of s_2 at $t=10^6$ yrs; $\exp(is_2 t) = \exp(2\pi i s_2 / (\frac{2\pi}{t})) = \exp(2\pi i \times 50)$. In solving real problems, estimating postseismic deformation for periods of up to 10^5 yrs would be sufficient. For $t < 10^5$ yrs, the number of alternations is at most several times. Thus, the cancellation of significant digits is avoided. An approximate indication in determining s_2 from the viewpoint of

Condition 2 is therefore $s_2/(\frac{2\pi}{t}) < O(10)$. Taking these conditions into account, we search for an appropriate value of s_2 by trial-and-error so that the numerical integration converges for smaller integration steps.

In determining s_1 and s_3 , we only have to consider that all the poles are included and that s_3 is sufficiently small in case $\exp(st)$ in Eqs. (32) and (33) becomes infinite.

3.2.1 Minimizing computation time

For numerical Laplace integrations, the integration step along the path is set to $\sim 10^{-15} \text{sec}^{-1}$. It follows that a computation of $\tilde{y}_i(a, s; n, m)$ is carried out more than 10^4 times for each degree of spherical harmonics. Although computation time depends on the specifications of the computer, it is useful to introduce the following techniques that reduce the computation time of the integration.

(1) Select a symmetric path about the real axis (Fig. 7) to reduce the computation time for the integration along the real axis by 50%.

(2) Use the reciprocity theorem (Okubo 1993) to compute $\tilde{y}_i(a, s; n, m)$ (see also Section 3.5). This theorem saves computation time for different source depths (Okubo 1993). Therefore, the computational time required to calculate a surface deformation using a finite fault model expressed by assembling point sources with different depths is greatly reduced.

(3) Interpolate $\tilde{y}_i(a, s; n, m)$ in Eqs. (32) and (33) before $\exp(st)/s$ is multiplied, rather than the entire integrand. For this we use the ordinary spline function.

3.3 Visible effects of compressibility on the integrand

Compressibility does not affect the integrand in such a way that the accuracy of the integration deteriorates on the appropriate path. Figure 9 shows $\tilde{y}_1(a, s; n = 2, m = 2)$ and $\tilde{y}_1(a, s; n = 1000, m = 2)$ on the path for the compressible and incompressible models, respectively. To compute the solution for the incompressible model by the proposed method, the Lamé constant λ is replaced by ∞ in the compressible Earth model (Piersanti et al. 1995) (see also Section 4.1.2). $\tilde{y}_1(a, s; n, m)$ along the intervals B and C on the rectangular path is also smooth. The effect of

compressibility is clearly evident in the difference between the two $\tilde{y}_i(a, s; n, m)$ s as an ‘offset’. $\tilde{y}_i(a, s; n, m)$ for higher harmonic degrees ($n > 1,000$) remains smooth in a similar fashion.

3.4 Growth mode

It is worth noting that positive roots appear when both self-gravitation and compressibility are considered (Plag & Juttner 1995) for realistic Earth models such as PREM (Dziewonski & Anderson 1981) and 1066A (Gilbert & Dziewonski 1975). The contribution of positive poles to postseismic deformation is negligible at geologically short time-scales (Vermeersen & Mitrovica 2000) (times of more than 10 Ma). In our computation, however, positive roots are included in the path because the coseismic changes at $t = 0$ that are calculated without the positive poles do not agree with those computed using elastic theory (Sun & Okubo 1993). The neglected second-order terms in the linearized basic equation must be considered for such a time-scale (Plag & Juttner 1995).

3.5 Formulation of the new method

Having explained the principle of the new algorithm (Sections 3.1 and 3.2), we next derive the specific expression used to compute the integration (Eqs. (32) and (33)). Finally, we will express equations (32) and (33) with a non-dimensional viscoelastic Green’s function that corresponds to each dislocation type. We compute the Green’s function at the surface, as observers are generally located at the surface.

3.5.1 Vertical displacement, gravity, and change in geoid height

Only the spheroidal mode causes deformation in the vertical direction (Eqs. (6)-(12)). We begin with the expression for the radial functions $\tilde{y}_1(a, t; n, m)$ and $\tilde{y}_5(a, t; n, m)$ in Eq. (32). These functions are equivalent to the solution denoted by Eqs. (18)-(21) at $r=a$ for a complex s on the integration path. In the actual computation, however, we use the reciprocity theorem (Okubo 1993) to convert the $\tilde{y}_i(a, s; n, m)$ into $\tilde{x}_i(r_s, s; n, m)$, viscoelastic deformations obtained for surface boundary conditions (see Table 4 and Eqs. (37)-(40)). According to the theorem, deformation at the surface that is caused by an internal dislocation is expressed as a linear combination of the

deformation at the source depth caused by a potential change, load, and traction applied at the surface. With this mathematical relationship, there is no need to integrate the last term in Eq. (18) that is associated with the source condition. Because of this, accuracy is preserved in the integration of the basic equation for higher-degrees of spherical harmonics for shallow earthquakes.

Substituting the Laplace transform of Eqs. (43)-(52) in Okubo (1993) into Eq. (32) of the present thesis gives the following for the surface displacement ($i = 1$):

$$y_1(a, t; n, 0) = [(n_1\nu_1 + n_2\nu_2)F_u^1(t; n) + n_3\nu_3F_u^2(t; n)]UdS \quad (34)$$

$$y_1(a, t; n, \pm 1) = [\pm(n_3\nu_1 + n_1\nu_3) - i(n_2\nu_3 + n_3\nu_2)]F_u^3(t; n)UdS \quad (35)$$

$$y_1(a, t; n, \pm 2) = [(-n_1\nu_1 + n_2\nu_2) \pm i(n_1\nu_2 + n_2\nu_1)]F_u^4(t; n)UdS \quad (36)$$

where we define

$$F_u^1(t; n) \equiv -\frac{1}{2\pi i} \frac{G}{g_0 a} \oint \left[\frac{3\lambda(r_s, s) + 2\mu(r_s, s)}{\lambda(r_s, s) + 2\mu(r_s, s)} \frac{1}{r_s} X^{Press}(r_s, s; n) + \frac{\lambda(r_s, s)}{\lambda(r_s, s) + 2\mu(r_s, s)} x_2^{Press}(r_s, s; n) \right] \frac{e^{st}}{s} ds \quad (37)$$

$$F_u^2(t; n) \equiv -\frac{1}{2\pi i} \frac{G}{g_0 a} \oint x_2^{Press}(r_s, s; n) \frac{e^{st}}{s} ds \quad (38)$$

$$F_u^3(t; n) \equiv -\frac{1}{2\pi i} \frac{G}{2g_0 a} \oint x_4^{Press}(r_s, s; n) \frac{e^{st}}{s} ds, \quad (39)$$

and

$$F_u^4(t; n) \equiv \frac{1}{2\pi i} \frac{G}{2g_0 a r_s} \oint x_3^{Press}(r_s, s; n) \frac{e^{st}}{s} ds. \quad (40)$$

Here, g_0 , n , and ν denote gravity at the surface, a unit vector normal to the infinitesimal fault surface dS , and a unit dislocation vector, the norm of which is U (Fig. 11), respectively. In Fig. 11, the axes 1 and 2 are within the horizontal surface and axis 3 denotes the vertical axis. x_i^{Press} is the solution of the homogeneous version of Eq. (15) on the surface boundary condition (Table 4) and $X^{Press} = 2x_1^{Press} - n(n+1)x_3^{Press}$ (Okubo 1993).

For the surface potential change ($i = 5$),

$$y_5(a, t; n, 0) = [(n_1\nu_1 + n_2\nu_2)F_\psi^1(t; n) + n_3\nu_3F_\psi^2(t; n)]UdS \quad (41)$$

$$y_5(a, t; n, \pm 1) = [\pm(n_3\nu_1 + n_1\nu_3) - i(n_2\nu_3 + n_3\nu_2)]F_\psi^3(t; n)UdS \quad (42)$$

$$y_5(a, t; n, \pm 2) = [(-n_1\nu_1 + n_2\nu_2) \pm i(n_1\nu_2 + n_2\nu_1)]F_\psi^4(t; n)UdS \quad (43)$$

where F_ψ^i is obtained by replacing X^{Press} and x^{Press} in Eqs. (37)-(40) with X^{Tide} and x^{Tide} (Okubo 1993), respectively.

Using the above representation, we derive the final expression for postseismic deformation using the viscoelastic Green's function that includes the dependency on the angular distance θ . Substituting Eqs. (34)-(36) and (41)-(43) into Eqs. (6) and (8), respectively, the vertical displacement is written as

$$\begin{aligned} u_r(a, \theta, \phi, t) = & \{(n_1\nu_1 + n_2\nu_2)G_u^1(\theta, t) + n_3\nu_3G_u^2(\theta, t) \\ & + [(n_1\nu_3 + n_3\nu_1)\cos\phi + (n_2\nu_3 + n_3\nu_2)\sin\phi]G_u^3(\theta, t) \\ & + [(n_1\nu_1 - n_2\nu_2)\cos 2\phi + (n_1\nu_2 + n_2\nu_1)\sin 2\phi]G_u^4(\theta, t)\} \frac{UdS}{a^2} \end{aligned} \quad (44)$$

where

$$G_u^1(\theta, t) \equiv \sum_{n=0}^{\infty} a^2 F_u^1(t; n) P_n^0(\cos\theta) \quad (45)$$

$$G_u^2(\theta, t) \equiv \sum_{n=0}^{\infty} a^2 F_u^2(t; n) P_n^0(\cos\theta) \quad (46)$$

$$G_u^3(\theta, t) \equiv \sum_{n=1}^{\infty} 2a^2 F_u^3(t; n) P_n^1(\cos\theta) \quad (47)$$

and

$$G_u^4(\theta, t) \equiv \sum_{n=2}^{\infty} 2a^2 F_u^4(t; n) P_n^2(\cos\theta). \quad (48)$$

Here, the factor a^2 is inserted to make G_u^i dimensionless. The same manipulation is performed by Sun & Okubo (1993). Note that the normalization factor of the Green's function is arbitrary because we assume a point dislocation. The gravity potential $\psi(a, t)$ is obtained by replacing u with ψ in Eqs. (37)-(40). Finally, the gravity change at a point fixed on the free surface is given by

$$\delta g(a, \theta, \phi, t) = -\frac{\partial \psi(a, \theta, \phi, t)}{\partial a} - (\beta - 4\pi G\rho)u_r(a, \theta, \phi, t) \quad (49)$$

where $\beta = 2g_0/a$ (Sun & Okubo 1993).

The physical meaning of $G_{u,\psi}^i$ ($i=1, \dots, 4$) associated with the geometry of a point source (n_i, ν_i) is shown in Table 5. $G_{u,\psi}^1$ is an isotropic component ($m=0$) of a vertical tensile fault (Eq. (37)).

$G_{u,\psi}^2$, $G_{u,\psi}^3$, and $G_{u,\psi}^4$ represent responses to a horizontal tensile, a vertical dip-slip on azimuth $\phi = 0^\circ$, and a vertical strike-slip on azimuth $\phi = 45^\circ$, respectively.

3.5.2 Horizontal displacements

For horizontal displacements, we combine the spheroidal and toroidal modes. Strictly following the same procedure as in the vertical deformation, we derive the expression for the radial functions $\tilde{y}_3(a, t; n, m)$ and $\tilde{y}_1^T(a, t; n, m)$ in Eqs. (32) and (33). These functions are equivalent to the solutions described by Eqs. (18)-(21) for \tilde{y}_3 and (25)-(27) for \tilde{y}_1^T at $r=a$ for a complex s on the integration path. We use the reciprocity theorem (Okubo 1993) to convert the $\tilde{y}_3(a, s; n, m)$ and $\tilde{y}_1^T(a, s; n, m)$ into $\tilde{x}_i^{Shear}(r_s, s; n, m)$ and $\tilde{x}_i^T(r_s, s; n, m)$, respectively. The boundary conditions applied at the surface to obtain \tilde{x}_i^{Shear} and \tilde{x}_i^T are listed in Table 4. Substituting the Laplace transform of Eqs. (53)-(56) and Eq. (63) in Okubo (1993) into Eqs. (32) and (33) of the present thesis, respectively, gives the following for the surface horizontal displacement:

$$y_3(a, t; n, 0) = [(n_1\nu_1 + n_2\nu_2)F_v^1(t; n) + n_3\nu_3F_v^2(t; n)]UdS \quad (50)$$

$$y_3(a, t; n, \pm 1) = [\pm(n_3\nu_1 + n_1\nu_3) - i(n_2\nu_3 + n_3\nu_2)]F_v^3(t; n)UdS \quad (51)$$

$$y_3(a, t; n, \pm 2) = [(-n_1\nu_1 + n_2\nu_2) \pm i(n_1\nu_2 + n_2\nu_1)]F_v^4(t; n)UdS \quad (52)$$

$$y_1^T(a, t; n, \pm 1) = [\pm(n_2\nu_3 + n_3\nu_2) - i(n_3\nu_1 + n_1\nu_3)]F_l^1(t; n)UdS \quad (53)$$

$$y_1^T(a, t; n, \pm 2) = [(n_1\nu_2 + n_2\nu_1) \pm i(n_1\nu_1 - n_2\nu_2)]F_l^2(t; n)UdS \quad (54)$$

where we define F_v^i by replacing X^{Press} and x^{Press} in Eqs. (37)-(40) with X^{Shear} and x^{Shear} (Okubo 1993), respectively, and

$$F_l^1(t; n) \equiv \frac{1}{2\pi i} \frac{G}{2g_0a} \oint x_2^T(r_s, s; n) \frac{e^{st}}{s} ds \quad (55)$$

$$F_l^2(t; n) \equiv -\frac{1}{2\pi i} \frac{G}{2g_0a} \oint \frac{\mu(r_s, s)}{r_s} x_1^T(r_s, s; n) \frac{e^{st}}{s} ds. \quad (56)$$

The final form of postseismic deformation using the viscoelastic Green's function that includes dependency on the angular distance θ is derived as follows. Substituting Eqs. (50)-(54) into Eqs. (6) and (8), the horizontal displacement in the direction perpendicular to the plumb line, within

the plane of $\phi = \text{constant}$, is written as

$$\begin{aligned}
u_\theta(a, \theta, \phi, t) = & \{ (n_1\nu_1 + n_2\nu_2)G_\theta^1(\theta, t) + n_3\nu_3G_\theta^2(\theta, t) \\
& + [(n_1\nu_3 + n_3\nu_1)\cos\phi + (n_2\nu_3 + n_3\nu_2)\sin\phi]G_\theta^3(\theta, t) \\
& + [(n_1\nu_1 - n_2\nu_2)\cos 2\phi + (n_1\nu_2 + n_2\nu_1)\sin 2\phi]G_\theta^4(\theta, t) \\
& + [-(n_2\nu_3 + n_3\nu_2)\sin\phi + (n_3\nu_1 + n_1\nu_3)\cos\phi]G_\theta^{l1}(\theta, t) \\
& + [(n_1\nu_2 + n_2\nu_1)\sin 2\phi + (n_1\nu_1 - n_2\nu_2)\cos 2\phi]G_\theta^{l2}(\theta, t) \} \frac{UdS}{a^2}
\end{aligned} \tag{57}$$

where

$$G_\theta^1(\theta, t) \equiv \sum_{n=0}^{\infty} a^2 F_v^1(t; n) \frac{dP_n^0(\cos\theta)}{d\theta} \tag{58}$$

$$G_\theta^2(\theta, t) \equiv \sum_{n=0}^{\infty} a^2 F_v^2(t; n) \frac{dP_n^0(\cos\theta)}{d\theta} \tag{59}$$

$$G_\theta^3(\theta, t) \equiv \sum_{n=1}^{\infty} 2a^2 F_v^3(t; n) \frac{dP_n^1(\cos\theta)}{d\theta} \tag{60}$$

$$G_\theta^4(\theta, t) \equiv \sum_{n=2}^{\infty} 2a^2 F_v^4(t; n) \frac{dP_n^2(\cos\theta)}{d\theta} \tag{61}$$

$$G_\theta^{l1}(\theta, t) \equiv \sum_{n=1}^{\infty} 2a^2 F_l^1(t; n) \frac{P_n^1(\cos\theta)}{\sin\theta} \tag{62}$$

and

$$G_\theta^{l2}(\theta, t) \equiv \sum_{n=2}^{\infty} 4a^2 F_l^2(t; n) \frac{P_n^2(\cos\theta)}{\sin\theta}. \tag{63}$$

The horizontal displacement in the direction perpendicular to the vertical and perpendicular to the plane of $\phi = \text{constant}$ is written as

$$\begin{aligned}
u_\phi(a, \theta, \phi, t) = & [-(n_1\nu_3 + n_3\nu_1)\sin\phi + (n_2\nu_3 + n_3\nu_2)\cos\phi]G_\phi^1(\theta, t) \\
& + [-(n_1\nu_1 - n_2\nu_2)\sin 2\phi + (n_1\nu_2 + n_2\nu_1)\cos 2\phi]G_\phi^2(\theta, t) \\
& - [(n_2\nu_3 + n_3\nu_2)\cos\phi + (n_3\nu_1 + n_1\nu_3)\sin\phi]G_\phi^{l1}(\theta, t) \\
& + [(n_1\nu_2 + n_2\nu_1)\cos 2\phi - (n_1\nu_1 - n_2\nu_2)\sin 2\phi]G_\phi^{l2}(\theta, t) \} \frac{UdS}{a^2}
\end{aligned} \tag{64}$$

where

$$G_\phi^1(\theta, t) \equiv \sum_{n=1}^{\infty} 2a^2 F_v^3(t; n) \frac{P_n^1(\cos\theta)}{\sin(\theta)} \tag{65}$$

$$G_{\phi}^2(\theta, t) \equiv \sum_{n=2}^{\infty} 4a^2 F_v^4(t; n) \frac{P_n^2(\cos \theta)}{\cos(\theta)} \quad (66)$$

$$G_{\phi}^{t1}(\theta, t) \equiv \sum_{n=1}^{\infty} 2a^2 F_l^1(t; n) \frac{dP_n^1(\cos \theta)}{d\theta} \quad (67)$$

and

$$G_{\phi}^{t2}(\theta, t) \equiv \sum_{n=2}^{\infty} 2a^2 F_l^2(t; n) \frac{dP_n^2(\cos \theta)}{d\theta}. \quad (68)$$

The physical meaning of $G_{\theta, \phi}^i$ associated with the geometry of a point source (n_i, ν_i) is shown in Table 5.

3.6 Summary

The following points summarize the entire computational process.

(1) Search the largest and smallest poles to determine the complex path for each degree n and determine the appropriate path

(2) Calculate a complex viscoelastic deformation on the boundary condition (Table 4) that corresponds to the Laplace variable s on the path (Fig. 7)

(3) Carry out the numerical integration in Eqs. (32) and (33) for each degree n

(4) Calculate Green's function with spherical harmonics (Eqs. (45)-(48), (58)-(63), and (65)-(68))

(5) Obtain the final response with the Green's function and given geometry of a dislocation (Eqs. (44), (57), and (64))

4 COMPUTATIONAL RESULTS

In this chapter, we first confirm the validity of the numerical algorithm (Section 4.1) before describing the Green's function obtained with the new method (Section 4.2) and considering the physical mechanism of the time variation (Sections 4.3 and 4.4). Finally, we evaluate differences in the result obtained from the present method with that obtained from previously published methods (Sections 4.5 and 4.6).

4.1 Confirmation of the algorithm

4.1.1 Coseismic responses

To confirm that the contributions from innumerable modes are calculated correctly, we first checked coseismic responses. We compared the elastic deformation computed by our method with that of Sun (1992).

We calculated the Green's functions for the 1066A Earth model (Gilbert & Dziewonski 1975) for four dislocation types. The vertical displacements for the source depth of 100 km at $t = 0+$ yr coincide with the elastic solution listed in Tables E.1-E.4 in Sun (1992) (Fig. 12). We also found good agreements for other source depths and horizontal deformations.

In addition, the coseismic changes for different viscosity models (Models 1 and 2 in Fig. 10) were in agreement (e.g., Fig. 18 and Fig. 21, $D_s=10$ km), reflecting that the coseismic part of the deformation was calculated correctly, as elastic responses depend only on elastic structures in Maxwell rheology.

4.1.2 Viscoelastic response

Next, we examined the viscoelastic responses. Because there are no previous results in which compressibility and a large number of layers have been considered simultaneously, we undertook comparisons using an incompressible Earth model by setting $\lambda = \infty$ in the Earth model (Piersanti et al. 1995). In our calculation, we set $\lambda = 100 \mu$. Figure 13 shows the postseismic displacement for a vertical strike-slip source with the relatively simple Earth model P2, as used in Piersanti

et al. (1995) (Fig. 14). The source depth is 100 km. The results are in good agreement. Thus, it is confirmed that the viscous part is also computed correctly.

4.2 Green's function

4.2.1 Green's function for a globally averaged viscosity model

We computed the Green's function for four source depths: 10 km, 32 km, 100 km, and 200 km. The PREM (Dziewonski & Anderson 1981) was used as an Earth model for the density and the elastic constants (Fig. 10). The model consists of approximately 2000 layers in practice. The P- and S-wave velocities of the surface liquid layer, however, were replaced by those of the crust below the surface layer so that the boundary condition at the surface was given appropriately by the reciprocity theorem (Section 3.5). For a viscosity profile under the lithosphere, a convex profile (Ricard & Wuming 1991) was interpolated with a fourth order polynomial. The same viscosity profile was used to study the effects of stratification on the relaxation process (Vermeersen & Sabadini 1997). The thickness of the elastic lithosphere was assumed to be 120 km (Model 1 in Fig. 10), representing a globally averaged value including the continental crust. We take this viscous profile as a reference in the following discussion.

Figures 15-18 portray time variations of the Green's functions for different dislocation types (Table 5) and source depths (Ds) of 10 km, 32 km, 100 km, and 200 km, at $t = 0+$ yr (immediately after an event), 1 kyr, 10 kyr, and 100 kyr, respectively. The magnitude of the deformations are normalized by $UdS = 10^{11} m^3$ (equivalent to $M_w \sim 8.3$ when μ is 30 GPa). (a)-(e) in Figs. 15-18 indicate the vertical displacement u_r , gravity change, geoid change, horizontal displacement u_θ , and u_ϕ , respectively. Note that the change in geoid height $N = \psi/g_0$ is shown in place of the gravity potential.

Assembling the four Green's functions, a postseismic deformation raised by an arbitrary point source is computed. Figures 19 and 20 show the deformations for vertical tensile and dip-slip dislocations, respectively.

4.2.2 Use of the Green's function

As an example, we illustrate the procedure used to calculate a postseismic vertical displacement caused by a dip-slip point dislocation with a dip angle of 45° . We compute the displacement at $t=0+$ yr and $t=10$ kyr when $Ds = 100$ km, $U = 1$ m, $dS = 30$ km \times 30 km, and the observer is located at $\theta = 1^\circ$, $\phi = 0^\circ$. First, the geometry of the source (\mathbf{n} and ν) is determined (see Fig. 11 and Table 5). Substituting these vectors into Eq. (44), the necessary Green's functions are determined. In this case, they are $G_u^1(\theta, t)$, $G_u^2(\theta, t)$, and $G_u^4(\theta, t)$. Figure 20 (a) shows the assembled displacement on $\phi = 0$ at arbitrary angular distance. The dependency of these Green's functions on angular distance is shown in Table 5. We read the normalized displacement at $\theta = 1^\circ$ at $t = 0+$ yr and 10 kyr = 0.067 m and 0.53 m, respectively. The actual displacement is given by multiplying both 0.067 m and 0.053 m by $1 \times 30 \times 30 / 10 \times 100^2$. Finally, the displacements at $t = 0+$ yr and $t = 10$ kyr are 0.6 mm and 4.8 mm, respectively. The horizontal displacement, geoid height, and gravity changes are estimated in the same manner. Responses to various source depths at arbitrary times can be computed by interpolating the Green's function with respect to depth and time.

4.2.3 Comparison with a thin-lithosphere model

To assess the effect of the thickness of the lithosphere, we computed the Green's function for a viscous profile with a thinner lithosphere (Model 2 in Fig. 10). In this case, thickness of the lithosphere was 30 km, assuming a plate boundary zone. The viscosity at depths between 30 km and 120 km was set at 3×10^{20} Pas, the same value at the depth of 120 km in Model 1 (Fig. 10). Figures 21-23 show results for vertical strike-slip, tensile, and dip-slip (a dip angle of 45°) dislocations, respectively.

4.3 Behavior of Green's function

The Green's functions show diverse spatial and temporal changes according to source depth and dislocation type. In the following text, we summarize the characteristics of the Green's functions.

(1) The characteristic time is several thousands of years (Figs. 15-20). This is natural because the viscosity in the asthenosphere used here is approximately 10^{21} Pas on average, the same order

of magnitude as the value derived from observations of postglacial rebound (e.g., Mitrovica & Forte 1997). We confirm that the characteristic time diminishes by a factor of 100 when the viscosity is replaced by a value that is two orders of magnitude less; this is reasonable considering the rheology (Eqs. (4) and (5); $\frac{1}{s} \propto \eta$). The spatial change, however, does not vary, indicating that the viscosity under the lithosphere affects the time-scale of the deformation.

(2) The deeper the source depth relative to the thickness of the lithosphere becomes, the larger the magnitude of postseismic deformation relative to the coseismic deformation tends to become. Furthermore, the area in which distinct postseismic deformation occurs is extended (e.g., Figs. 18 (a) and 21 (a); $D_s = 10$ km). This is because with a deeper source the coseismic stress change in the asthenosphere is larger, resulting in greater deformation corresponding to spherical harmonics of lower-degrees that reflect the viscous structure of the asthenosphere. As a consequence, deformation with longer wave lengths occurs and is observed in the far-field. In the near-field, strong postseismic deformation does not occur for shallow earthquakes because the near-field deformation corresponds to spherical harmonics of higher-degrees that reflect only the elastic structure in the lithosphere.

(3) The occurrence of marked increases or decreases in initial coseismic displacements at the surface is dependant on source depths and angular distances. For example, the coseismic uplift caused by the dip-slip dislocation (Fig. 20 (a)) increases in the near-field for $D_s = 100$ km but decreases for $D_s = 32$ km, and vice versa in the far-field.

The above features (1)-(3) are consistent with the known characteristics of incompressible models (e.g., Piersanti et al. 1995).

(4) The amount of postseismic displacement relative to coseismic displacement is proportional to the postseismic gravity change relative to coseismic gravity change (Figs. 15a, b-18a, b); however, the rate of change in the height of the postseismic geoid relative to the coseismic geoid is several times greater than the rate of change for the displacement and gravity change (Figs. 15c-18c). This tendency is more pronounced for deeper earthquakes (Figs. 15c-18c). For example, the postseismic geoid height change for $D_s = 100$ km approaches that of the coseismic geoid for $D_s = 10$ km after a certain time (Fig. 18c, $D_s = 10$ km and 100 km). This discrepancy between

rates indicates a large-scale mass transport beneath the lithosphere that cannot be inferred from displacements and gravity changes at the surface.

The above observations give rise to three important aspects of postseismic deformation. First, the thickness of the lithosphere and the source depth relative to lithosphere thickness are prime factors that affect the diverse patterns of postseismic deformation. Second, postseismic deformation associated with deeper earthquakes can approach the deformation associated with shallow earthquakes (here, deep means that the source depth is sufficient for the coseismic change to cause significant deformation within the asthenosphere). This is more pronounced in terms of potential change. Finally, in the far-field, the rate of postseismic deformation relative to coseismic deformation tends to be large, even if the coseismic deformation is much smaller than that in the near-field.

4.4 Mechanisms that govern various patterns of postseismic deformation

The diverse patterns of postseismic deformation resulting from varying source depth and epicentral distance are reasonably explained by stress relaxation within the asthenosphere. We can confirm this without the need to directly compute the internal stress field (the new method proposed in this thesis is currently able to compute only surface deformation. Internal deformation can be computed with minor modifications). Postseismic deformation at 10^5 yrs after the event almost converges (note the interval of displacement at each time step in Figs. 15-20). This limit is in agreement with the elastic deformation for an Earth model in which μ is replaced by a very small value ($\frac{1}{10,000}\mu$). This means that after a sufficient time, the asthenosphere will behave as a liquid and that stress within the asthenosphere will reduce to zero. Therefore, postseismic deformation for vertical dip-slip and strike-slip dislocations in the asthenosphere are shown to approach zero because shear dislocations do not occur within liquid (Figs. 17 and 18, $D_s=200$ km). The fact that these dislocations in the asthenosphere do not contribute to surface deformation is also noted by Sato & Matsu'ura (1988). In the vertical and horizontal tensile cases, however, the large isotropic component ($m = 0$) does not vanish at the limit of liquid (Figs. 15 and 16, $D_s=200$ km).

We can also explain the deformation pattern intuitively from the result in Section 4.3 (2). As an example, we consider horizontal displacement u_θ for a vertical strike-slip dislocation (Fig. 21

(d), $Ds=20$ km and 30 km). We can infer from the time variation of u_θ at the surface for $Ds=30$ km that a viscoelastic flow occurs immediately beneath the lithosphere to the left in the near-field and to the right in the far-field. In contrast, when the source is shallow ($Ds=20$ km), only the right-hand flow is observed in the near and far-fields. This indicates that the near-field deformation that occurs for $Ds=30$ km disappears in the case of $Ds=20$ km. As the source depth becomes shallow, the deformation corresponding to the spherical harmonics of higher-degrees raises only elastic deformation (Section 4.3 (2)); consequently, no left-hand flow occurs in the asthenosphere. As a result, only the right-hand flow, corresponding to the lower-degree, is observed at the surface.

The same explanation holds for the dip-slip fault (Fig. 23 (d)). The right-hand flow seen for $Ds=30$ km in the near-field gradually decreases for shallow earthquakes ($Ds=20$ km and 10 km).

4.5 Effect of fine layering

We have demonstrated that the new method enables us to precisely and readily compute the total strength of innumerable modes (Sections 4.1 and 4.2). In contrast, when using the normal mode method it is possible but laborious to determine a large number of modes associated with a finely-layered model. Therefore, it is important for users of the normal mode method to know whether the Earth's viscoelastic structure can be well approximated with a smaller number of layers. To test the approximation, Vermeersen & Sabadini (1997) assessed the effect of increased number of layers on relaxation processes for surface load and tidal forcing with incompressible Earth models. They showed that models with approximately 50 to 60 layers reached continuum limits at all time-scales and for all harmonic degrees up to 150. The authors also showed that fine-graded stratification of shallow layers is important for higher-degree deformation. The effects of stratification on postseismic deformation have been studied by Sabadini & Vermeersen (1997) using 4-layer and 10-layer models. The authors found that elastic stratification within the lithosphere has a major influence on estimating postseismic deformation associated with large earthquakes. In this section, we perform a similar analysis to that of Vermeersen & Sabadini (1997) to confirm that their saturation findings occur in postseismic deformation using compressible models. In addition, we discuss the detectability of the effects of fine layering.

We computed postseismic deformation associated with a vertical strike-slip fault and a dip-slip fault with a dip angle of 20° for four Earth models of differing numbers of layers (Figs. 10 (Model 1), 24, 25, and 26.). Figures 27 and 28 show time series data for an epicentral distances of 100 km and 200 km in the direction where the maximum change is expected, i.e., $\phi = 45^\circ$ for the strike-slip and $\phi = 0$ for the dip-slip fault. The moment is the same as that used to compute the Green's function; however, we rescale the time variation assuming that the viscosity is just 1% of the values shown in the figures for the four Earth models (10^{18-19} Pas immediately below the lithosphere). The purpose of this rescaling is to make the predicted postseismic deformation rates more realistic. The validity of the viscosity value is shown in Section 5.1.3.

The result clearly shows that the effect of fine layering is saturated at 60 layers throughout all time-scales, as noted by Vermeersen & Sabadini (1997) (Figs. (27) and (28)). This means that a continuously-layered viscoelastic structure below the lithosphere can also be replaced by a discrete structure with approximately several tens of layers in the case of compressible models. Time variation for the 11-layer model of Wang (1999) still shows a remarkable difference from the finely-layered model, especially for deeper earthquake (Figs. (27) and (28), $D_s=100$ km).

Next, we examine whether differences in deformation rates for the four Earth models over the first 30 yrs after the event are detectable using current observational techniques such as GPS. Figures 29 and 30 show the averaged rates over each period. For shallow earthquakes ($D_s=32$ km), the difference between the trends for the 60-layer model and that for the 11-layer one is approximately 1 cm/yr over the first 10 yrs in both the horizontal and vertical components for the two dislocation types. Surprisingly, the difference in velocities for deep earthquake ($D_s=100$ km) also reaches 1 cm/year (Figs. (29b) and (30)). This result indicates that we should use Earth models with several tens of layers to calculate postseismic deformation caused by events of magnitude ~ 8 , considering the accuracy of GPS, VLBI etc. The differences of the four models over the first 10 yrs, however, are too small to detect (~ 1 mm/year).

4.6 Effect of compressibility

Having confirmed the necessity of a finely-layered Earth model or an Earth model with several tens of layers, we next explore the effects of compressibility. The evaluation is carried out in the same manner as that described in the previous section.

Figures 31 and 32 show time series data of postseismic deformation for strike-slip and the dip-slip mechanisms, respectively. The Earth model is the finely-layered model (Fig. 10 (Model 1)). Incompressible deformations are computed using the method described in Section 4.1.2. Comparison of the time series indicates that the effects of compressibility for shallow earthquakes is mostly elastic (i.e., only initial offset occurs), except for change in the geoid height. For deep events, however, significant differences are observed at time-scales ranging from 1 yr to 1,000 yrs. These differences are more pronounced in terms of vertical motion (Figs. (31) and (32)). In addition, a difference more than 50% is seen in terms of permanent deformation (= fluid limit minus elastic limit) (Figs. (31) and (32), $t = 10^3$ and 10^4 yrs). This illustrates the importance of considering compressibility when calculating long-term deformation such as landform development, gravity anomalies, and geoid height.

Next, we estimate deformation rates to assess if they are detectable (Figs. (33) and (34)). Differences between compressible and incompressible models vary from several mm/yr to 1 cm/yr over the first 10 yrs for both dislocation types and source depths. These differences are sufficiently large to be observable using modern observation techniques. In addition, we note that the effect of compressibility retains a detectable rate difference (several mm/year) for up to 25 yrs after the event (Fig. (33) and (34b), $D_s=32$ km). This mid-term effect of compressibility is more pronounced in terms of vertical motion. Our results indicate that neglecting compressibility affects evaluations of sea level change from tide gauge records (Melini et al. 2004). The rate difference for times in excess of 25 yrs after the earthquake is too small to be detected.

4.7 Summary

The following points summarize the main findings of this chapter.

(1) The Green's function was obtained for the first time using an Earth model that simultaneously considers continuously varying viscoelastic structure and compressibility.

(2) The mechanism of the diverse pattern of postseismic deformation is explained by stress relaxation in the asthenosphere.

(3) The effect of fine layering is saturated at several tens of layers, as indicated by Vermeersen & Sabadini (1997); however, the difference between the 60-layer model and Wang's (1999) 11-layer model is detectable for the event ($M=8.3$).

(4) The effect of compressibility on postseismic deformation rate in the first few decades after the event exceeds a few mm/yr in both horizontal and vertical components, which is observable. Furthermore, the effect of compressibility on permanent deformation for 1,000 yrs after the event reaches 10-20% for shallower earthquakes and more than 50% for deeper ones.

The above results (3) and (4) strongly indicate the need to consider a finely-layered viscoelastic structure and compressibility when estimating global postseismic deformation, except for those cases where accuracy is not required.

5 APPLICATION OF THE NEW METHOD

We have demonstrated that the effects neglected in existing methods are detectable (Sections 4.5 and 4.6). In this chapter, as an actual application of our new method, we use the obtained Green's function (Section 5.1) to estimate the postseismic deformation associated with the 2003 Tokachi-Oki Earthquake ($M_w = 8.0$). As an example of truly global-scale deformation, we also compute the variation of Earth's flattening due to the Sumatra-Andaman Islands Earthquake of 26 December 2004 (Section 5.2).

5.1 The 2003 Tokachi-Oki Earthquake

5.1.1 Purpose of this case study

The goals of this section are (1) to apply the new method to observed data to verify the validity of the method, and (2) to evaluate the contribution of viscoelasticity to postseismic deformation. The 2003 Tokachi-Oki Earthquake is suitable for this purpose because there is a large amount of GPS data on the event and previous studies have explain these data in terms of afterslip (Miyazaki et al. 2004; Ozawa et al. 2004); here we present a countereview to the findings of these earlier studies.

To achieve the above goals, we employ a simple point-dislocation model to calculate the viscoelastic deformation. In other words, we make a forward calculation with a given fault parameter and a viscoelastic structure. We do not determine the best-fit viscosity profile and fault parameter to fully explain the observation by inversion, as this is beyond the scope of this study. We focus on far-field deformation and use point sources so that we can ignore the complex shape of the fault plane. Despite the simplicity of the model, we produce an excellent agreement between the theory and observation (Section 5.1.5).

5.1.2 Observation data

The 2003 Tokachi-Oki Earthquake occurred on 26 September 2003 southeast of Hokkaido, Japan, where the Pacific Plate is subducting beneath the Eurasian Plate (Fig. 3). The magnitude of the earthquake was 8.0 according to the Japan Meteorological Agency, and had a dip-slip mechanism.

Here we use the daily coordinate data of GEONET, the Japan-wide GPS observation network

operated by the Geographical Survey Institute (GSI) since 1994. There are approximately 200 GEONET stations on Hokkaido Island. The average distance between stations is 25 km. Daily coordinates, based on the International Terrestrial Reference Frame (ITRF2000) (Altamimi et al. 2002), are routinely calculated and published by the GSI (Hatanaka et al. 2003). Using these daily data, Ozawa et al. (2004), for example, inferred the slip distribution along the plate boundary for coseismic and postseismic deformation related to the Tokachi-Oki event.

Figure 35 shows horizontal coseismic displacement detected at selected continuous observation stations in the far-field. We chose those stations with the longest observation period. The coseismic displacement vectors relative to the fixed site O, where no significant deformation was recorded, are obtained by subtracting the average daily coordinates for two weeks before the event from those after the event. Figure 35 also displays the rectangular fault determined by the GSI from a displacement inversion based on Okada (1985); this provides the realistic size of the fault.

Figures 36 (a) and (b) show the time series of displacements before and after the earthquake. We removed the secular trend and annual and semi-annual variations from the time series by using the data for the 7 yrs preceding the earthquake (May 1996 to May 2003) and the conventional least squares method with linear and sinusoidal functions.

From the above figures, we can summarize the observational results as follows.

(1) The coseismic change amounts to several cm to ten cm in horizontal displacement for an epicentral distance of 100-200 km (Fig. 35).

(2) Postseismic deformation in the region is approximately 2-3 cm/yr (Fig. 36).

(3) The postseismic trend consists roughly of two characteristic times. The rapid change during the period several tens of days after the event seems to have already converged. The trend after that, however, has not yet returned to zero, at least not as of September, 2005 (Fig. 36).

(4) In terms of vertical displacements, seasonal variations obscure even coseismic change, except at station H.

5.1.3 Viscoelastic structure of the lithosphere and the asthenosphere

For elastic structure, we employ the PREM as in previous sections. For viscous structure, we adopt a lithosphere of 30 km thickness (Model 2 in Fig. 10), as the event occurred in a subduction zone (Fig. (37), upper figure). We also replace the viscosity beneath the lithosphere with a value that is just 1% of the original value. It follows that the value of the viscosity just beneath the lithosphere is $3 \times 10^{18} \text{ Pas}$. This value is reasonable for subduction zones like the Japan island arc because it is usual in computations of postseismic deformation to assume low-viscosity layers in the lower crust or upper asthenosphere. For example, Ueda et al. (2003) explained postseismic deformation related to the 1993 Hokkaido Nanseioki Earthquake, northern Japan, assuming a 40-km-thick low-viscosity layer under the lithosphere with a value of $4 \times 10^{18} \text{ Pas}$. Ueda et al. (2003) demonstrated that the low-viscosity layer corresponded to the high-temperature zone of the mantle in the region. Matsu'ura et al. (1998) explained interseismic leveling data along the Nankai Trough, Japan, assuming lithosphere with a thickness of 30 km and the viscosity value of $5 \times 10^{18} \text{ Pas}$ in the asthenosphere. Melini et al. (2004) estimated the contribution from past large earthquakes to long-term sea level variation assuming a 200 km low-viscosity asthenosphere with a viscosity of 10^{19} Pas .

5.1.4 The fault model

Figures 35 (bottom figure) and 37 (upper figure) illustrate the fault model used for the forward calculation. We construct a 'two point-source' model. The reason that we do not employ single point dislocation is that we cannot explain the postseismic trend very well. The proposed model is justified as follows. This model is based on a coseismic slip distribution determined from seismic data (Fig. 37, lower figure) (Yamanaka, 2003, available at http://www.eic.eri.u-tokyo.ac.jp/EIC/EIC_News/030926.html, Earthquake Research Institute). We note that the direction of slip is subvertical near the surface but eastward at depth. Therefore, we assume two point sources (S1 and S2) with different slip directions (Fig. 37, upper-right figure). The depths of the two sources are 20 km and 30 km, allowing us to employ the Green's function used to draw Figs. 21-23. Source parameters are listed in Table 6; the strike and dip angles of S1 and S2, rake angle

of S2, and sum of the moment magnitude of the two sources are the same as in Yamanaka's (2003) model. The horizontal positions of S1 and S2 are determined geometrically from the source depth and dip angle.

5.1.5 *Results and consideration of the mechanism of postseismic deformation*

The calculated coseismic and postseismic deformations are superimposed in Figs. 35 and 36 using red vectors and lines, respectively (see Appendix C for a computation at an arbitrary latitude and longitude). On the basis of these figures, we discuss the contribution of viscoelastic mechanisms to the postseismic deformation.

First, we note an excellent agreement between the theory and observations in the coseismic horizontal displacement (Fig. 35). This indicates that the fault parameter and the elastic model used for the forward calculation are reasonable, at least in terms of coseismic deformation.

Next, we compare the time series of observed postseismic deformation with trends predicted by the above model (Fig. 36). Note that we give only the initial coseismic moment. Nevertheless, the predicted trend fits remarkably well with the observed rate, except for the north-south component at Site A and the east-west component at Site F (Fig. 36). This agreement strongly suggests that the viscoelastic mechanism has already begun to work on the postseismic deformation with a detectable signal level, provided the value of the viscosity is true. There is therefore scope to re-examine results that explain the postseismic deformation during the period purely by afterslip, such as Ozawa et al. (2004). The short-term deformation for several tens of days after the event, however, cannot be explained by viscoelastic relaxation because such an explanation requires an unreasonably low viscosity ($\sim 10^{17} \text{Pas}$). Therefore, our result does not rule out the possibility of short-term afterslip, as shown by Miyazaki et al. (2004). If the viscosity value is higher than 10^{19}Pas , on the other hand, it is difficult for viscoelastic mechanisms to account for the trend, as the displacement rate becomes too small to be observed. In this case, postseismic deformation is purely explained by after-slip (Ozawa et al. 2004) or other mechanisms. It follows that we must wait until longer-term data accumulate before evaluating the contribution of viscoelastic mechanisms.

The vertical deformation predicted by the theory is only a few mm in scale, which is smaller than the observation noise (Fig. 36). To distinguish viscoelastic deformation from after-slip, however, vertical motion is important. Figure 38 shows the pattern difference of the coseismic and postseismic vertical displacements according to epicentral distance. At all stations, the coseismic change is uplift. Postseismic change, in contrast, changes to subsidence with increasing epicentral distance (A, B, C, and F in Fig. 38). In the case of after-slip, however, the direction of postseismic vertical deformation at all stations is expected to be uplift because the afterslip area is viewed the same as the coseismic slip area from far-field stations ($\sim \pm 100$ km around the epicenter (Ozawa et al. 2004)). We can therefore determine the dominant mechanism of postseismic deformation by carefully studying the far-field vertical displacement rate. As the signal-to-noise ratio in the vertical motion is small, an observation period of at least several years is necessary. In addition, techniques to correct the secular trend due to plate subduction and seasonal effects are important in extracting the postseismic trend.

Thus, we have confirmed the validity of our method and demonstrated the necessity of reconsidering the mechanism of postseismic deformation.

5.2 The Sumatra-Andaman Islands Earthquake of 26 December 2004

5.2.1 J_2 representing the Earth's flatness and earthquakes

Chao & Gross (1987) was the first to compute changes in Earth flatness caused by earthquakes. Figure 39 presents their model of how an earthquake changes the Earth flatness. In this model, large earthquakes tend to make the shape of Earth more spherical because they accelerate plate subduction at mid to low latitudes, thus pulling cool and heavy masses downward.

The theory of such a model is explained in the following text. The flattening of Earth, f , is defined as the flatness of the mean ellipsoidal surface that best approximates the equipotential surface of Earth's gravity field (e.g., Seeber 2003). f is represented by the degree-two and order-zero coefficient of the potential field expanded with spherical harmonics, J_2 , and a term that is dependant on the rotational velocity of the Earth, m :

$$f = \frac{3}{2}J_2 + \frac{m}{2} + O(J_2^2, J_2m, m^2) \quad (69)$$

(e.g., Seeber 2003). The higher-order terms are approximately 1/1,000 that of the first term in magnitude. Since we may consider m as a constant, it follows that only changes of J_2 account for the variation in flatness. Furthermore, from the orthogonality of the spherical harmonics, the degree-two and order-zero components of the potential variation caused by an earthquake contribute to the change in J_2 . Therefore, from Eq. (41), we have

$$\begin{aligned} \delta J_2 = -\frac{a}{GM}\psi(a, t; n=2, m=0) = -\frac{a}{GM}[(n_1\nu_1 + n_2\nu_2)F_\psi^1(t; n=2) \\ + (n_3\nu_3)F_\psi^2(t; n=2)] \times UdS. \end{aligned} \quad (70)$$

Thus, we obtain the relationship between variations of flatness and potential changes caused by earthquakes.

5.2.2 Observations of J_2

The average rate of J_2 currently observed using space geodetic techniques is -2.8×10^{-11} /year (Cox & Chao 2002), which can largely be explained by postglacial rebound (Han & Wahr 1995). The amplitude of the seasonal fluctuation of J_2 amounts to 3.2×10^{-10} , mostly driven by mass redistribution in the atmosphere, oceans, and continental water (Nerem et al. 2000). Earthquake-induced changes in J_2 , in contrast, are considered to be difficult to detect. According to Chao & Gross (1987), contributions from events of magnitude ~ 8 are estimated to be in the order of 10^{-13} , equal to approximately 1% of the observed secular trend. Even the change caused by the Sumatra-Andaman Islands Earthquake (Mw = 9.3) (Stein & Okal 2005) is -9×10^{-12} , which is barely detectable given the current observational precision of SLR ($\sim 10^{-11}$) (Chao & Gross 2005). Therefore, a postseismic change of J_2 related to the Sumatra-Andaman Islands event has yet to be reported, because it is considered to be too small a change to detect. In the next section, we compute this postseismic deformation from a theoretical interest.

5.2.3 Model and result

For this calculation we employ the Earth model shown in Model 1, Fig. 10, considering a globally averaged viscoelastic structure. As a fault parameter, we use the result of Yamanaka (http://www.eri.u-tokyo.ac.jp/sanchu/Seismo_Note/2004/EIC161e.html; Earthquake Research Institute, 2004); the source depth, dip, and rake angles are 32 km, 8° and 90° , respectively. Substituting $\mathbf{n} = (-\sin \delta, 0, \cos \delta)$, $\boldsymbol{\nu} = (\cos \delta, 0, \sin \delta)$, where $\delta = 8^\circ$ and $UdS = 3 \times 10^{12} m^3$ (Mw=9.3 for $\mu = 30$ GPa), and the y -functions at each time, which were used to calculate the Green's function in Figs. 15 (c) and 16 (c), into Eq. (70), we obtain the time variation of δJ_2 .

Fig. 40 shows the computed time variation of δJ_2 . The coseismic mass redistribution acts to make the Earth round, as expected; we obtained the same value of coseismic mass redistribution as that of Chao & Gross (2005). This coseismic offset remains unchanged for up to 1,000 yrs after the event. From 1,000 to 10,000 yrs, however, the Earth begins to recover its original shape. After 10^4 yrs, it starts to become more spherical again.

Variation obtained via the incompressible model using the method described in Section 4.1.2 is superimposed on the compressible trend in Fig. 40. Difference in the two trends up to the first 1,000 yrs are too small to be detected. The maximum difference, however, amounts to approximately 30% at $t=10,000$ yrs.

In conclusion, postseismic variation in Earth flatness associated with the Sumatra-Andaman Islands Earthquake event is not detectable using current observational techniques, even if we consider compressibility.

6 CONCLUSIONS

This study presents the first calculations of viscoelastic deformation caused by earthquakes in a spherically symmetric self-gravitating Earth model without the need for unjustified assumptions. The new computational scheme employs the numerical inverse Laplace integration and reciprocity theorem, which enables compressibility and the continuous radial structure of the Earth to be considered simultaneously. This is in marked contrast to previous methods that required such assumptions to avoid computational difficulties.

Using the new method, a complete set of Green's functions for an arbitrary point dislocation was computed using the PREM and a convex viscosity profile. The behavior of the obtained Green's functions is physically reasonable, indicating the validity of the numerical algorithm. We also revealed the effects of a fine-graded viscoelastic structure and compressibility on the postseismic deformation rate in the far-field for strike-slip and dip-slip sources. The effect of fine layering was saturated at approximately several tens of layers, as indicated by Vermeersen & Sabadini (1997). The difference between Wang's (1999) 11-layer model and the finely-layered model with 60 layers, however, is detectable with current observational techniques such as GPS. The effect of compressibility amounts to 10-20% of the horizontal displacement velocity in the first few decades after the event and 50-60% on the vertical scale on average. These rate differences are also observable. The above results strongly indicate the need to consider effects that have been previously neglected if the theory is to achieve observational-type accuracy.

The fact that these effects are not negligible suggests that we should re-examine the role of viscoelastic relaxation as a mechanism of postseismic deformation. As an example, we estimated the coseismic and postseismic deformation associated with the 2003 Tokachi-Oki Earthquake ($M_w=8.0$). The predicted deformation rate is in good agreement with that observed by GPS. This result contradicts previous studies that explained the postseismic deformation for approximately 2 yrs after the event purely in terms of afterslip; however, the short-term afterslip for the month following the earthquake, as shown by Miyazaki et al. (2004), cannot be explained by the viscoelastic model.

Finally, we computed the postseismic change of the Earth's flatness due to the Sumatra-

Andaman Islands Earthquake ($M_w=9.3$) as an example of truly global-scale deformation. Although the variation is not detectable with present observational techniques, we confirmed that the effect of compressibility produces a 30% difference in deformation over geological time-scales such as several tens of thousands of years.

The new method can be applied to a wide range of applications, such as modeling interseismic deformation within plate boundary zones (Savage 1983; Sato & Matsu'ura 1988) and correcting uplift/subsidence at tide gauge stations for detecting sea level change (Melini et al. 2004). In such applications, we may have to examine the effects of lateral variations in viscosity, topography, and crustal thickness etc. (Suito & Hirahara 1999). To accommodate the effects of lateral variations, a direct numerical approach may be the only versatile method available, as recently used in the computation of postglacial rebound. Even considering this, our semi-analytical method provides a benchmark for a spherically symmetric, compressible Earth model with an arbitrary viscoelastic structure.

ACKNOWLEDGMENTS

I would like to express my sincere appreciation to my advisor, Dr. Shuhei Okubo for his insightful advice and encouraging me to complete this thesis. I also appreciate Dr. Wenke Sun, Dr. Masato Furuya, and Dr. Jun'ichi Okuno at the Earthquake Research Institute, University of Tokyo, and Dr. Takuya Nishimura, Dr. Hisashi Suito, Dr. Shinzaburo Ozawa and Dr. Yuki Kuroishi at the Geographical Survey Institute for the valuable discussions and comments. I acknowledge Mr. Hiroaki Saita at the Geo-Referencing Information Section and my supervisors, Mr. Akira Yamada, Mr. Yasutomo Shirai, and Mr. Masaki Murakami at the GSI. I also thank many other colleagues and staffs who have supported this work. I used GMT software (Wessel & Smith 1991) to make a lot of figures in this thesis.

REFERENCES

- Altamimi Z., Boucher, C. & Sillard, P., 2002. ITRF2000: A new release of the International Terrestrial Reference Frame for earth science applications, *J. Geophys. Res.*, **107**, B10, 2214, doi:10.1029/2001JB000561.
- Alterman, Z., Jarosch, H. & Pekris, C. L., 1959. Oscillation of the Earth, *Proc. R. Soc. Lond.*, **A252**, 80-95.
- Antonoli, A., Piersanti, A. & Spada, G. Stress diffusion following large strike slip earthquakes: a comparison between spherical and flat-earth models, *Geophysical Journal International*, **133**, 85-90.
- Barrientos, S. E., Plafker, G. & Lorca, E., 1992. Postseismic coastal uplift in southern Chile, *Geophysical Research Letters*, **19**, 701-704.
- Beutler, G., Rothacher, M., Schaer, S., Springer, T.A., Kouba, J. & Neilan, R.E., 1999. The International GPS Service (IGS): An Interdisciplinary Service in Support of Earth Sciences, *Adv. Space Res.* **23**, No. 4, 631-635.
- Bock, Y., Agnew, D. C., Fang, P., Genrich, J. F., Hager, B. H., Herring, T., Hudnut, K., King, R., Larsen, S., Minster, J. B., Stark, K., Wdowinski, S. & Wyatt, F., 1993. Detection of crustal deformation from the Landers earthquake sequence using continuous geodetic measurements, *Nature*, **361**, 337-340.
- Boschi, L., Piersanti, A. & Spada, G., 1997. Time-dependent residual deformations associated with the June 9, 1994 Bolivia earthquake, *Geophys. Res. Lett.*, **24**, 2849-2852.
- Boschi, L., Tromp, J. & O'Connell, R., 1999. On maxwell singularities in postglacial rebound, *Geophys. J. Int.*, **136**, 492-498.
- Chao, B. F., & Gross, R. S., 1987. Changes in the Earth's rotation and low-degree gravitational field induced by earthquakes, *Geophys. J. Roy. Astron. Soc.*, **91**, 569-596.
- Chao, B. F., & Gross, R. S., 2005. Did the 26 December 2004 Sumatra, Indonesia, Earthquake Disrupt the Earth's Rotation as the Mass Media Have Said? *Eos*, **86**, No. 1, 4 January 2005.
- Cox, C. & Chao, B. F., 2002. Detection of large-scale mass redistribution in the terrestrial system since 1998, *Science*, **297**, 831-832.
- Deng, J., Gurnis, M., Kanamori, H. & Hauksson, E., 1998. Viscoelastic flow in the lower crust after the 1992 Landers, California, Earthquake, *Science*, **282**, 1689-1692.
- Dickey, J. O. et al., *Satellite Gravity and the Geosphere*, National Research Council Report, 112 pp., Nat. Acad. Washington, D.C.
- Dragert G, Wang K, & James TS., 2001. A silent slip event on the deeper Cascadia subduction interface. *Science*, **292** (5521): 1525-8.
- Dziewonski, A. M. & Anderson, A., 1981. Preliminary reference earth model, *Phys. Earth planet. Inter.*, **25**, 297-356.
- Fang, M. & Hager, B. H., 1994. A singularity free approach to postglacial rebound calculations, *Geophys. Res. Lett.*, **21**, 2131-2134.

- Fang, M. & Hager, B. H., 1995. The singularity mystery associated with a radially continuous Maxwell viscoelastic structure, *Geophys. J. Int.* **123**, 849-865.
- Farrell, W. E., 1972. Deformation of the Earth by surface loads., *Rev. Geophys. Space Phys.*, **10**, 761-797.
- Fujii, Y. & Nakane, K., 1983. Horizontal crustal movements in the Kanto-Tokai district, Japan, as deduced from geodetic data, *Tectonophys.*, **97**, 115-140.
- Gilbert, F. & Dziewonski A. M., 1975. An application of normal mode theory to the retrieval of structural parameters and source mechanisms from seismic spectra, *Phil. Trans. R. Soc. Lond.*, **A278**, 187-269.
- Han, D. & Wahr, J., 1995. The viscoelastic relaxation of a realistically stratified earth, and a further analysis of postglacial rebound, *Geophys. J. Int.* **120**, 287-311.
- Hanyk, L., Moser, J., Yuen, D. A. & Matyska, C., 1995. Time-domain approach for the transient responses in stratified viscoelastic Earth models, *Geophys. Res. Lett.*, **22**, 1285-1288.
- Haskell, N. A., 1935. The motion of a fluid under the surface load. *Physics*, **6**, 265-269.
- Hatanaka, Y., Iizuka, T., Sawada, M., Yamagiwa, A., Kikuta, Y., Johnson, J. M. & Rocken, C., 2003. Improvement of the analysis strategy of GEONET, *Bull. Geogr. Surv. Inst.*, **49**, 11-38.
- Heki, K. & Tamura, Y., 1997. Short term afterslip in the 1994 Sanriku-Haruka-Oki earthquake, *Geophys. Res. Lett.*, **24**, 3285-3288.
- Hetland, E. A. & Hager, B. H., 2003. Postseismic relaxation across the Central Nevada Seismic Belt, *J. Geophys. Res.*, **108(B8)**, 2394, doi:10.1029/2002JB002257.
- Imanishi, Y., Sato, T., Higashi, T., Sun, W. & Okubo, W., 2004. A Network of Superconducting Gravimeters Detects Submicrogal Coseismic Gravity Changes, *Science*, **306**, 476-478.
- Jonsson, S., Segall, P., Pedersen, R. & Bjornsson, G., 2003. Post-earthquake ground movements correlated to pore-pressure transients, *Nature*, **424**, 179-183.
- Kawasaki I., Asai Y., Tamura Y., Sagiya T., Mikami N., Okada Y., Sakata M. & Kasahara M., 1995. The 1992 Sanriku-Oki, Japan, Ultra-Slow Earthquake, *Journal of Physics of the Earth*, **43**: (2) 105-116.
- Larsen, C. F., Echelmeyer, K. A., Freymueller, J. T. & Motyka R. J., 2003. Tide gauge records of uplift along the northern Pacific-North American plate boundary, 1937 to 2001, *J. Geophys. Res.*, **108 (B4)**, 2216, doi:10.1029 / 2001JB001685.
- Love, A. E. H., *Some Problems of Geodynamics*, Cambridge Univ. Press, London and New York.
- Longman, I.M., 1962. A Green's Function for determining the deformation of the Earth undersurface mass loads 1. Theory, *J. geophys. Res.*, **67(2)**, 845-950.
- MacMillan, D. S. & Gipson, J. M., 1994. Atmospheric pressure loading parameters from very long baseline interferometry observations, *J. Geophys. Res.*, **99**, 18081-18087.
- Massonnet, D., Rossi, M., Carmona, C., Adragna, F., Peltzer, G., Feigl, K. & Rabaute, T., 1993. The displacement field of the Landers earthquake mapped by radar interferometry, *Nature*, **364**, 138-142.
- Matsu'ura, M., 1977. Inversion of geodetic data. II: Optimal model of conjugate fault system for the 1927

- Tango earthquake, *J. Phys. Earth*, **25**, 233-255.
- Matsu'ura, M., Tanimoto, T. & Iwasaki, T., 1981. Quasi-static displacements due to faulting in a layered half-space with an intervenient viscoelastic layer, *J. Phys. Earth*, **29**, 23-54.
- Matsu'ura, M. & Iwasaki, T., 1983. Study on coseismic and postseismic crustal movements associated with the 1923 Kanto earthquake, *Tectonophysics*, **97**, 201-215.
- Matsu'ura, M., & Sato, T., 1989. A dislocation model for the earthquake cycle at convergent plate boundaries, *Geophys. J. Int.*, **96**, 23-32.
- Matsu'ura, M., Nishitani, A. & Fukahata, Y., 1998. Slip history during one earthquake cycle at the Nankai subduction zone, inferred from the inversion analysis of levelling data with a viscoelastic slip response function, *Eos Trans. AGU*, **79(45)**, Fall Meet. Suppl., F891.
- Melbourne, T. I., Webb, F. H., Stock, J. M. & Reigber, C., 2002. Rapid postseismic transients in subduction zones from continuous GPS, *J. Geophys. Res.*, **107 (B10)**, 2241, doi:10.1029 / 2001JB000555.
- Melini, D., Piersanti, A., Spada, G., Soldati, G., Casarotti, E. and Boschi, E., 2004. Earthquakes and relative sealevel changes, *Geophys. Res. Lett.*, **31**, L09601, doi:10.1029/2003GL019347.
- Mitrovica, J. X. & Forte, A. M., 1997. Radial profile of mantle viscosity: Results from the joint inversion of convection and postglacial rebound observable. *J. Geophys. Res.*, **102**, 2751-2769.
- Miyazaki, S., Segall, P., Fukuda, J., & Kato, T., 2004. Space time distribution of afterslip following the 2003 Tokachi-oki earthquake: Implications for variations in fault zone frictional properties, *Geophys. Res. Lett.*, **31 (6)**, L06623, doi:10.1029/2003GL019410.
- Nerem, R. S., Eanes, R. J., Thompson, P. F. & Chen, J. L., 2000. Observations of annual variations of the Earth's gravitational field using satellite laser ranging and geophysical models, *Geophys. Res. Lett.*, **27**, 1783-1786.
- Nishimura, T., Imakiire, T., Yagai, H., Ozawa, T., Murakami, M., & Kaidzu, M., 2003. A preliminary fault model of the 2003 July 26, M6.4 northern Miyagi earthquake, northeastern Japan, estimated from joint inversion of GPS, leveling, and InSAR data, *Earth Planets Space*, **55**, 751-757.
- Nostro, C., Piersanti, A., Antonioli, A. & Spada, G., 1999. Spherical versus flat models of coseismic and postseismic deformations, *J. Geophys. Res.*, **104**, 13115-13134.
- Okada, Y., 1985. Surface deformation due to shear and tensile faults in a half-space, *Bull. Seismol. Soc. Am.*, **75**, 1135-1154.
- Okada, Y., 1992. Internal deformation due to shear and tensile faults in a half-space, *Bull. Seismol. Soc. Am.*, **82**, 1018-1040.
- Okubo, S., 1992. Potential and gravity changes due to shear and tensile faults in a half-space, *J. Geophys. Res.*, **97**, 7137-7144.
- Okubo, S., 1993. Reciprocity theorem to compute the static deformation due to a point dislocation buried in a spherically symmetric earth, *Geophys. J. Int.* **115**, 921-928.

- Ozawa, S., Murakami, M., Kaidzu, M., Tada, T., Sagiya, T., Yarai, H. & Nishimura, T., 2020. Detection and monitoring of ongoing aseismic slip in the Tokai region, central Japan, *Science*, **298**, 1009-1012.
- Ozawa, S., Kaidzu, M., Murakami, M., Imakiire, T. & Hatanaka, Y., 2004. Coseismic and postseismic crustal deformation after the M8 Tokachi-oki earthquake in Japan, *Earth Planets Space*, **56** (No. 7), 675-680.
- Parsons, B. E., 1972. Changes in the earth's shape, PhD thesis, Cambridge University, London.
- Paulson, A., Zhong, S. & Wahr, J., 2005. Modelling post-glacial rebound with lateral viscosity variations, *Geophysical Journal International*, **163** (1), 357-371. doi: 10.1111/j.1365-246X.2005.02645.x
- Pekeris, C. L. & Jarosch, H. (Eds.), 1958. *The free oscillations of the Earth, in Contributions in Geophysics*, pp. 171, Pergamon Press, London, New York, Paris, Los Angeles.
- Peltier, W. R., 1974. The impulse response of a Maxwell Earth, *Rev. Geophys. Space Phys.*, **12**, 649-669.
- Piersanti, A., Spada, G., Sabadini, R. & Bonafede, M., 1995. Global postseismic deformation, *Geophys. J. Int.*, **120**, 544-566.
- Piersanti, A., Spada, G. & Sabadini, R., 1997. Global postseismic rebound of a viscoelastic Earth: Theory for finite faults and application to the 1964 Alaska earthquake, *J. Geophys. Res.*, **102**, 477-492.
- Plag, H. P. & Juttner, H. U., 1995, Rayleigh-Taylor instabilities of a self-gravitating earth, *J. Geody.*, **20**, 267-288.
- Pollitz, F. F., 1992. Postseismic relaxation theory on the spherical earth, *Bull. seism. Soc. Am.*, **82**, 422-453.
- Pollitz, F. F., 1997. Gravitational viscoelastic postseismic relaxation on a layered spherical Earth, *J. Geophys. Res.*, **102**, 17921-17941.
- Pollitz F. F., Wicks, C. & Thatcher, W., 2001. Mantle flow beneath a continental strike-slip fault: postseismic deformation after the 1999 Hector Mine earthquake, *Science*, **293**, 1814-1818.
- Pollitz, F. F., 2003. Transient Rheology of the Uppermost Mantle Beneath the Mojave Desert, California, *Earth and Planetary Science Letters*, **215** / 1-2, 89-104.
- Pollitz, F. F., 2003. Post-seismic relaxation theory on a laterally heterogeneous viscoelastic model, *Geophys. J. Int.*, **155**, 57-78.
- Ricard, Y., & Wuming, B., 1991. Inferring the viscosity and 3-D density structure of the mantle from geoid, topography and plate velocities, *Geophys. J. Int.*, **105**, 561-571.
- Richter, F. M. & Parson, B., 1975. On the interaction of two scales of convection in the mantle, *JGR*, **80**, 2529-2541.
- Rundle, J.B., 1982. Viscoelastic gravitational deformation by a rectangular thrust fault in a layered earth, *J. Geophys. Res.*, **87**, 7787 - 7796.
- Sabadini, R. & Yuen, D. A., 1989. Mantle stratification and long-term polar wander, *Nature*, **339**, 373-375.
- Sabadini, R. & Vermeersen, L. L. A., 1997. Influence of lithospheric and mantle stratification on global postseismic deformation, *Geophys. Res. Lett.*, **24**, 2075-2078.

- Saito, M., Excitation of free oscillations and surface waves by a point source in a vertically heterogeneous Earth, 1967. *J. Geophys. Res.*, **72**, 3689-3699.
- Sagiya, T., 2004. Interplate coupling in the Kanto District, central Japan, and the Boso Silent earthquake in May 1996, *PAGEOPH*, **161**, 11-12, 2601-2616.
- Sato, R. & Matsu'ura, M., 1973. Static deformations due to the fault spreading over several layers in a multi-layered medium. I: Displacement, *J. Phys. Earth*, **21**, 227-249.
- Sato, T., & Matsu'ura, M., 1988. A kinematic model for deformation of the lithosphere at subduction zones, *J. Geophys. Res.*, **93**, 6410-6418.
- Savage, J. C., 1983. A dislocation model of strain accumulation and release at a subduction zone, *J. Geophys. Res.* **88**, 4984-4996.
- Seeber, G., 2003. Satellite Geodesy, 2nd edition, Walter de Gruyter, Berlin, New York.
- Soldati, G., Boschi, L., Piersanti, A. & Spada, G., 2001. The effect of global seismicity on the polar motion of a viscoelastic Earth, *J. Geophys. Res.*, **106**, 6761-6767.
- Stein, S. & Okal, E. A., 2005. Speed and size of the Sumatra earthquake, *Nature*, **434**, 581-582.
- Steketee, J. A., 1958. Some geophysical applications of the elasticity theory of dislocations, *Can. J. Phys.*, **36**, 1168-1197.
- Suito, H. & Hirahara, K., 1999. Simulation of postseismic deformations caused by the 1896 Riku-u earthquake, northeast Japan: Re-evaluation of the viscosity in the upper mantle, *Geophys. Res. Lett.*, **26**, 2561-2564.
- Sun, W., 1992. Potential and gravity changes caused by dislocations in spherically symmetric Earth models, *Bull. Earthq. Res. Inst. Univ. of Tokyo.*, **67**, 89-238.
- Sun, W. & Okubo, S., 1993. Surface potential and gravity changes due to internal dislocations in a spherical earth I. Theory for a point dislocation, *Geophys. J. Int.*, **114**, 569-592.
- Sun, W., Okubo, S. & Vanicek, P., 1996. Global displacements caused by point dislocations in a realistic Earth model, *J. Geophys. Res.*, **101 (B4)**, 8561-8577.
- Takeuchi, H. & Saito, M., 1972. Seismic surface waves, *Methods Comput. Phys.*, **11**, 217-295.
- Tapley, B. D., Bettadpur, S., Watkins, M. & Reigber, C., 2004. The gravity recovery and climate experiment: Mission overview and early results *Geophys. Res. Lett.*, **31**, No. 9, L09607, 10.1029/2004GL019920, 08 May 2004.
- Thatcher, W. & Rundle, J. B., 1979. A model for the earthquake cycle in underthrust zones, *J. Geophys. Res.*, **84**, 5540-5556.
- Thatcher, W., 1984. The earthquake deformation cycle on the Nankai Trough, southwest Japan, *J. Geophys. Res.*, **89**, 3087-3101.
- Tromp, J. & Mitrovica, J. X., 1999. Surface loading of a viscoelastic earth -I. General theory, *Geophys. J. Int.*, **137**, 847-855.

- Tromp, J. & Mitrovica, J. X., 1999. Surface loading of a viscoelastic earth -II. Spherical models, *Geophys. J. Int.*, **137**, 856-872.
- Tse, S. T. & Rice, J. R., 1986. Crustal earthquake instability in relation to the depth variation of frictional slip properties, *J. Geophys. Res.* **91**, 9452-9472.
- Tsuji, H., Hatanaka, Y., Sagiya, T., & Hashimoto, M., 1995. Coseismic crustal deformation from the 1994 Hokkaido-Toho-Oki earthquake monitored by a nationwide continuous GPS array in Japan, *Geophys. Res. Lett.*, **22**, 1669-1672.
- Ueda, H., Ohtake, M. & Sato, H., 2003. Postseismic crustal deformation following the 1993 Hokkaido Nanseioki earthquake, northern Japan: Evidence for a low-viscosity zone in the uppermost mantle, *J. Geophys. Res.*, **108 (B3)**, 2151, doi:10.1029/2002JB002067.
- Van Dam, T.M., & Wahr, J.M., 1987. Displacements of the Earth's Surface Due to Atmospheric Loading: Effects on Gravity and Baseline Measurements, *J. Geophys. Res.*, **92**, 1281-1286.
- Vergnolle, M., Pollitz, F. & Calais, E., 2003. Constraints on the viscosity of the continental crust and mantle from GPS measurements and postseismic deformation models in western Mongolia Mathilde Vergnolle, *J. Geophys. Res.*, **108 (B10)**, 2502, doi:10.1029/2002JB002374.
- Vermeersen, L. L. A. & Sabadini, R., 1996. Compressible rotational deformation, *Geophys. J. Int.*, **126**, 735-761.
- Vermeersen, L. L. A. & Sabadini, R., 1997. A new class of stratified viscoelastic models by analytical techniques, *Geophys. J. Int.*, **129**, 531-570.
- Vermeersen, L.L.A., & Mitrovica, J. X., 2000. Gravitational stability of spherical self-gravitating relaxation models, *Geophys. J. Int.*, **142**, 351-360.
- Wang, H., 1999. Surface vertical displacements, potential perturbations and gravity changes of a viscoelastic earth model induced by internal point dislocations, *Geophys. J. Int.* **137**, 429-440.
- Wessel, P. & Smith, W.H.F., 1991. Free software helps map and display data. *EOS Trans. Amer. Geophys. U.*, **72**, 445-446.
- Wu, P. & Peltier, W. R., 1982. Viscous gravitational relaxation, *Geophys. J. R. astr. Soc.* **70**, 435-485.
- Yoder, C.F., Williams, J.G., Dickey, J.O., Schutz, B.E., Eanes, R.J & Tapley, B.D., 1983. Secular variation of Earth's gravitational harmonic J_2 coefficient from Lageos and nontidal acceleration of Earth rotation, *Nature*, **303**, 757-762.
- Zweck, C., Freymueller, J. T. & Cohen, S. C., 2002. The 1964 Great Alaska Earthquake: Present Day and Cumulative Postseismic Deformation in the Western Kenai Peninsula, *Phys. Earth Planet. Int.*, **132**, 5-20.

APPENDIX A: NUMERICAL SOLUTION OF THE DIFFERENTIAL EQUATION**A1 Spheroidal mode**

We explain how to obtain the numerical solution of Eq. (15) when the equation does not include exciting terms:

$$\frac{d\tilde{y}}{dr}(r, s; n, m) = \tilde{A}(r, s; n)\tilde{y}(r, s; n, m). \quad (\text{A1})$$

(A1) is specifically written as

$$\frac{d\tilde{y}_1}{dr} = \frac{1}{\lambda + 2\mu}(\tilde{y}_2 - \frac{\lambda}{r}[2\tilde{y}_1 - n(n+1)\tilde{y}_3]), \quad (\text{A2})$$

$$\begin{aligned} \frac{d\tilde{y}_2}{dr} &= -s^2\rho\tilde{y}_1 + \frac{2}{r}(\lambda\frac{d\tilde{y}_1}{dr} - \tilde{y}_2) \\ &+ \frac{1}{r}(\frac{2(\lambda - \mu)}{r} - \rho g)[2\tilde{y}_1 - n(n+1)\tilde{y}_3] \\ &+ \frac{n(n+1)}{r}\tilde{y}_4 - \rho(\tilde{y}_6 - \frac{n+1}{r}\tilde{y}_5 + \frac{2g}{r}\tilde{y}_1), \end{aligned} \quad (\text{A3})$$

$$\frac{d\tilde{y}_3}{dr} = \frac{1}{\mu}\tilde{y}_4 + \frac{1}{r}(\tilde{y}_3 - \tilde{y}_1), \quad (\text{A4})$$

$$\begin{aligned} \frac{d\tilde{y}_4}{dr} &= -s^2\rho\tilde{y}_3 - \frac{\lambda}{r}\frac{d\tilde{y}_1}{dr} - \frac{\lambda + 2\mu}{r^2}[2\tilde{y}_1 - n(n+1)\tilde{y}_3] \\ &+ \frac{2\mu}{r^2}(\tilde{y}_1 - \tilde{y}_3) - \frac{3}{r}\tilde{y}_4 - \frac{\rho}{r}(\tilde{y}_5 - g\tilde{y}_1), \end{aligned} \quad (\text{A5})$$

$$\frac{d\tilde{y}_5}{dr} = \tilde{y}_6 + 4\pi G\rho\tilde{y}_1 - \frac{n+1}{r}\tilde{y}_5, \quad (\text{A6})$$

$$\frac{d\tilde{y}_6}{dr} = \frac{n-1}{r}(\tilde{y}_6 + 4\pi G\rho\tilde{y}_1) + \frac{4\pi G\rho}{r}[2\tilde{y}_1 - n(n+1)\tilde{y}_3] \quad (\text{A7})$$

where $\lambda = \lambda(s)$ and $\mu = \mu(s)$ (Eqs. (4) and (5)), and $g = |\mathbf{g}(\mathbf{r})|$ denotes the magnitude of the gravity (Takeuchi & Saito 1972). We integrate the sixth-order ordinary differential equation upward from the initial value at $r \rightarrow 0$. We obtain the initial value by regarding the innermost core ($r \leq \varepsilon$) as homogeneous (Takeuchi & Saito 1972) using the analytic solution for a uniform, compressible and self-gravitating sphere (Love 1911; Pekeris & Jarosch 1958). The three independent solutions that are regular at $r = 0$ are reported to be as shown below.

Two of the independent solutions $\{y_{i1}, y_{i2}, i=1, \dots, 6\}$ are

$$ry_1(r) = nhj_n(x) - fxj_{n+1}(x), \quad (\text{A8})$$

$$r^2 y_2(r) = -(\lambda + 2\mu) f x^2 j_n(x) + 2\mu[n(n-1)h j_n(x) + [2f + n(n+1)]x j_{n+1}(x)], \quad (\text{A9})$$

$$r y_3(r) = h j_n(x) + x j_{n+1}(x), \quad (\text{A10})$$

$$r^2 y_4(r) = \mu[x^2 j_n(x) + 2(n-1)h j_n(x) - 2(f+1)x j_{n+1}(x)], \quad (\text{A11})$$

$$y_5(r) = 3\gamma f j_n(x), \quad (\text{A12})$$

$$r y_6(r) = (2n+1)y_5(r) - 3n\gamma h j_n(x) \quad (\text{A13})$$

where j_n is the spherical Bessel function of the first kind and x stands for kr , α and β are the compressional and shear velocities, respectively, and

$$k^2 = \frac{1}{2} \left(\frac{\omega^2 + 4\gamma}{\alpha^2} + \frac{\omega^2}{\beta^2} \mp \left[\left(\frac{\omega^2}{\beta^2} - \frac{\omega^2 + 4\gamma}{\alpha^2} \right)^2 + \frac{4n(n+1)\gamma^2}{\alpha^2\beta^2} \right]^{1/2} \right), \quad (\text{A14})$$

$$\gamma = 4\pi G\rho/3, \quad (\text{A15})$$

$$f = \frac{\beta^2}{\gamma} \left(k^2 - \frac{\omega^2}{\beta^2} \right), \quad h = f - (n+1). \quad (\text{A16})$$

The third solution $\{y_{i3}, i=1, \dots, 6\}$ is given by

$$r y_1(r) = n r^n, \quad (\text{A17})$$

$$r^2 y_2(r) = 2\mu n(n-1) r^n, \quad (\text{A18})$$

$$r y_3(r) = r^n, \quad (\text{A19})$$

$$r^2 y_4(r) = 2\mu(n-1) r^n, \quad (\text{A20})$$

$$y_5(r) = (n\gamma - \omega^2) r^n \quad (\text{A21})$$

$$r y_6(r) = (2n+1)y_5(r) - 3n\gamma r^n. \quad (\text{A22})$$

The values of these three solutions ((A8)-(A22)) at $r = \varepsilon$ are used as the initial value for integrating Eq. (A1). Thus, we obtain three numerically independent solutions for (A1) (See Eq. (16)).

A2 Toroidal mode

Eq. (22) without exciting terms is solved as follows:

$$\frac{d\tilde{y}^T}{dr}(r, s; n, m) = \tilde{B}(r, s; n)\tilde{y}^T(r, s; n, m). \quad (\text{A23})$$

(A23) is specifically written as

$$\frac{d\tilde{y}_1^T}{dr} = \frac{1}{r}\tilde{y}_1^T + \frac{1}{\mu}\tilde{y}_2^T, \quad (\text{A24})$$

$$\frac{d\tilde{y}_2^T}{dr} = \left(\frac{(n-1)(n+2)\mu}{r^2} + s^2\rho\right)\tilde{y}_1^T - \frac{3}{r}\tilde{y}_2^T \quad (\text{A25})$$

(Takeuchi & Saito 1972). This time, we integrate the second-order ordinary differential equation upward from the initial value at the core-mantle boundary ($r = b$) because the toroidal mode is not excited in the liquid core:

$$\begin{aligned} \tilde{y}_1^T(b, s; n, m) &= 1, \\ \tilde{y}_2^T(b, s; n, m) &= 0. \end{aligned} \quad (\text{A26})$$

Note that no other independent initial value than (A26) exists for obtaining the non-trivial solution.

Thus, we obtain the numerical solution for Eq. (A23) (See Eq. (23)).

APPENDIX B: PROOF THAT S IS A REAL NUMBER

Through the following two steps, we prove that the solution of the characteristic function is a real number.

First, we show that if $y_i(s_k)$ is the eigenfunction for an eigenvalue $s = s_k$, then $s = s_k^*$ is also an eigenvalue and the corresponding eigenfunction is $y_i(s_k^*) = y_i^*(s_k)$. The asterisk indicates the complex conjugate. The eigenfunction $y_i(s_k)$ satisfies the homogeneous terms of Eq. (15):

$$\frac{d}{dr}y_i(s = s_k) = A_{ij}(\lambda(s_k), \mu(s_k))y_j(s_k) \quad (\text{B1})$$

where tildes are omitted. We confirm that

$$\lambda(s_k^*) = \lambda^*(s_k) \quad (\text{B2})$$

$$\mu(s_k^*) = \mu^*(s_k). \quad (\text{B3})$$

Therefore, taking the complex conjugate of Eq. (B1),

$$\frac{d}{dr}y_i^*(s = s_k) = A_{ij}(\lambda^*(s_k), \mu^*(s_k))y_j^*(s_k) \quad (\text{B4})$$

$$= A_{ij}(\lambda(s_k^*), \mu(s_k^*))y_j^*(s_k). \quad (\text{B5})$$

This means that $y_j^*(s_k)$ satisfies the ordinary differential equation for $s = s_k^*$. Furthermore, $y_j^*(s_k)$ satisfies the boundary condition at the surface (Eq. (17));

$$y_2^*(a, s_k) = [y_2(a, s_k)]^* = 0 \quad (\text{B6})$$

$$y_4^*(a, s_k) = y_6^*(a, s_k) = 0. \quad (\text{B7})$$

Thus, it is proved that $y_j^*(s_k)$ is an eigenfunction.

Second, using the above result, we prove that the complex part of $\mu(s = s_k) = 0$. We first modify the Lagrangian (Takeuchi & Saito 1972) using Eq. (B1):

$$\begin{aligned} L_s &\equiv \frac{d}{dr}(r^2[x_1y_2 + n(n+1)x_3y_4 + (4\pi G)^{-1}x_5y_6]) \\ &= K(s_k)[r\dot{x}_1 + (2x_1 - n(n+1)x_3)][r\dot{y}_1 + (2y_1 - n(n+1)y_3)] \\ &+ \frac{\mu(s_k)}{3}\{[2r\dot{x}_1 - (2x_1 - n(n+1)x_3)][2r\dot{y}_1 - (2y_1 - n(n+1)y_3)] \\ &\quad + n(n+1)\frac{1}{\mu(s_k^*)}(rx_4)(ry_4) + n(n^2 - 1)(n+2)\mu(s_k)x_3y_3 \\ &\quad + R\} \end{aligned} \quad (\text{B8})$$

where the tildes above x_i and y_i are omitted, and r denotes real terms. When the set of $x_i, i = 1, \dots, 6$ or $y_i, i = 1, \dots, 6$ is equivalent to the eigenfunction,

$$\int_0^a L_s dr = 0. \quad (\text{B9})$$

Here, $K(s_k)$ does not depend on s .

Next, we substitute the two sets of eigenfunctions into x_i and y_i .

(1) $y_i^*(s_k)$ as x_i and $y_i(s_k)$ as y_i

In this case, after some algebra, we obtain

$$\begin{aligned} L_s &= K|r\dot{y}_1(s_k) + 2y_1(s_k) - n(n+1)y_3(s_k)|^2 \\ &+ \mu(s_k)\left\{\frac{1}{3}|2r\dot{y}_1(s_k) - (2y_1(s_k) - n(n+1)y_3(s_k))|^2\right. \\ &\quad \left.+ \frac{n(n+1)}{|\mu(s_k)|^2}|ry_4(s_k)|^2 + n(n^2 - 1)(n+2)|y_3(s_k)|^2\right\} \end{aligned}$$

$$+R' \quad (\text{B10})$$

where R' denotes the real term.

(2) $y_i(s_k)$ as x_i and $y_i^*(s_k)$ as y_i

In this case, because the eigenvalue is s_k^* , $\lambda = \lambda(s_k^*)$ and $\mu = \mu(s_k^*)$, we obtain

$$\begin{aligned} L_s = & K|r\dot{y}_1(s_k^*) + 2y_1(s_k^*) - n(n+1)y_3(s_k^*)|^2 \\ & + \mu(s_k^*)\left\{\frac{1}{3}|2r\dot{y}_1(s_k^*) - (2y_1(s_k^*) - n(n+1)y_3(s_k^*))|^2\right. \\ & \left. + \frac{n(n+1)}{|\mu(s_k^*)|^2}|ry_4(s_k^*)|^2 + n(n^2-1)(n+2)|y_3(s_k^*)|^2\right\} \\ & + R'. \end{aligned} \quad (\text{B11})$$

Subtracting Eq. (B10) from Eq. (B11) and using the result of the first proof, we obtain

$$0 - 0 = [Im(\mu(s_k)) - Im(\mu(s_k^*))] \times P \quad (\text{B12})$$

where P is a positive real number. Thus, we obtain

$$Im(\mu(s_k)) = 0. \quad (\text{B13})$$

Finally, using Eq. (5), $Im(s_k) = 0$ is shown.

APPENDIX C: POSTSEISMIC DEFORMATIONS AT AN ARBITRARY POINT

We illustrate how to calculate the deformation at an arbitrary point using Fig. 41. The location of the source and the observation point are indicated as S with the latitude θ_1 and the azimuth ϕ_1 and O with θ_2 and ϕ_2 , respectively. N denotes the north pole. We need the angular distance from the epicenter Ψ and the azimuth angle γ from the strike Θ for using the Green's function. The angular distance Ψ is calculable by the spherical trigonometric formula for the NOS:

$$\cos(\Psi) = \cos\left(\frac{\pi}{2} - \theta_1\right) \cos\left(\frac{\pi}{2} - \theta_2\right) + \sin\left(\frac{\pi}{2} - \theta_1\right) \sin\left(\frac{\pi}{2} - \theta_2\right) \cos(\phi_2 - \phi_1). \quad (\text{C1})$$

α is computed with the formula as

$$\sin(\alpha) = \frac{\sin(\phi_2 - \phi_1)}{\sin(\Psi)} \sin\left(\frac{\pi}{2} - \theta_2\right). \quad (\text{C2})$$

Substituting $\gamma = \Theta - \alpha$ into ϕ in Eq. (44), (57) or (64), and referring to the angular distance Ψ as θ in the Green's function, we compute the deformation at point O. For more general cases, see (Sun & Okubo 1993; Sun et al. 1996).

Table 1. Representative methods for postseismic calculation

Author(s)	Basic algorithm	Compressibility	Radial structure
Pollitz (1997)	NMM	Y	3
Piersanti et al. (1995)	NMM	N	4-5
Sabadini & Vermeersen (1997)	NMM	N	10
Wang (1999)	NMM & RPT	Y	11
Present study	RPT & NIL	Y	No limit

NMM: Normal mode method (Peltier 1974) RPT: Reciprocity theorem (Okubo 1993)

NIL: Numerical inverse Laplace integration

Table 2. Classifying theories on global deformation

		Boundary conditions	
		surface stress/potential change	internal dislocation
Constitutive laws	elastic	tidal deformation deformation due to atmospheric pressure / ocean tide loading	free oscillation coseismic deformation
	viscoelastic	postglacial rebound polar wander	postseismic deformation (This study)

Table 3. Viscoelastic normal mode

Label	Cause	Boundary
M0	density contrast	the surface (the earth and the space)
M1		670 km discontinuity (upper / lower mantle)
M2		400 km discontinuity (shallow upper mantle / mantle transition zone)
Mi		other discontinuity of density
C0		core-mantle boundary
C1		inner-core boundary
Ti	Maxwell time's contrast	discontinuity of the ratio of rigidity and viscosity (two modes for each boundary)
L0		viscosity contrast
Di	compressibility	elastic lithosphere and viscoelastic asthenosphere
		innumerably degenerating eigenvalues into inverse Maxwell time for each layer are unlocked

Based on Wu & Peltier (1982); Vermeersen & Sabadini (1996)

Table 4. Boundary conditions for x^{Press} , x^{Tide} , x^{Shear} and x^T

Superscript	$x_2(a, s; n)$	$x_4(a, s; n)$	$x_6(a, s; n)$
Press	$-\frac{(2n+1)g_0}{4\pi Ga}$	0	0
Tide	0	0	$\frac{2n+1}{a}$
Shear	0	$\frac{(2n+1)g_0}{4\pi Gan(n+1)}$	0
T	$\frac{(2n+1)g_0}{4\pi Gan(n+1)}$		

Table 5. Relationship between Green's functions and geometry of point sources

u_r or ψ	$(n_1, n_2, n_3) (\nu_1, \nu_2, \nu_3)$	Dislocation type (figure #)
u_θ		
u_ϕ		
$G_{u,\psi}^1(\theta, t)$	(1,0,0) (1,0,0)	isotropic component
$G_\theta^1(\theta, t)$		of vertical tensile
0		(15a, b, c d)
$G_{u,\psi}^2(\theta, t)$	(0,0,1) (0,0,1)	horizontal tensile
$G_\theta^2(\theta, t)$		(16a, b, c, d)
0		
$G_{u,\psi}^3(\theta, t) \cos(\phi)$	(1,0,0) (0,0,1)	vertical dip-slip
$(G_\theta^3(\theta, t) + G_\theta^{l1}(\theta, t)) \cos(\phi)$		(17a, b, c, d, e)
$-(G_\phi^1(\theta, t) + G_\phi^{l1}(\theta, t)) \sin(\phi)$		
$G_{u,\psi}^4(\theta, t) \sin(2\phi)$	(1,0,0) (0,1,0)	vertical strike-slip
$(G_\theta^4(\theta, t) + G_\theta^{l2}(\theta, t)) \sin(2\phi)$		(18a, b, c, d, e)
$(G_\phi^2(\theta, t) + G_\phi^{l2}(\theta, t)) \cos(2\phi)$		
$G_{u,\psi}^1(\theta, t) + G_{u,\psi}^4(\theta, t) \cos(2\phi)$	(1,0,0) (1,0,0)	vertical tensile
$G_\theta^1(\theta, t) + (G_\theta^4(\theta, t) + G_\theta^{l2}(\theta, t)) \cos(2\phi)$		(19a, b, c, d, e)
$-(G_\phi^2(\theta, t) + G_\phi^{l2}(\theta, t)) \sin(2\phi)$		
$-\frac{1}{2}G_{u,\psi}^1(\theta, t) + \frac{1}{2}G_{u,\psi}^2(\theta, t) - \frac{1}{2}G_{u,\psi}^4(\theta, t) \cos(2\phi)$	$(-\frac{1}{\sqrt{2}}, 0, \frac{1}{\sqrt{2}}) (\frac{1}{\sqrt{2}}, 0, \frac{1}{\sqrt{2}})$	dip-slip with 45°
$-\frac{1}{2}G_\theta^1(\theta, t) + \frac{1}{2}G_\theta^2(\theta, t) - \frac{1}{2}(G_\theta^4(\theta, t) + G_\theta^{l2}(\theta, t)) \cos(2\phi)$		(20a, b, c, d, e)
$\frac{1}{2}(G_\phi^2(\theta, t) + G_\phi^{l2}(\theta, t)) \sin(2\phi)$		

Table 6. The source parameter

source	longitude (deg)	latitude (deg)	dpeth (km)	UdS (m^3)	strike (deg)	dip(deg)	rake(deg)
S1	144.15	41.85	20	2.1×10^{10}	230	20	90
S2	143.9	42.1	30	2.1×10^{10}	230	20	110

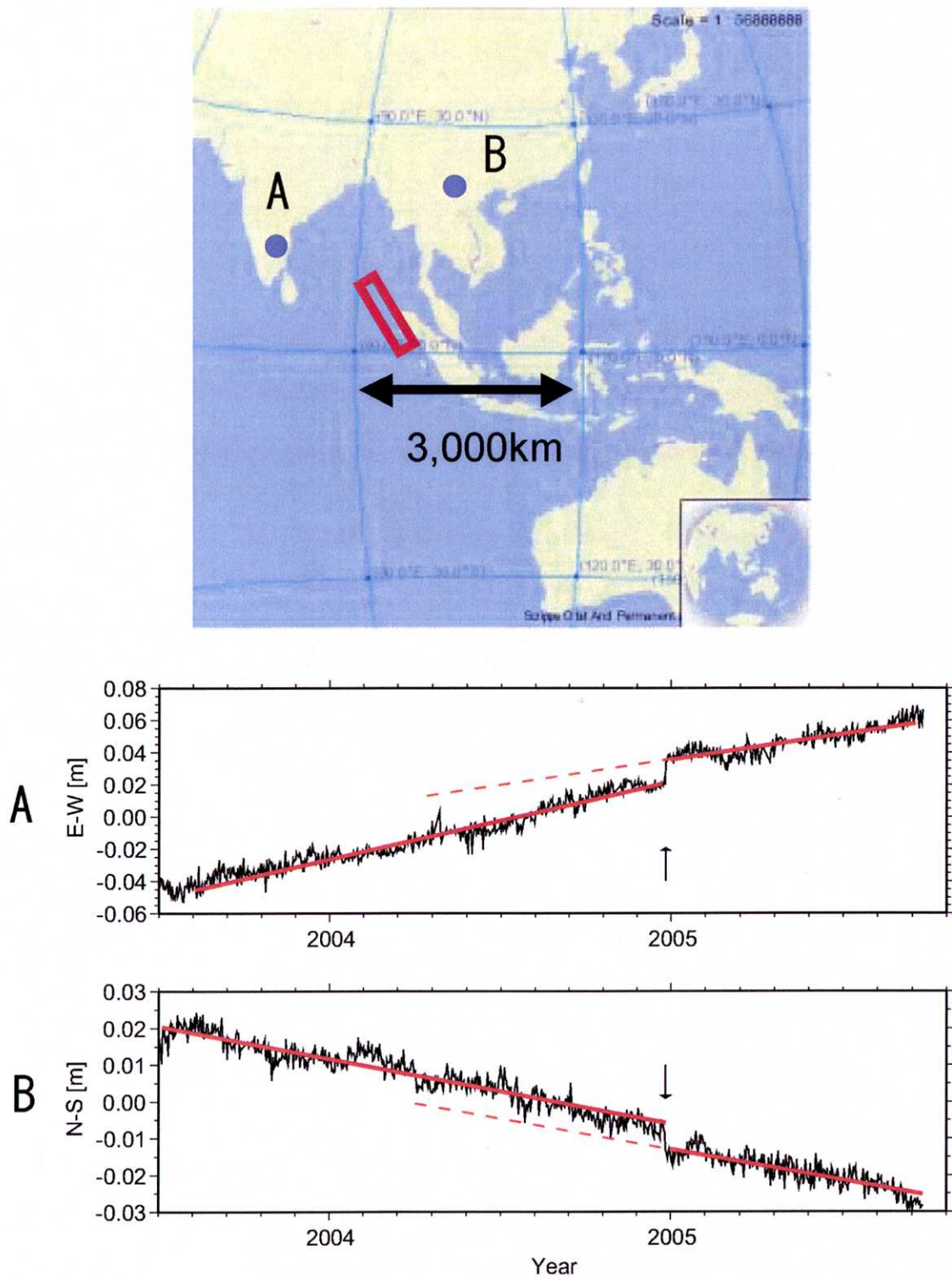


Figure 1. The coseismic and postseismic deformation observed with GPS in the far-field. The red box in the upper figure shows the fault. The GPS analysis result is derived from the Scripps Orbit and Permanent Array Center (SOPAC).

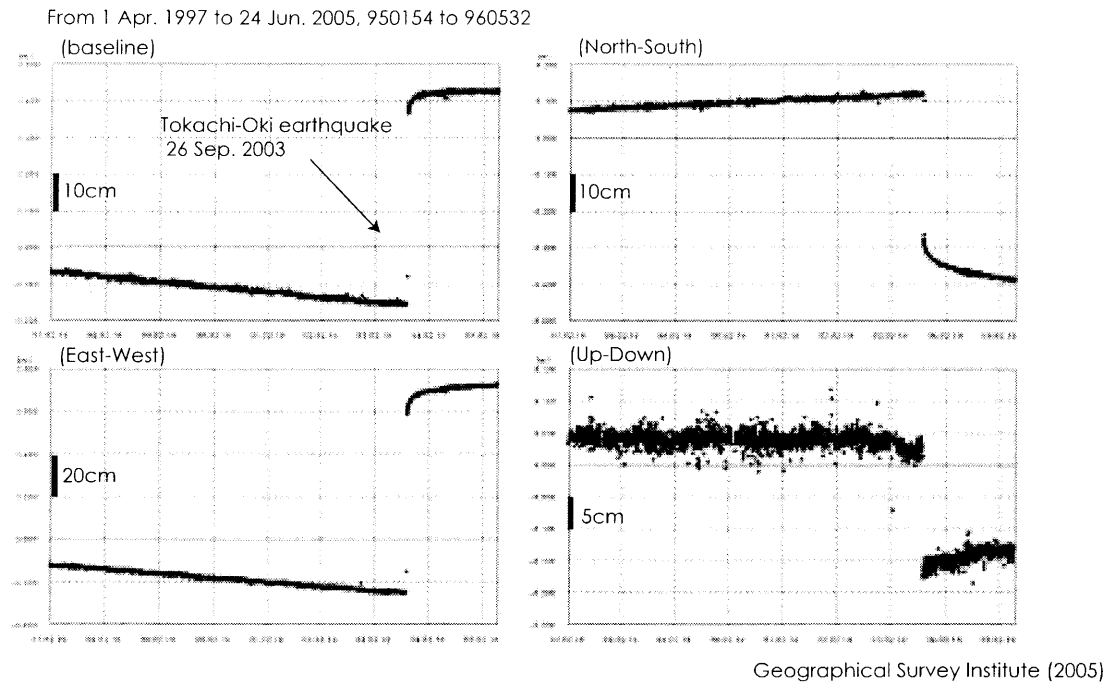


Figure 2. Postseismic deformation observed with GPS. Annual and semi-annual variations are being removed by fitting sinusoidal functions.

Location of the GPS and SG stations

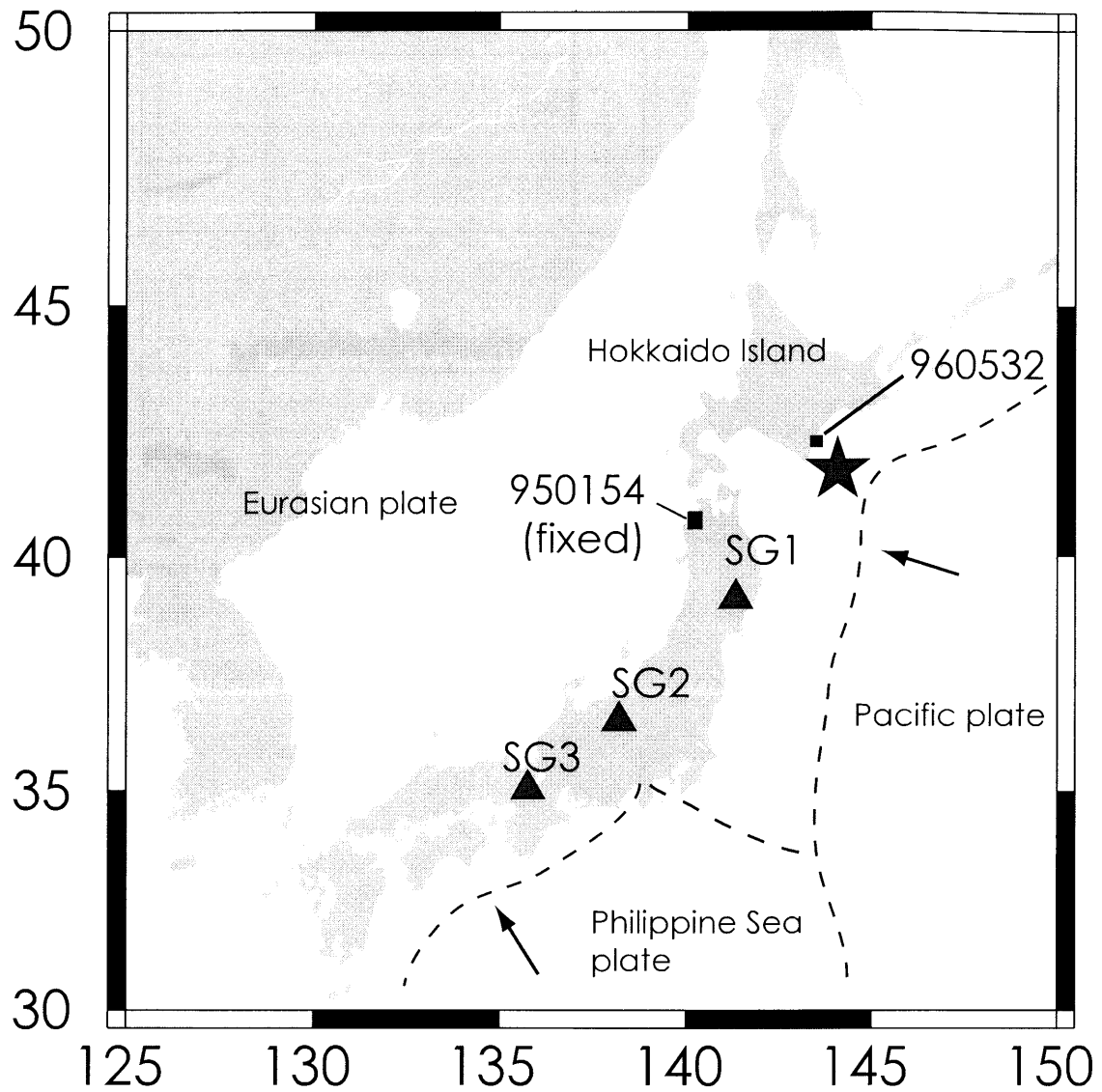


Figure 3. The location of observational points. The star denotes the epicenter. The vectors show the direction of plate subduction.

Comparison of the coseismic gravity change

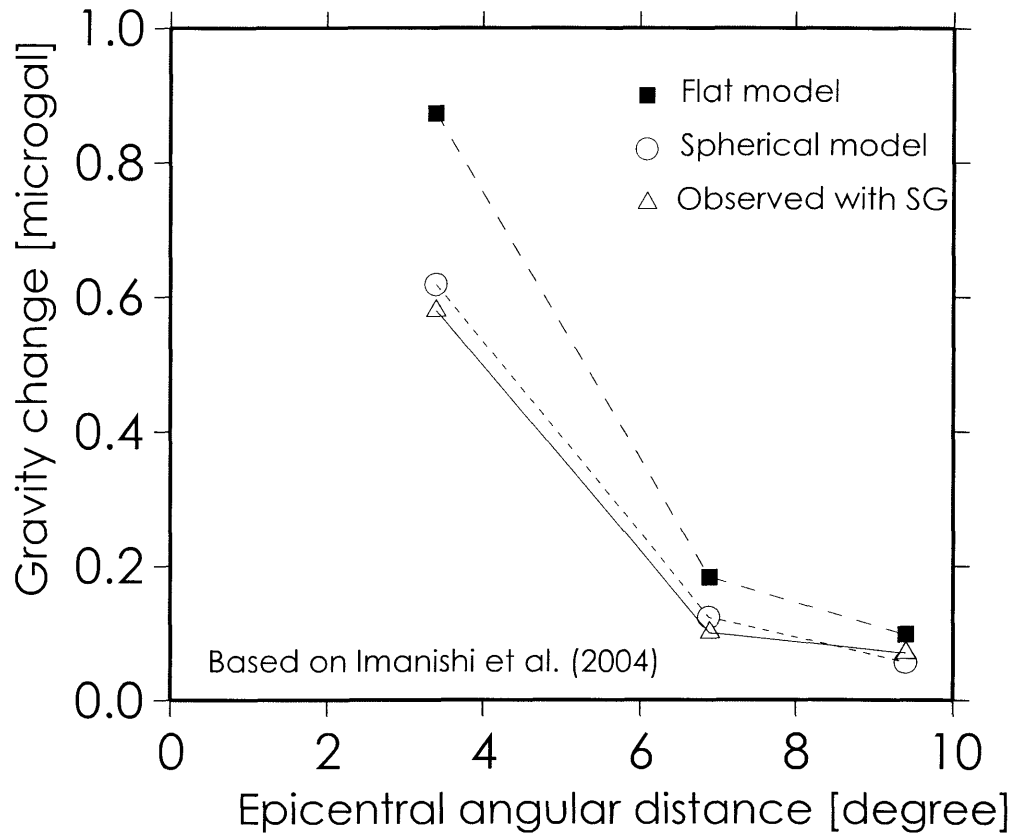


Figure 4. The effect of the curvature on a coseismic gravity change

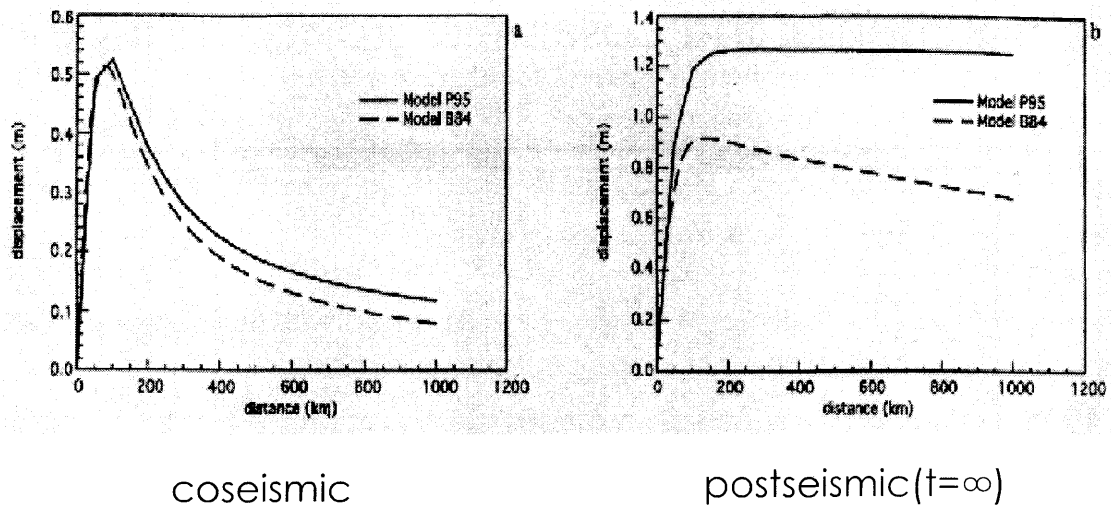
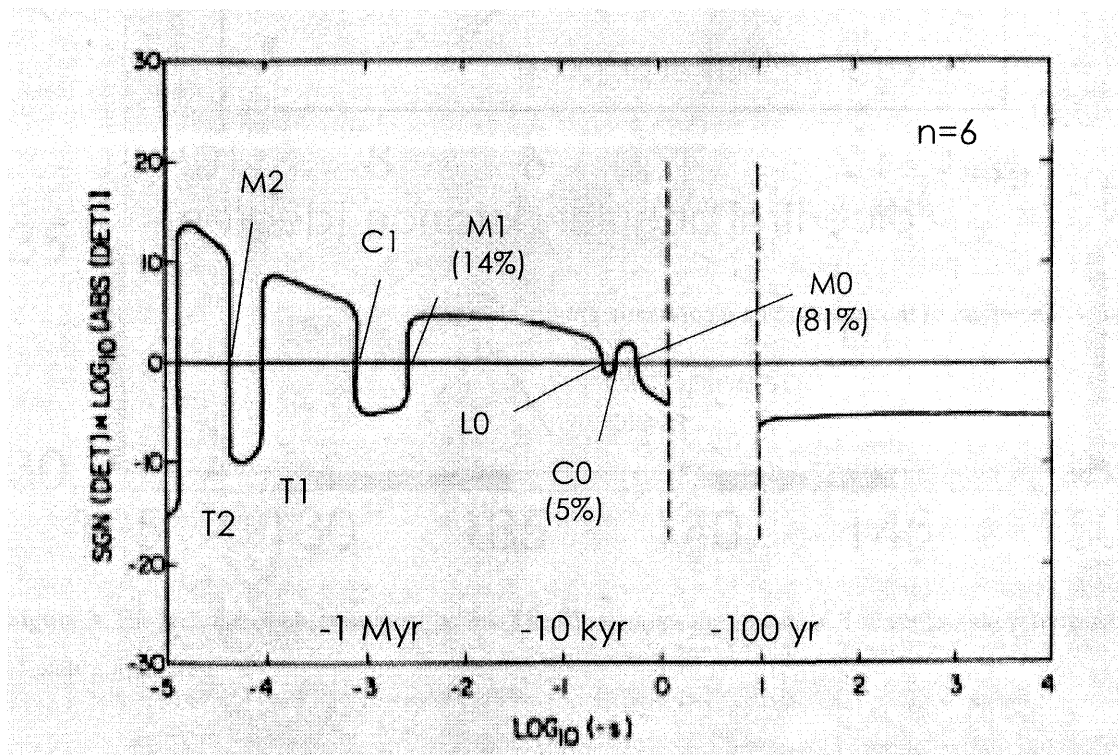


Figure 5. The effect of the curvature on a postseismic deformation (Nostro et al. 1999). A horizontal displacement for a strike-slip dislocation is shown. The dotted and the solid lines denote the displacement for a semi-finite medium and a spherical one, respectively.



Based on Wu & Peltier (1982)

Figure 6. Viscoelastic normal modes

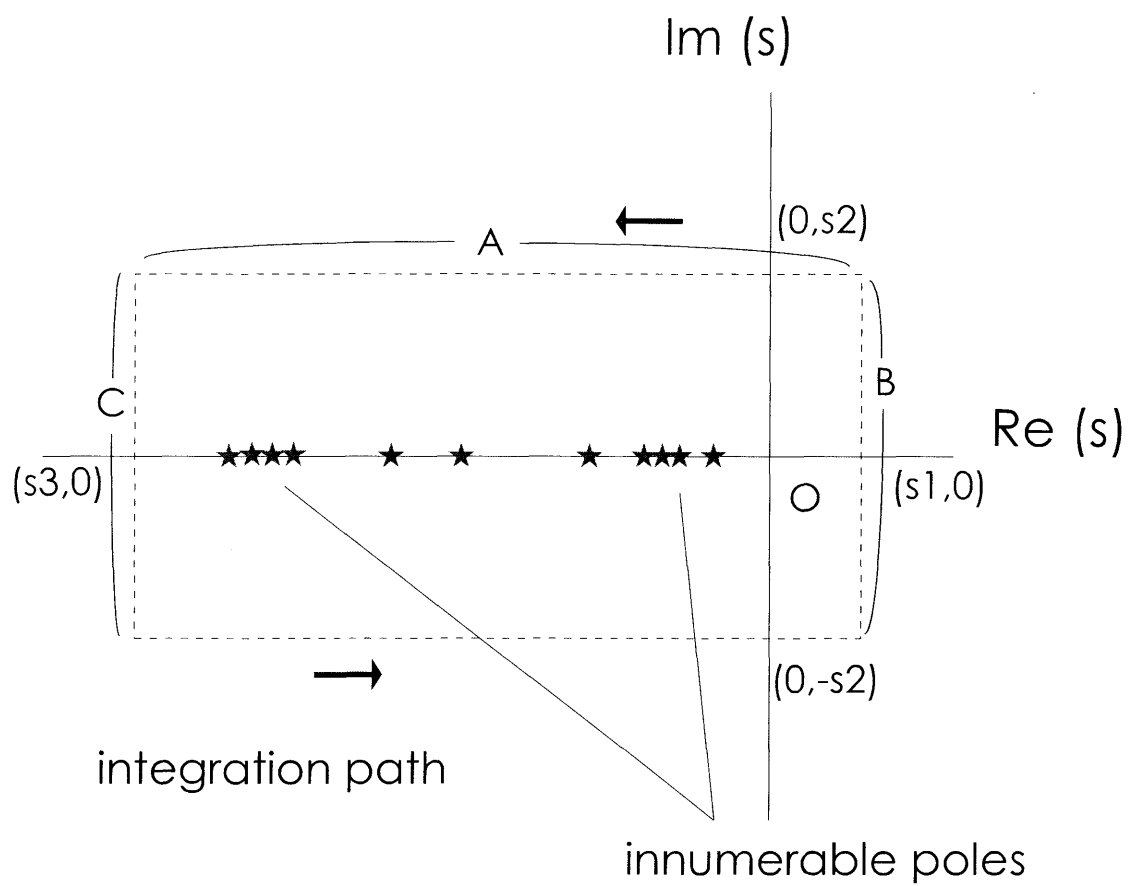


Figure 7. The integration path surrounding innumerable poles

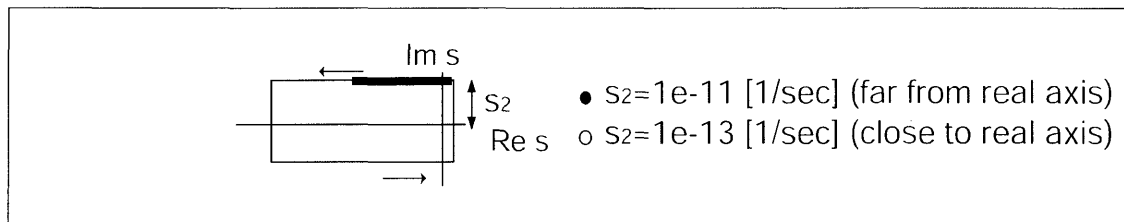
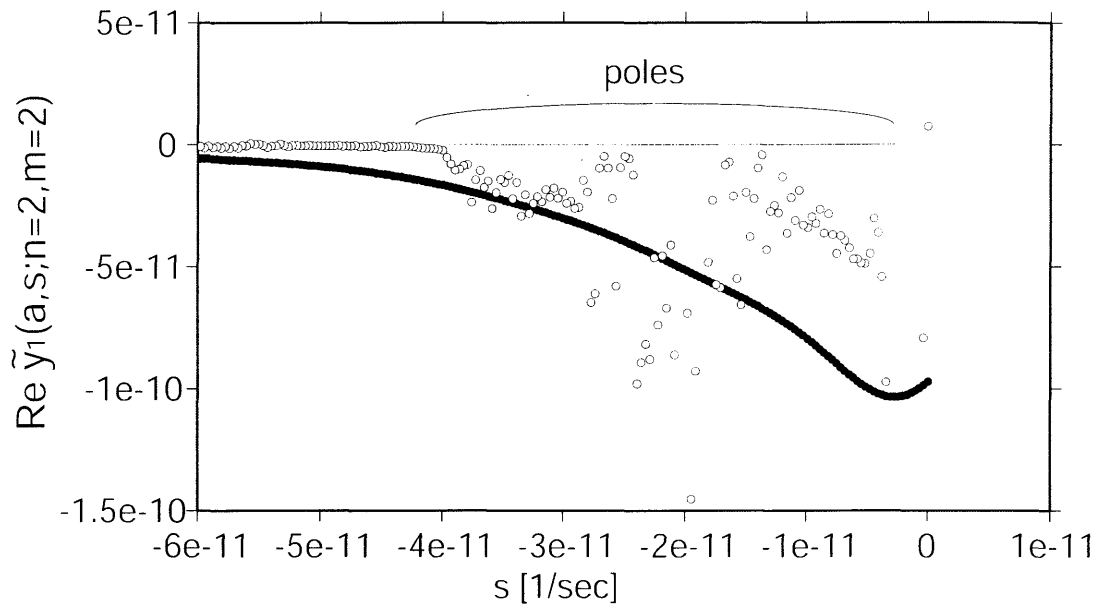


Figure 8. Smoothness of the integrand on the path. The solid line in the lower figure shows the interval on which $\tilde{y}_1(a, s; n=2, m=2)$ (Eq. (18)) is calculated.

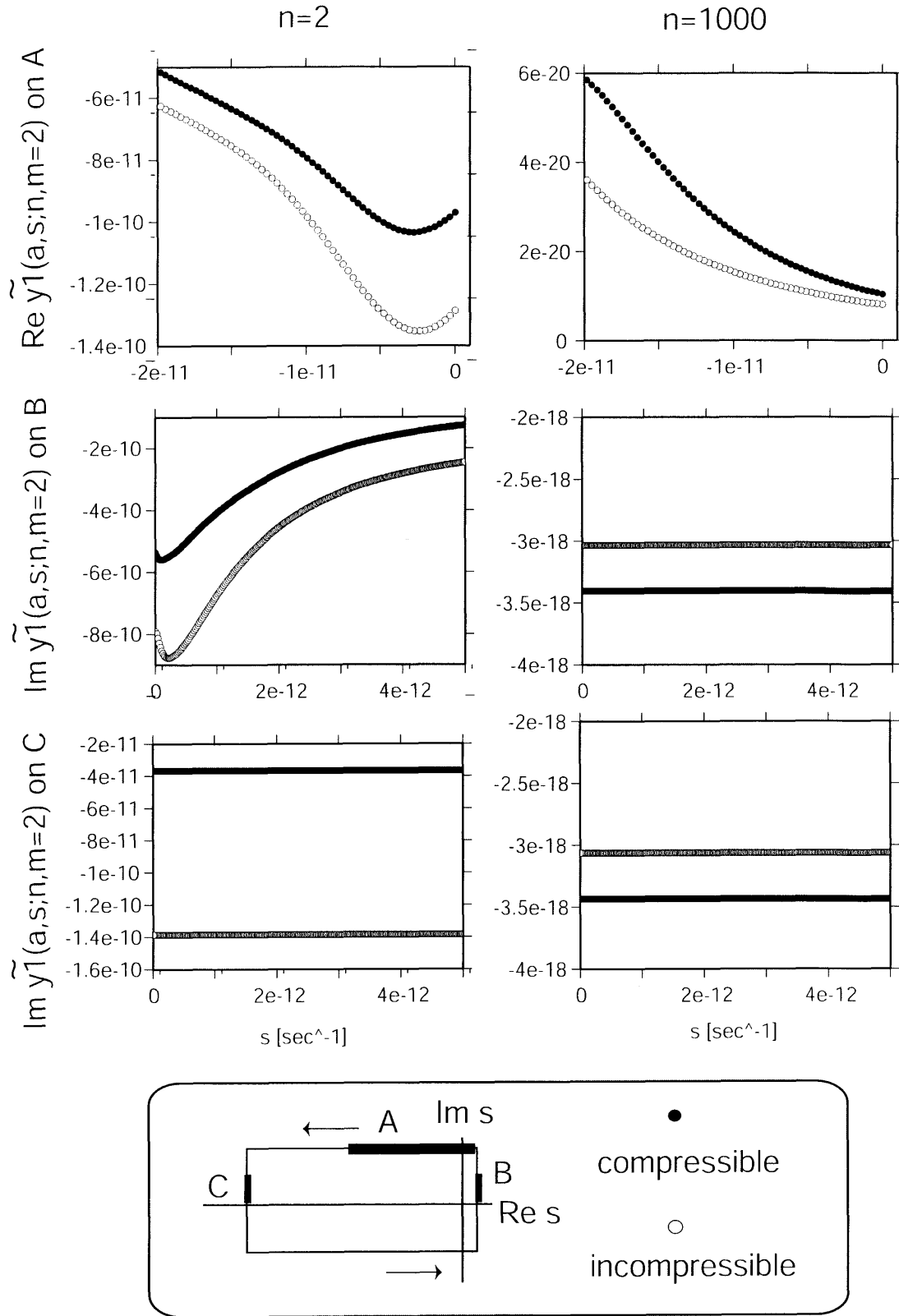


Figure 9. Visible effect of compressibility on the integrand. The solid line in the lower figure shows the interval on which $\tilde{y}_1(a, s; n=2, 1000, m=2)$ (Eq. (18)) is calculated.

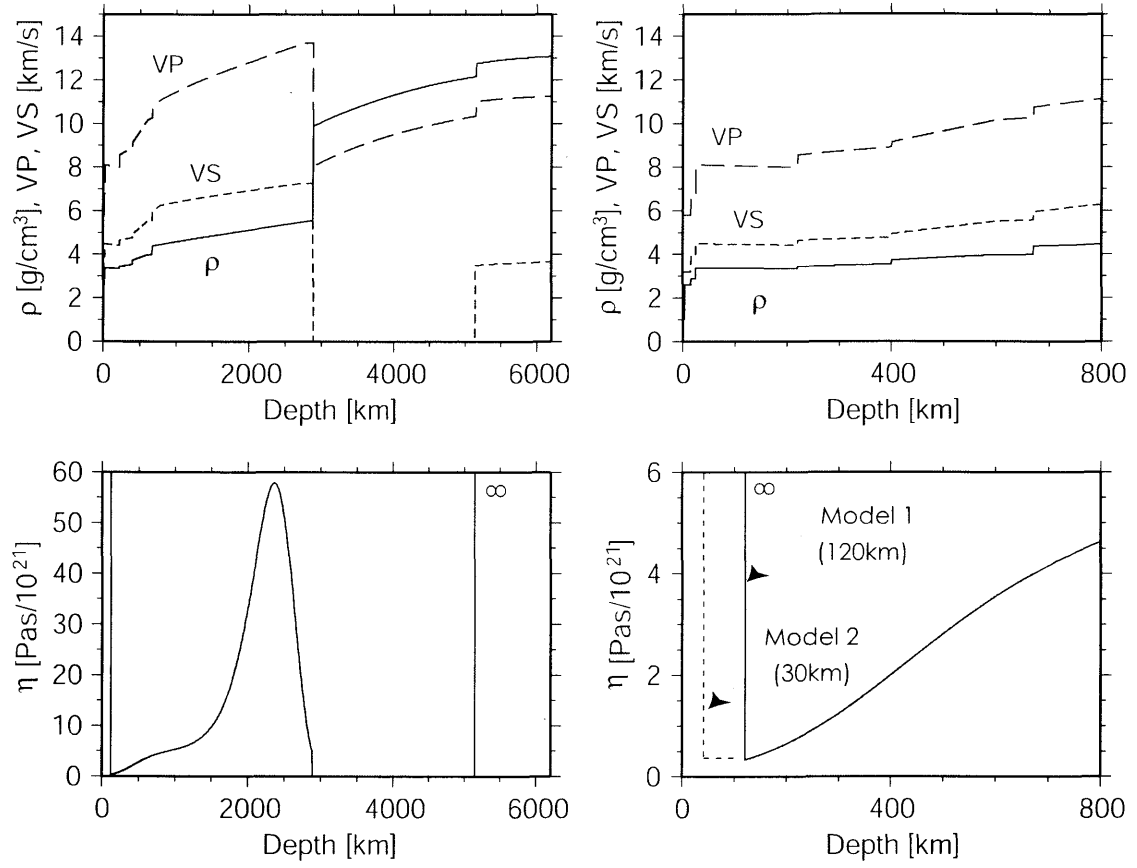


Figure 10. The elastic Earth model PREM and the viscosity profile used to compute the Green's function. Density ρ and P- and S-wave velocities (VP and VS) are shown. The viscosity equals to infinity (i.e., perfect elastic body) up to a depth of 120 km for Model 1 and 30 km for Model 2. The shallow part of the profile is magnified to the right. Perfect solid body is also assumed in the inner core.

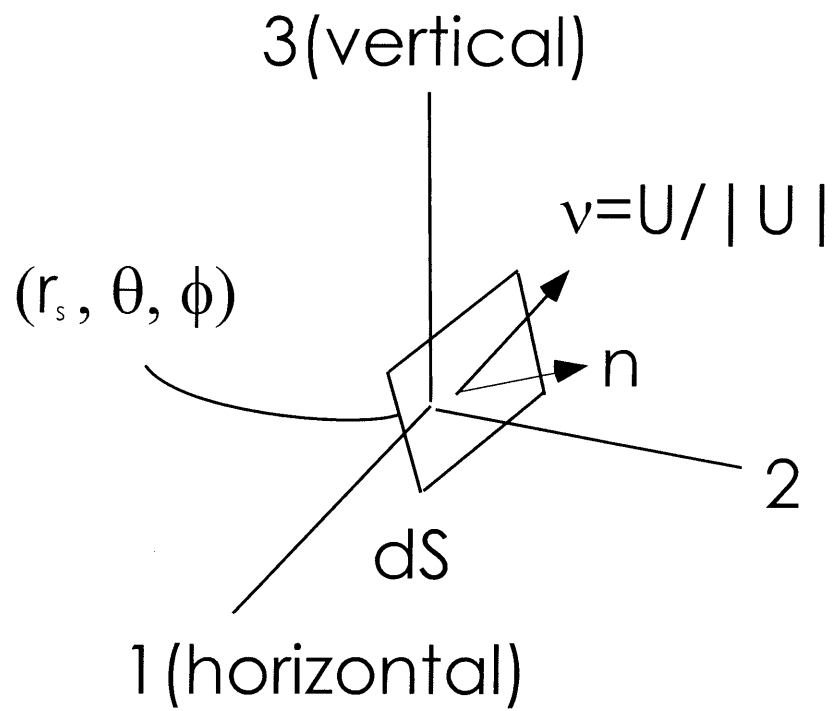


Figure 11. Diagram of the source

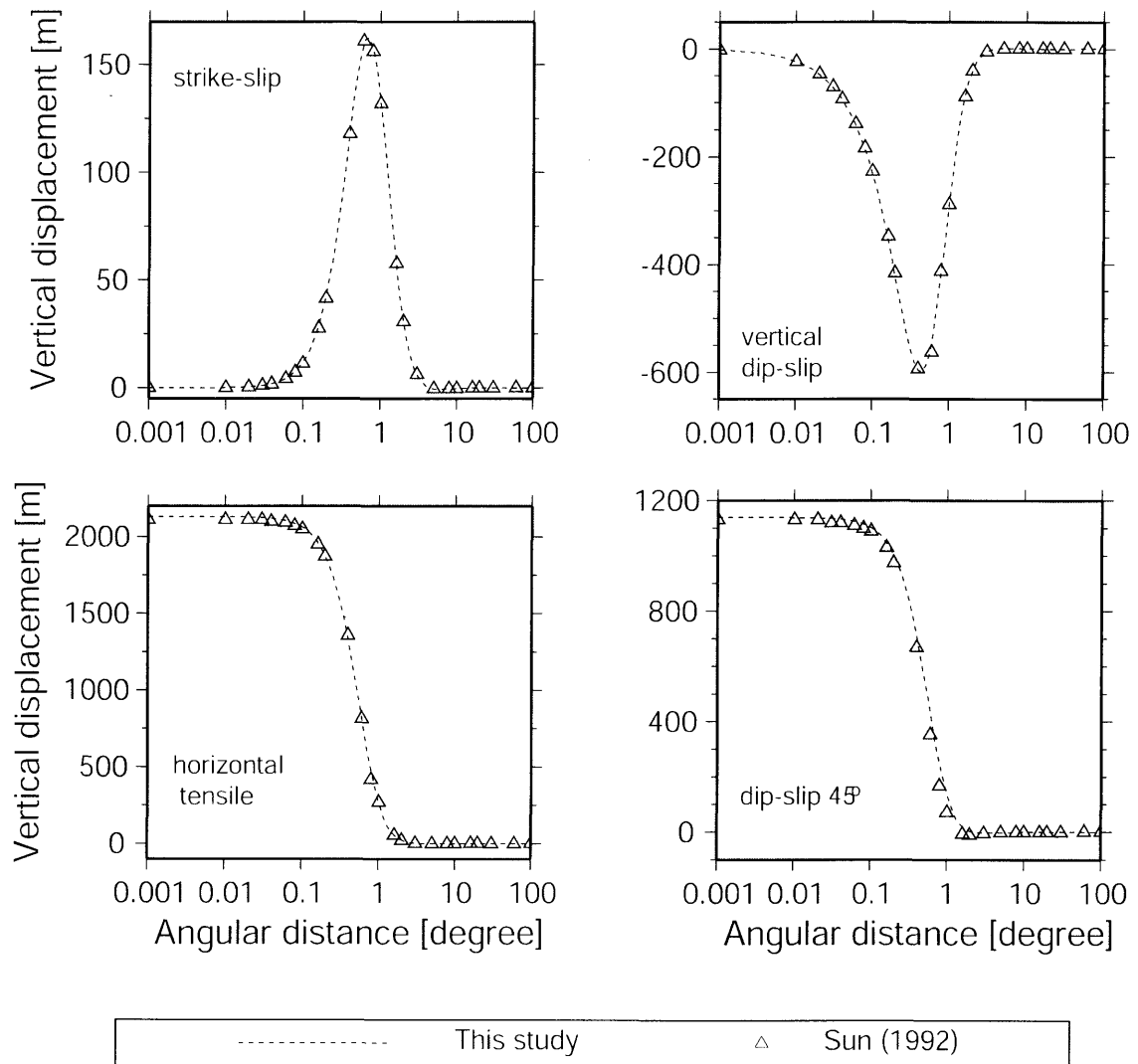


Figure 12. Coincidence of elastic deformations obtained with two different methods

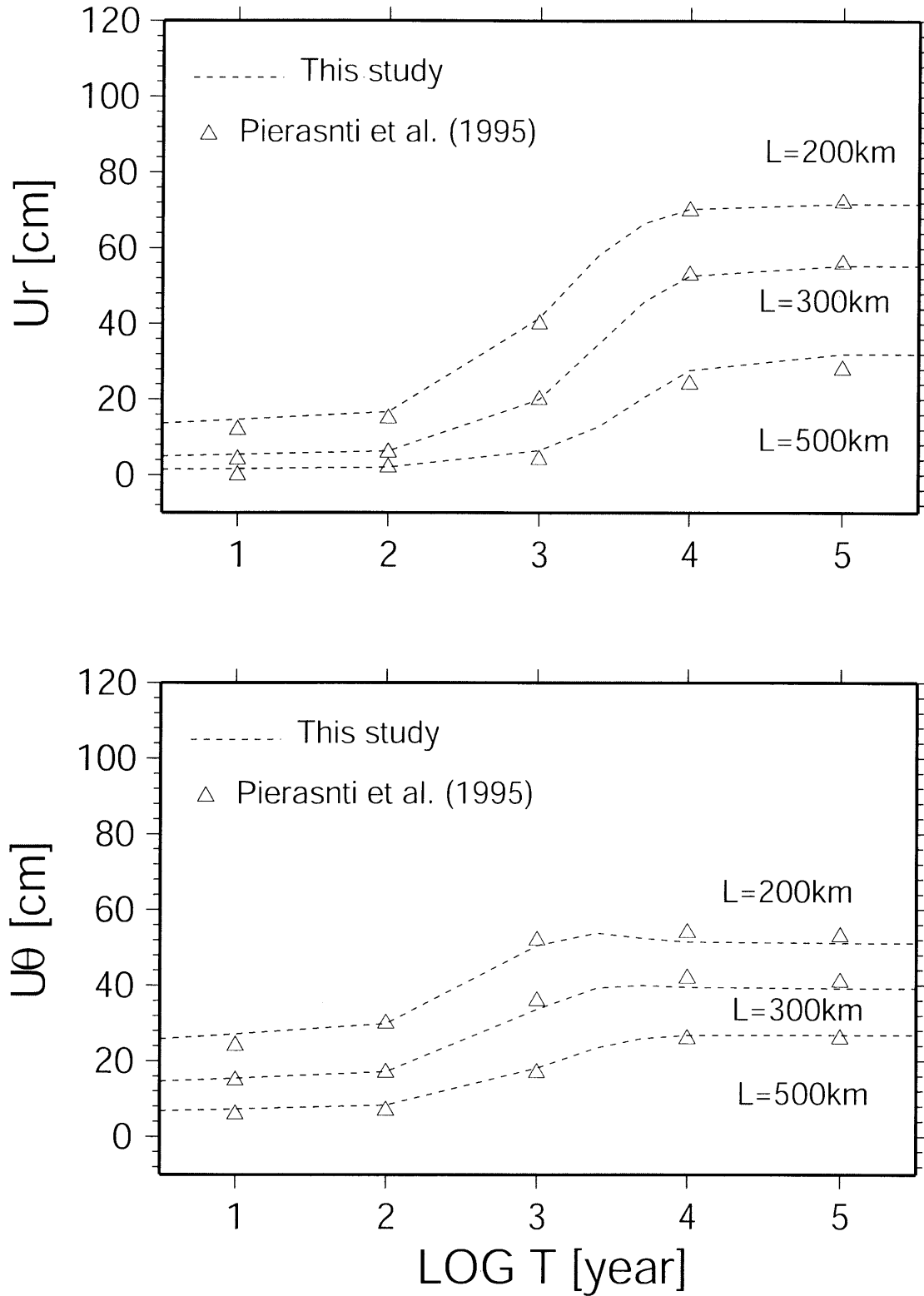


Figure 13. Comparison for the incompressible Earth model. The mechanism is strike-slip. L denotes the epicentral distance. The triangles are values read from Figures 8 and 9 in (Piersanti et al. 1995) and the dotted line shows those calculated with the new algorithm for the same Earth model P2 (Fig. 14).

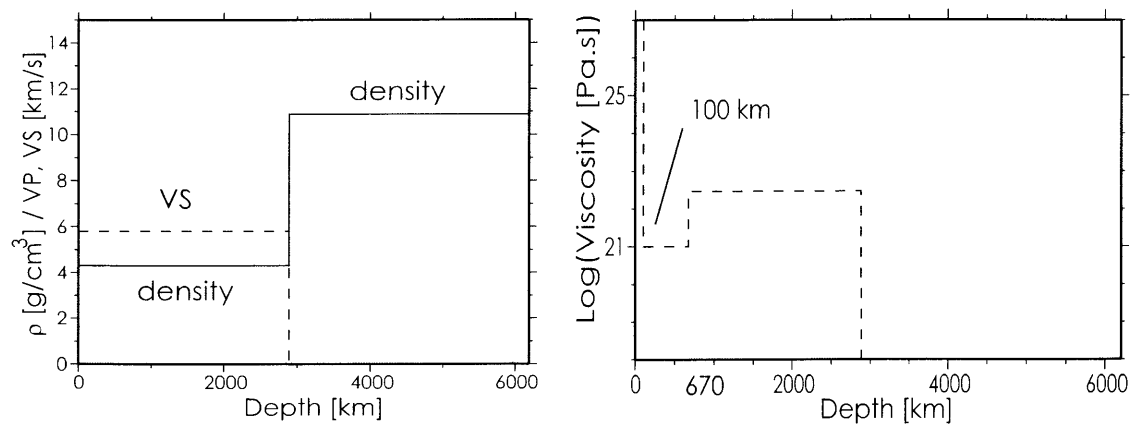


Figure 14. The incompressible earth model P2 (Piersanti et al. 1995). VS in the left-hand diagram denotes the S-wave velocity. VP is infinity in incompressible models and so is not shown.

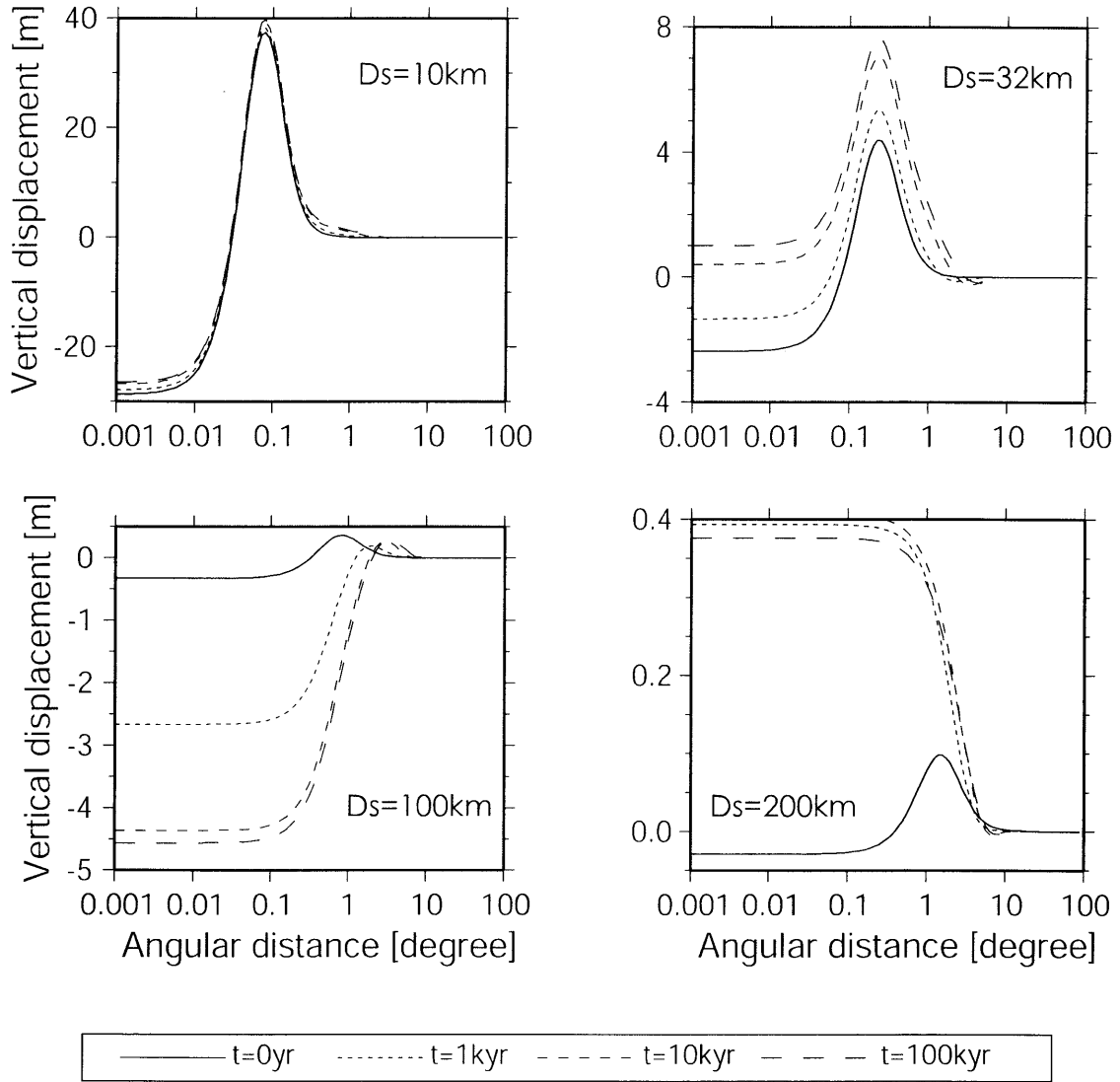


Figure 15. (a) Vertical displacement $G_{ii}^l(\theta, t)$ (isotropic component of vertical tensile. See Table 5.). Normalized by $UdS = 10 \text{ m} \times (100 \text{ km})^2$. t denotes the time after an event. Events at $t = 0 \text{ yr}$ indicate coseismic jumps. The Ds denotes the source depth.

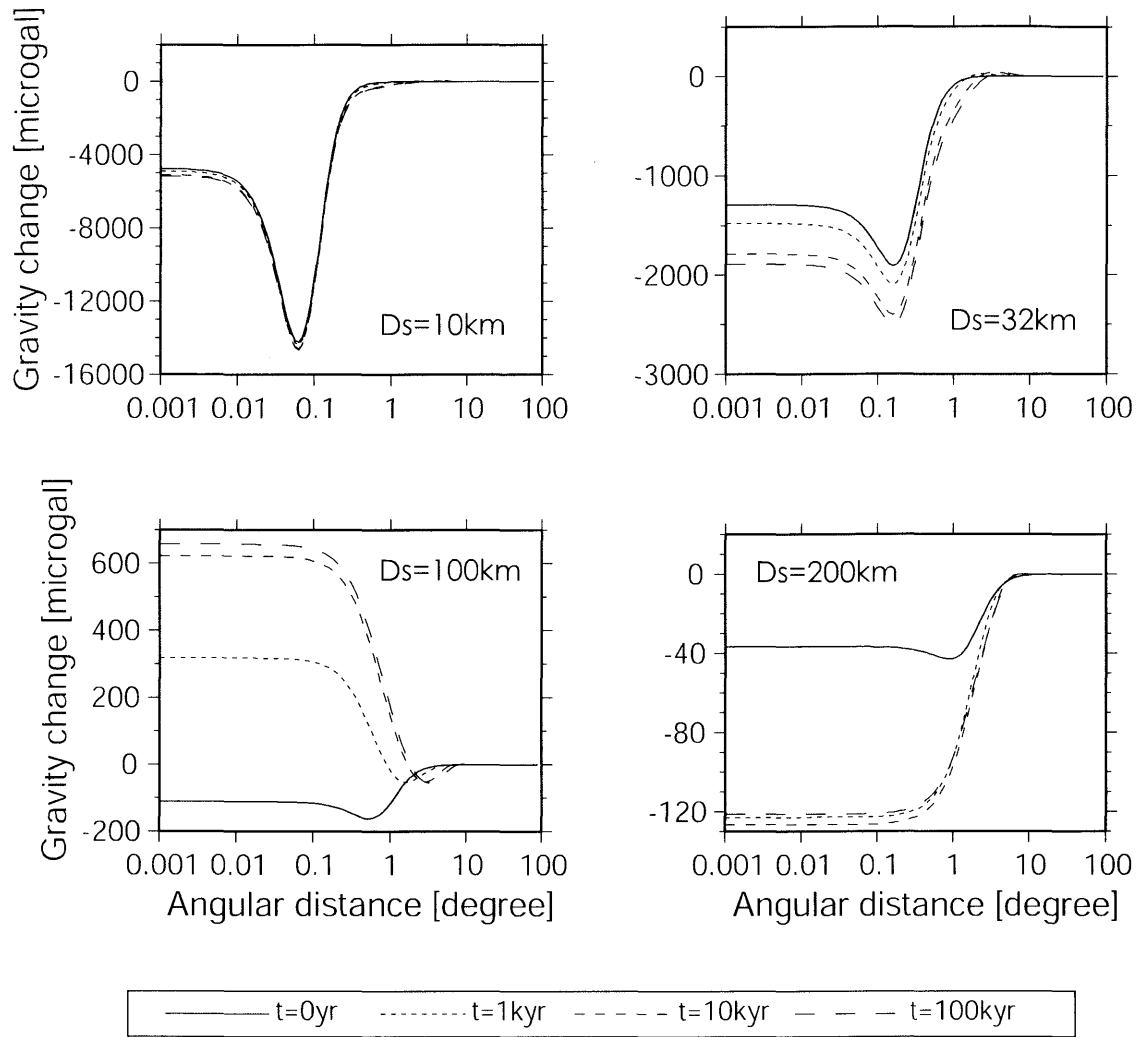


Figure 15. (b) Gravity change (isotropic component of vertical tensile)

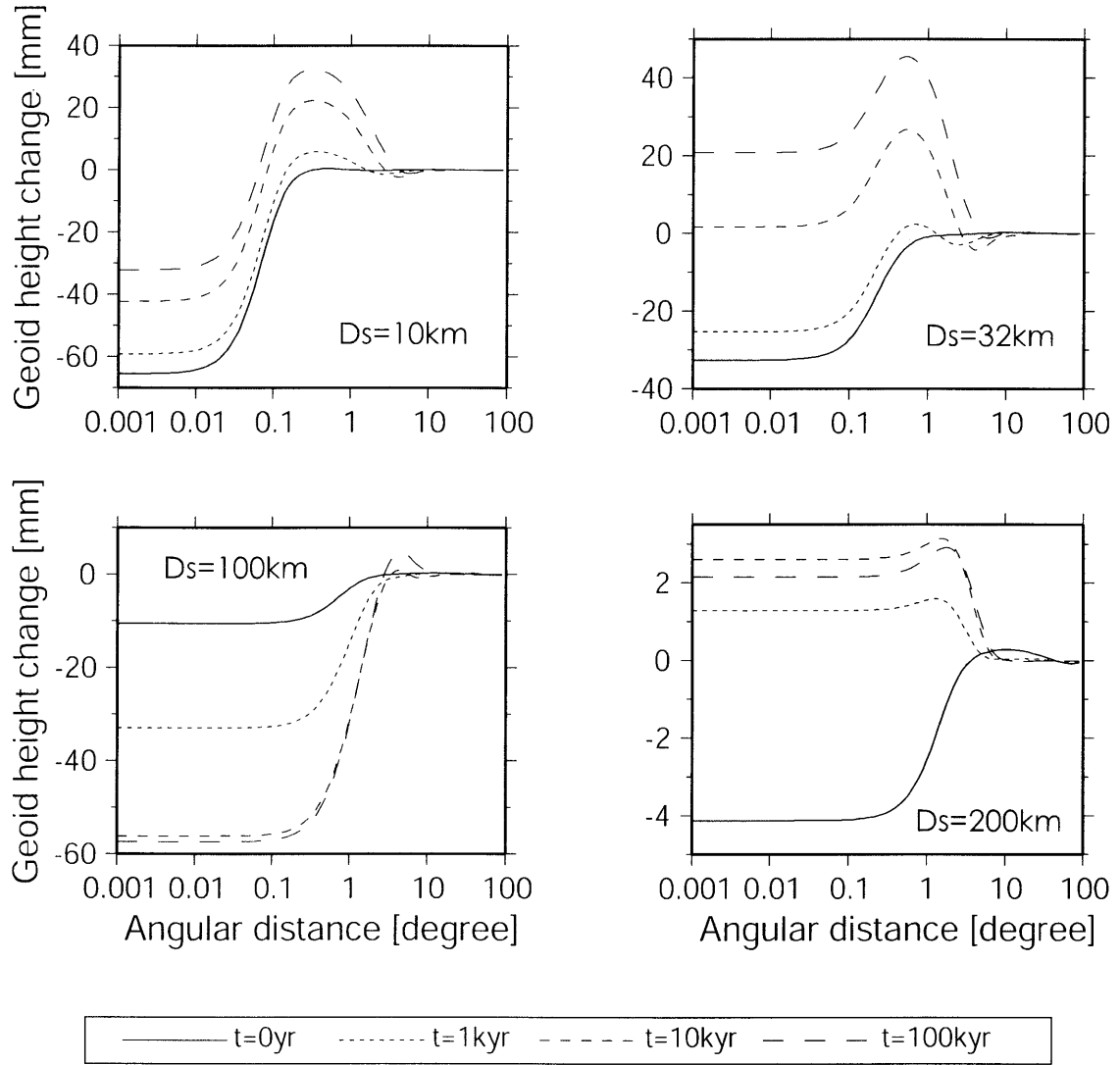


Figure 15. (c) Geoid height change $G_{\psi}^l(\theta, t)/g_0$ (isotropic component of vertical tensile)

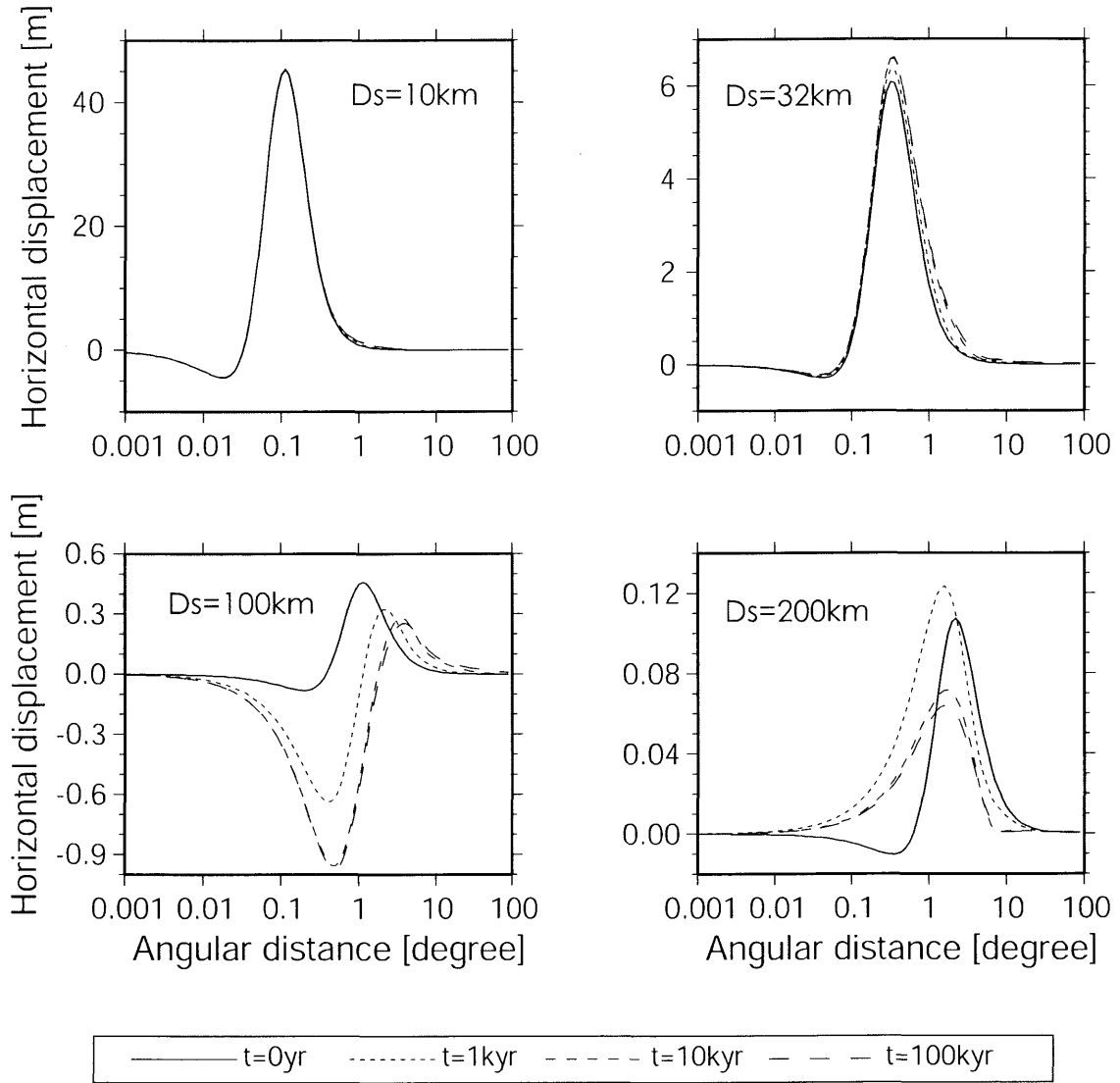


Figure 15. (d) Horizontal displacement $G_\theta^I(\theta, t)$ (isotropic component of vertical tensile)

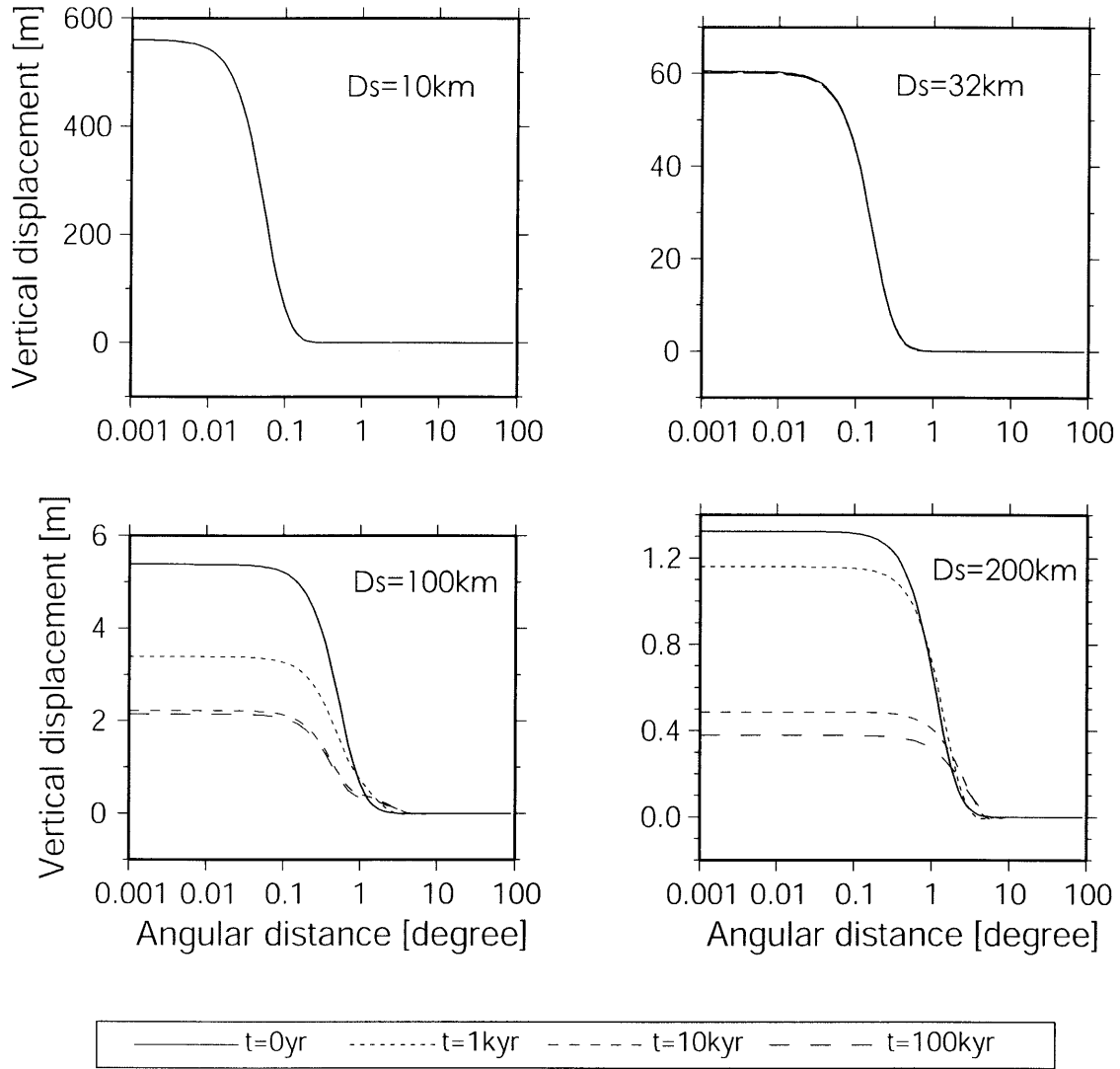


Figure 16. (a) Vertical displacement $G_u^2(\theta, t)$ (Horizontal tensile component. See Table 5.). Normalized by $UdS = 10 \text{ m} \times (100 \text{ km})^2$. t denotes the time after an event. Events at $t = 0 \text{ yr}$ indicate coseismic jumps. The D_s denotes the source depth.

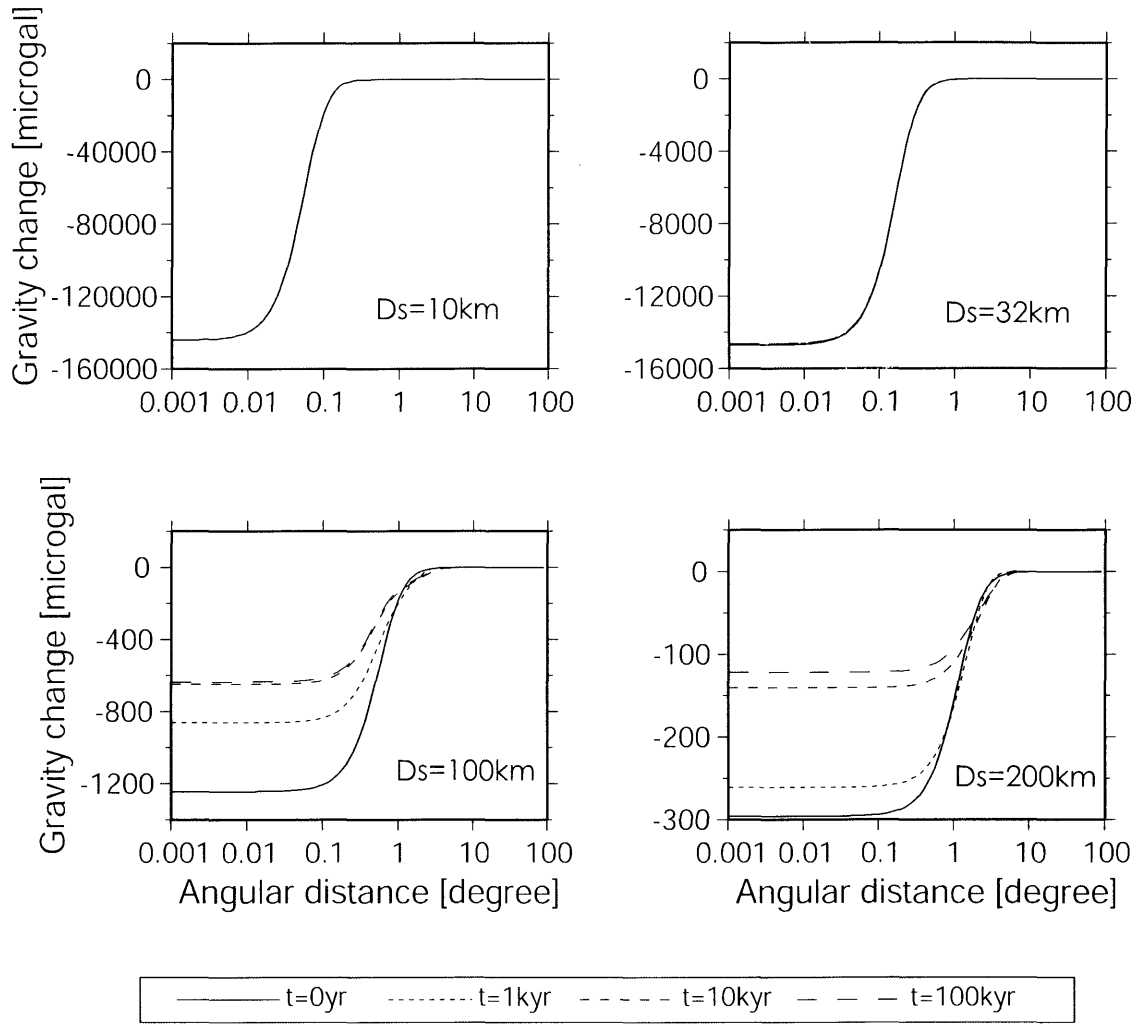


Figure 16. (b) Gravity change (horizontal tensile component)

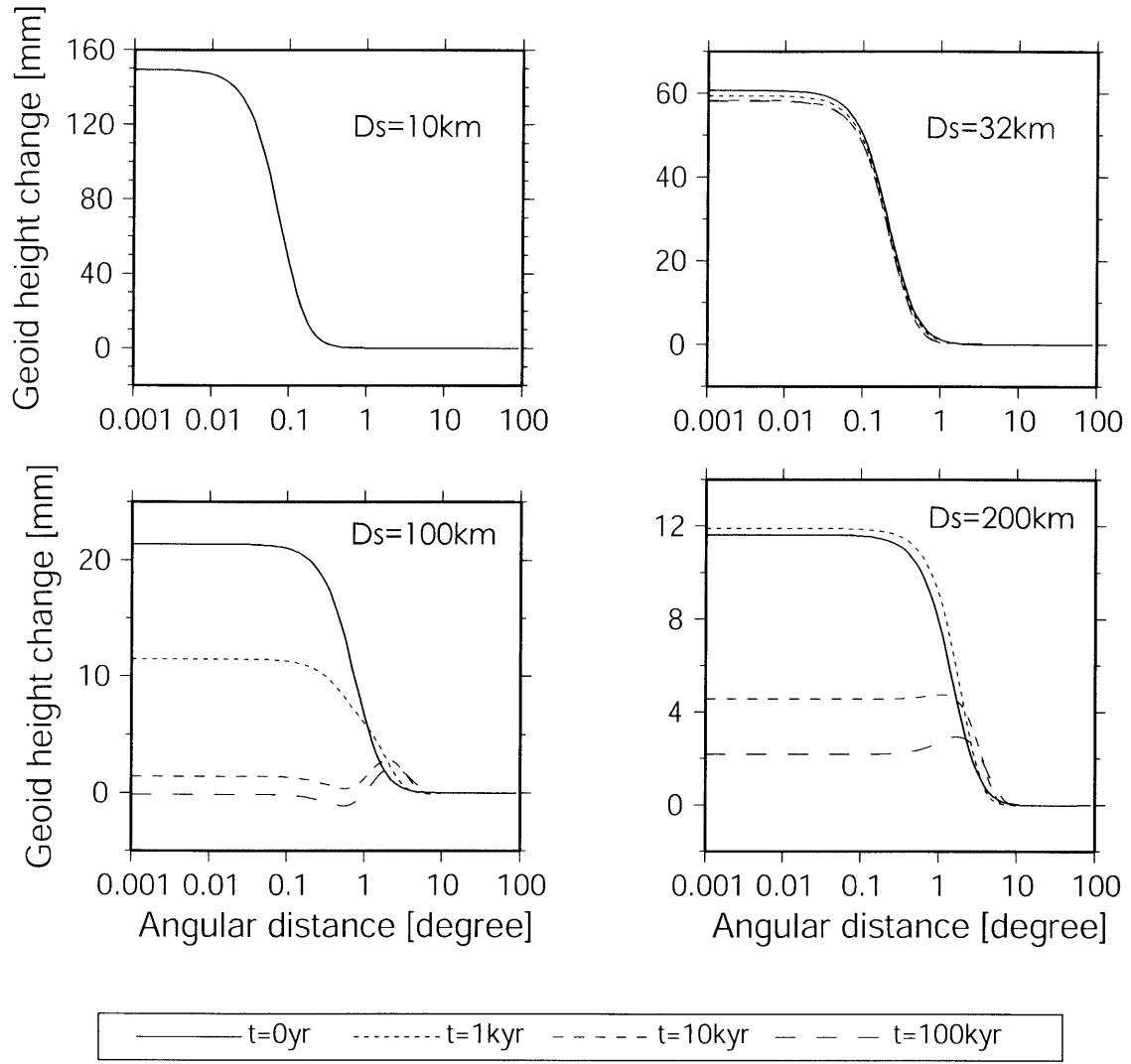


Figure 16. (c) Geoid height change $G_{\psi}^2(\theta, t)/g_0$ (horizontal tensile component)

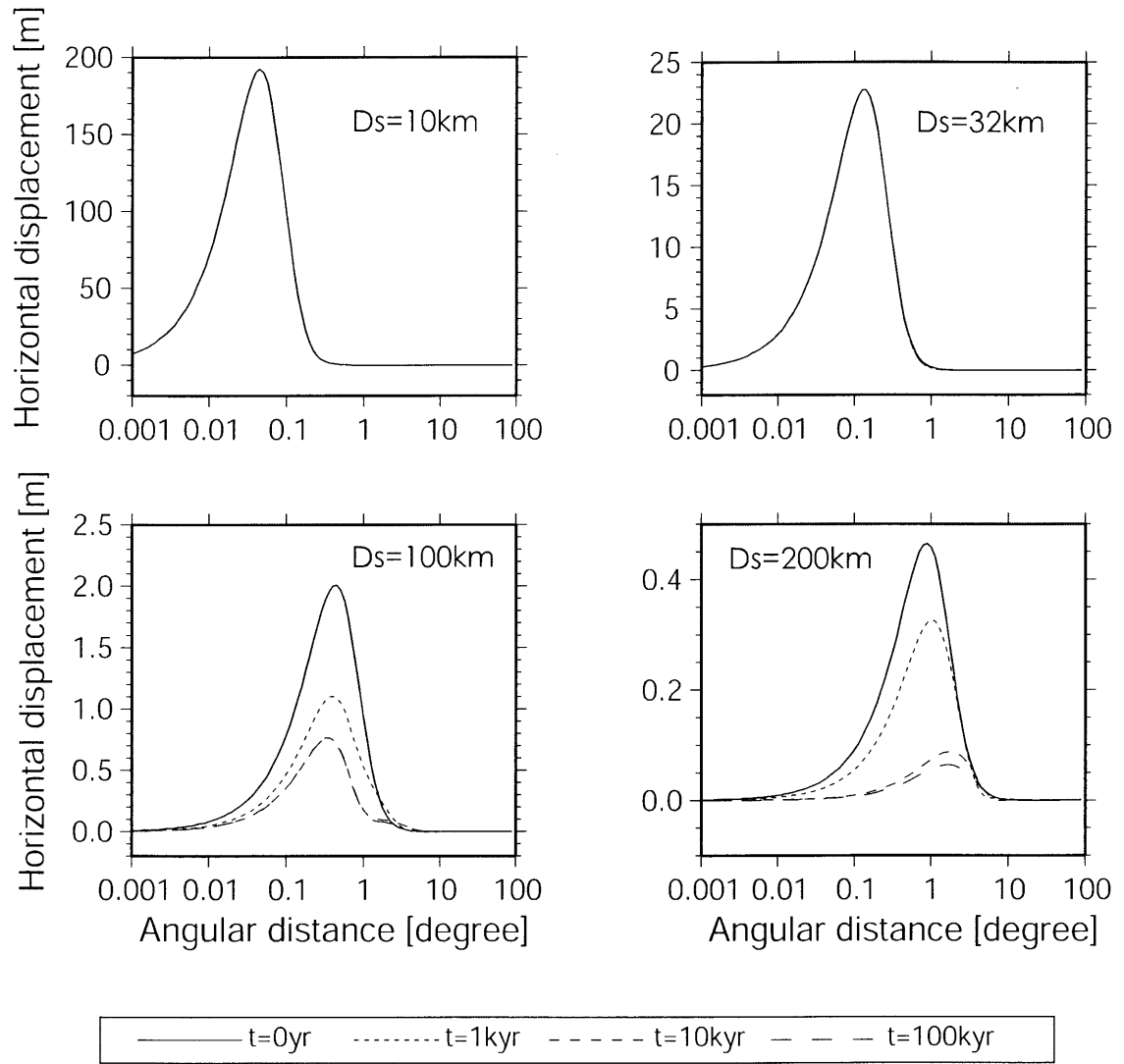


Figure 16. (d) Horizontal displacement $G_{\theta}^2(\theta, t)$ (horizontal tensile component)

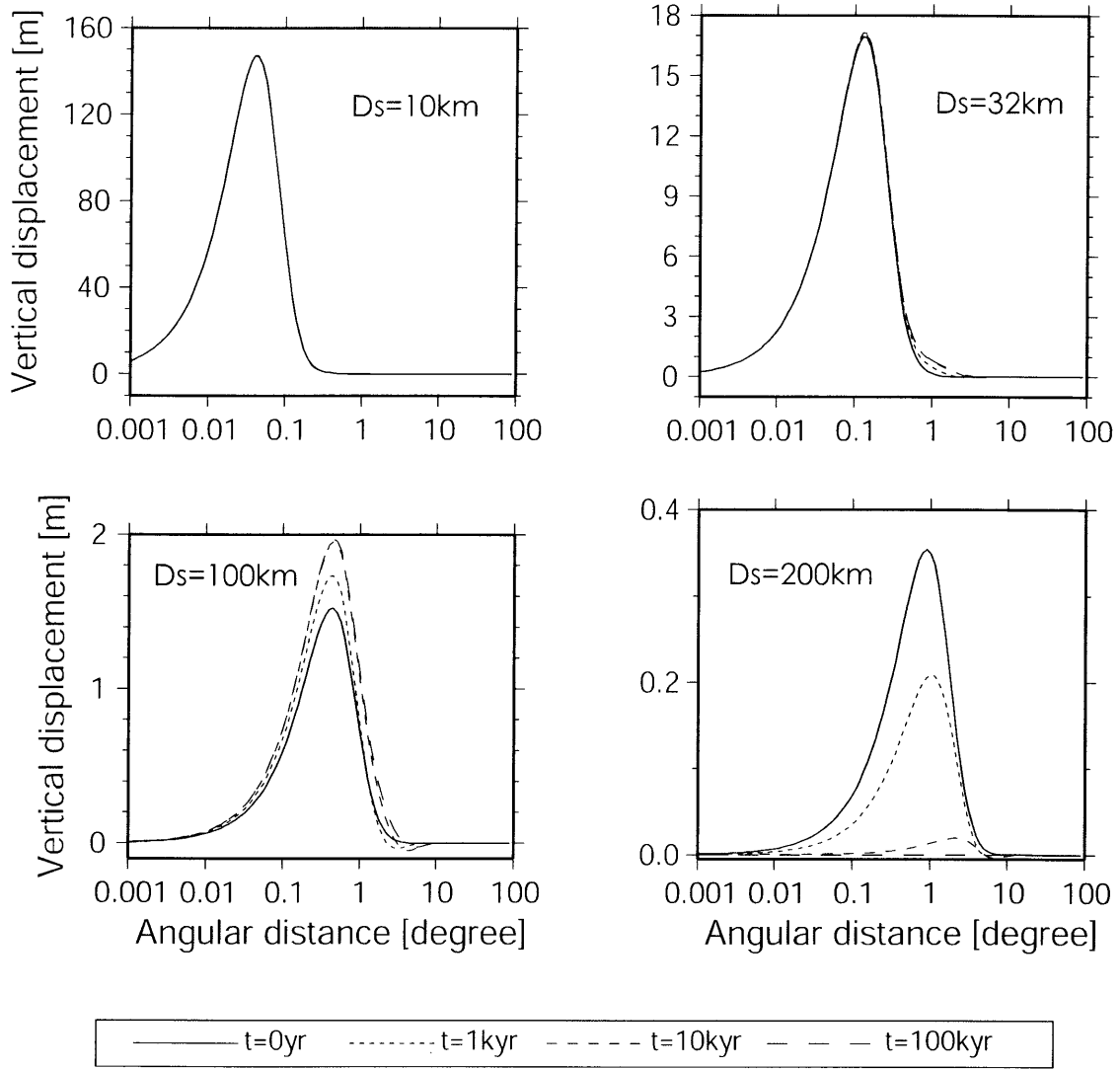


Figure 17. (a) Vertical displacement $G_u^3(\theta, t)$ (Vertical dip-slip component. See Table 5.). Normalized by $UdS = 10 \text{ m} \times (100 \text{ km})^2$. t denotes the time after an event. Events at $t = 0 \text{ yr}$ indicate coseismic jumps. The D_s denotes the source depth.

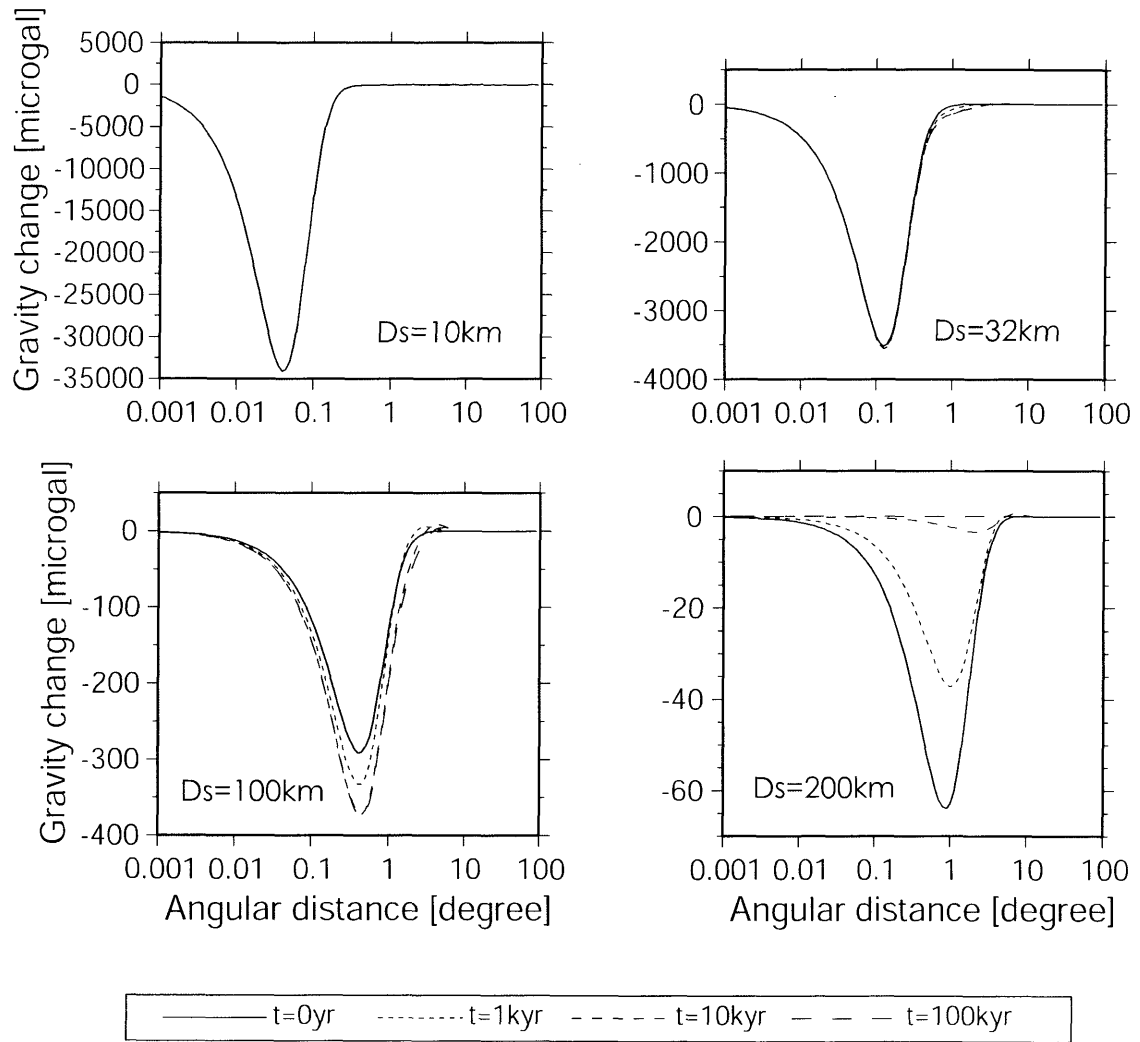


Figure 17. (b) Gravity change (vertical dip-slip component)

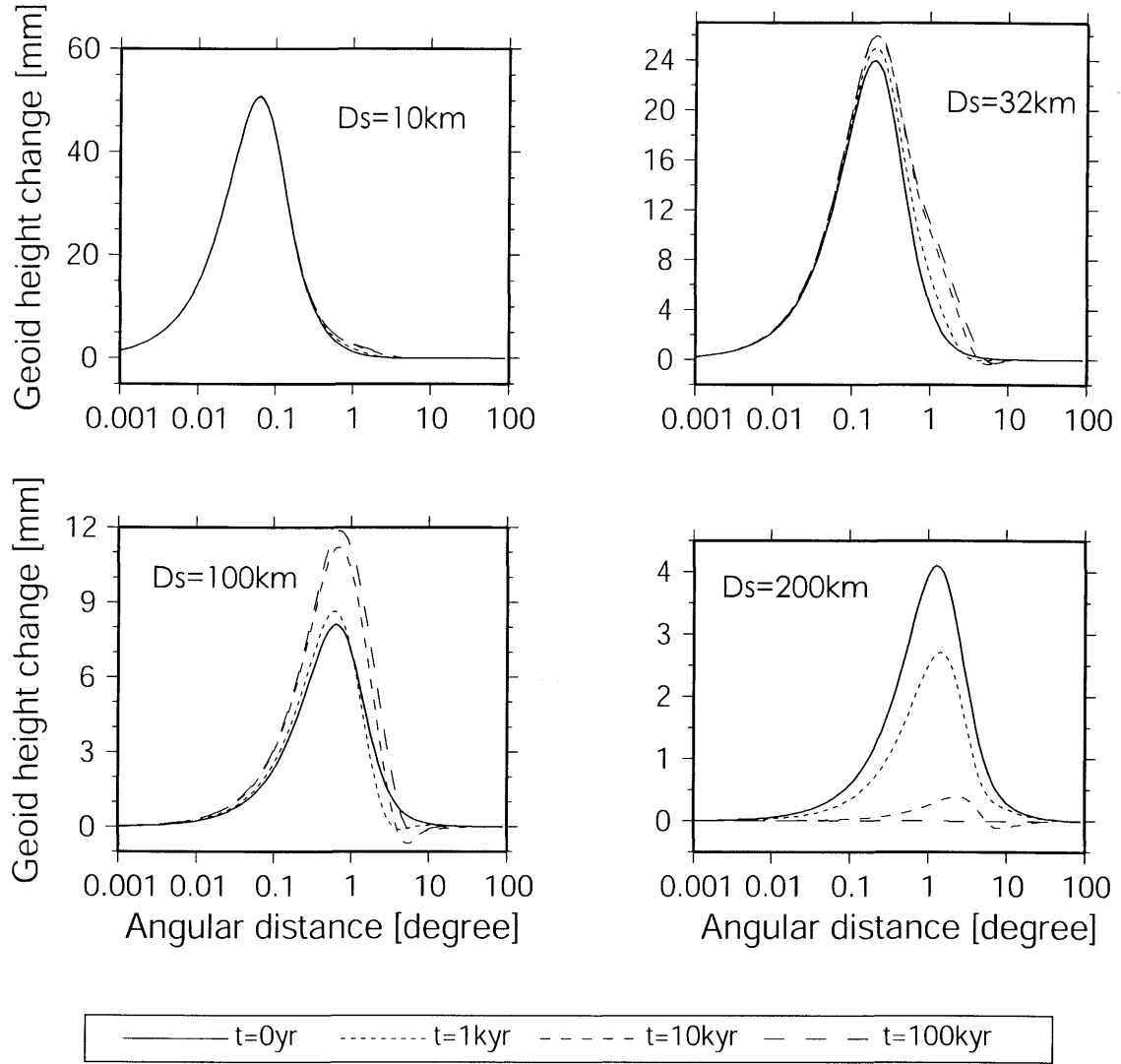


Figure 17. (c) Geoid height change $G_\psi^3(\theta, t)/g_0$ (vertical dip-slip component)

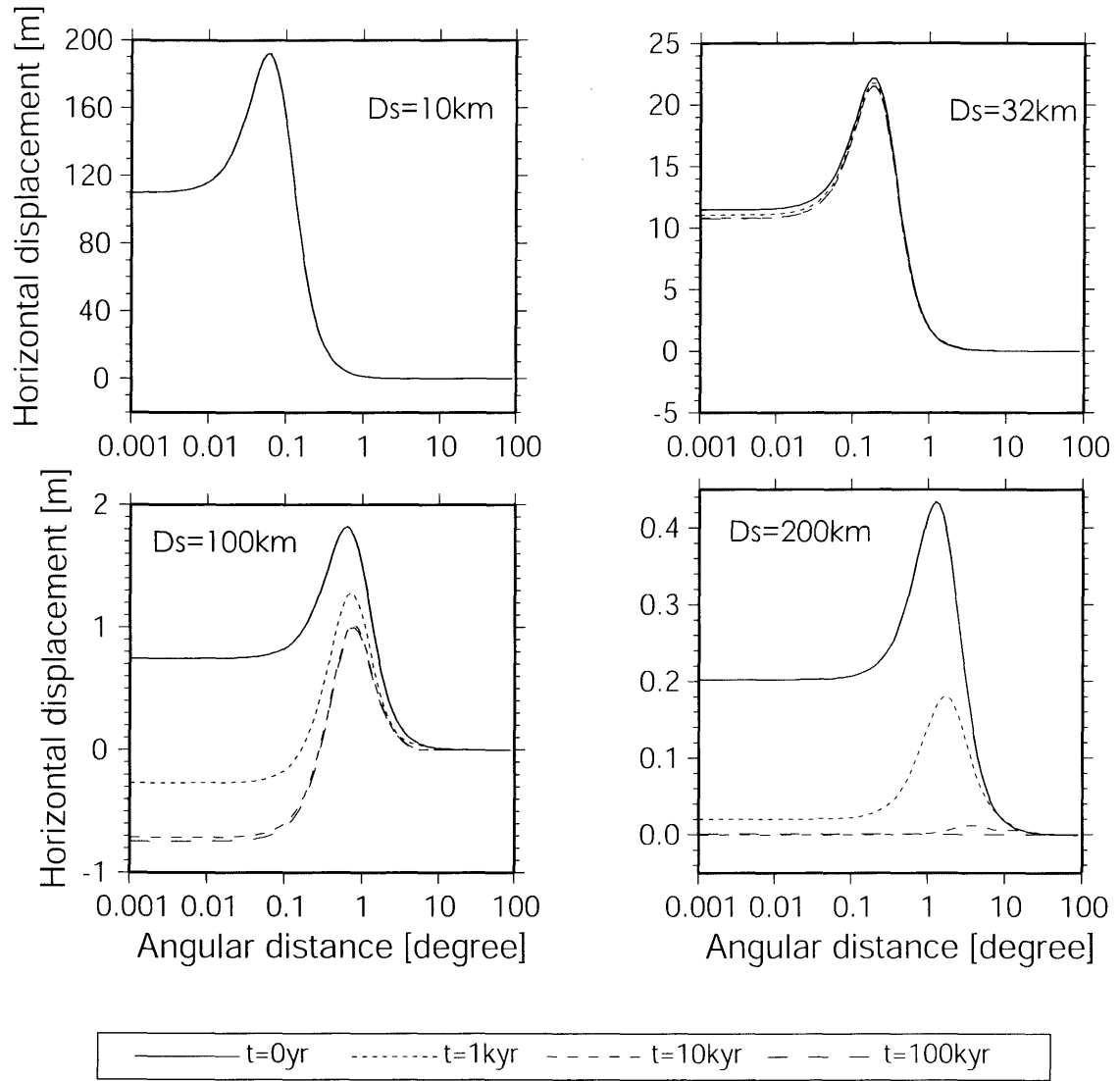


Figure 17. (d) Horizontal displacement $G_\theta^3(\theta, t) + G_\theta^{l1}(\theta, t)$ (vertical dip-slip component)

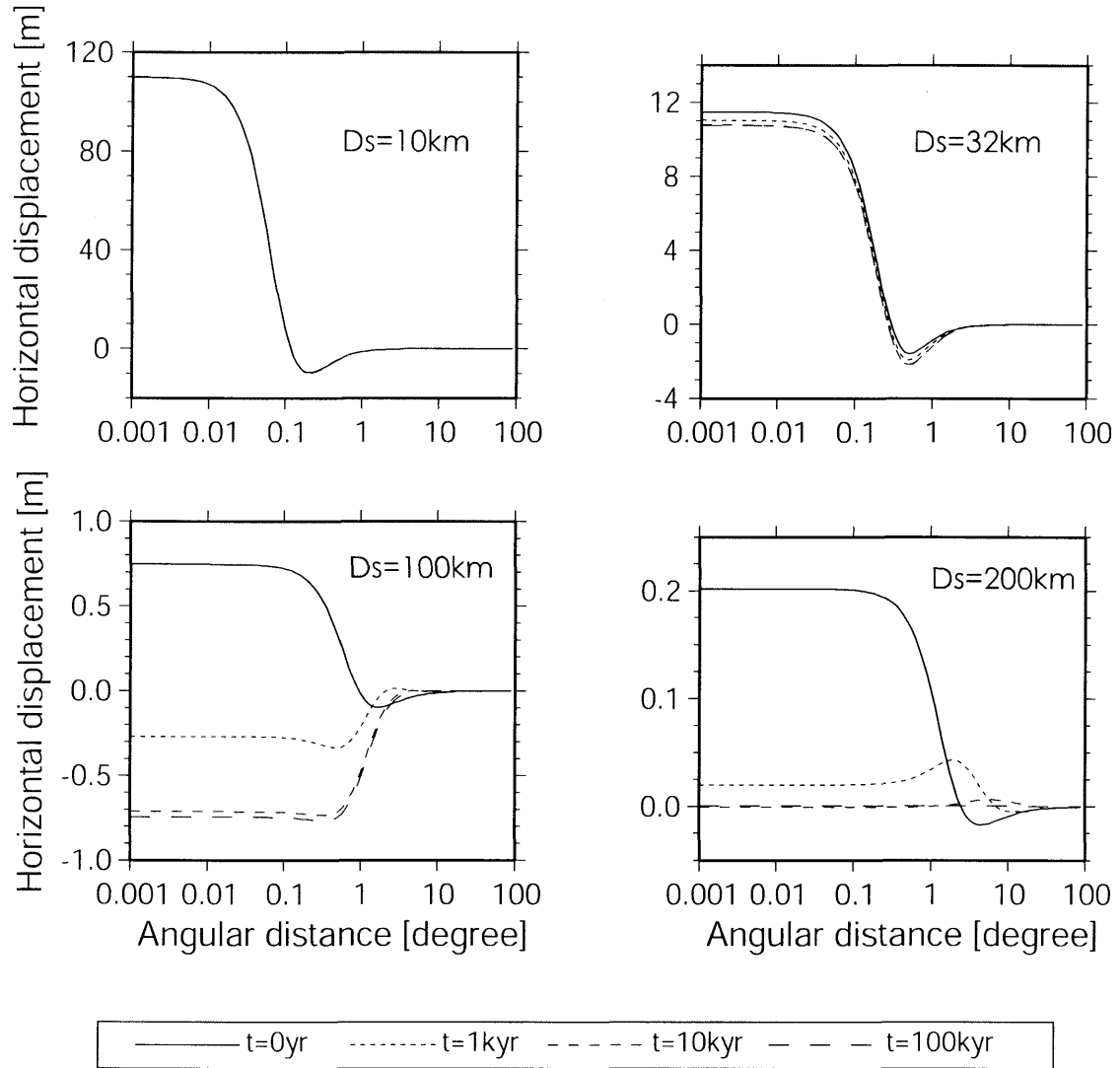


Figure 17. (e) Horizontal displacement $-(G_{\phi}^1(\theta, t) + G_{\phi}^{t1}(\theta, t))$ (vertical dip-slip component)

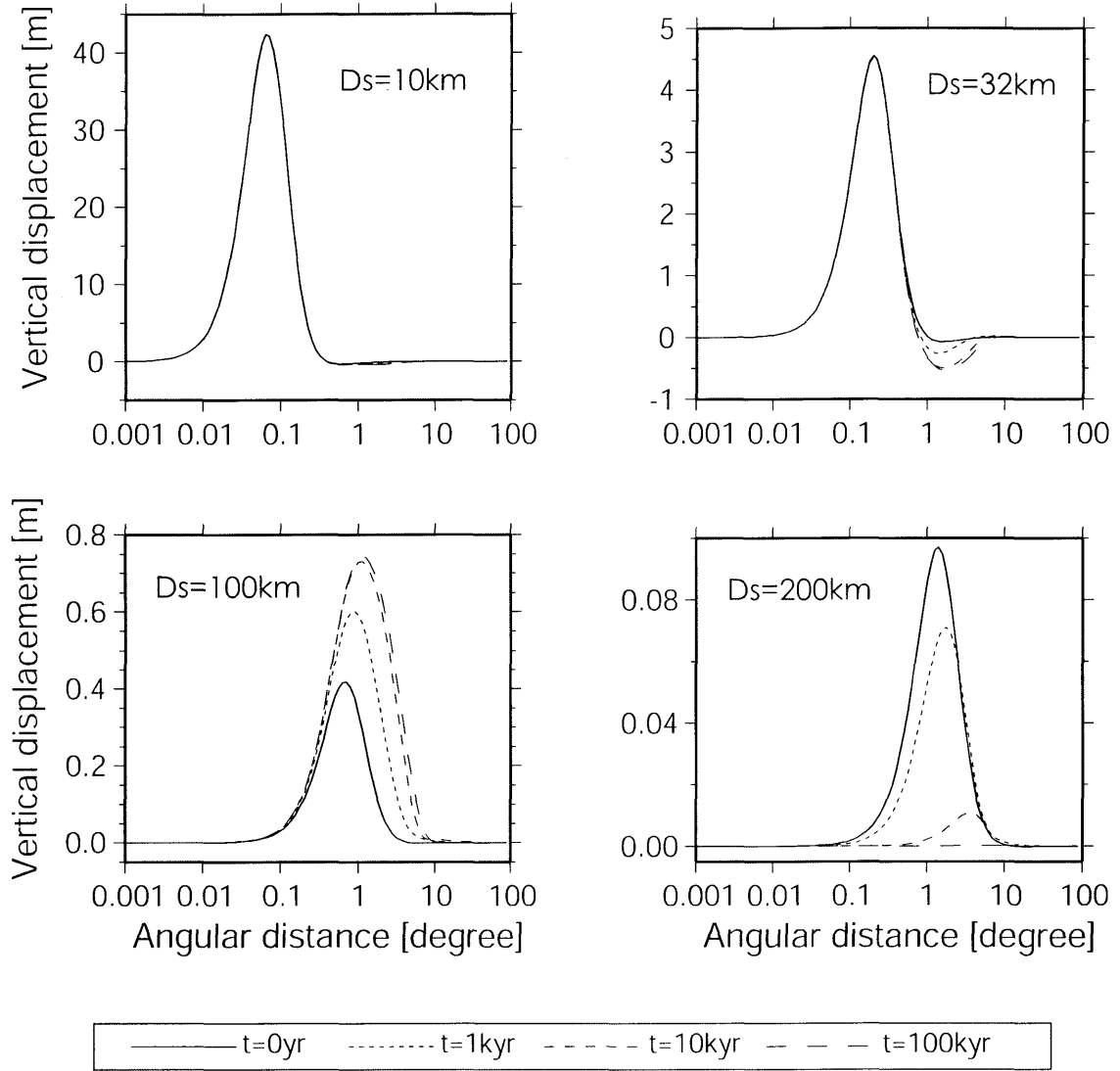


Figure 18. (a) Vertical displacement $G_{ut}^d(\theta, t)$ (vertical strike-slip component. See Table 5.). Normalized by $UdS = 10 \text{ m} \times (100 \text{ km})^2$. t denotes the time after an event. Events at $t = 0 \text{ yr}$ indicate coseismic jumps. The D_s denotes the source depth.

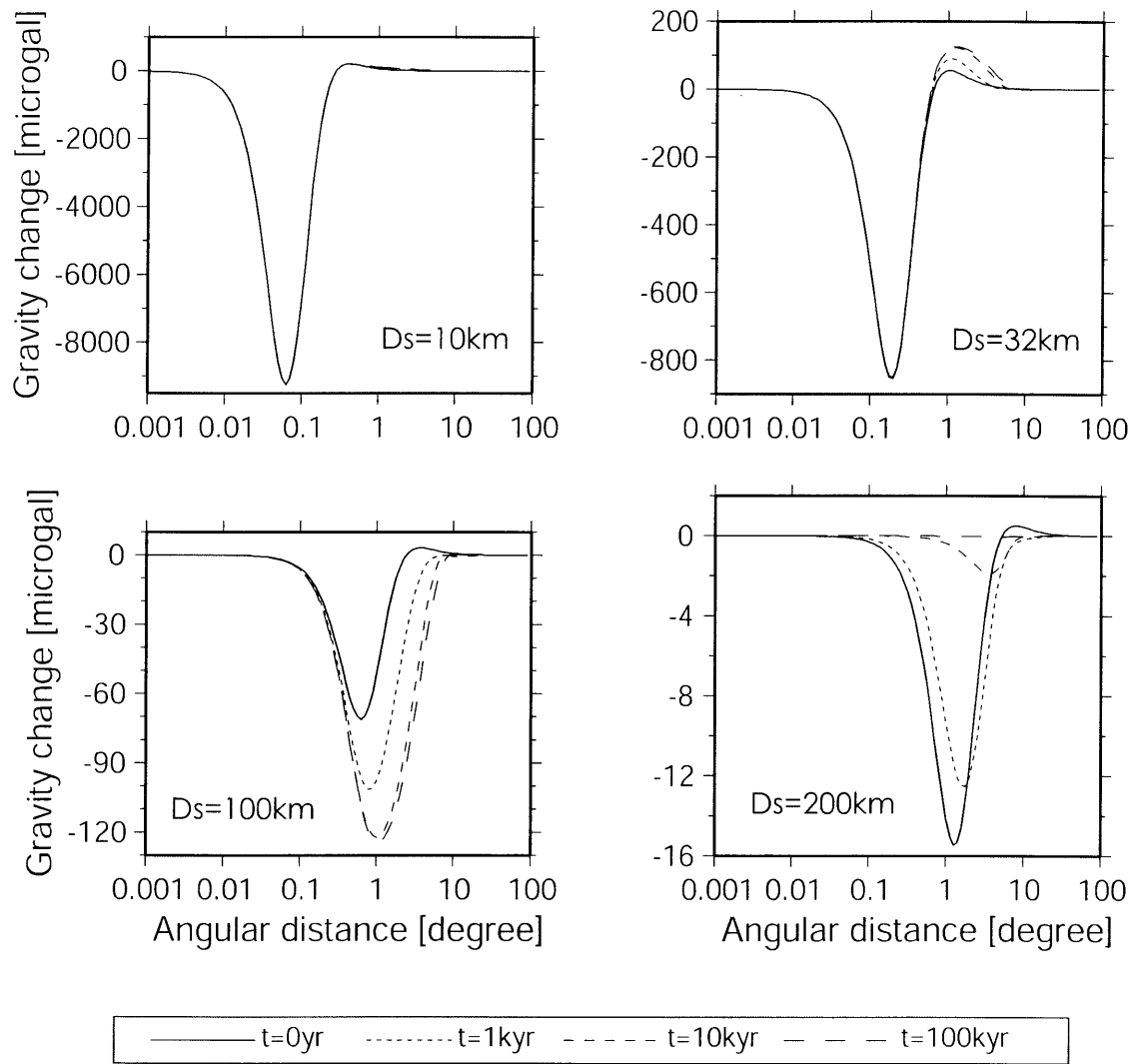


Figure 18. (b) Gravity change (vertical strike-slip component)

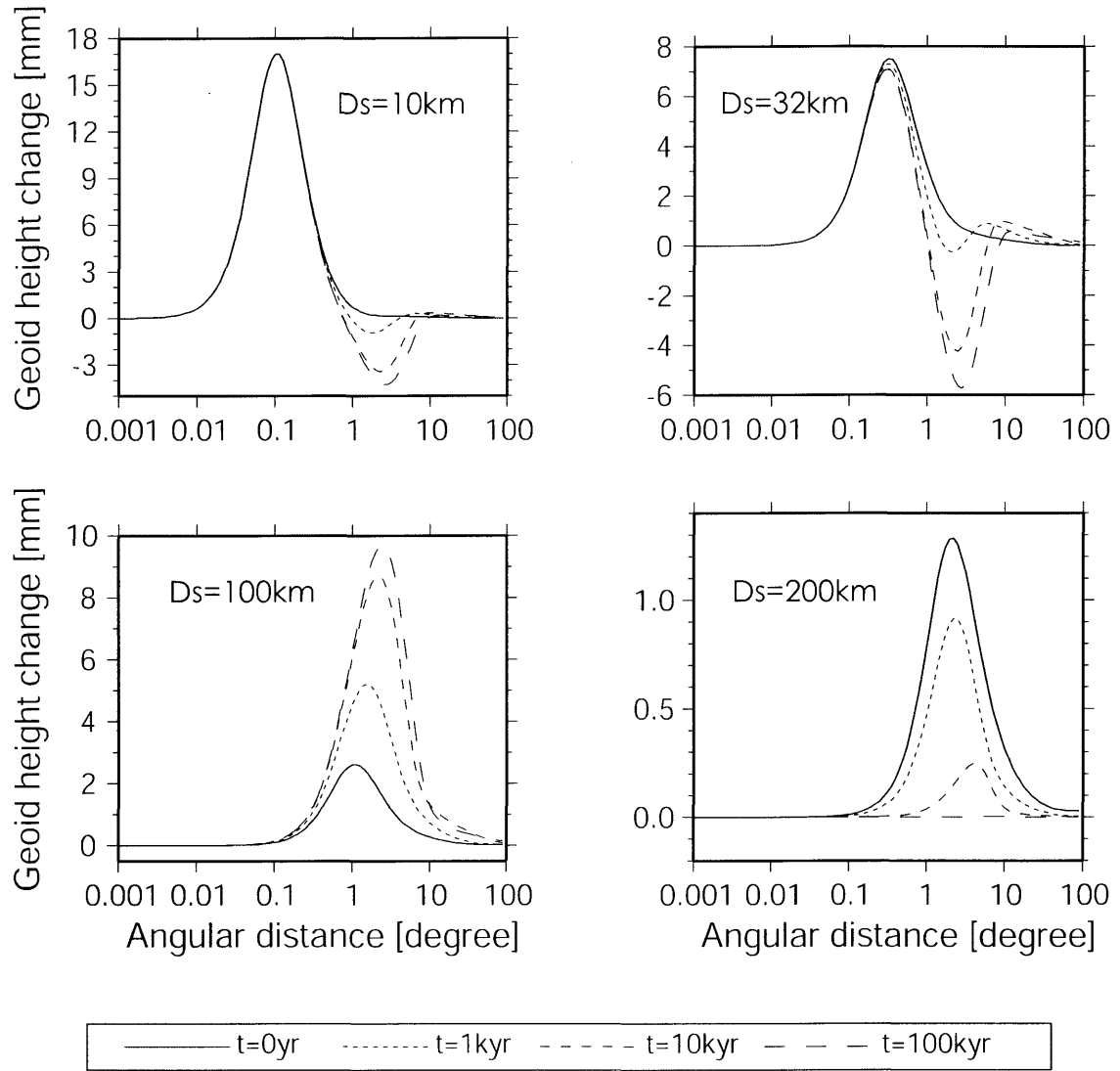


Figure 18. (c) Geoid height change $G_{\psi}^d(\theta, t)/g_0$ (vertical strike-slip component)

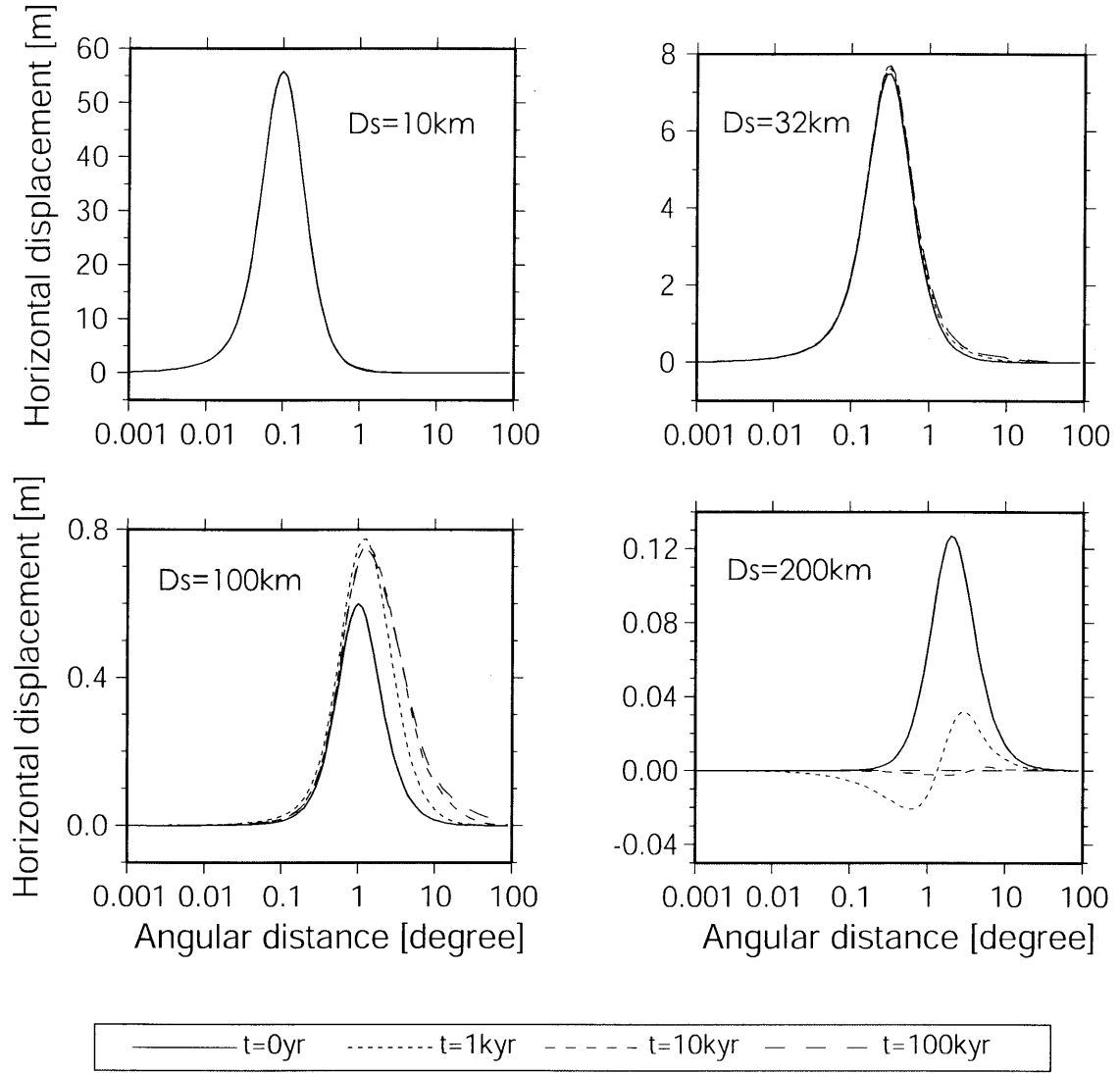


Figure 18. (d) Horizontal displacement $G_{\theta}^4(\theta, t) + G_{\theta}^{t2}(\theta, t)$ (vertical strike-slip component)

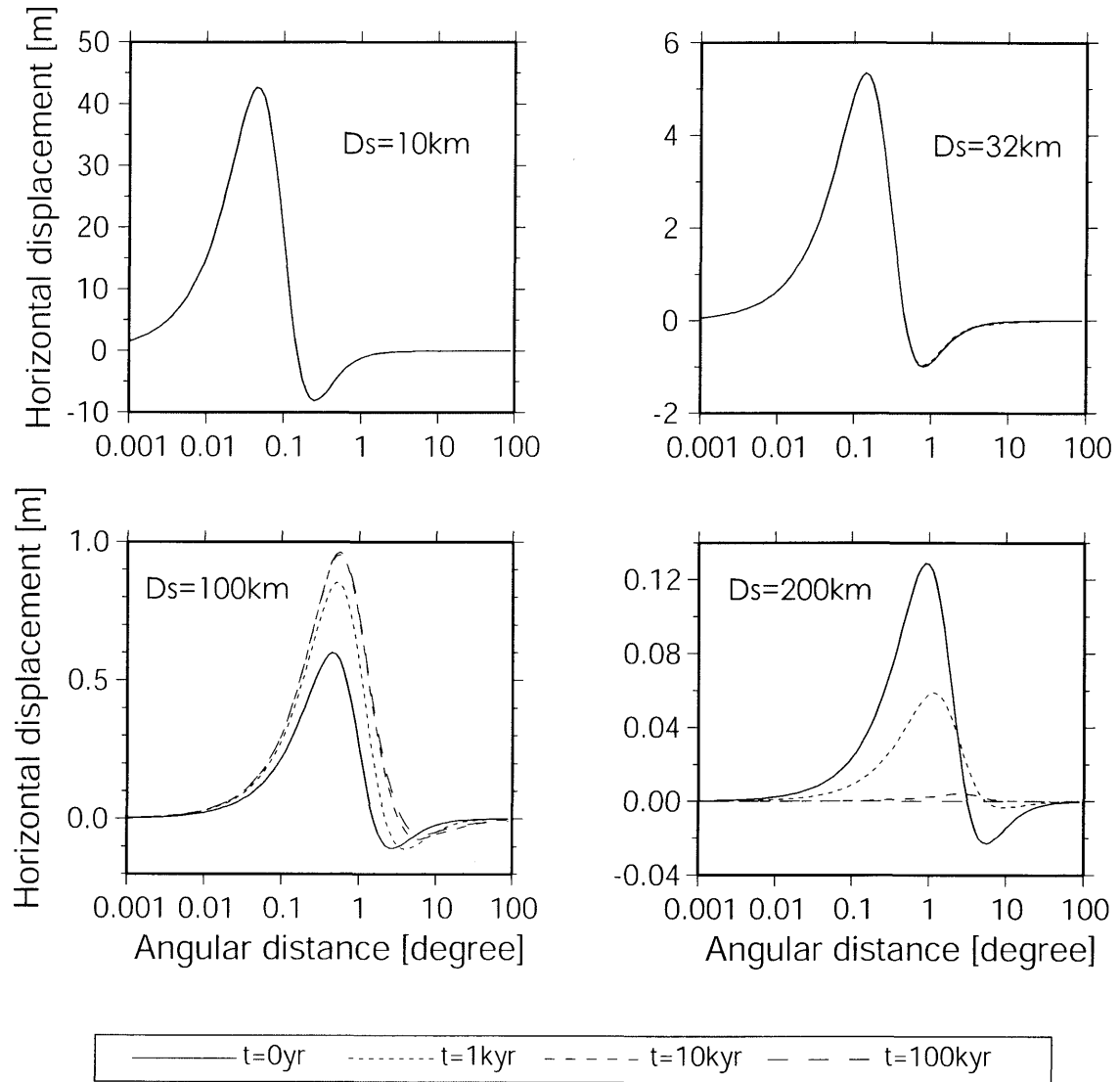


Figure 18. (e) Horizontal displacement $G_\phi^2(\theta, t) + G_\phi^{l2}(\theta, t)$ (vertical strike-slip component)

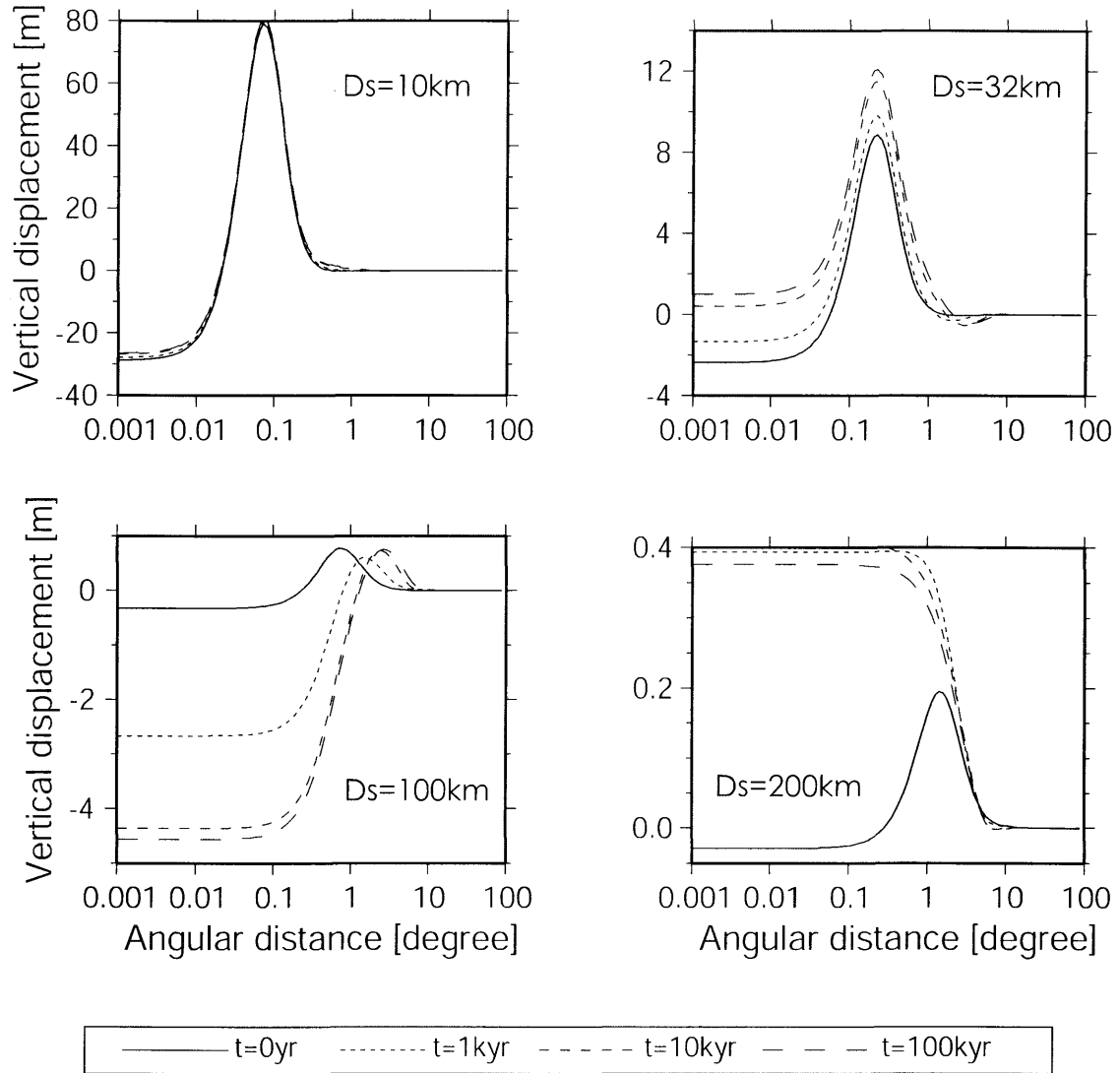


Figure 19. (a) Vertical displacement on $\phi = 0$ (vertical tensile. See Table 5.). Normalized by $UdS = 10 \text{ m} \times (100 \text{ km})^2$. t denotes the time after an event. Events at $t = 0 \text{ yr}$ indicate coseismic jumps. The Ds denotes the source depth.

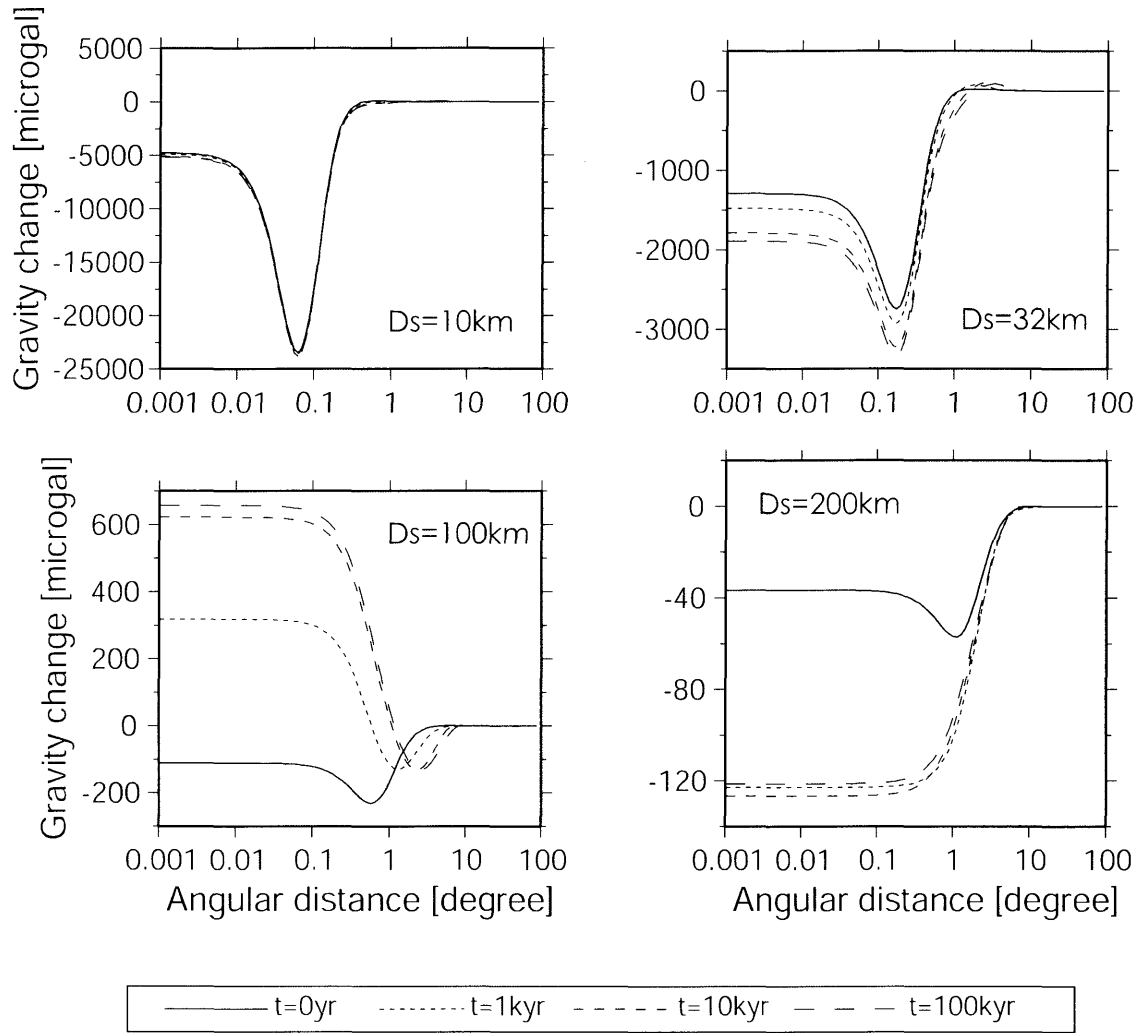


Figure 19. (b) Gravity change on $\phi = 0$ (vertical tensile)

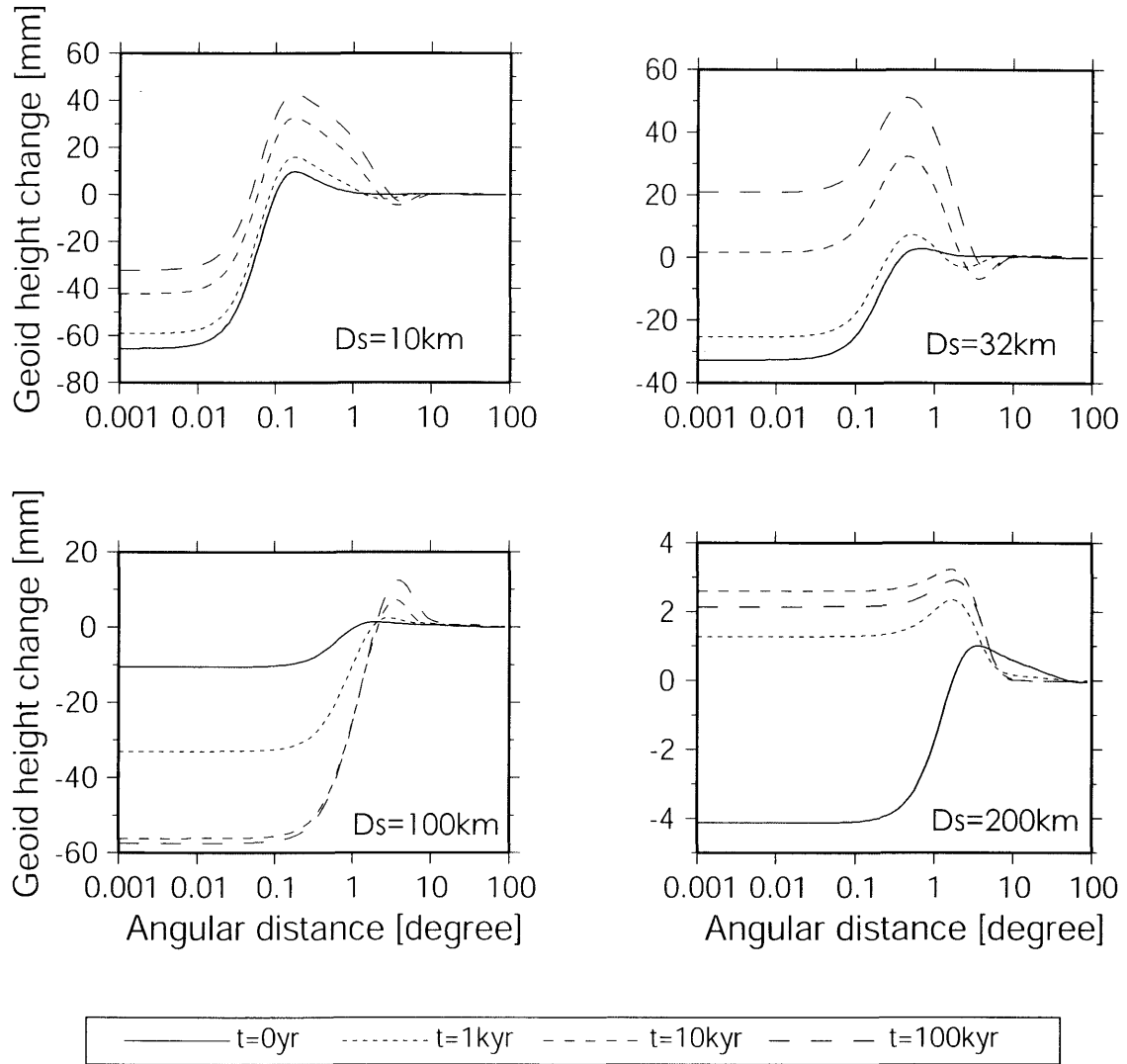


Figure 19. (c) Geoid height change on $\phi = 0$ (vertical tensile)

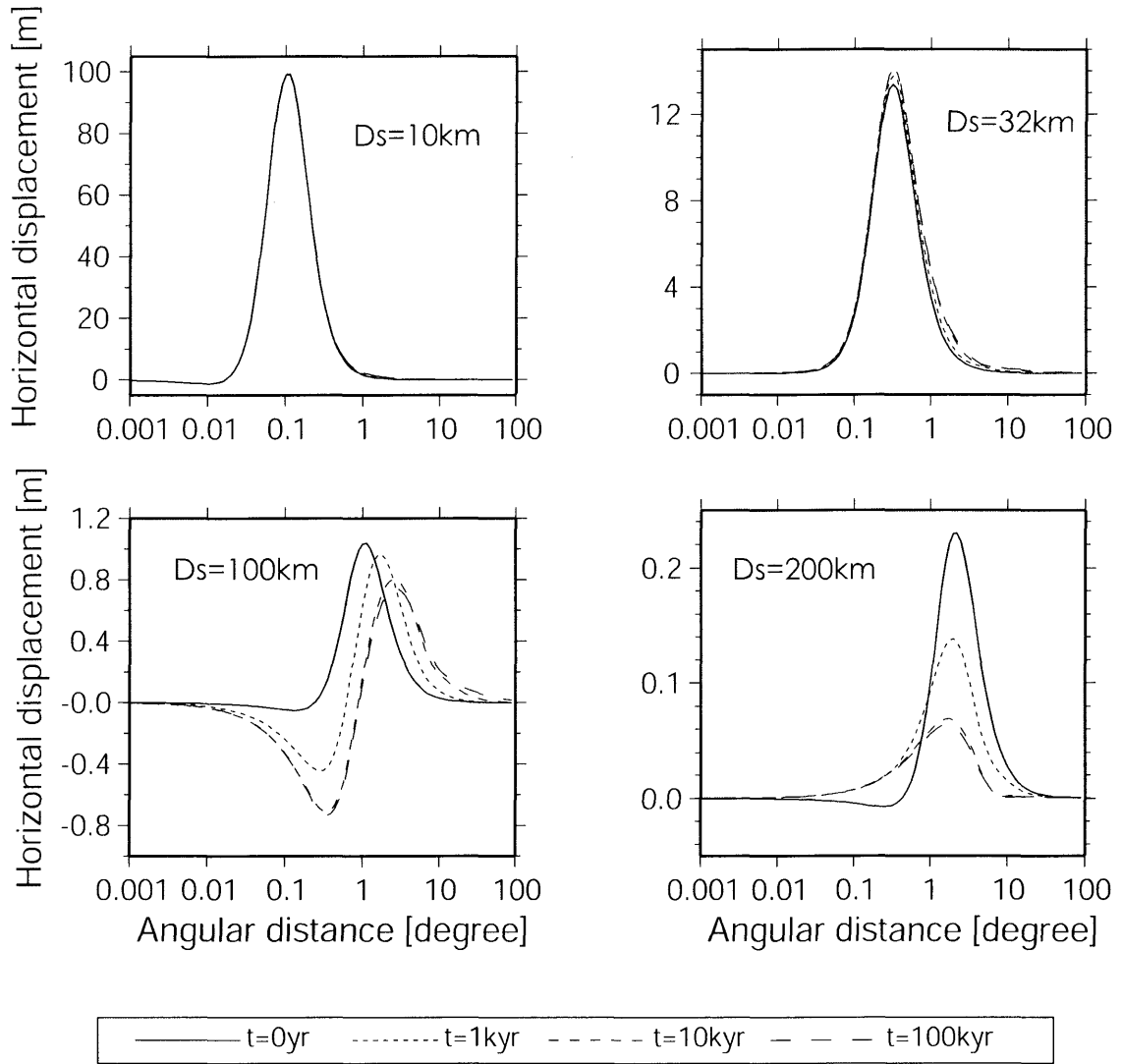


Figure 19. (d) Horizontal displacement u_θ on $\phi = 0$ (vertical tensile)

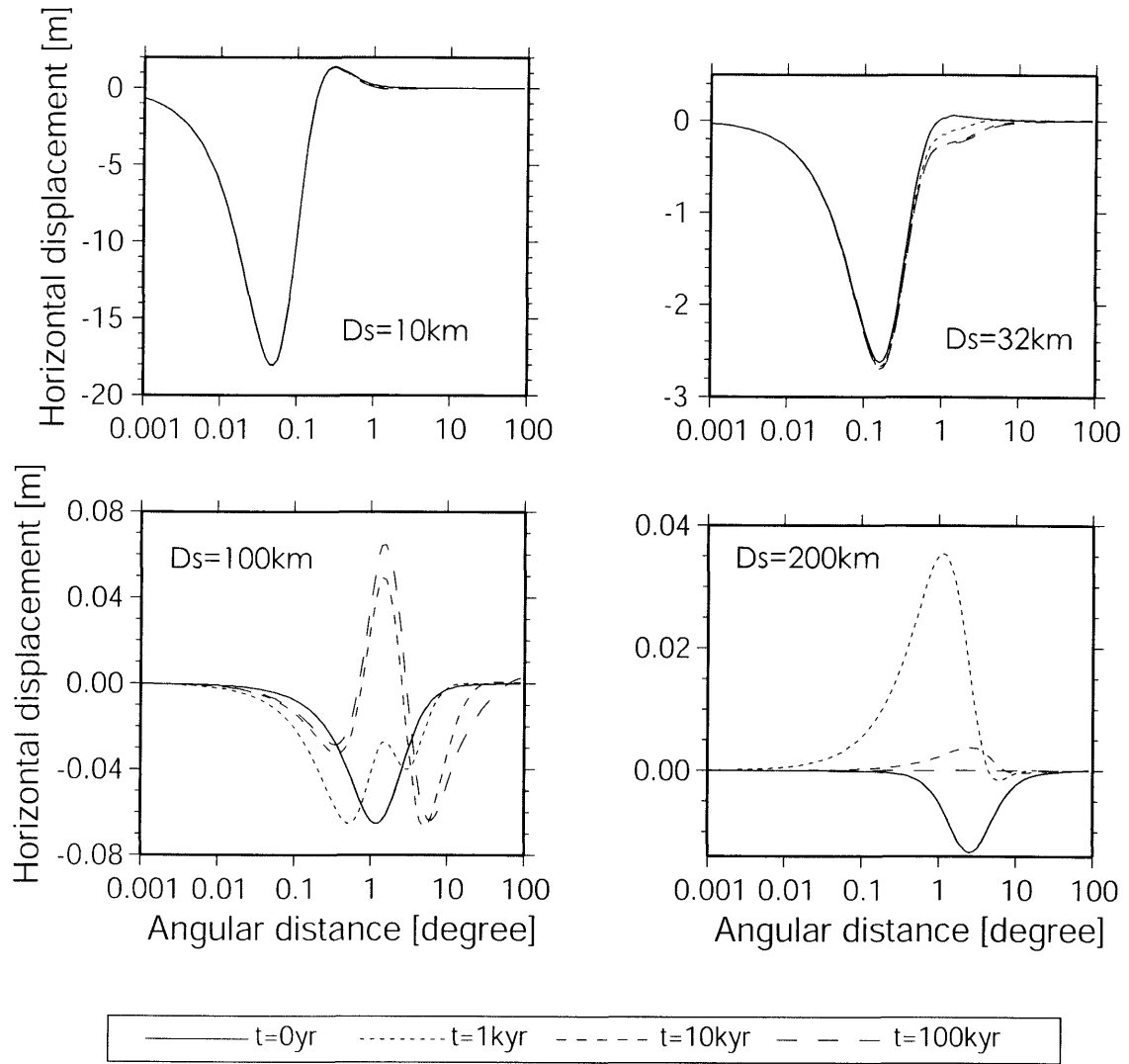


Figure 19. (e) Horizontal displacement u_ϕ on $\phi = 45^\circ$ (vertical tensile)

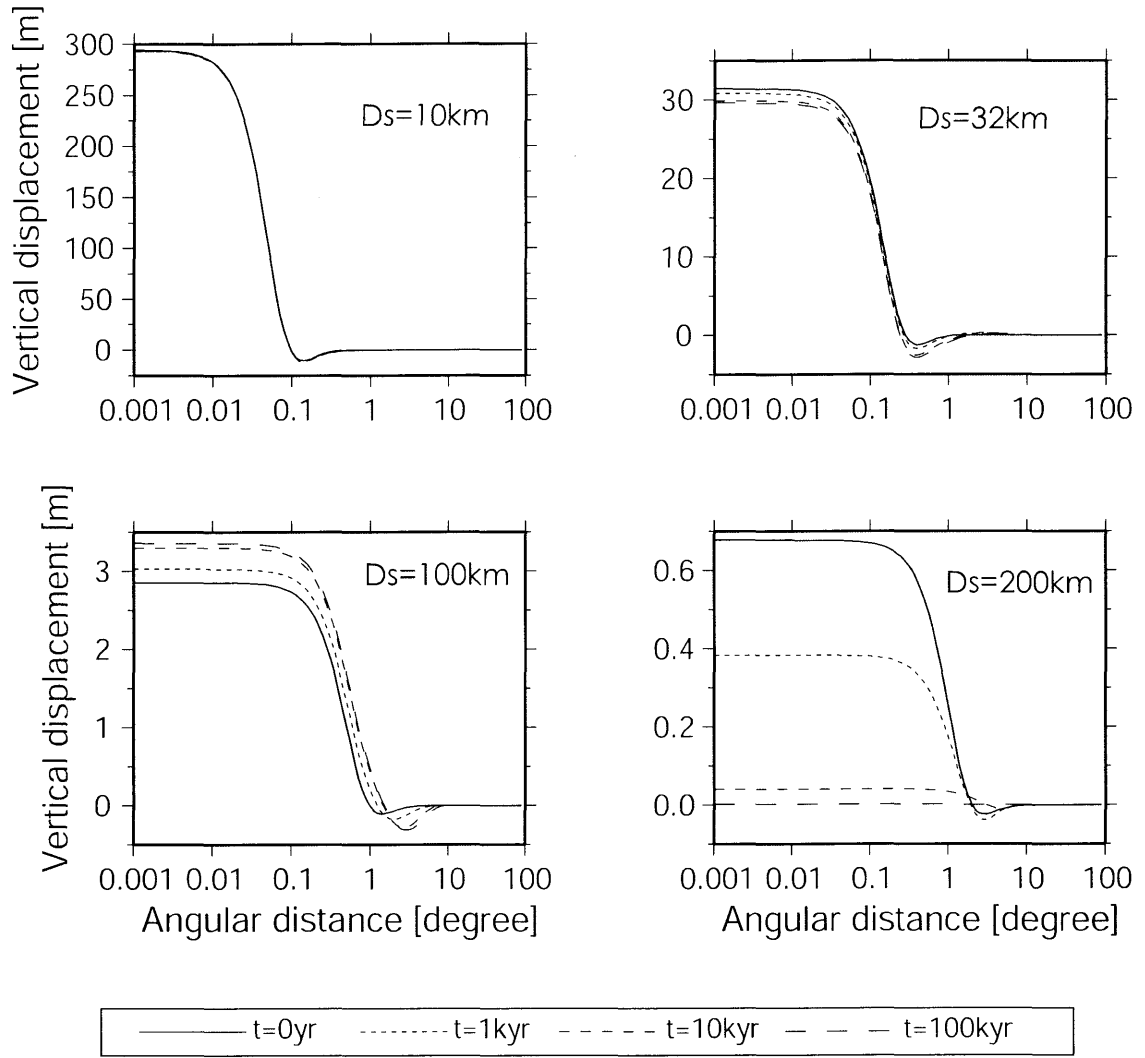


Figure 20. (a) Vertical displacement on $\phi = 0$ (dip-slip with dip angle 45° . See Table 5.). Normalized by $UdS = 10 \text{ m} \times (100 \text{ km})^2$. t denotes the time after an event. Events at $t = 0 \text{ yr}$ indicate coseismic jumps. The D_s denotes the source depth.

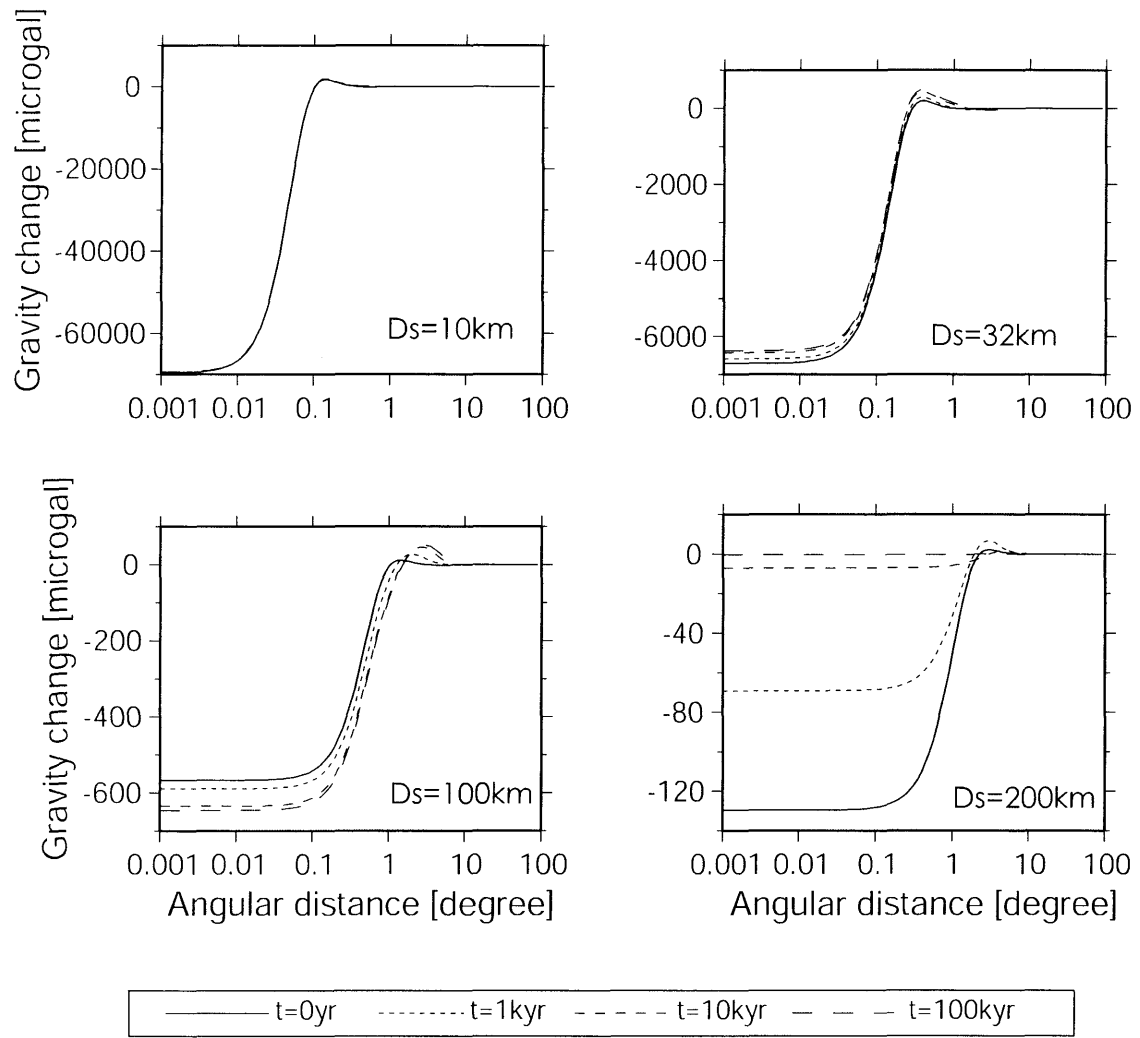


Figure 20. (b) Gravity change on $\phi = 0$ (dip-slip with dip angle 45°)

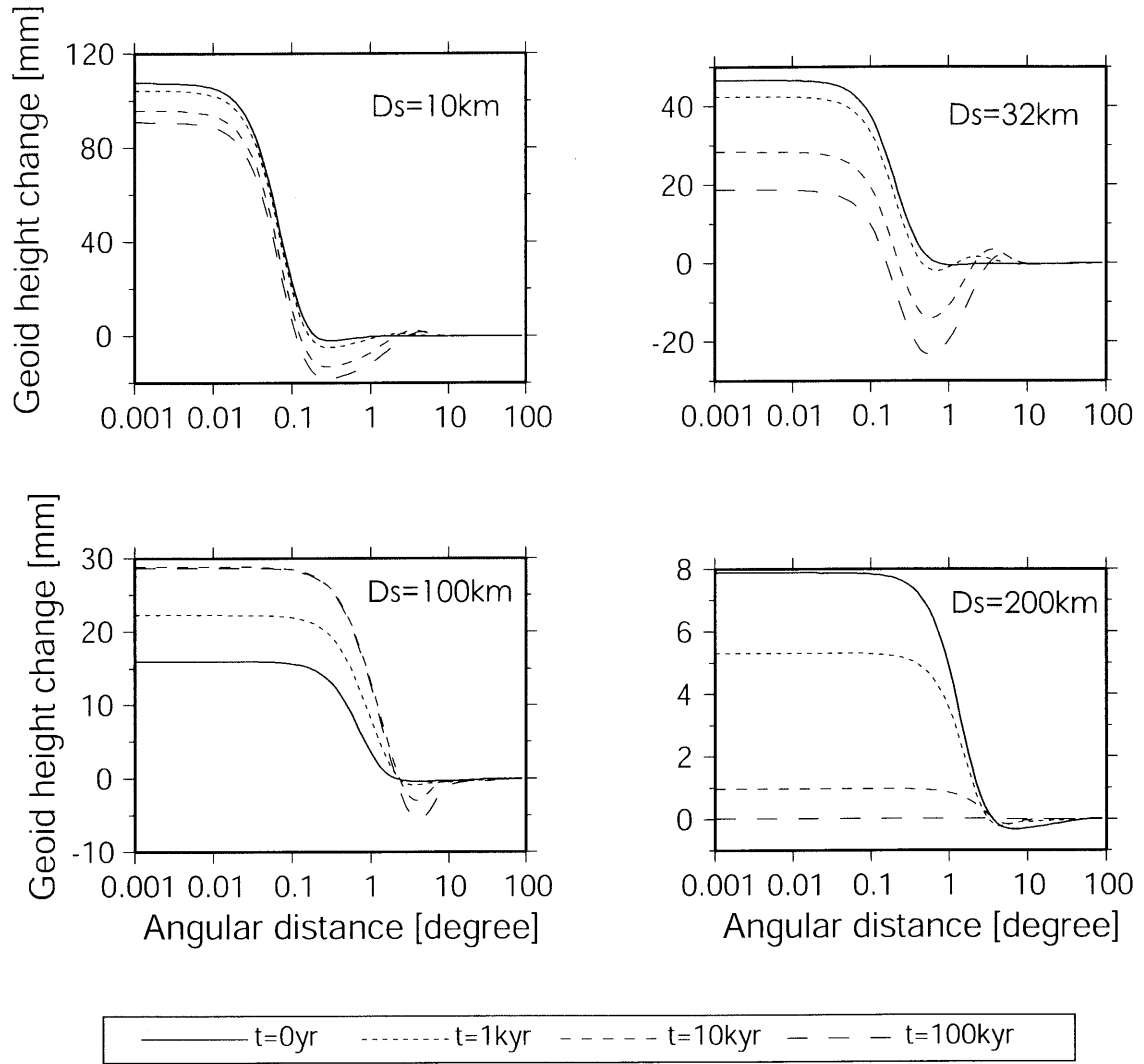


Figure 20. (c) Geoid height change on $\phi = 0$ (dip-slip with dip angle 45°)

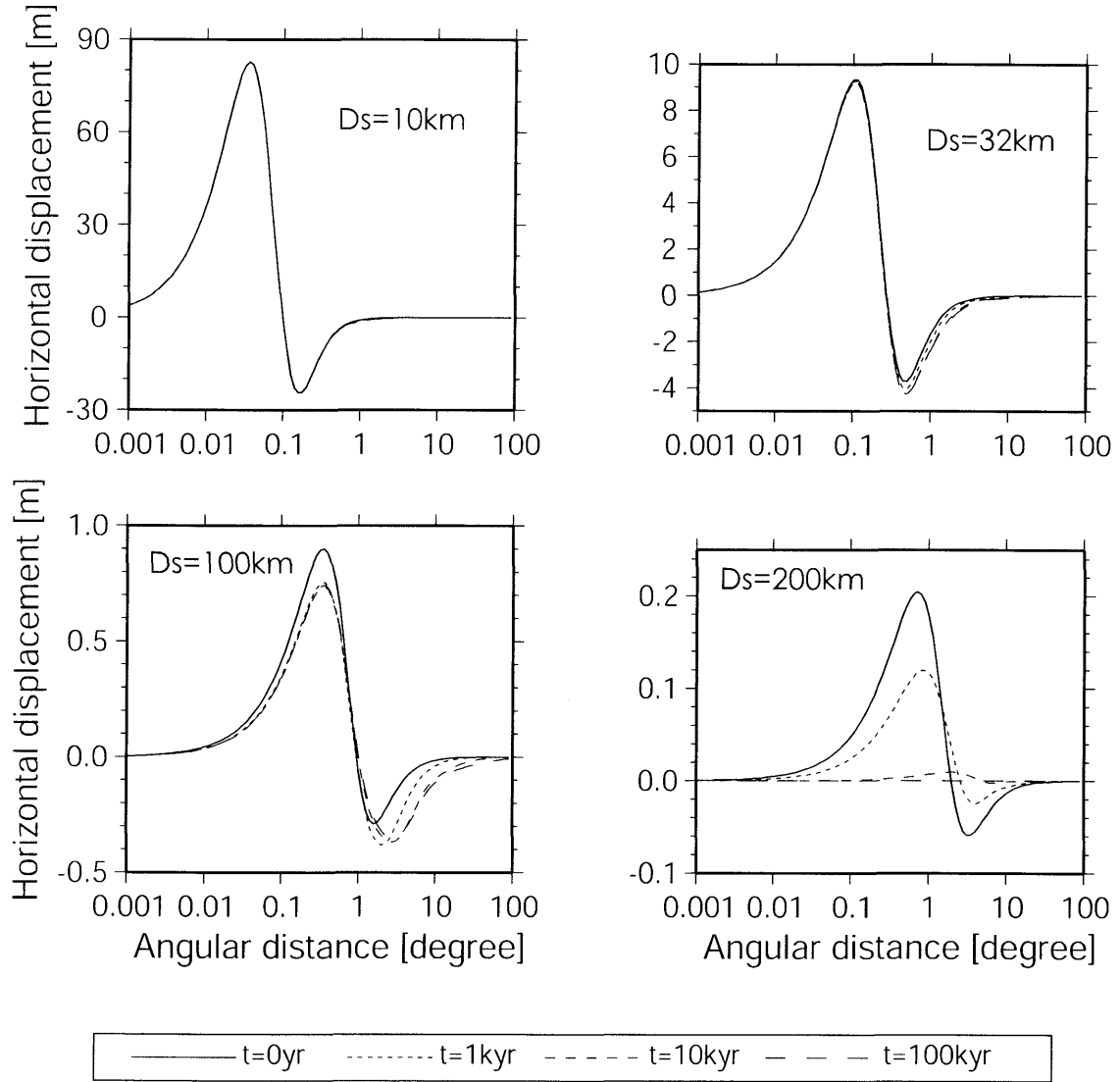


Figure 20. (d) Horizontal displacement u_θ on $\phi = 0$ (dip-slip with dip angle 45°)

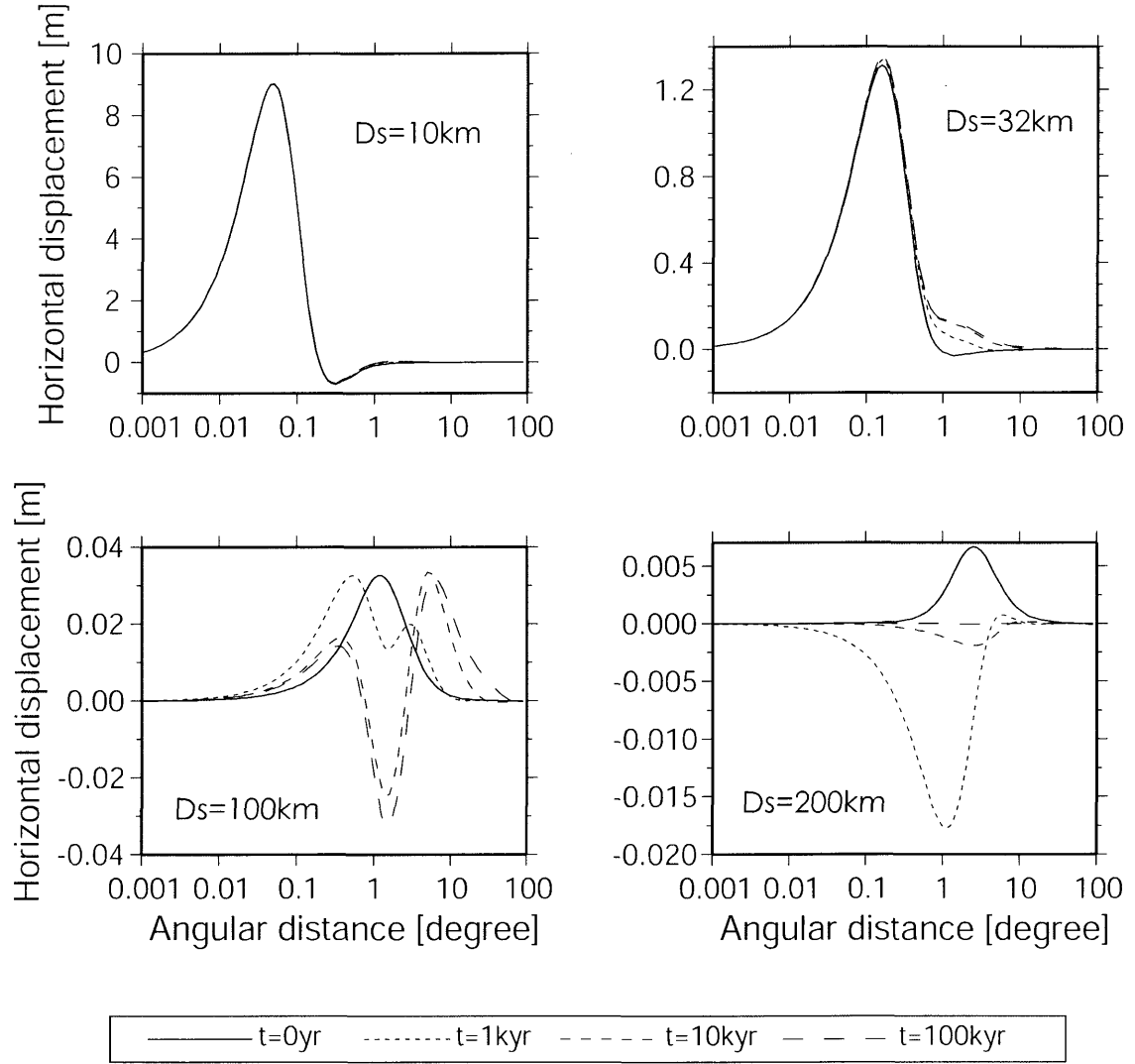


Figure 20. (e) Horizontal displacement u_ϕ on $\phi = 45^\circ$ (dip-slip with dip angle 45°)

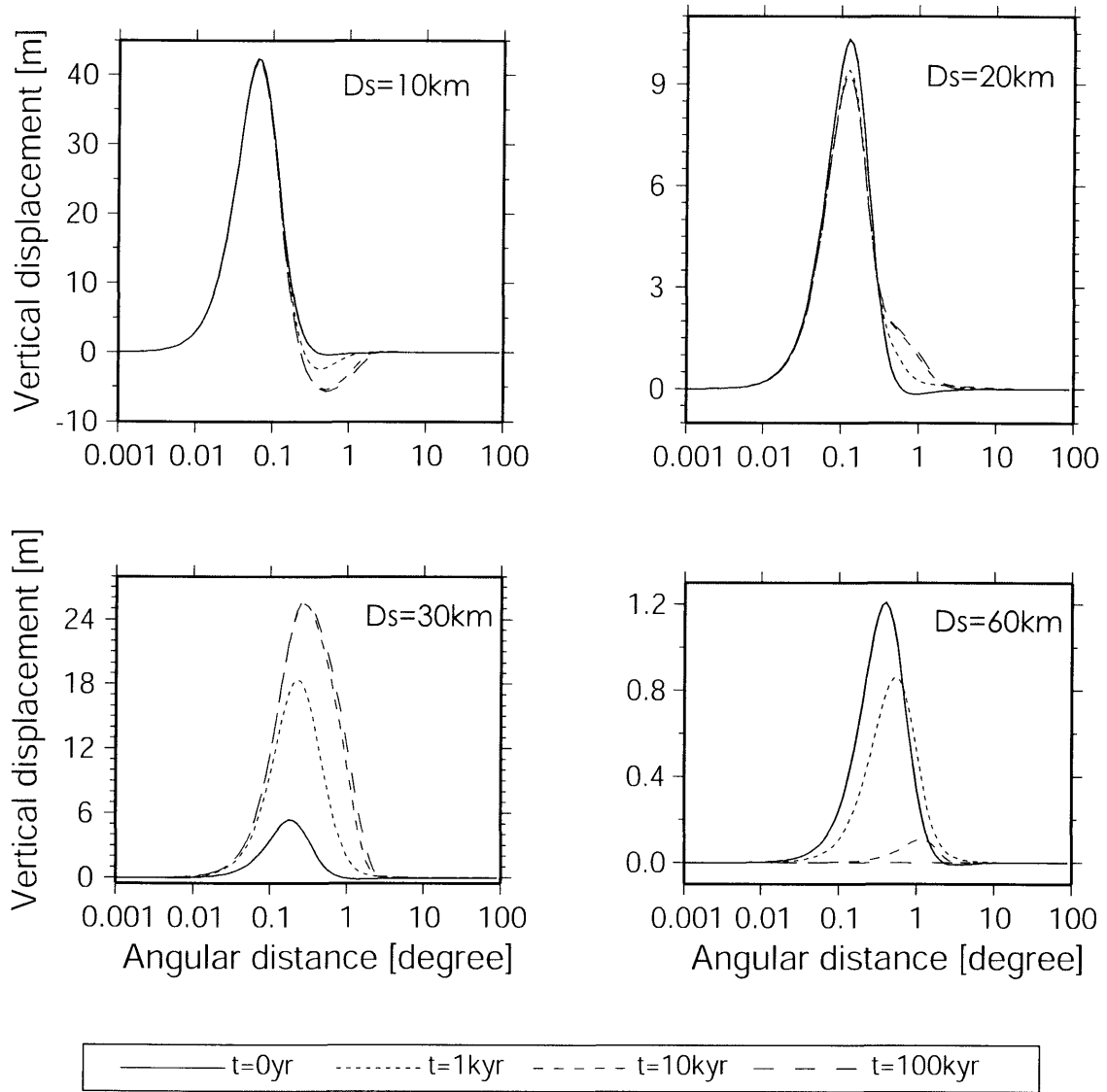


Figure 21. (a) Vertical displacement (vertical strike-slip). The same as Fig. 18 but for the viscous model 2 in Fig. 10 (the thickness of the lithosphere is 30 km). Normalized by $UdS = 10 \text{ m} \times (100 \text{ km})^2$. The D_s denotes the source depth.

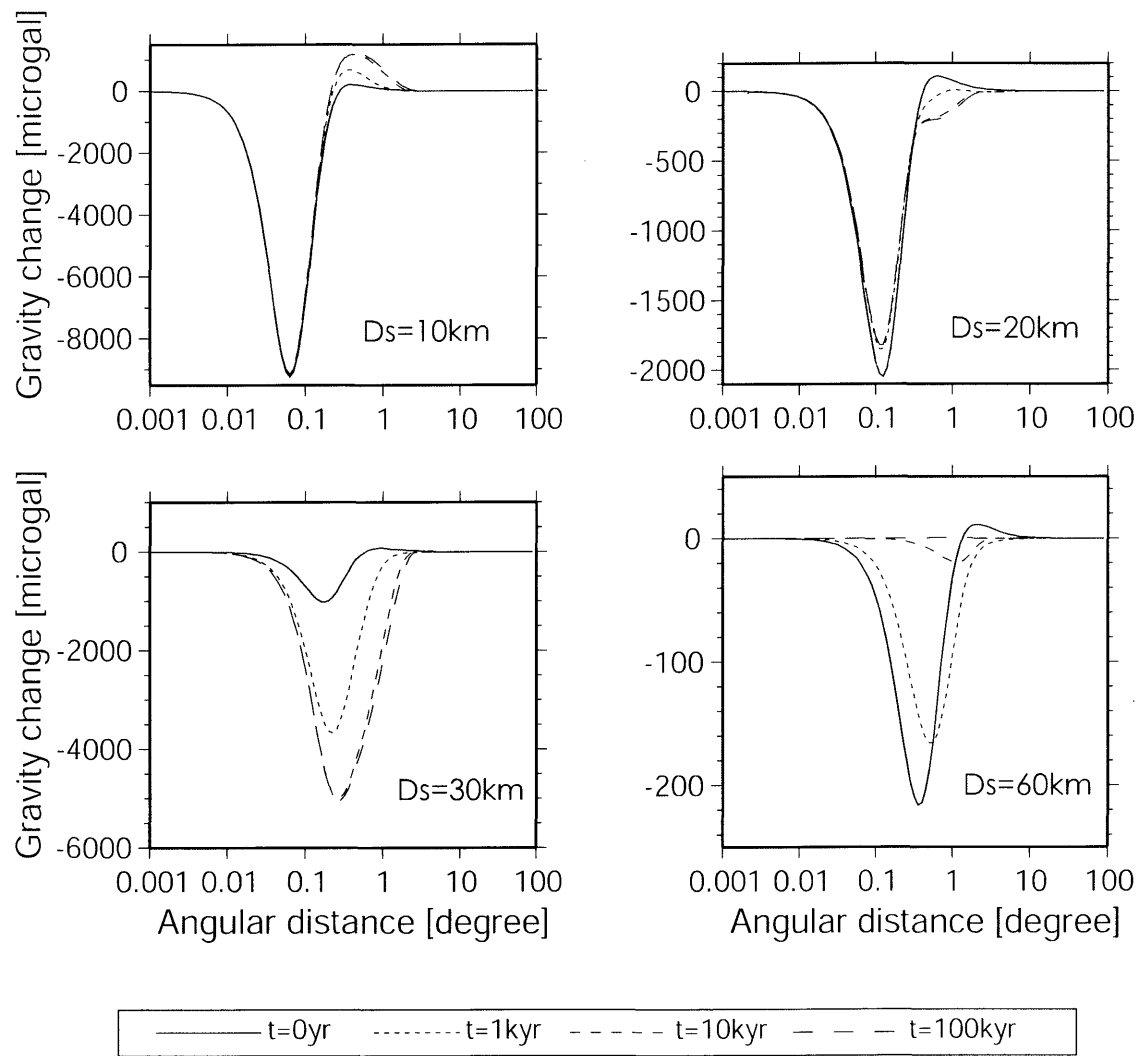


Figure 21. (b) Gravity change (vertical strike-slip)

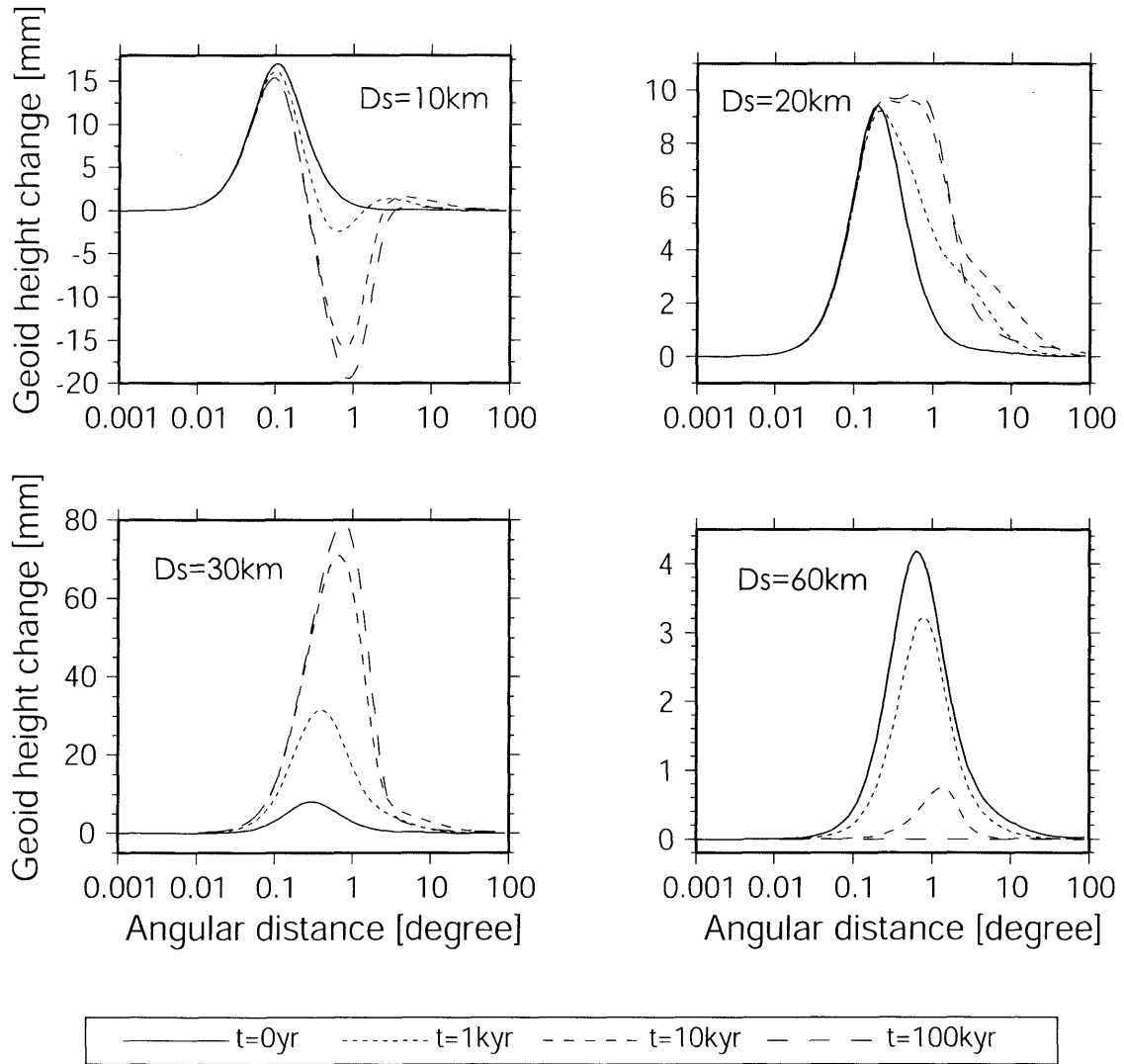


Figure 21. (c) Geoid height change (vertical strike-slip)

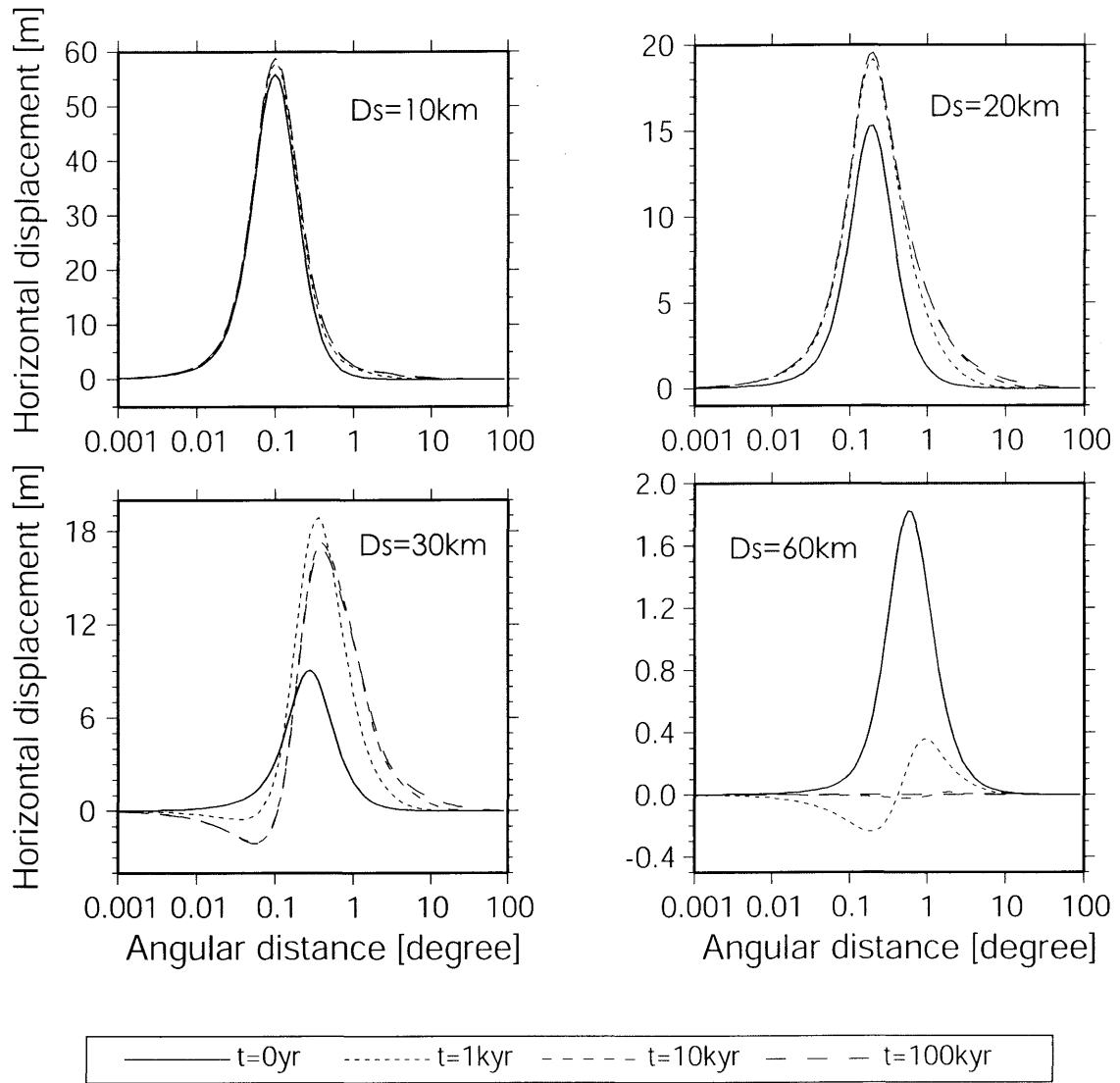


Figure 21. (d) Horizontal displacement u_θ on $\phi = 45^\circ$ (vertical strike-slip)

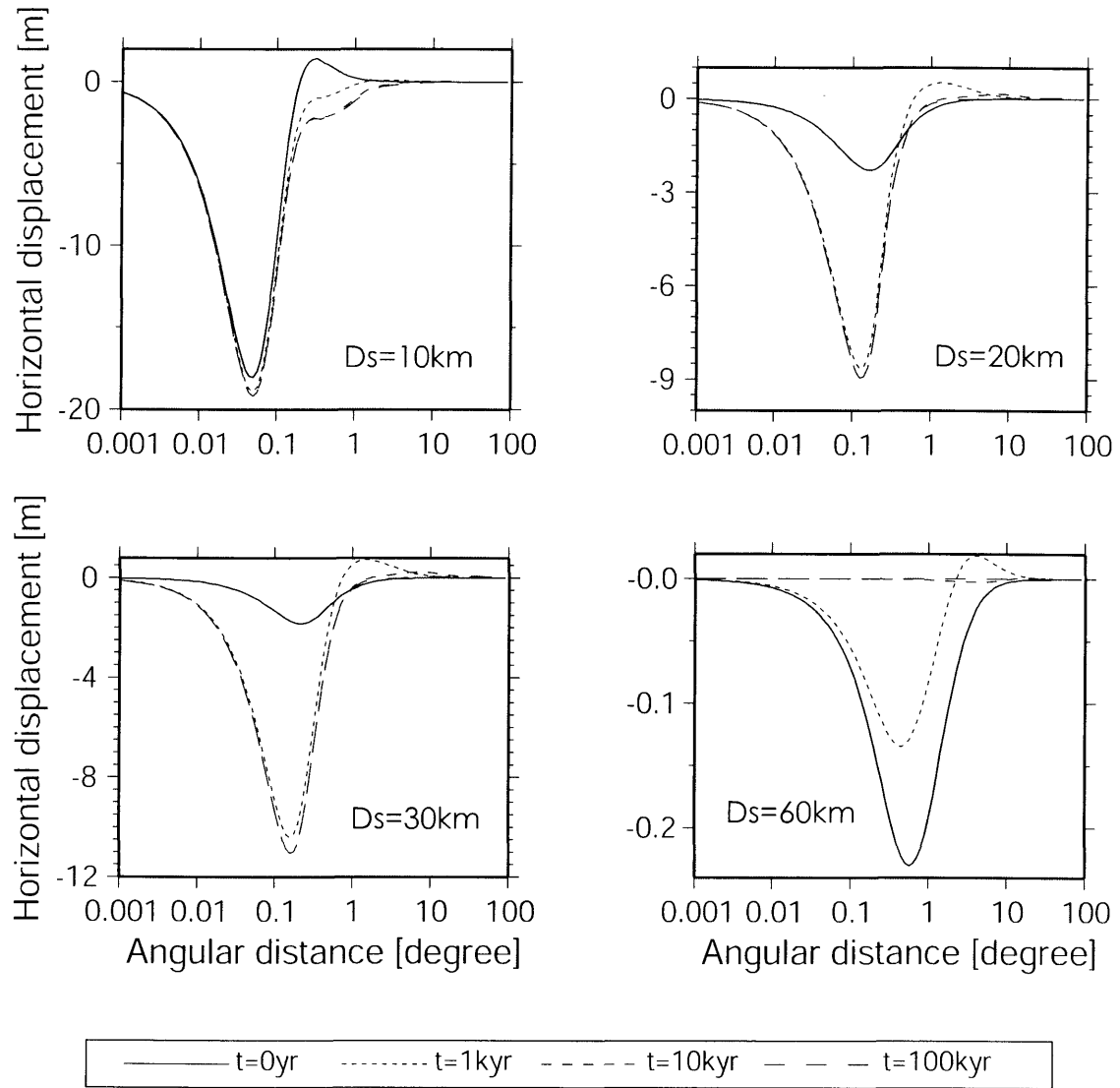


Figure 21. (e) Horizontal displacement u_ϕ on $\phi = 0^\circ$ (vertical strike-slip)

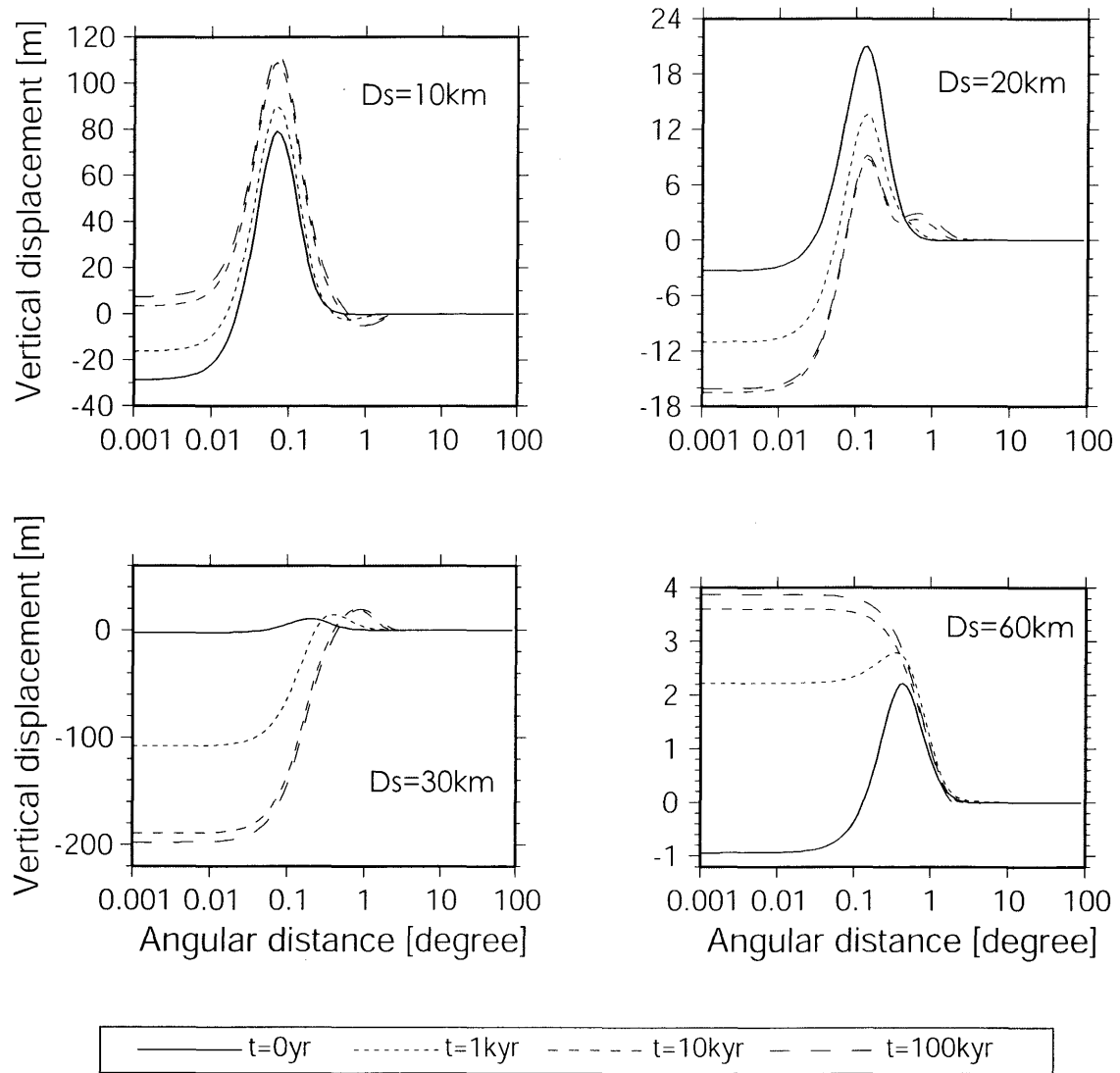


Figure 22. (a) Vertical displacement (tensile). The same as Fig. 19 but for the viscous model 2 in Fig. 10 (the thickness of the lithosphere is 30 km). Normalized by $UdS = 10 \text{ m} \times (100 \text{ km})^2$. The D_s denotes the source depth.

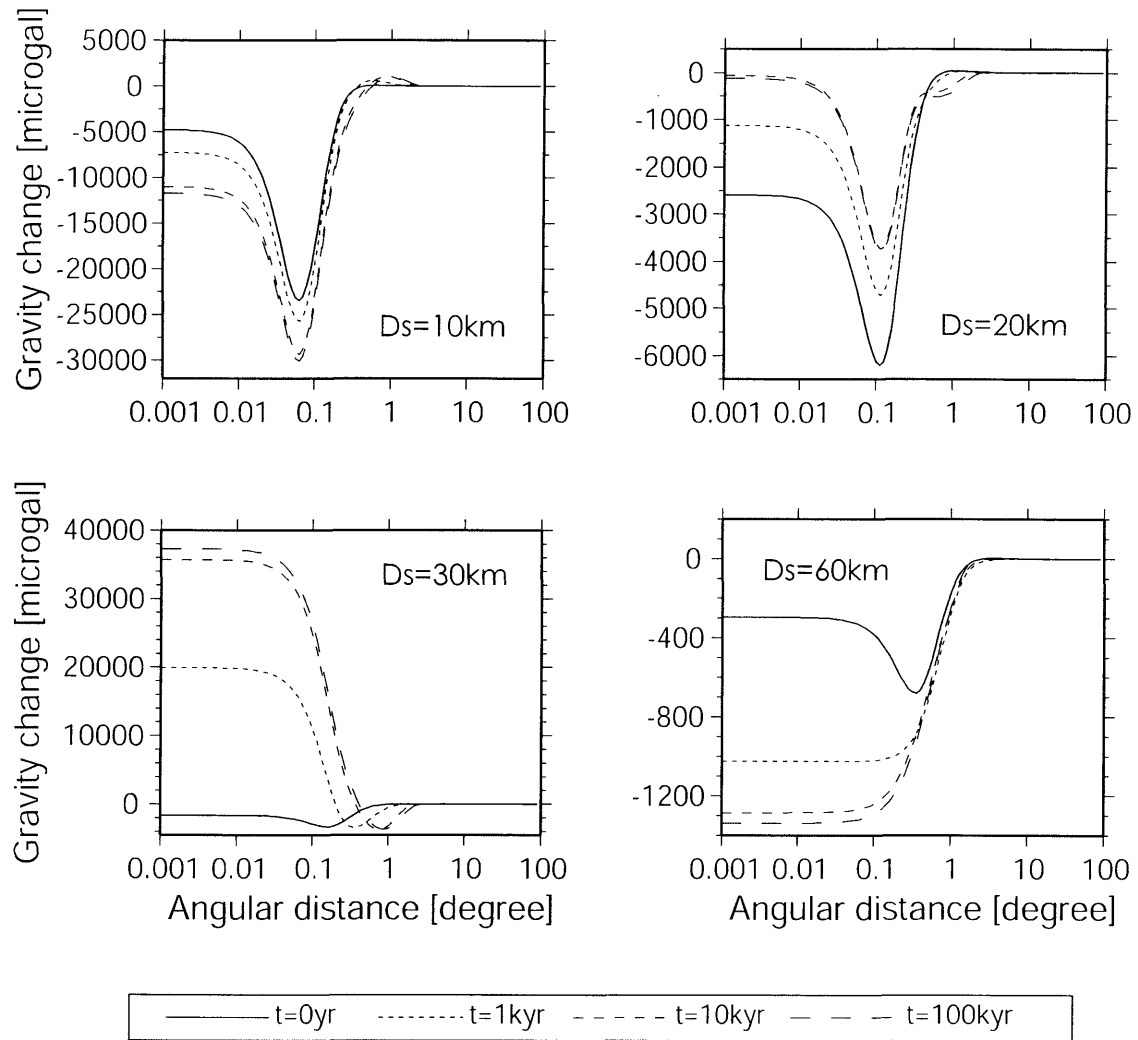


Figure 22. (b) Gravity change (tensile)

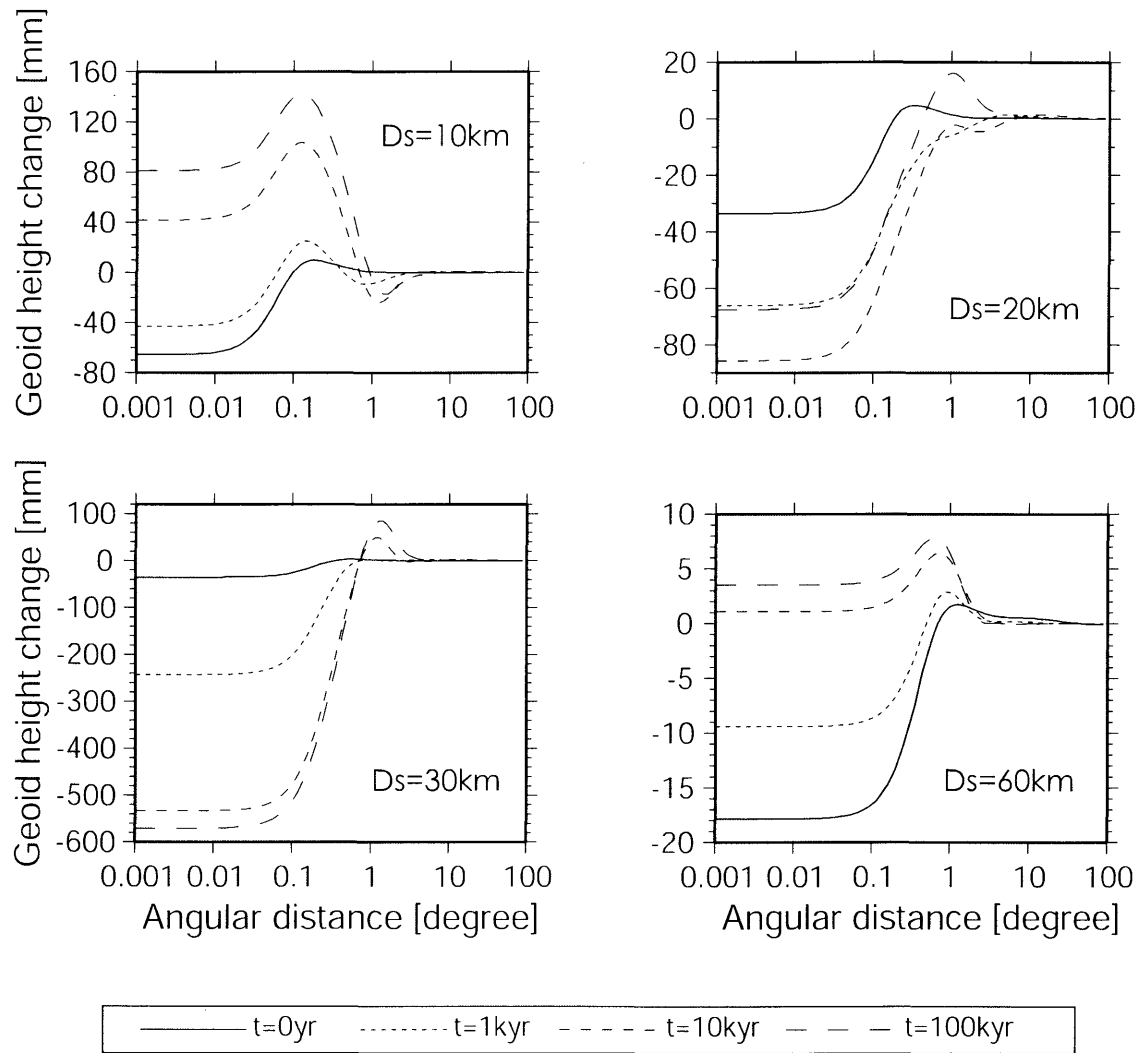


Figure 22. (c) Geoid height change (tensile)

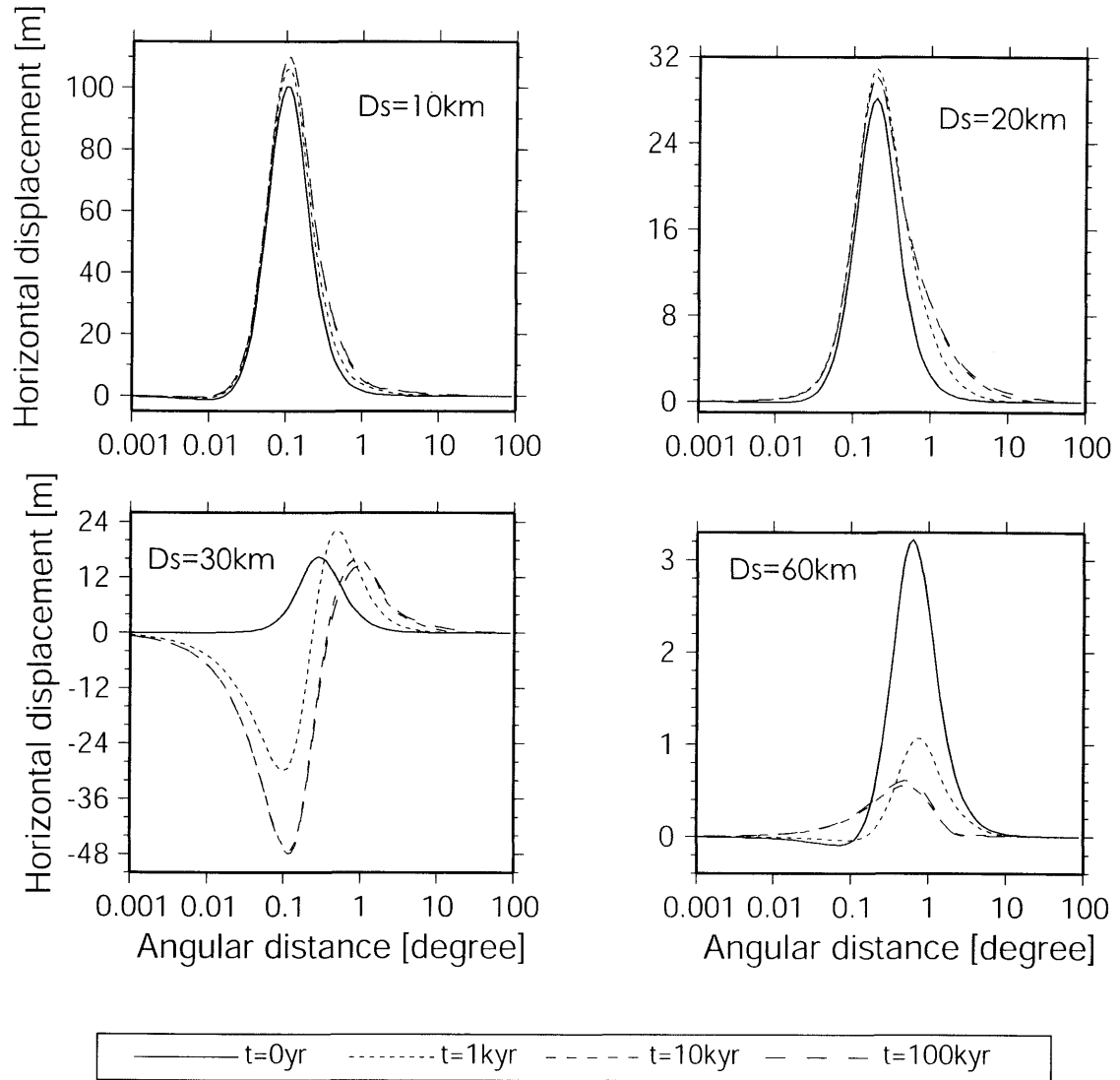


Figure 22. (d) Horizontal displacement u_θ on $\phi = 0^\circ$ (tensile)

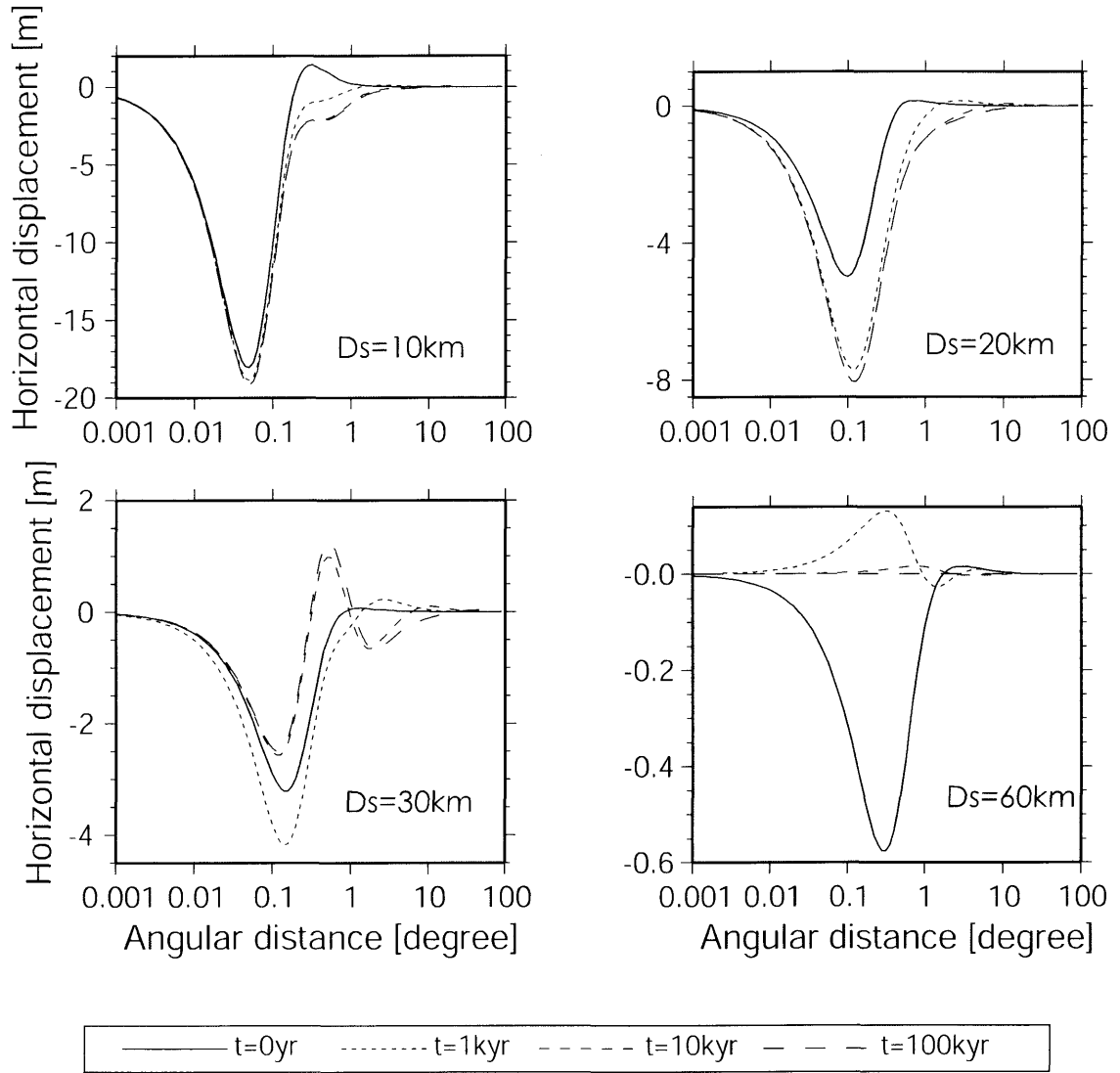


Figure 22. (e) Horizontal displacement u_ϕ on $\phi = 45^\circ$ (tensile)

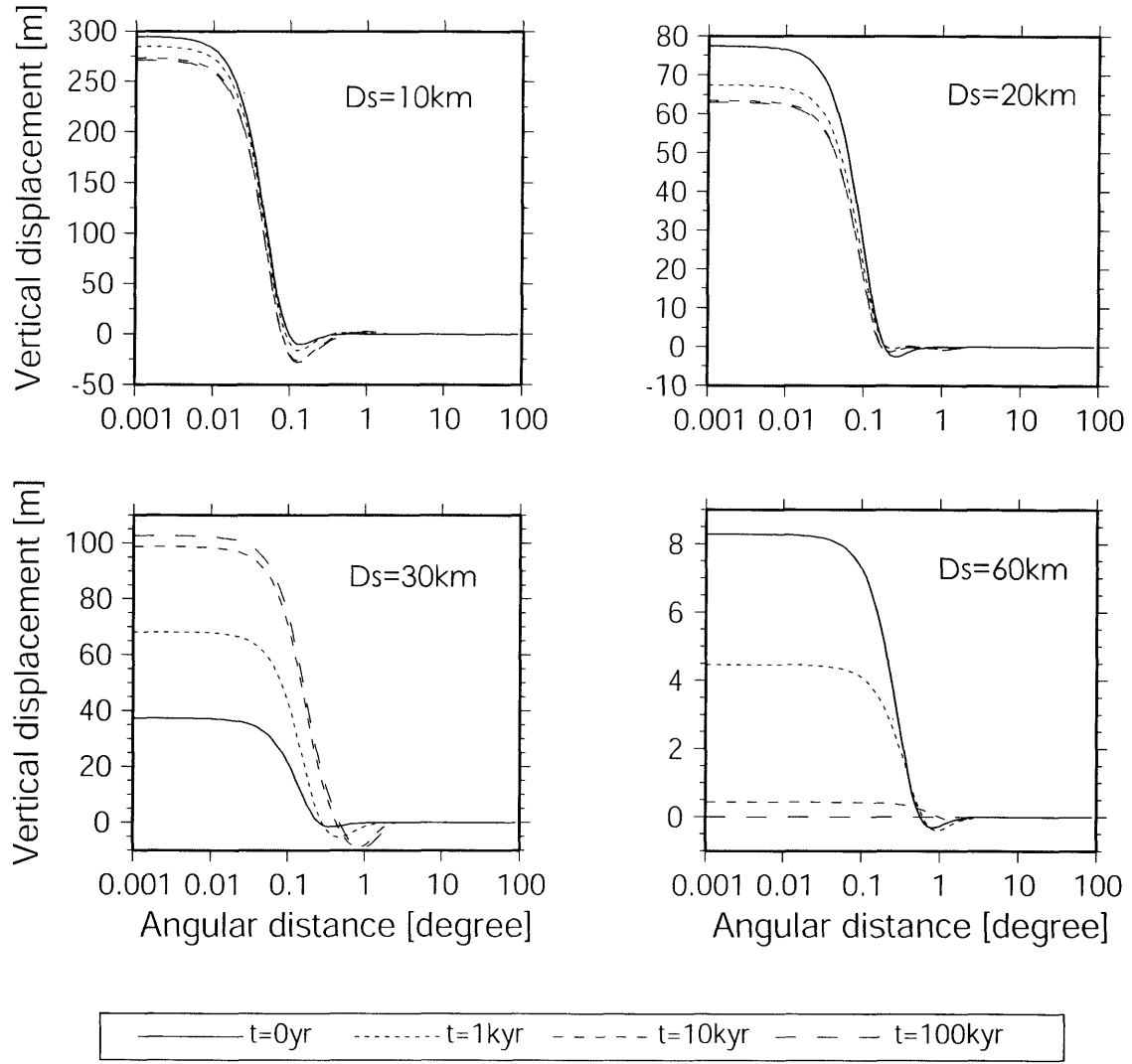


Figure 23. (a) Vertical displacement (dip-slip with dip angle of 45°). The same as Fig. 20 but for the viscous model 2 in Fig. 10 (the thickness of the lithosphere is 30 km). Normalized by $UdS = 10 \text{ m} \times (100 \text{ km})^2$. The D_s denotes the source depth.

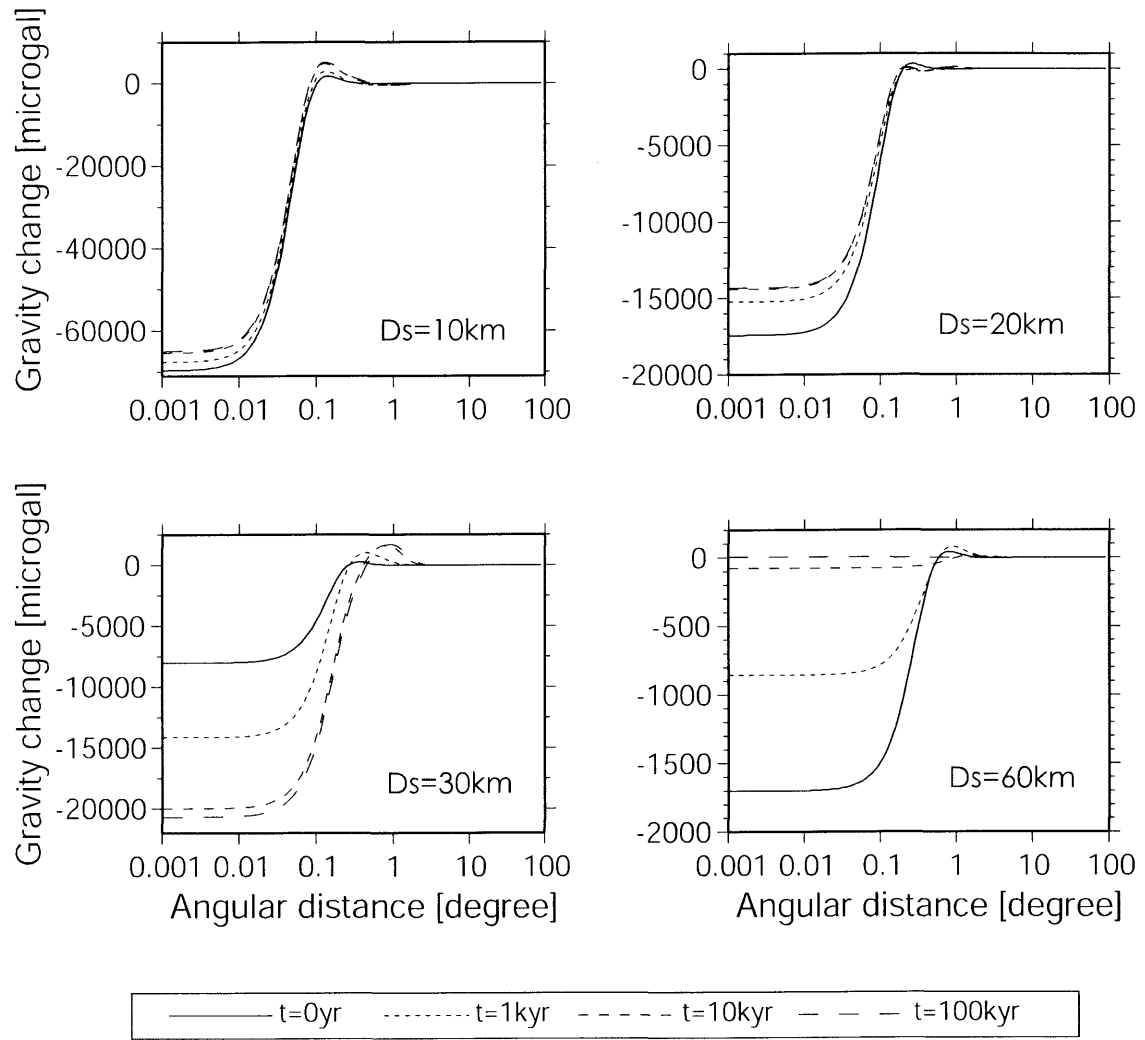


Figure 23. (b) Gravity change (dip-slip with dip angle of 45°)

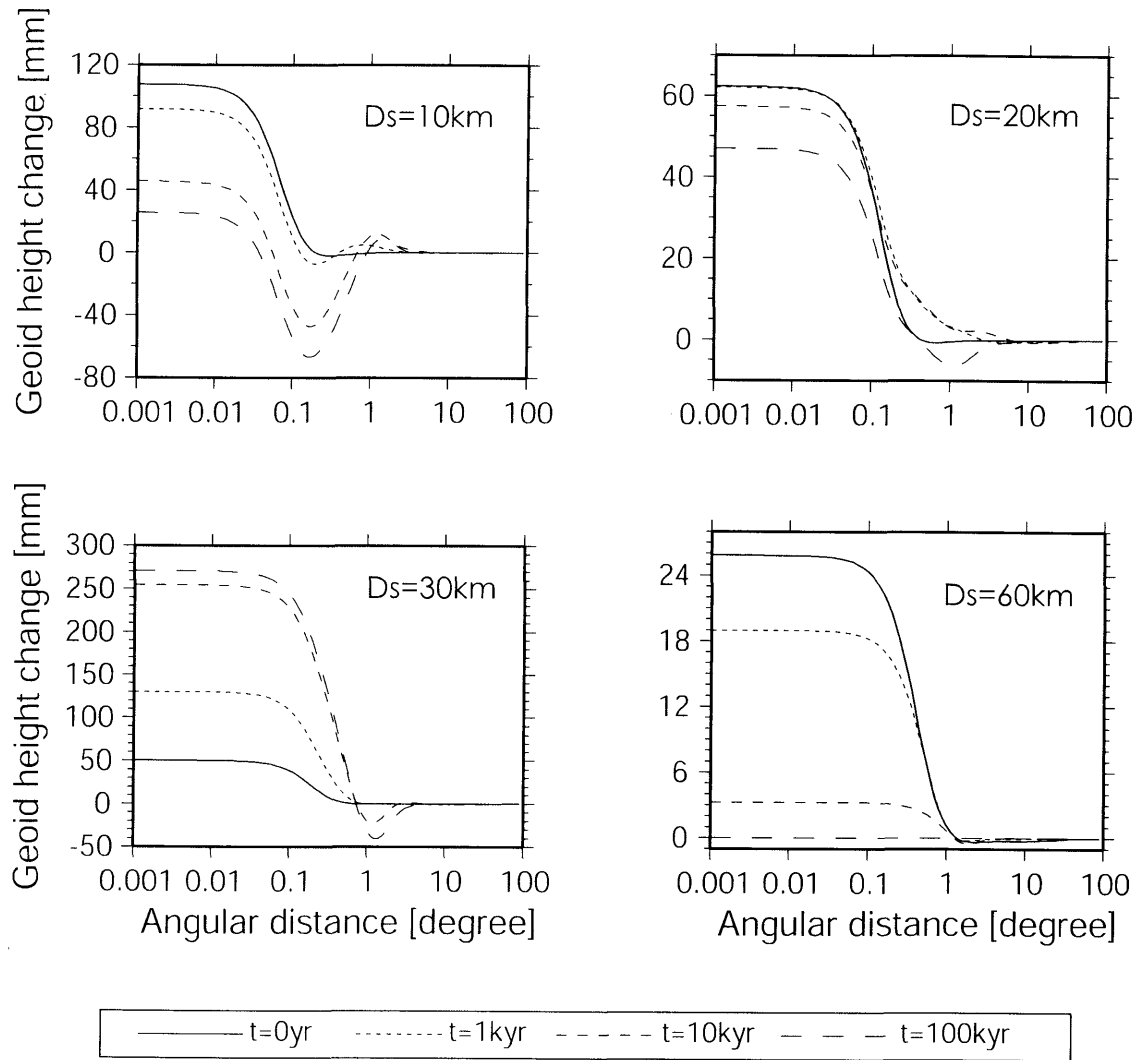


Figure 23. (c) Geoid height change (dip-slip with dip angle of 45°)

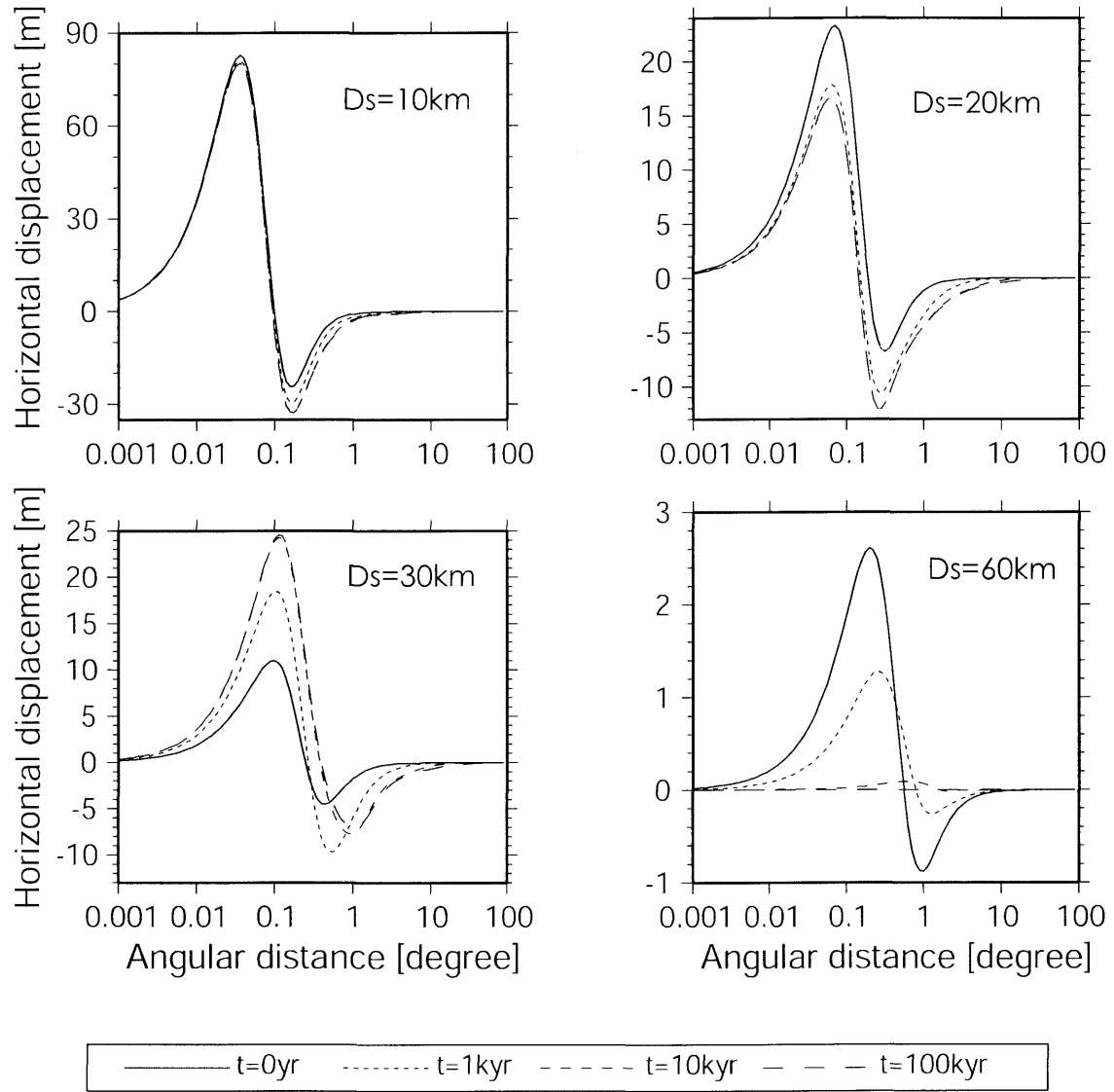


Figure 23. (d) Horizontal displacement u_ϕ on $\phi = 0^\circ$ (dip-slip with dip angle of 45°)

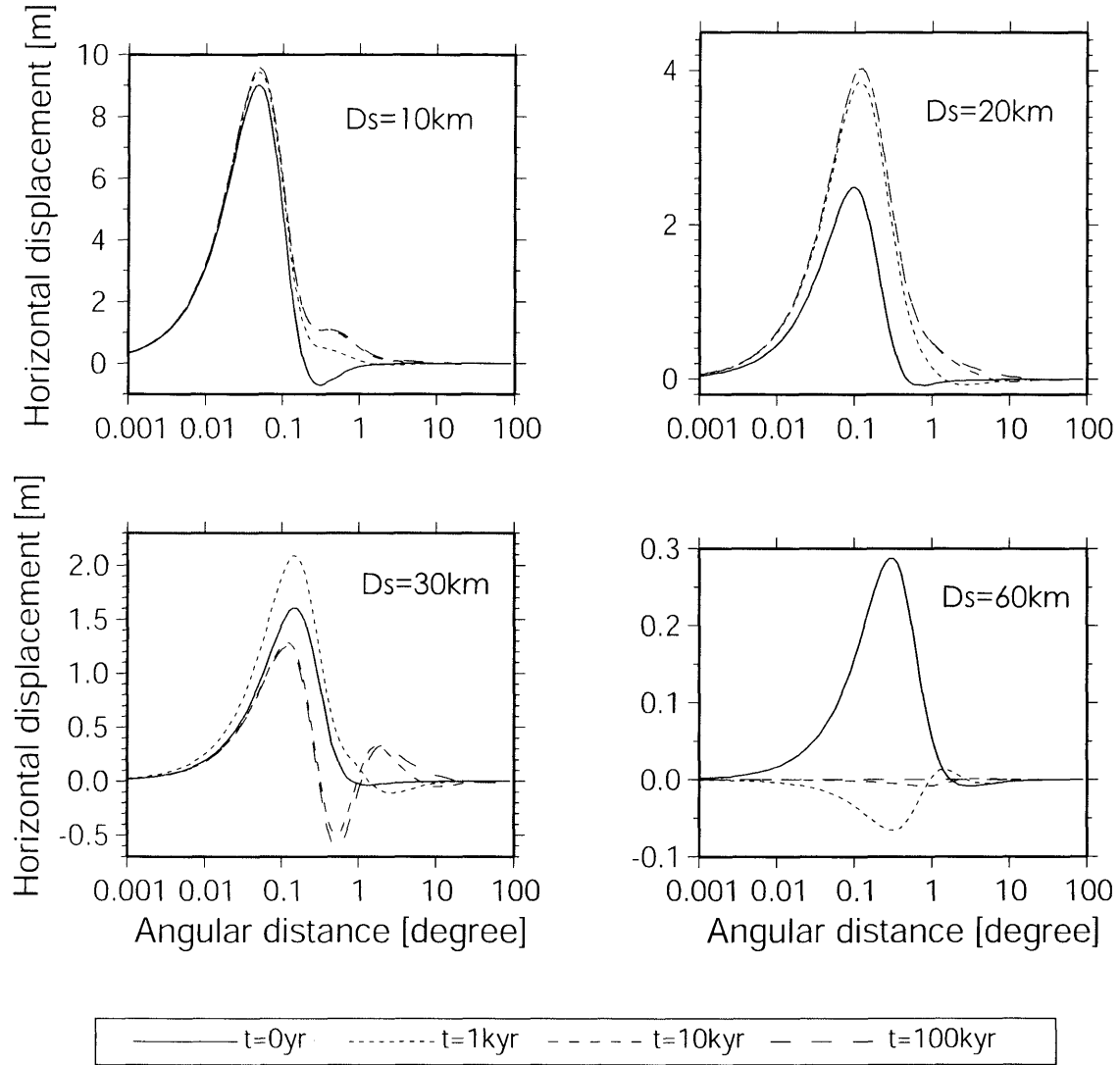


Figure 23. (e) Horizontal displacement u_ϕ on $\phi = 45^\circ$ (dip-slip with dip angle of 45°)

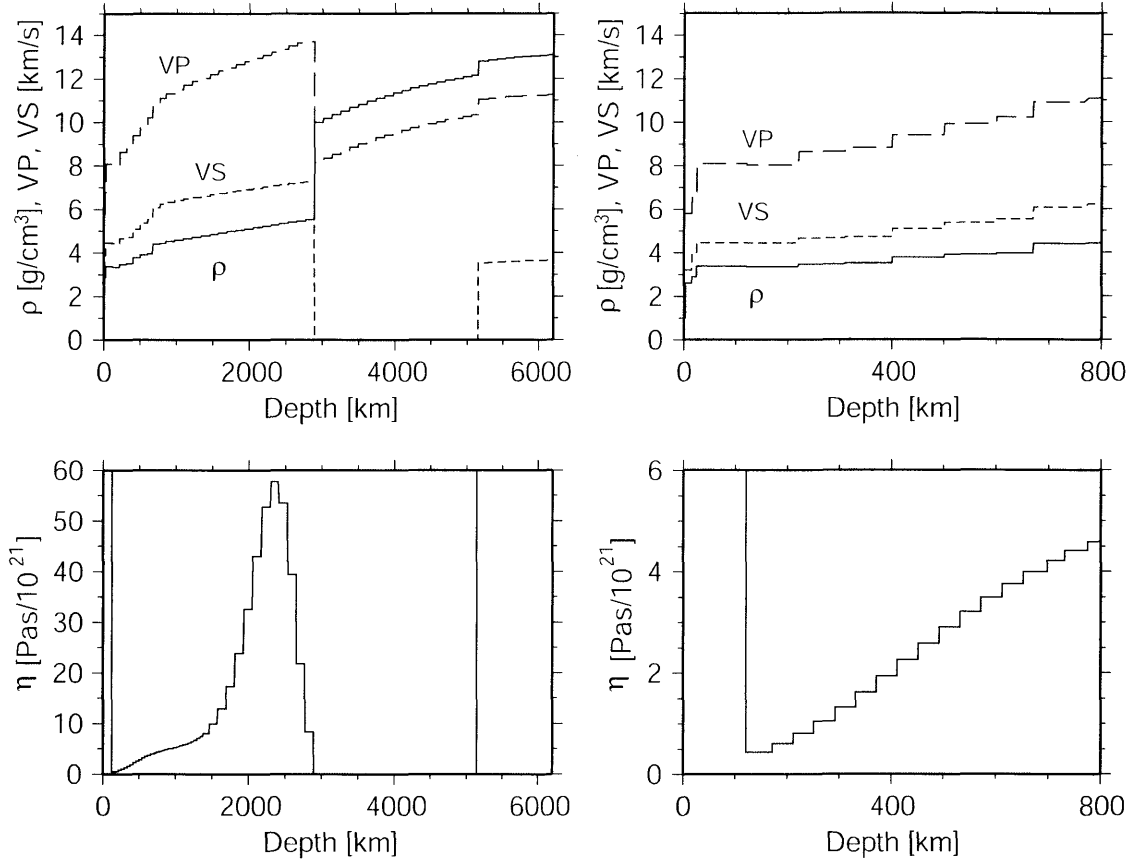


Figure 24. The discretely-layered Earth model with 60 layers based on the finely-graded model (Fig. 10). The profile of the density, elastic constants and viscosity below the lithosphere is discretized with the resolution of 40 km for the depth < 1,500 km and 120 km for the depth > 1,500 km. Those in the lithosphere remains the same as in Fig. 10. The discretization is carried out with a simple average in each interval, not with the volume-averaging method (Vermeersen & Sabadini 1997).

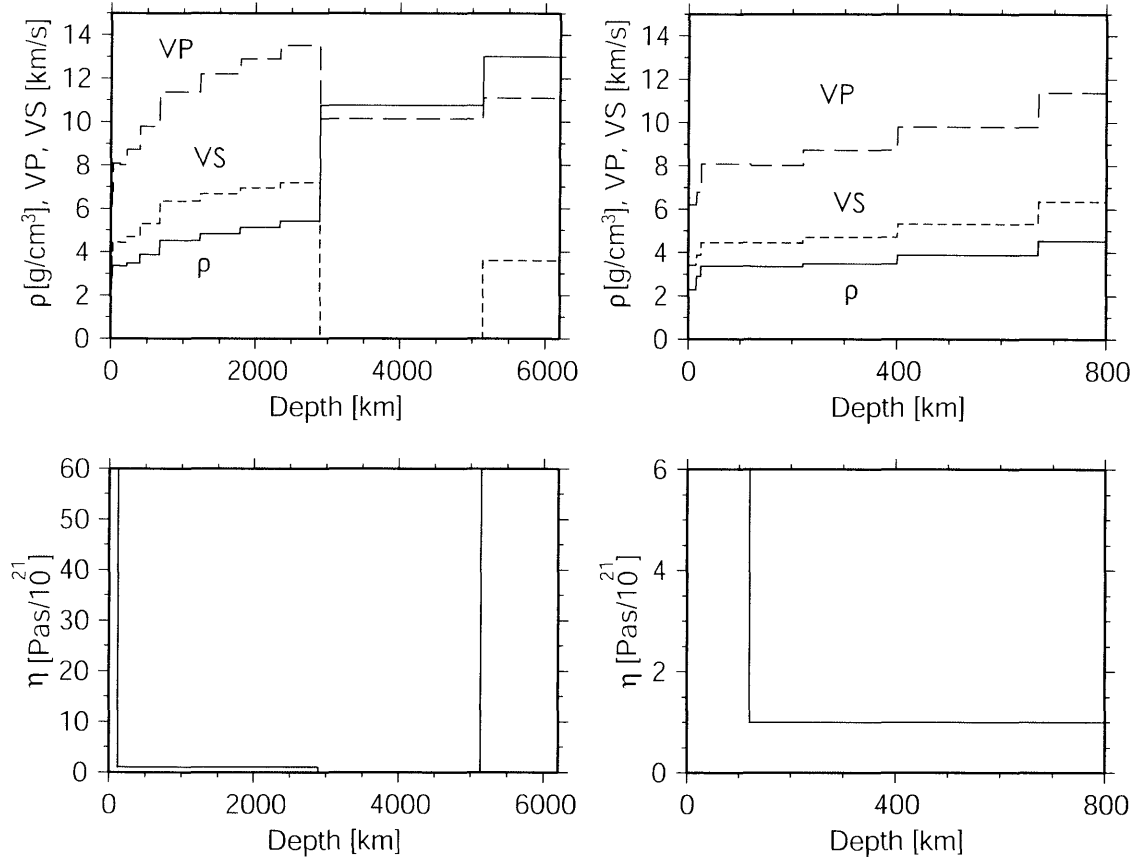


Figure 25. The discretely-layered Earth model with 11 layers. The same model as Wang (1999)'s.

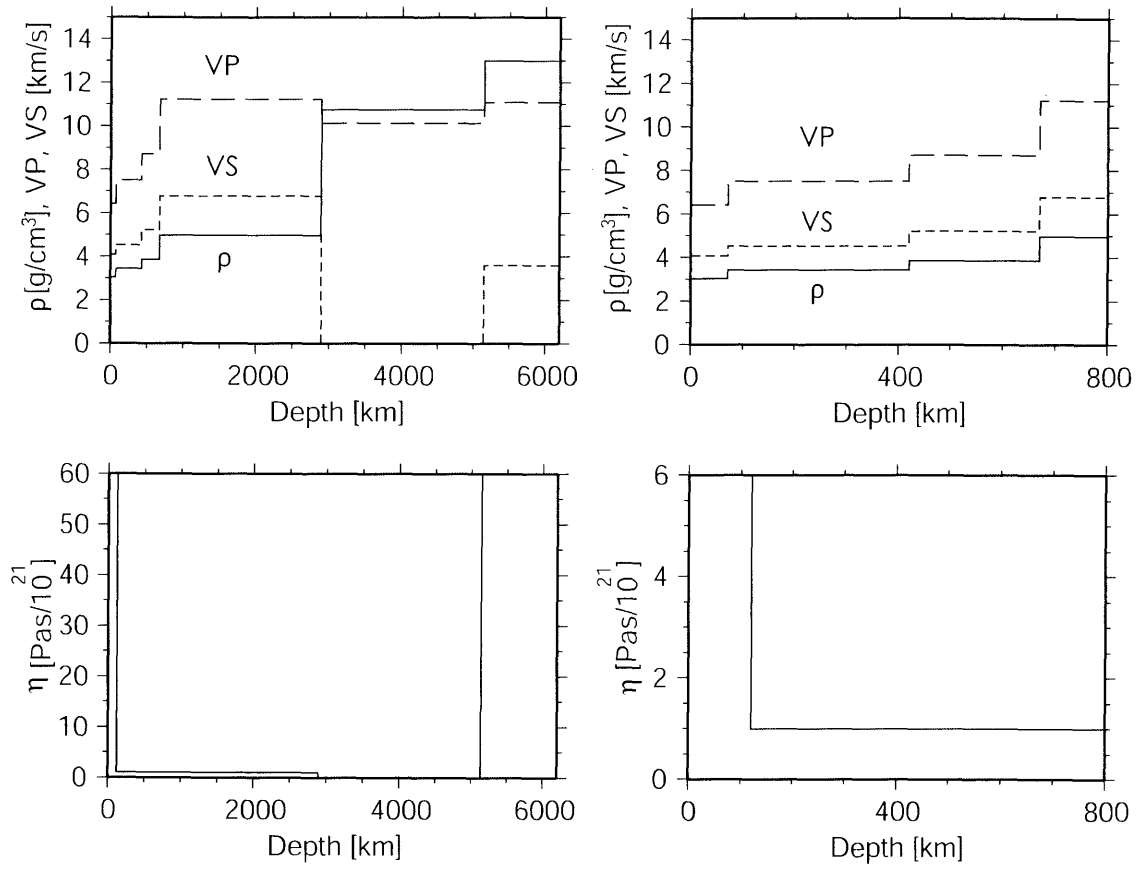


Figure 26. The discretely-layered Earth model with five layers. The compressible version of the volume-averaged PREM (http://www.rses.anu.edu.au/geodynamics/GIA_benchmark).

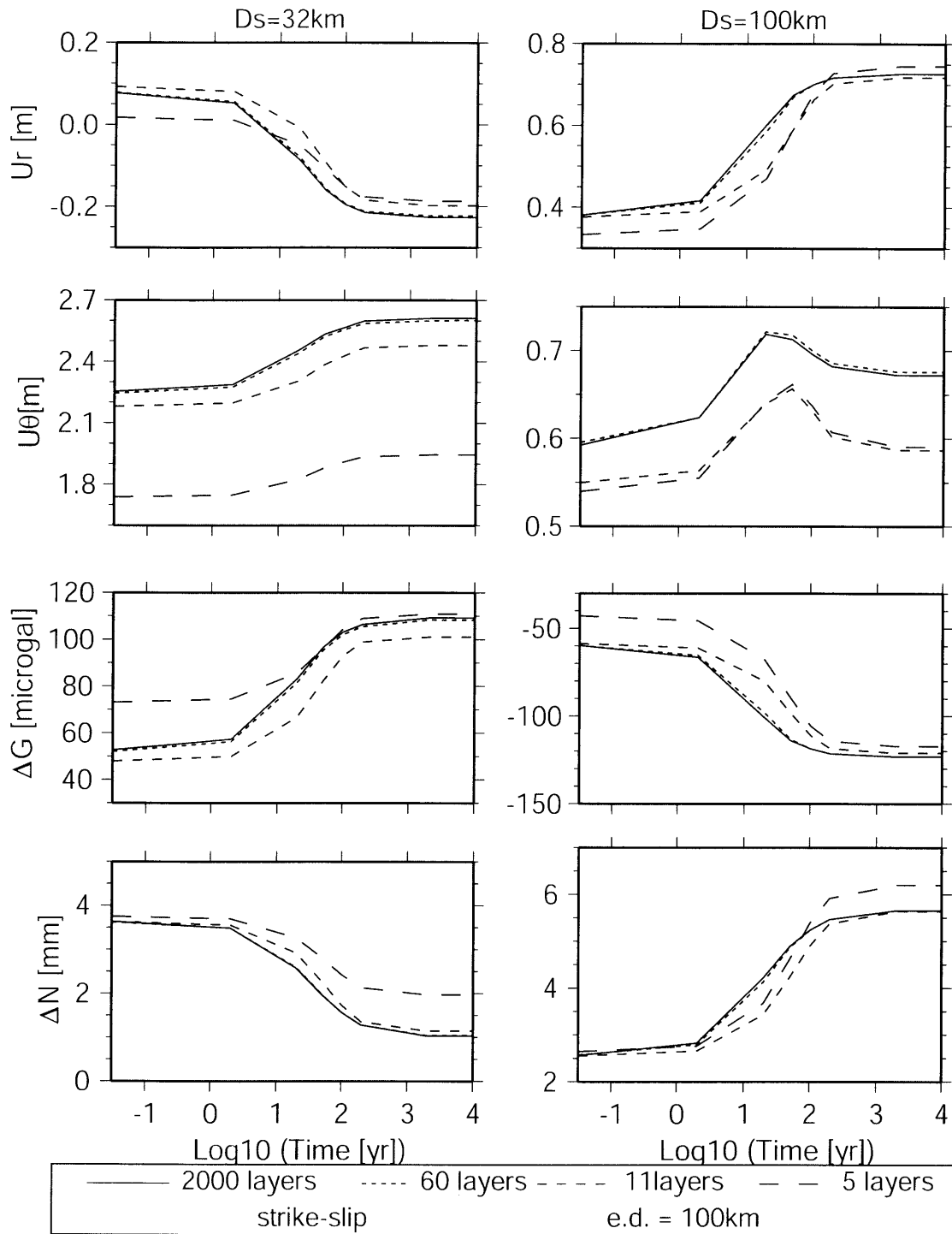


Figure 27. (a) The effect of fine layering.

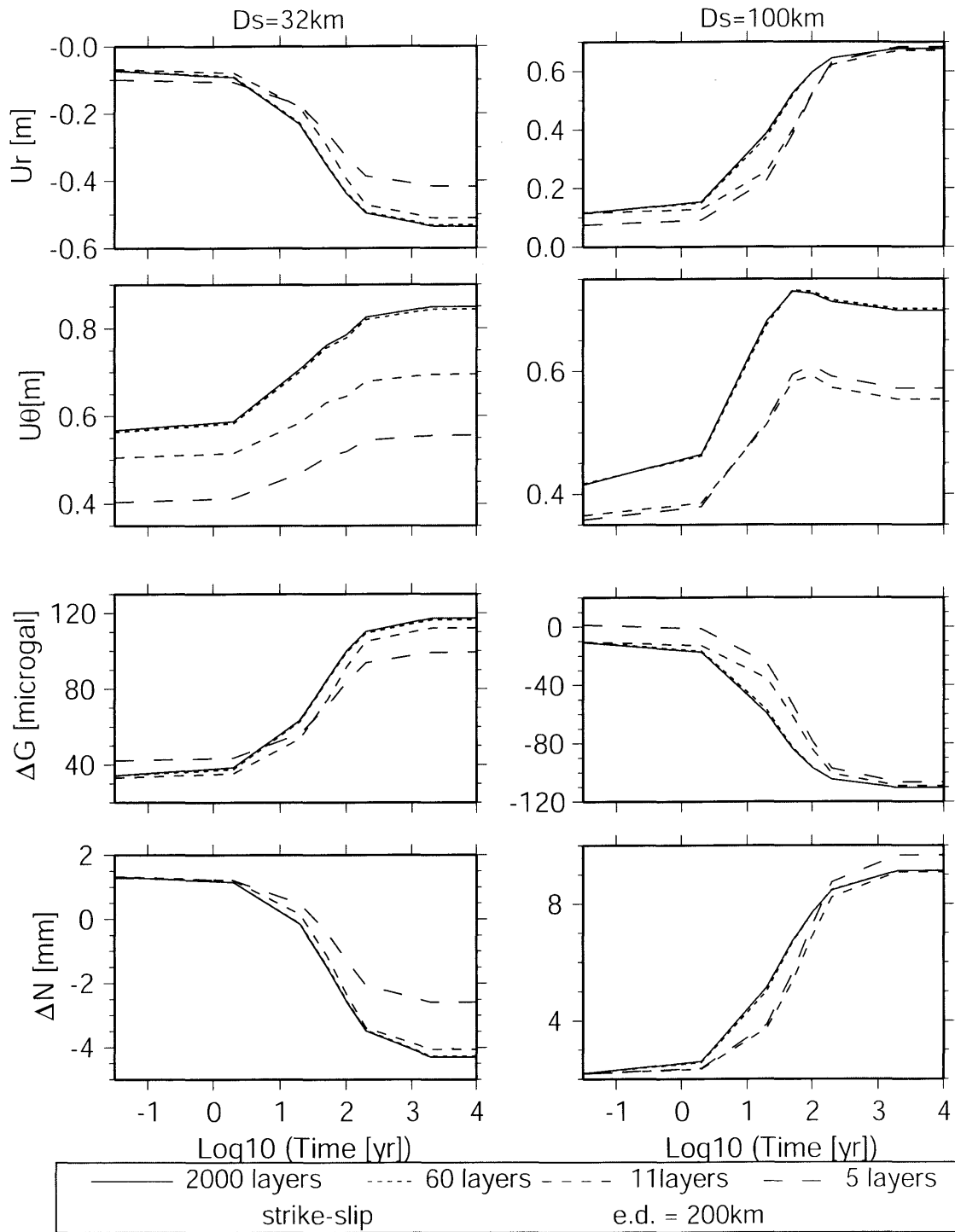


Figure 27. (b) The effect of fine layering.

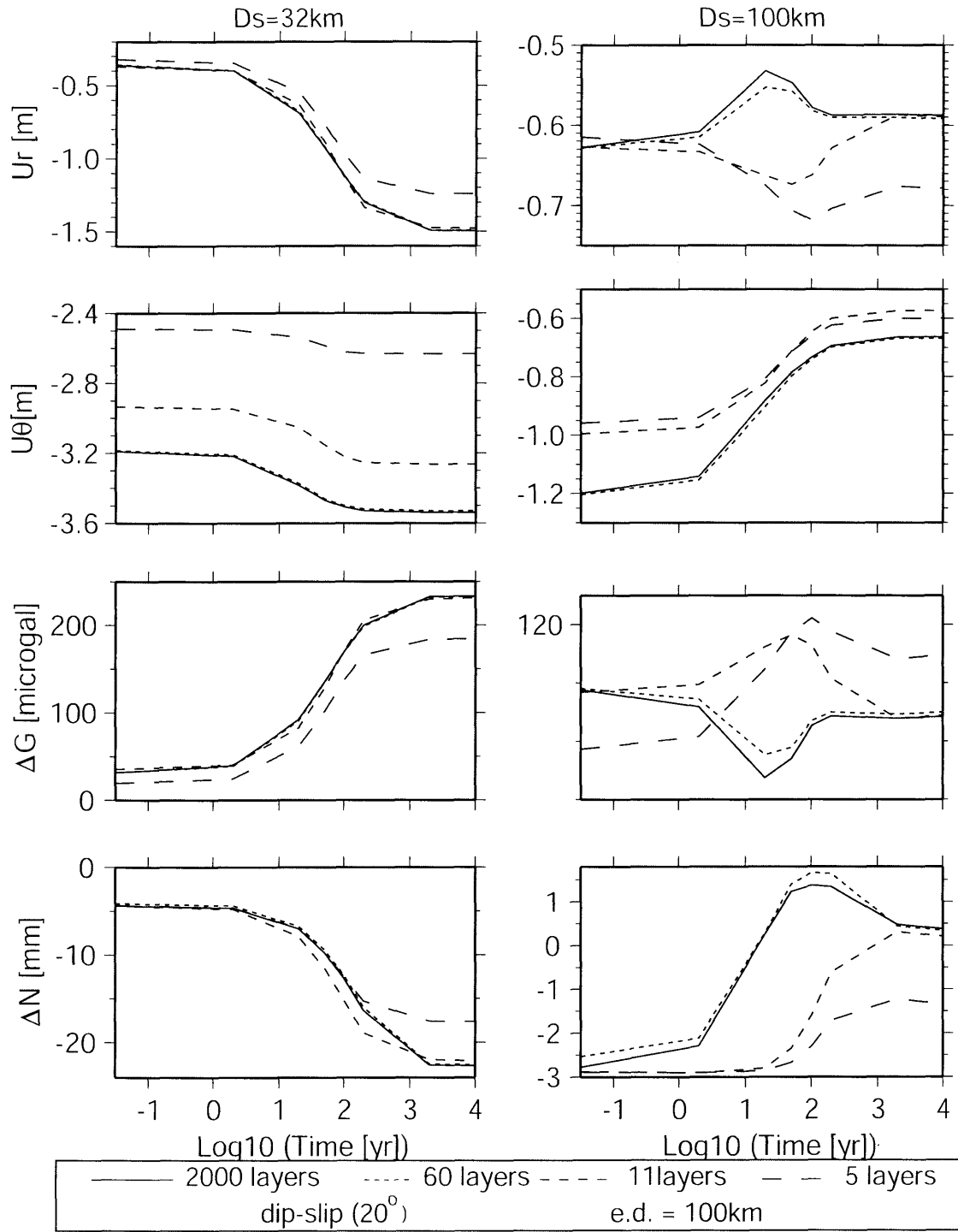


Figure 28. (a) The effect of fine layering.

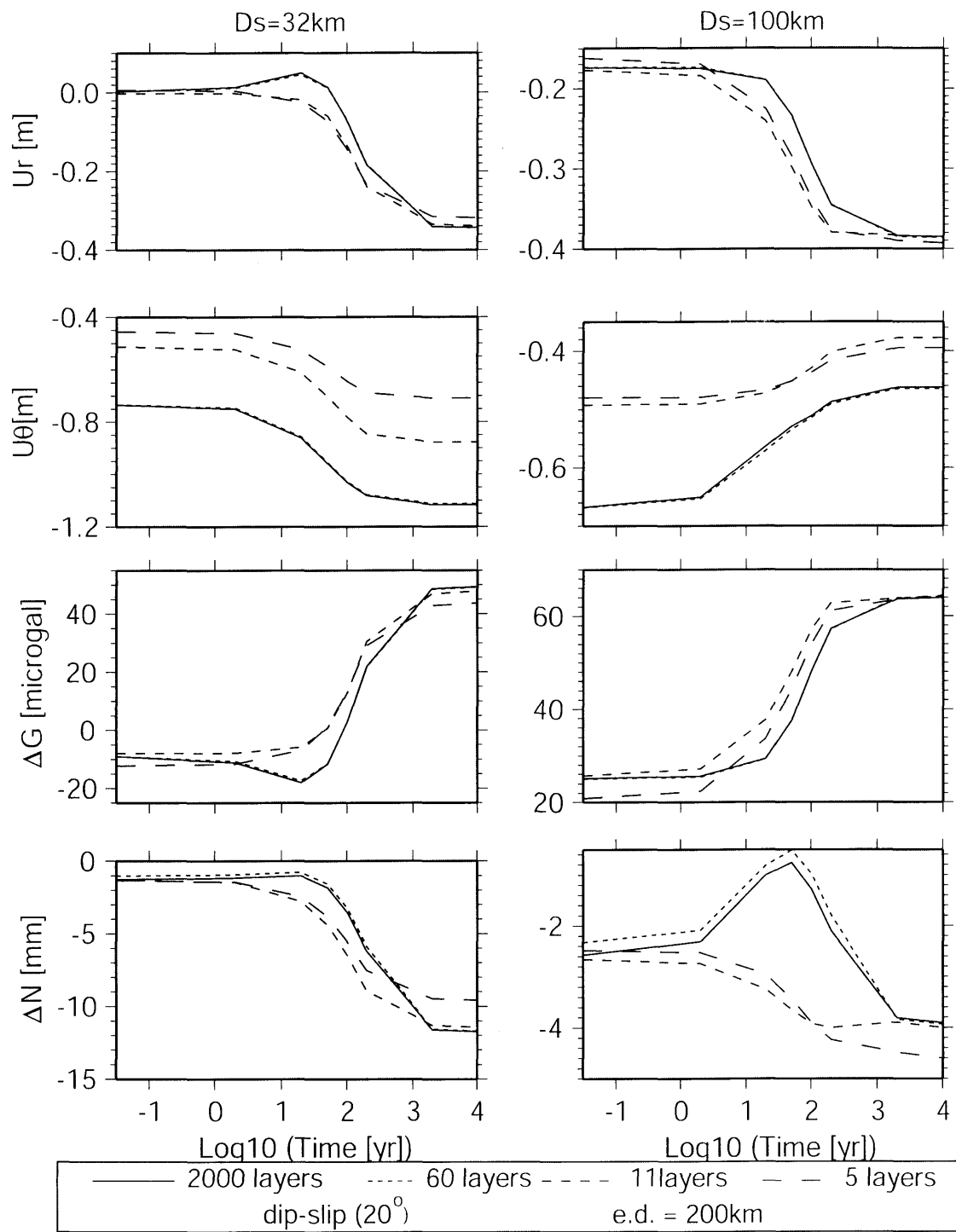


Figure 28. (b) The effect of fine layering.

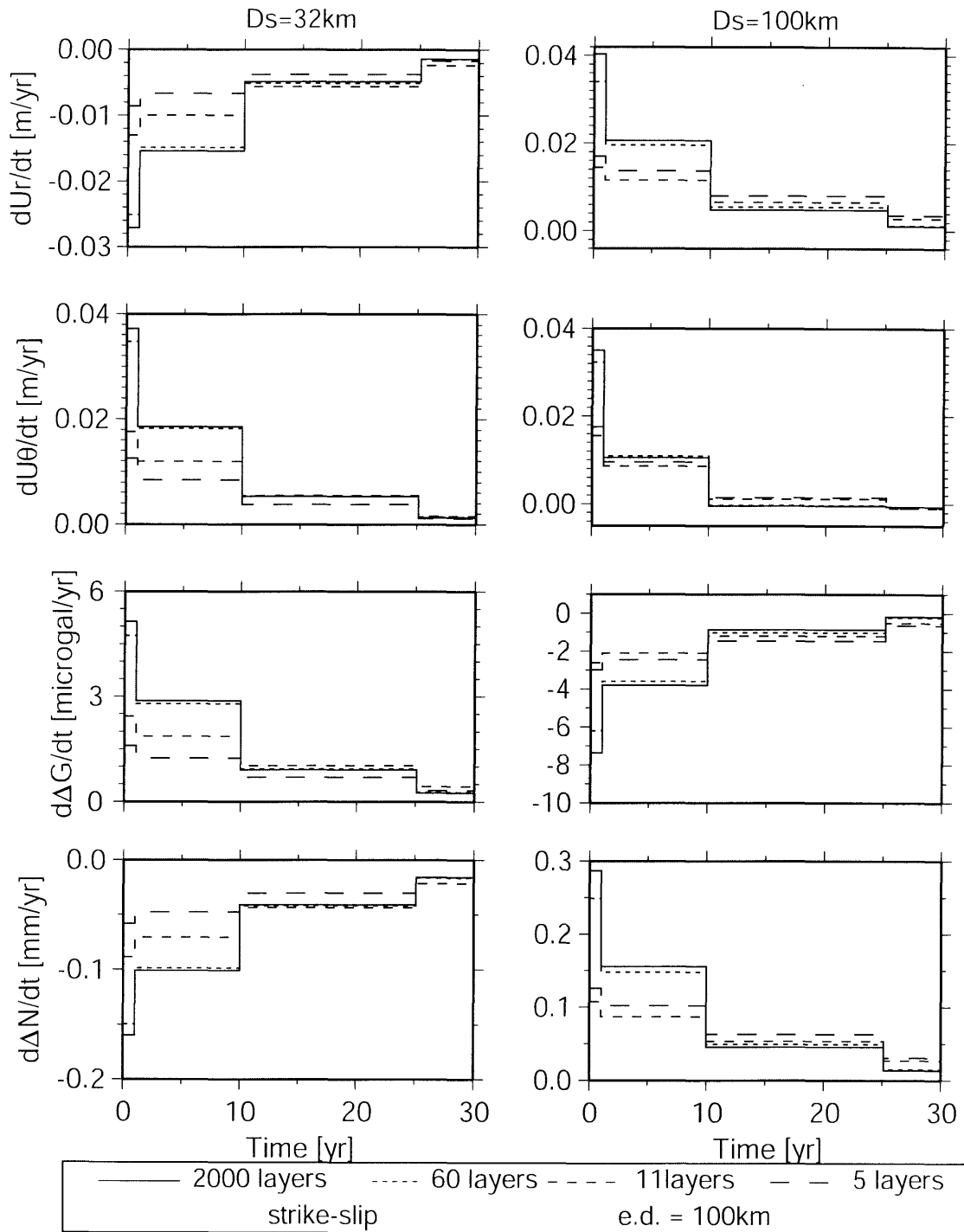


Figure 29. (a) The effect of fine layering on the deformation rate.

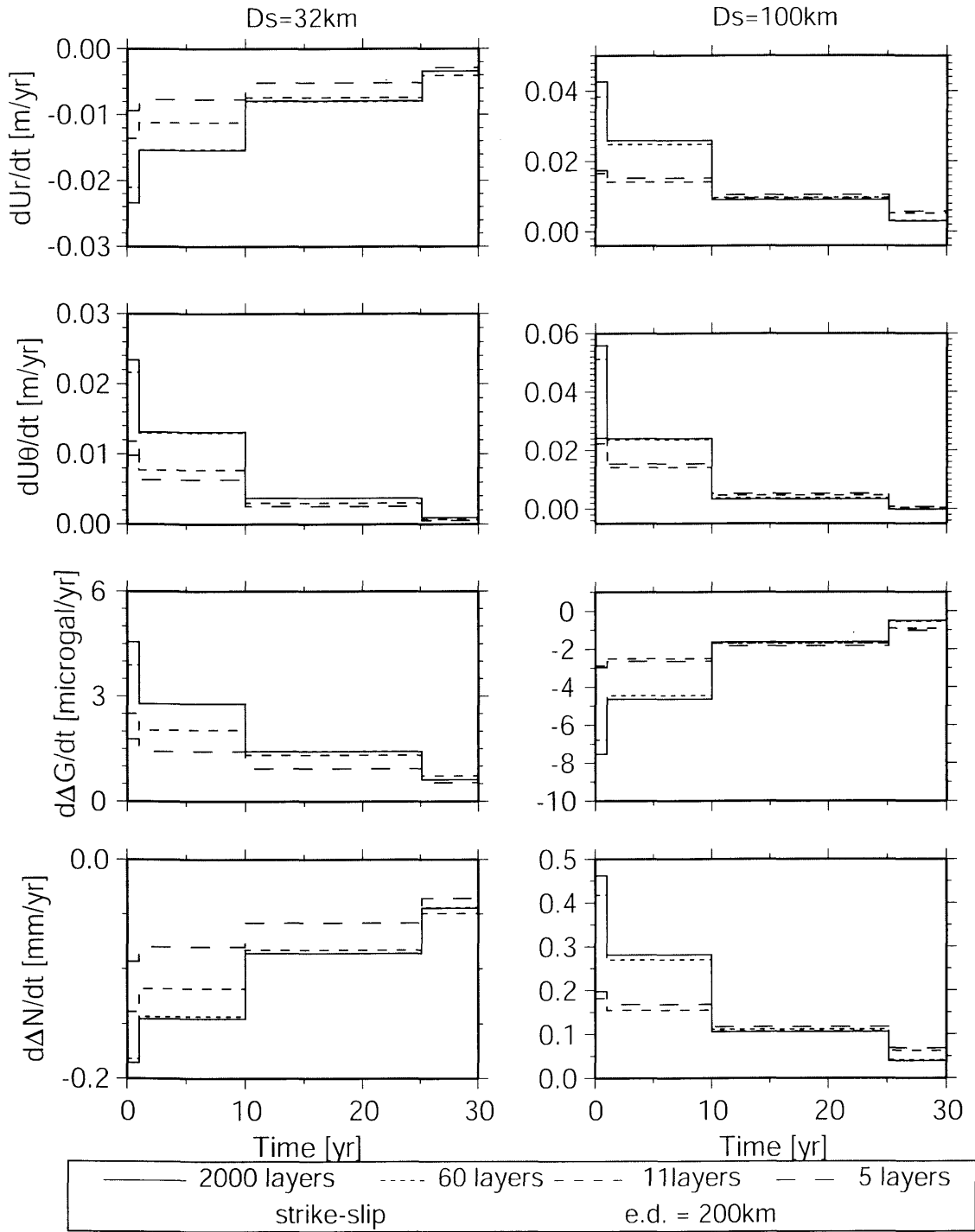


Figure 29. (b) The effect of fine layering on the deformation rate.

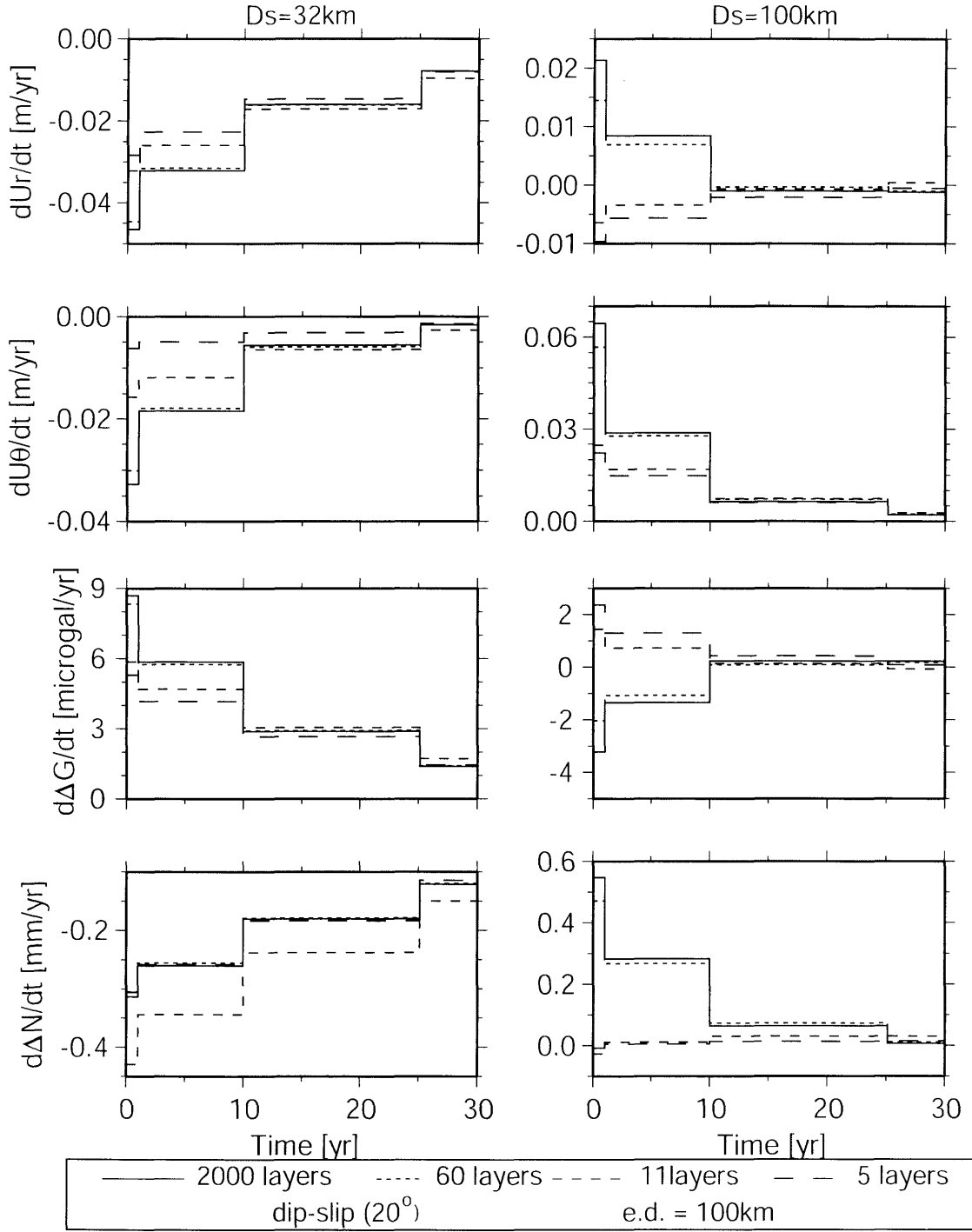


Figure 30. (a) The effect of fine layering on the deformation rate.

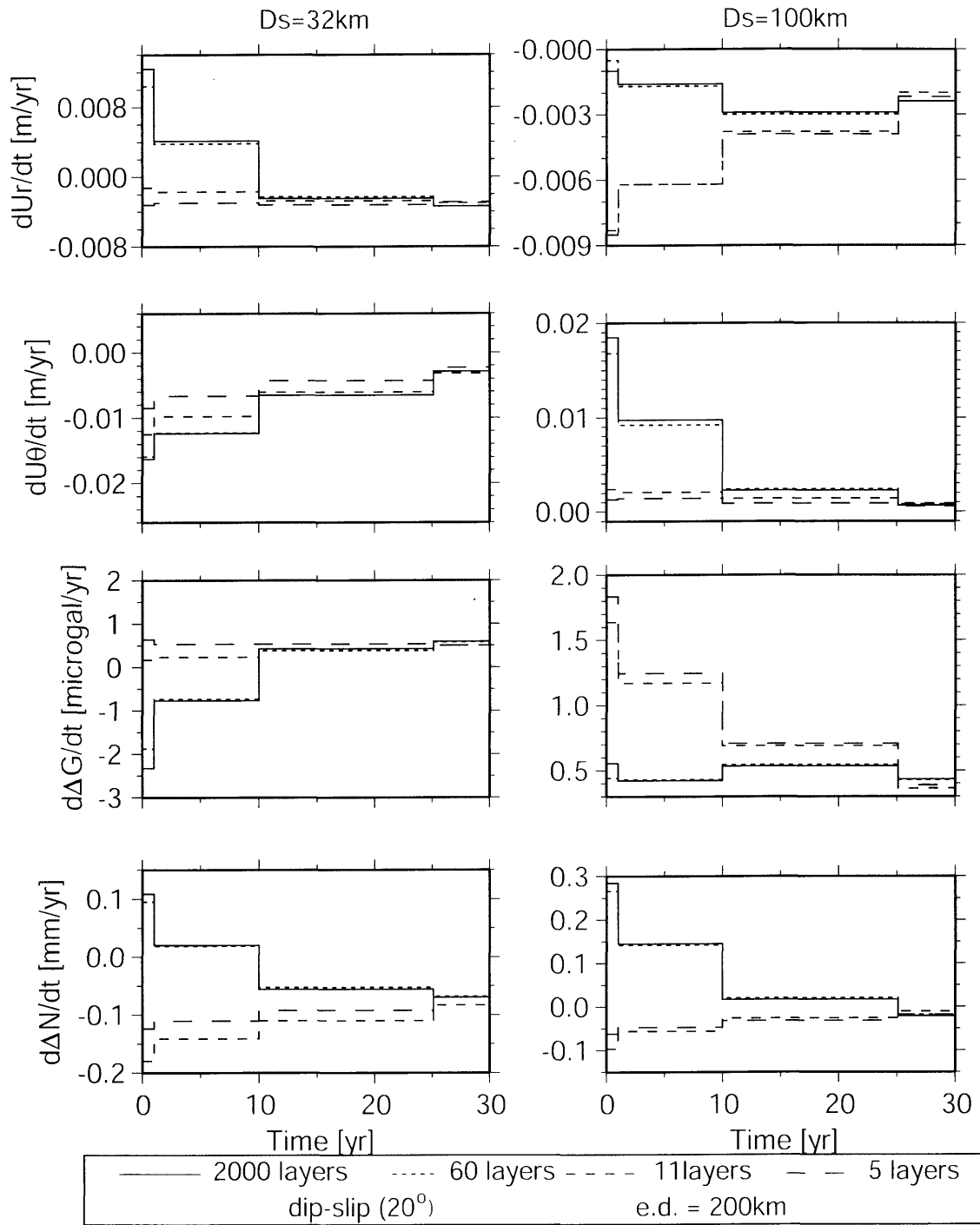


Figure 30. (b) The effect of fine layering on the deformation rate.

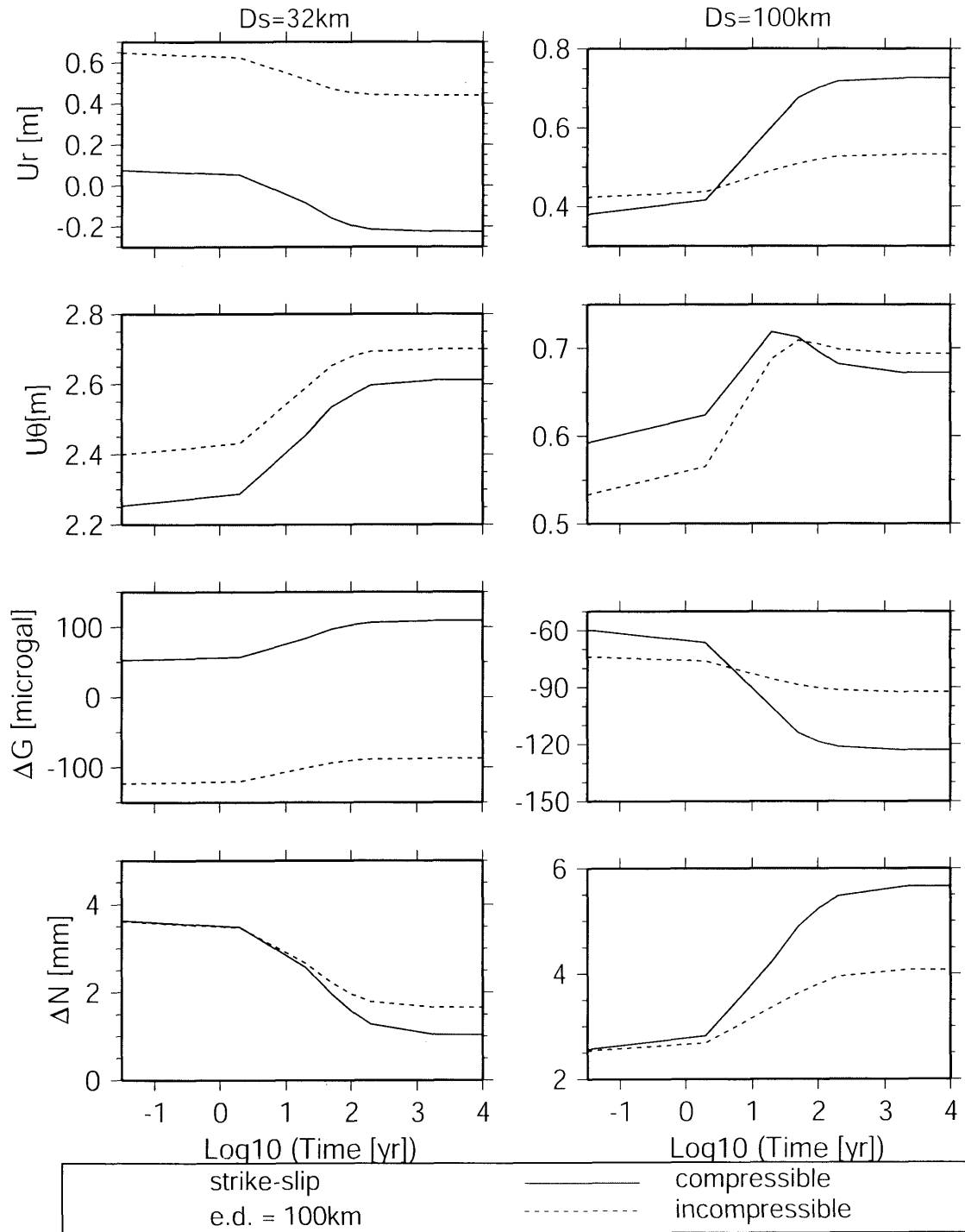


Figure 31. (a) The effect of compressibility.

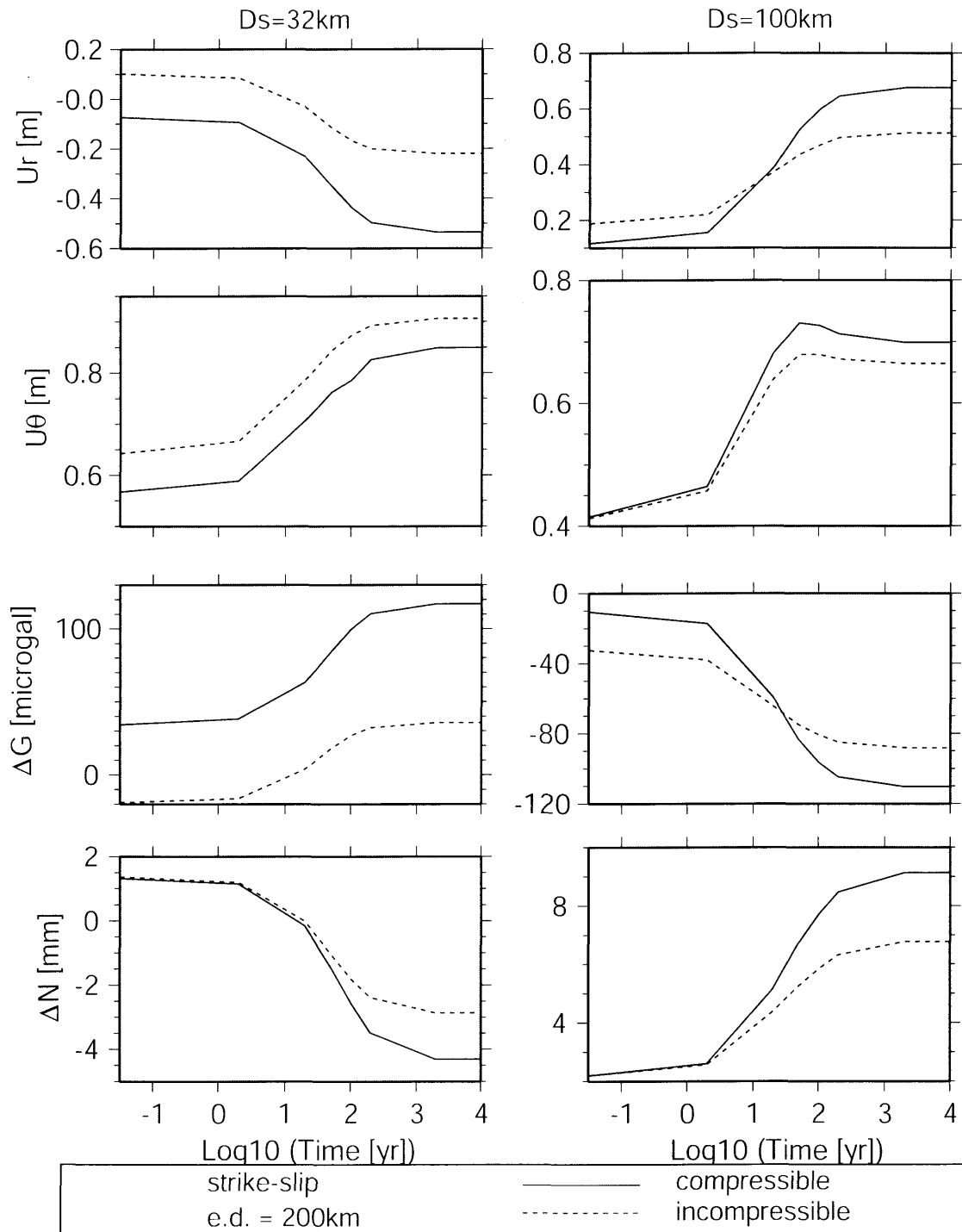


Figure 31. (b) The effect of compressibility.

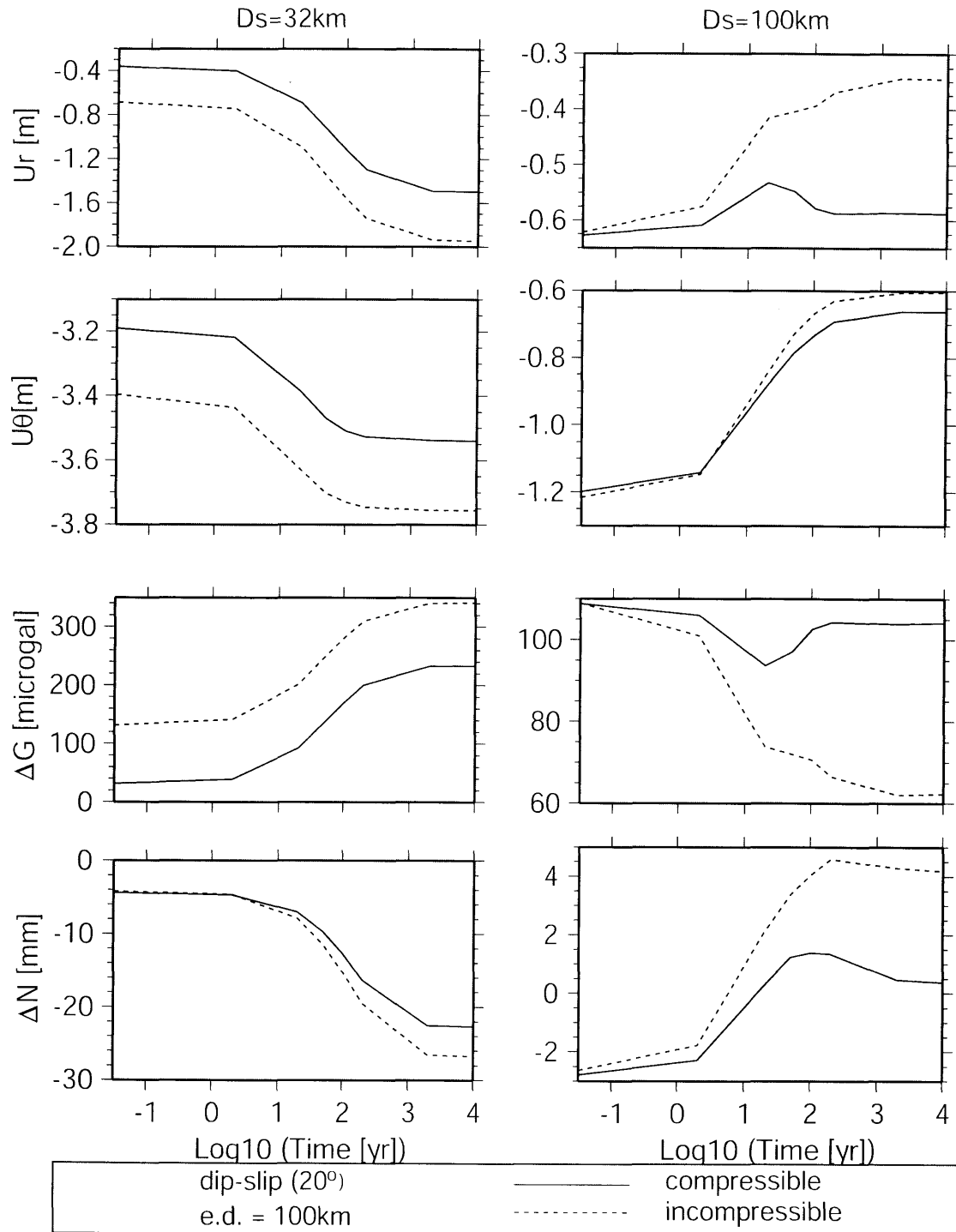


Figure 32. (a) The effect of compressibility.

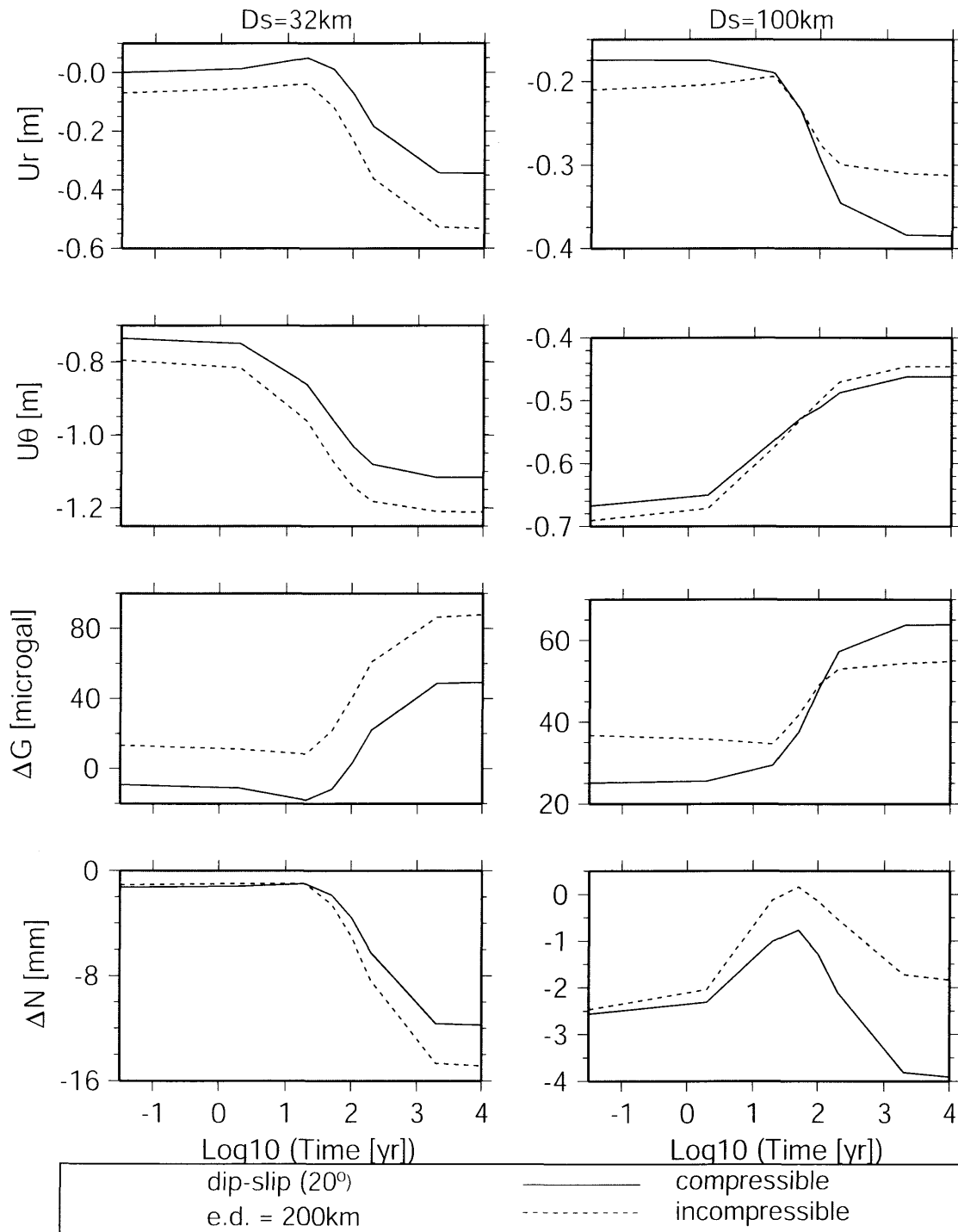


Figure 32. (b) The effect of compressibility.

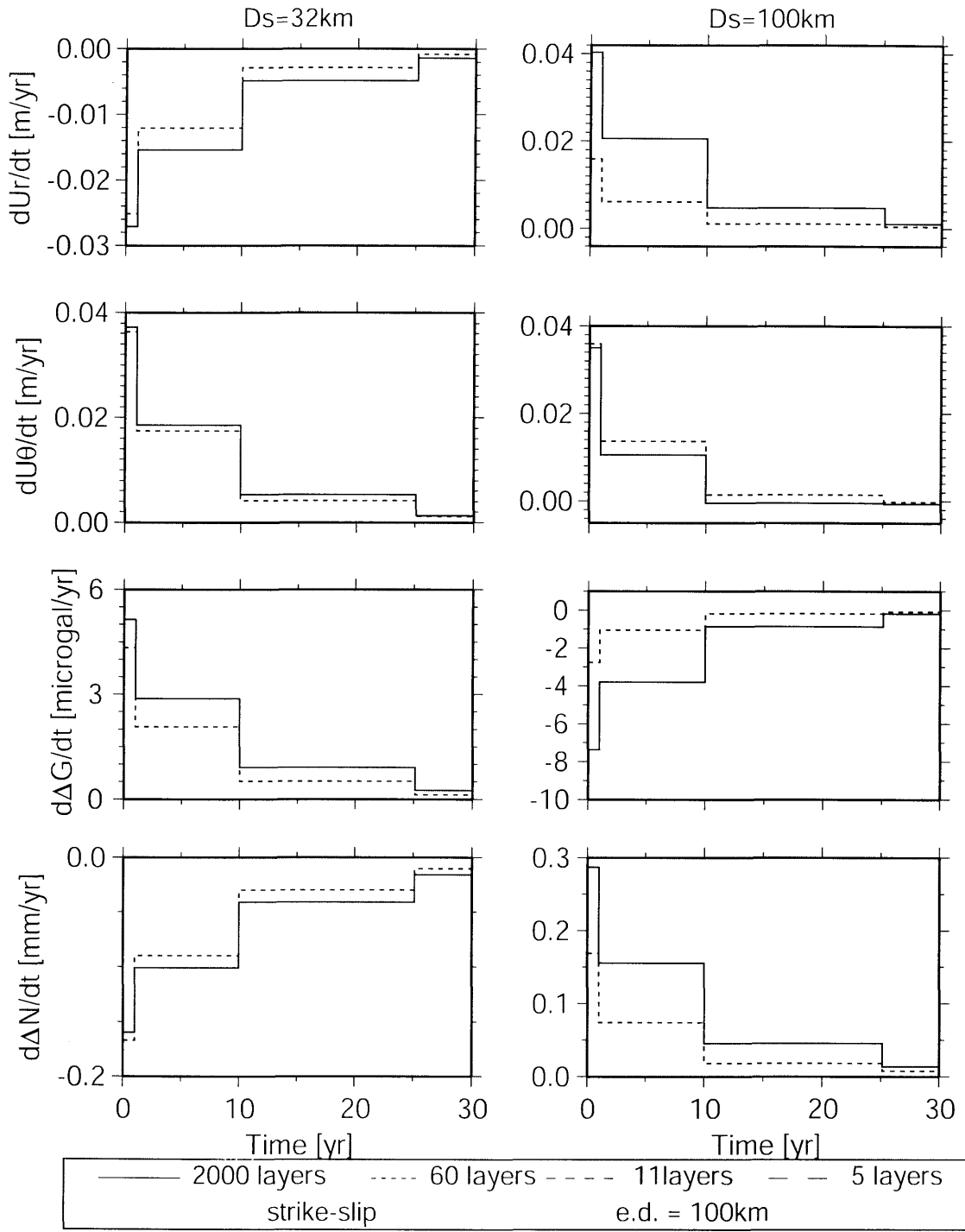


Figure 33. (a) The effect of compressibility on the deformation rate.

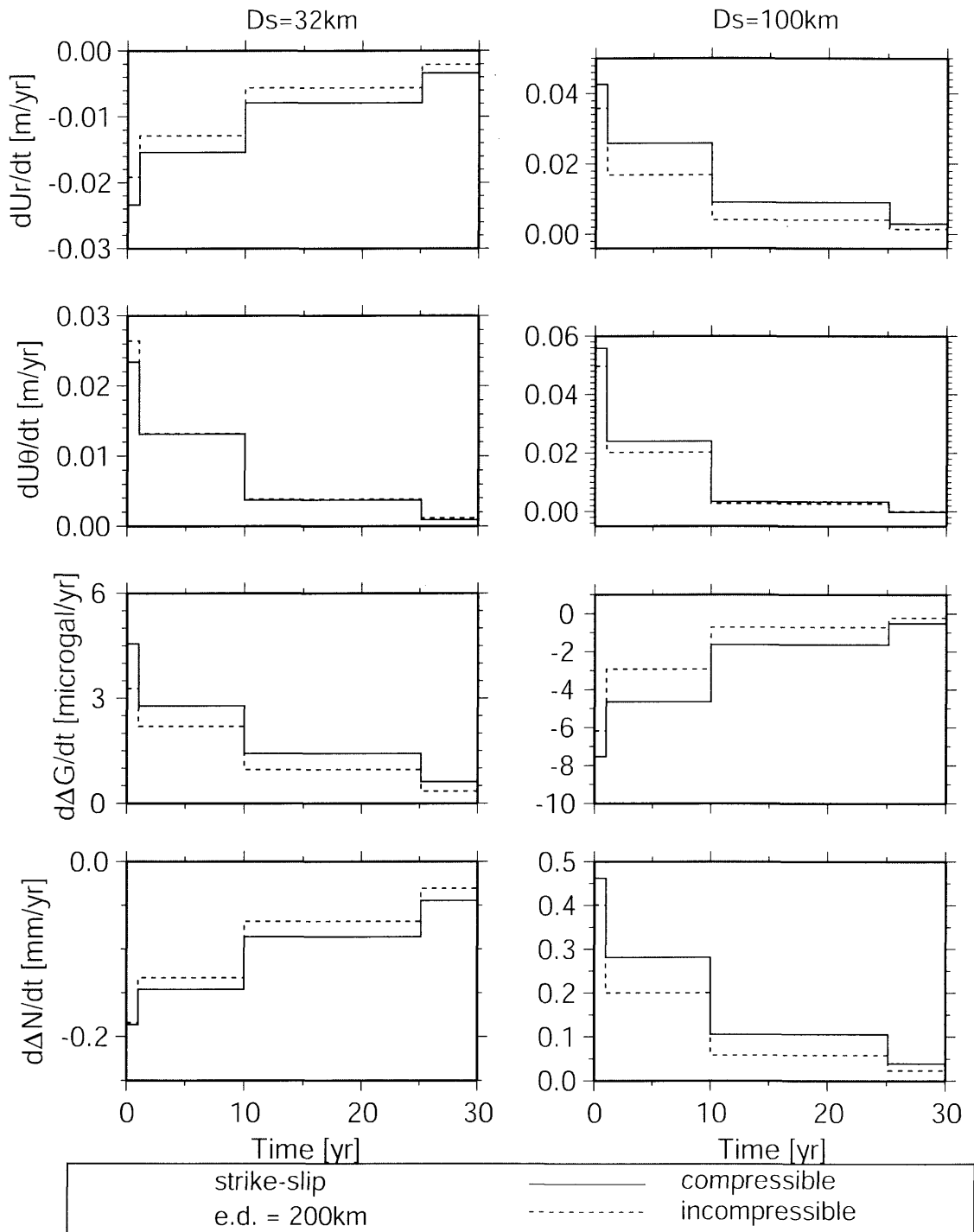


Figure 33. (b) The effect of compressibility on the deformation rate.

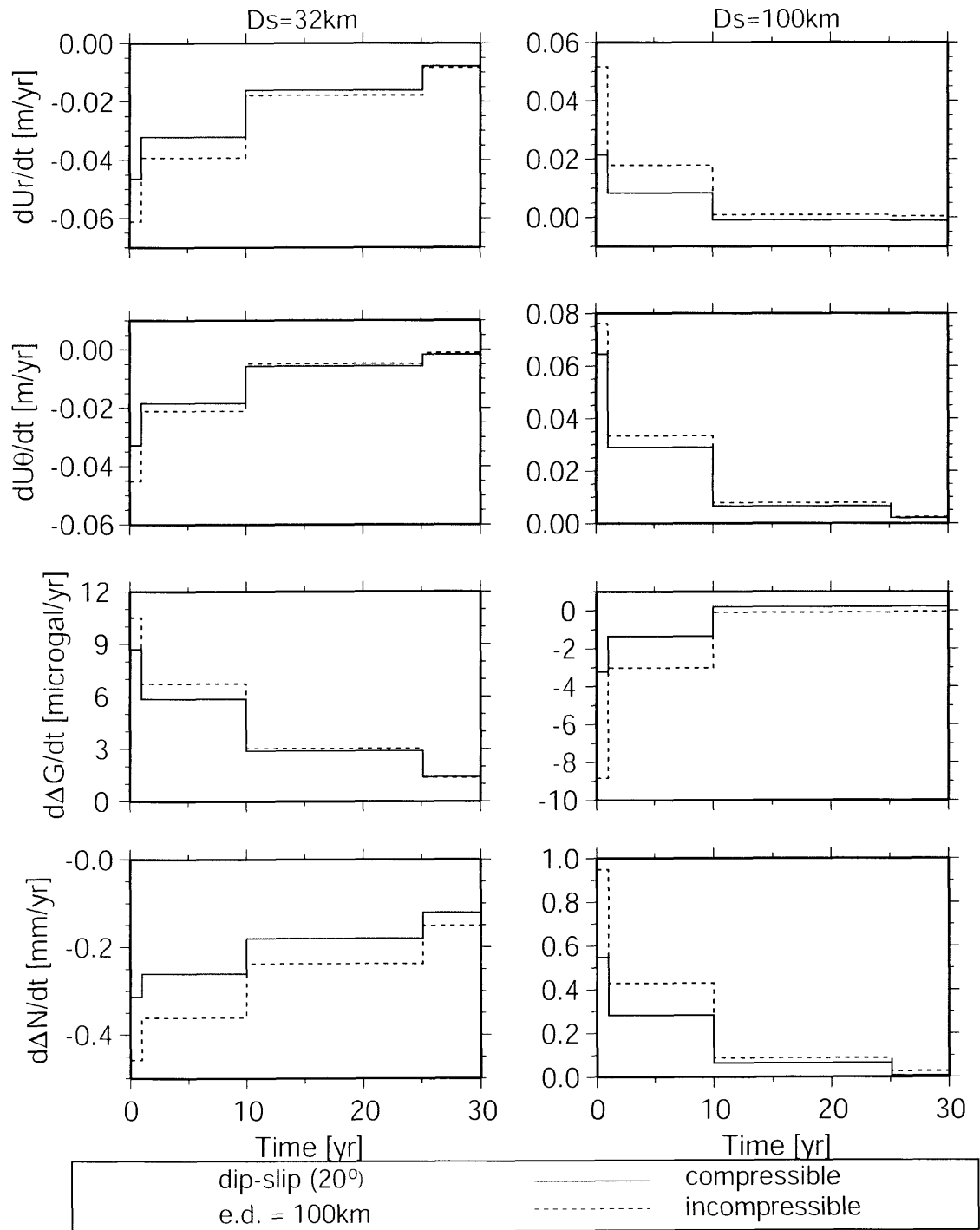


Figure 34. (a) The effect of compressibility on the deformation rate.

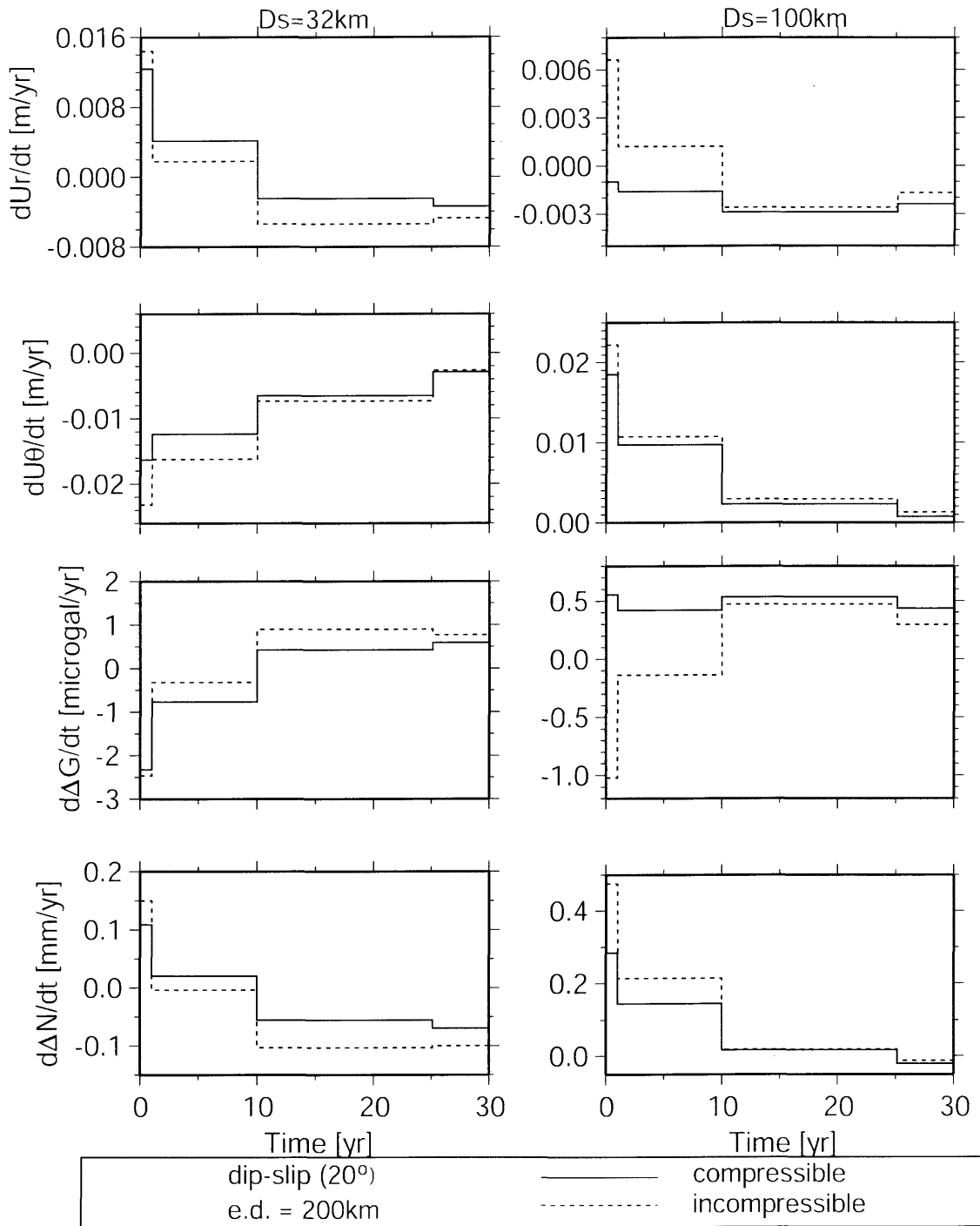


Figure 34. (b) The effect of compressibility on the deformation rate.

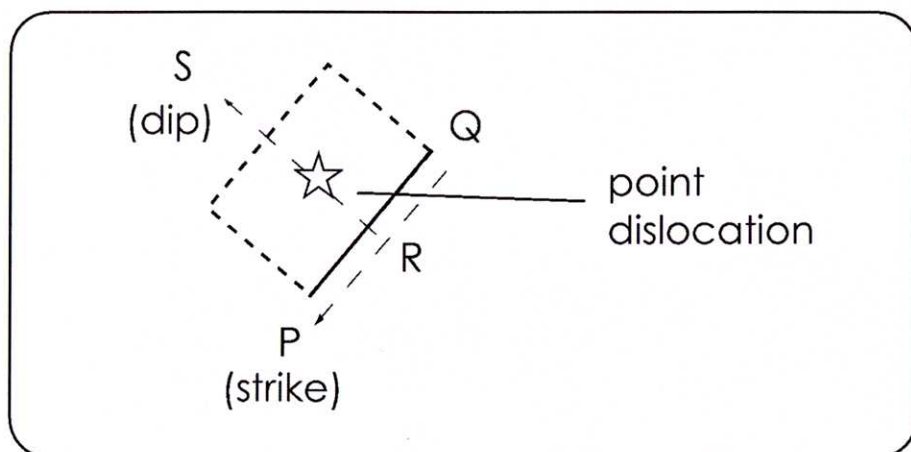
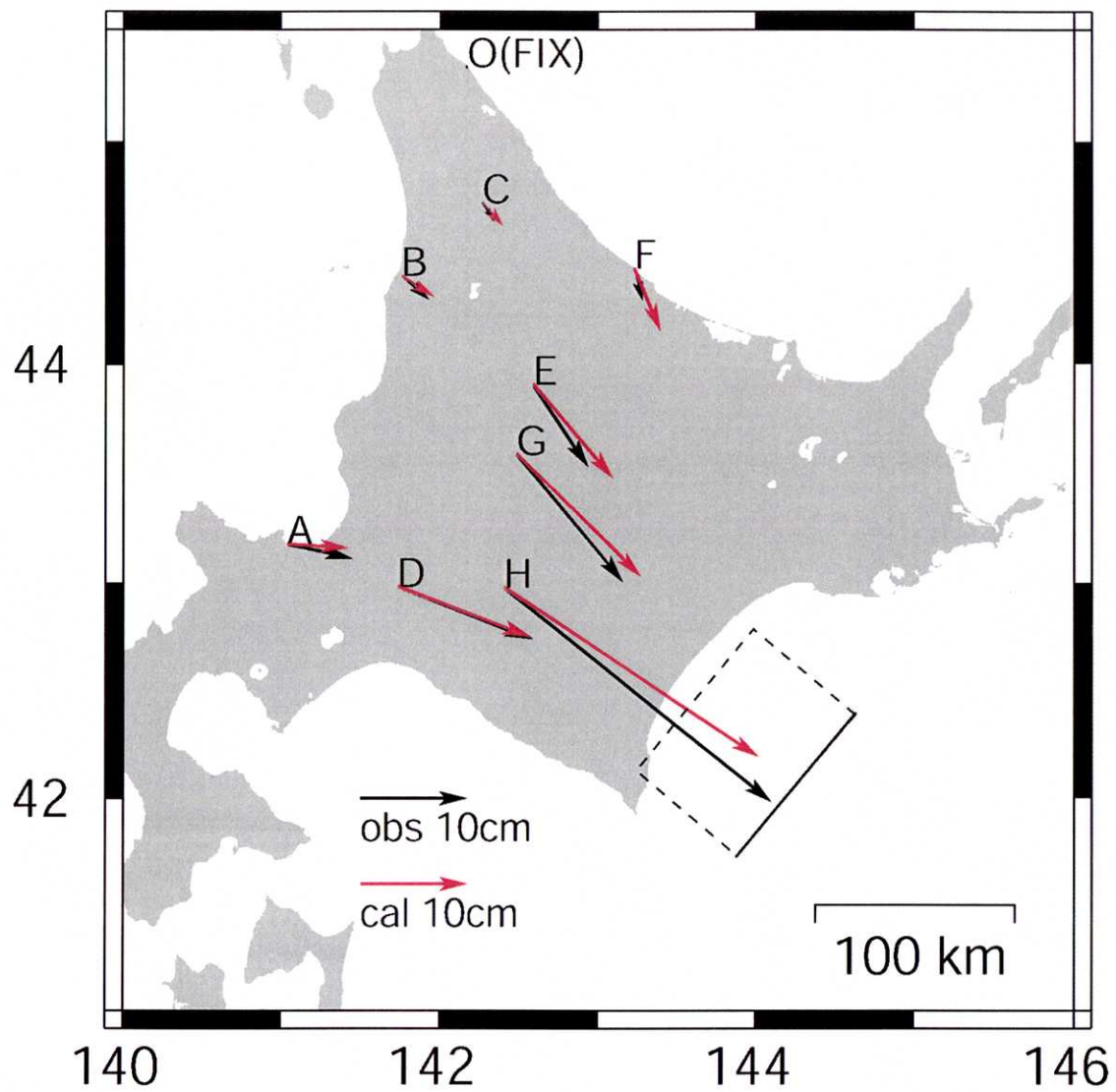


Figure 35. The coseismic deformation in the far field

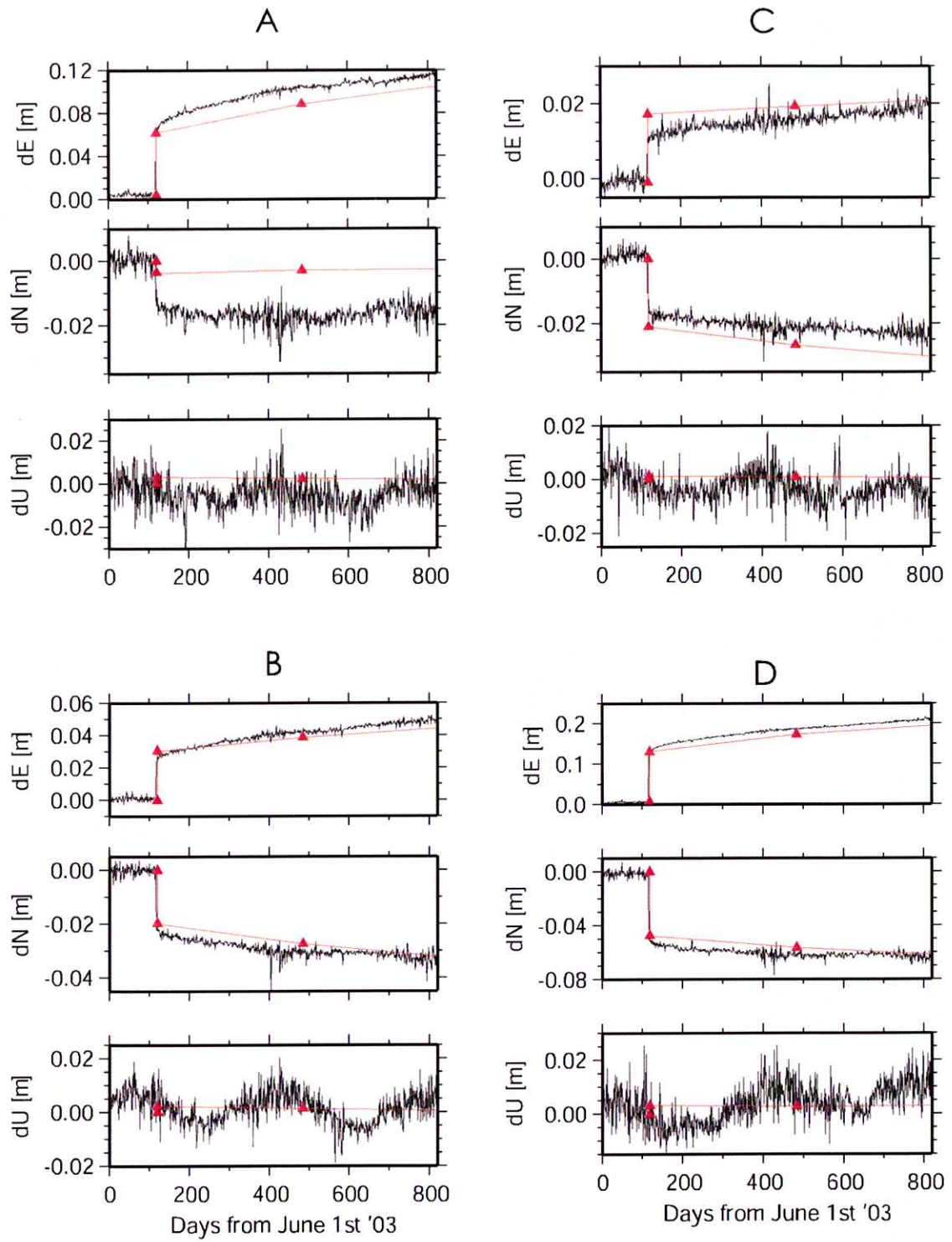


Figure 36. (a) The time series of the coseismic and postseismic deformation. A to D correspond to the stations in Fig. 35.

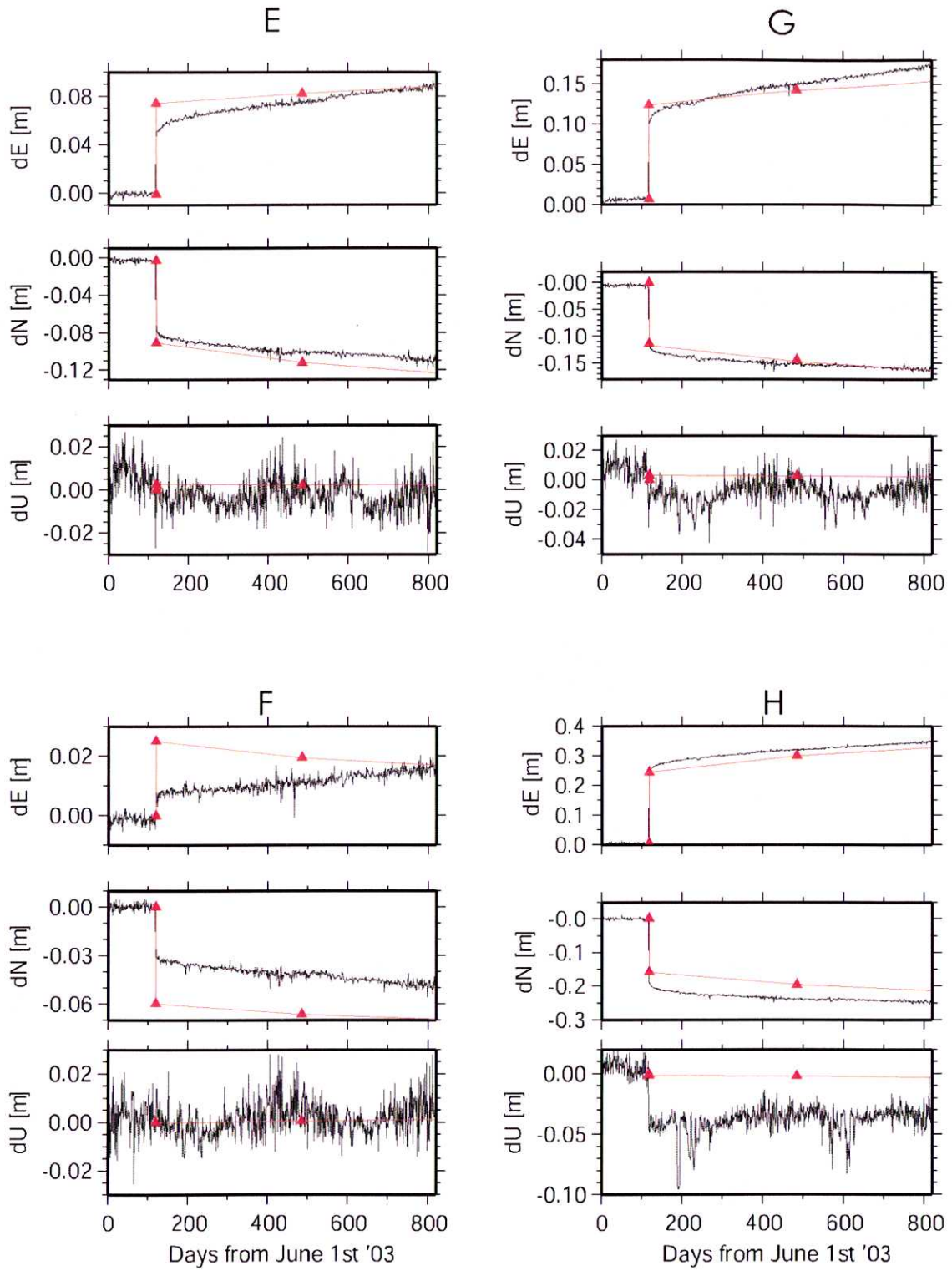
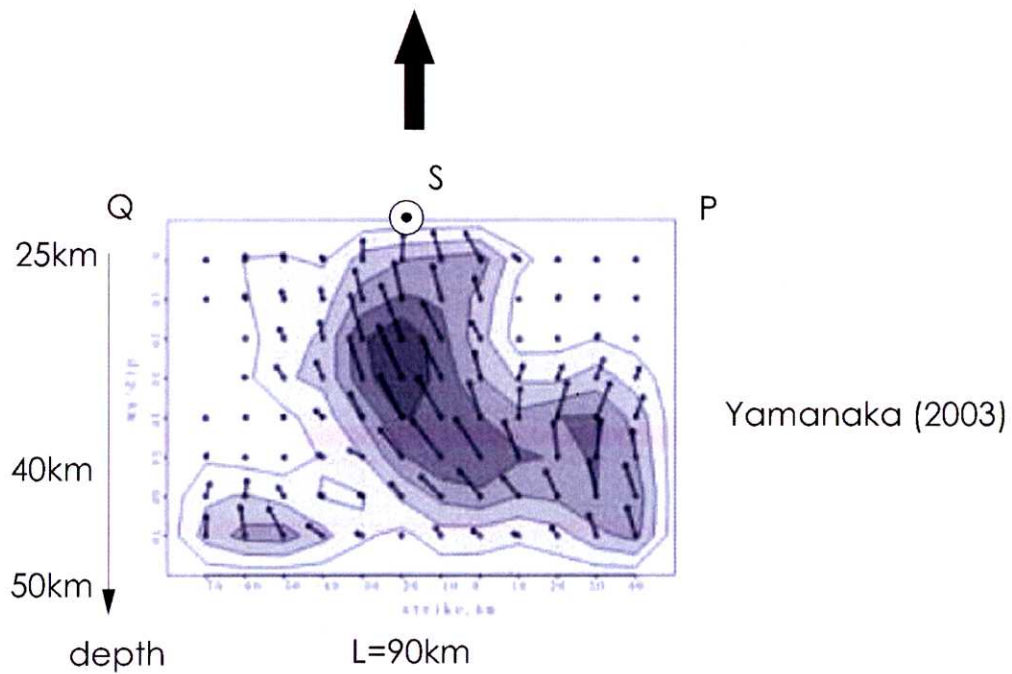
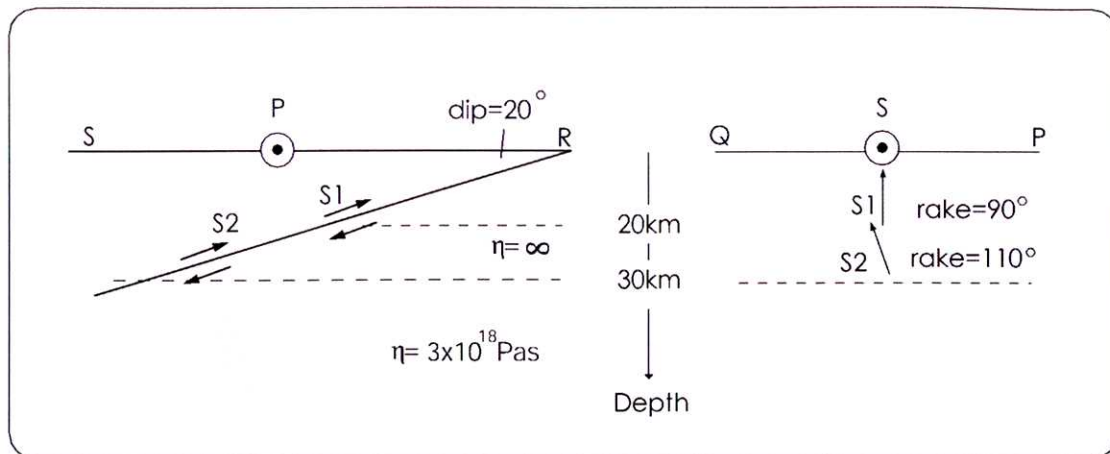


Figure 36. (b) The time series of the coseismic and postseismic deformation. E to H correspond to the stations in Fig. 35.

the two point-dislocation model

**Figure 37.** The viscoelastic structure and the fault model

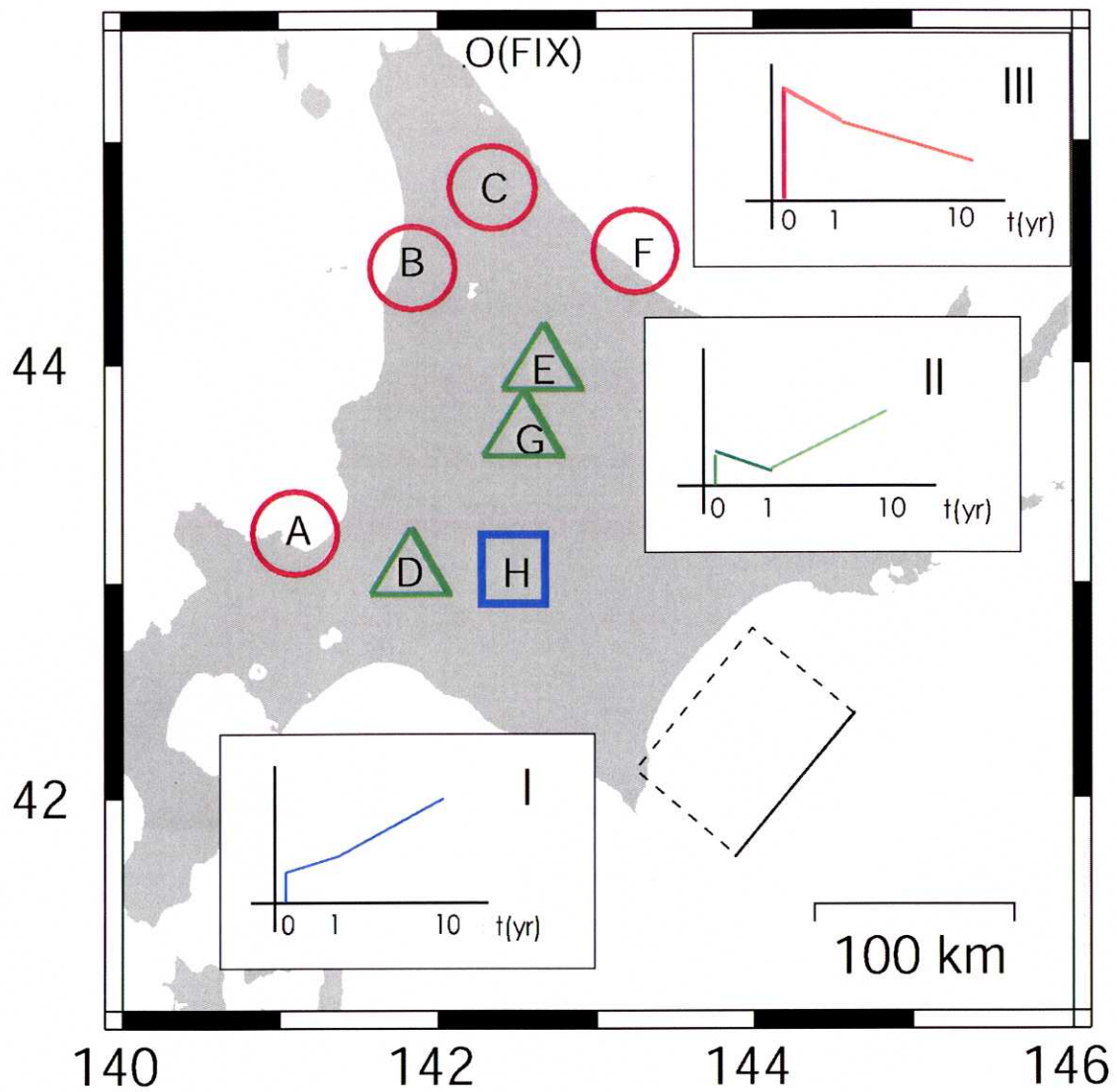
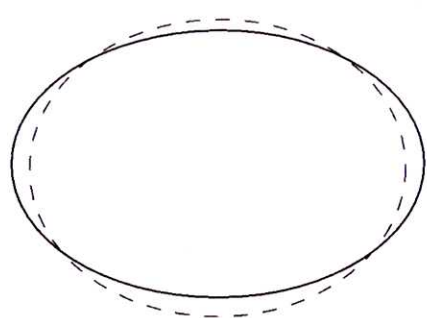
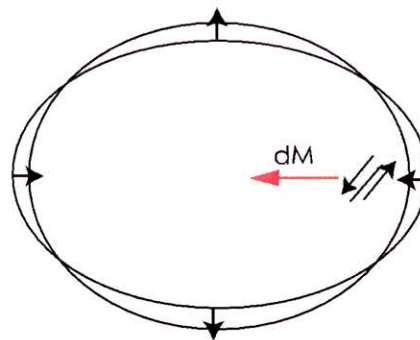


Figure 38. Pattern change of the postseismic vertical displacement. The station indicated by circles, triangles and squares correspond to the pattern I, II and III in the figure, respectively.



$$J_2 > 0$$

the reference ellipsoid



$$\delta J_2 < 0$$

mass redistribution
due to an earthquake

Figure 39. Earth's flattening and its change due to earthquakes

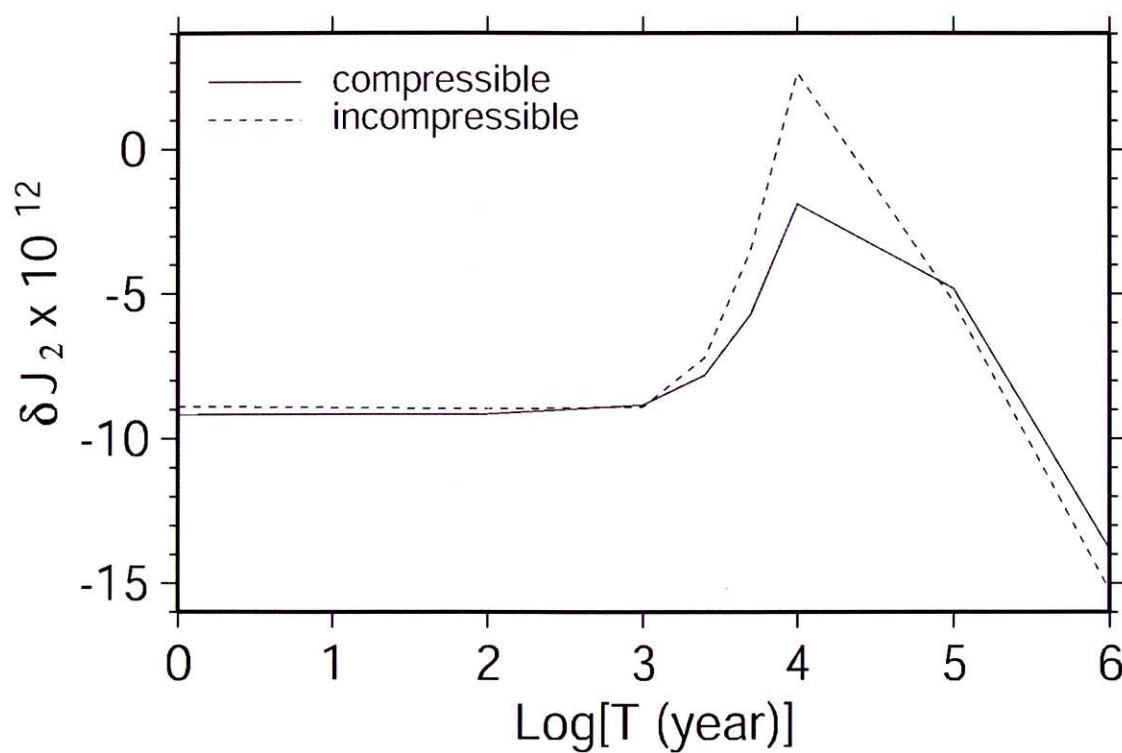


Figure 40. The time variation of J_2 due to the Sumatra-Andaman Islands Earthquake

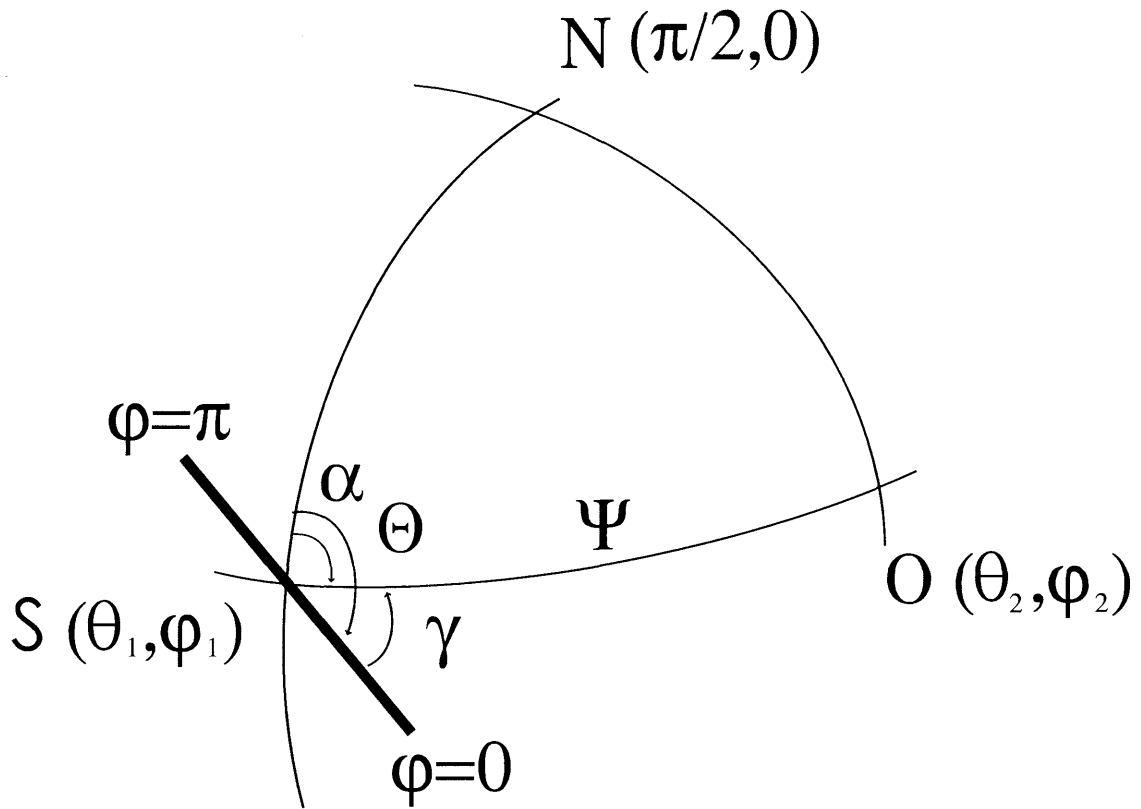


Figure 41. Calculation for the arbitrary point on the sphere